Fermilab

The Atacama Cosmology Telescope: DR6 Constraints on Extended Cosmological Models

FERMILAB-PUB-25-0157-PPD

arXiv:2503.14454

arXiv:2503.14454v1 [astro-ph.CO] 18 Mar 2025

The Atacama Cosmology Telescope: DR6 Constraints on Extended Cosmological Models

ERMINIA CALABRESE,[1, *] J. COLIN HILL,[2, 3, †] HIDDE T. JENSE,[1] ADRIEN LA POSTA,[4] IRENE ABRIL-CABEZAS,[5, 6]
GRAEME E. ADDISON,[7] PETER A. R. ADE,[1] SIMONE AIOLA,[3, 8] TOMMY ALFORD,[9] DAVID ALONSO,[4] MANDANA AMIRI,[10]
RUI AN,[11] ZACHARY ATKINS,[8] JASON E. AUSTERMANN,[12] ELEONORA BARBAVARA,[13] NICOLA BARBIERI,[14, 15]
NICHOLAS BATTAGLIA,[16, 17] ELIA STEFANO BATTISTELLI,[13] JAMES A. BEALL,[12] RACHEL BEAN,[16] ALI BEHESHTI,[18]
BENJAMIN BERINGUE,[17] TANAY BHANDARKAR,[19] EMILY BIERMANN,[20] BORIS BOLLIET,[21, 6] J RICHARD BOND,[22]
VALENTINA CAPALBO,[13] FELIPE CARRERO,[23] STEPHEN CHEN,[24] GRACE CHESMORE,[9] HSIAO-MEI CHO,[25, 12] STEVE K. CHOI,[26]
SUSAN E. CLARK,[27, 28] NICHOLAS F. COTHARD,[29] KEVIN COUGHLIN,[9] WILLIAM COULTON,[6, 5] DEVIN CRICHTON,[30]
KEVIN T. CROWLEY,[31] OMAR DARWISH,[32] MARK J. DEVLIN,[19] SIMON DICKER,[19] CODY J. DUELL,[33] SHANNON M. DUFF,[12]
ADRIAAN J. DUIVENVOORDEN,[34] JO DUNKLEY,[8, 35] ROLANDO DUNNER,[23] CARMEN EMBIL VILLAGRA,[5, 6] MAX FANKHANEL,[36]
GERRIT S. FARREN,[37, 38] SIMONE FERRARO,[37, 39, 38] ALLEN FOSTER,[8] RODRIGO FREUNDT,[16] BRITTANY FUZIA,[40]
PATRICIO A. GALLARDO,[9, 19] XAVIER GARRIDO,[41] MARTINA GERBINO,[15] SERENA GIARDIELLO,[1] AJAY GILL,[42]
JAHMOUR GIVANS,[35] VERA GLUSCEVIC,[11] SAMUEL GOLDSTEIN,[2] JOSEPH E. GOLEC,[9] YULIN GONG,[16] YILUN GUAN,[43]
MARK HALPERN,[10] IAN HARRISON,[1] MATTHEW HASSELFIELD,[3] ADAM HE,[11] ERIN HEALY,[9, 8] SHAWN HENDERSON,[25]
BRANDON HENSLEY,[44] CARLOS HERVÍAS-CAIMAPO,[23] GENE C. HILTON,[12] MATT HILTON,[45, 46] ADAM D. HINCKS,[47, 48]
RENÉE HLOŽEK,[43, 47] SHUAY-PWU PATTY HO,[8] JOHN HOOD,[49] ERIKA HORNECKER,[47] ZACHARY B. HUBER,[33]
JOHANNES HUBMAYR,[12] KEVIN M. HUFFENBERGER,[50] JOHN P. HUGHES,[51] MARGARET IKAPE,[47] KENT IRWIN,[27]
GIOVANNI ISOPI,[13] NEHA JOSHI,[19] BEN KELLER,[33] JOSHUA KIM,[19] KENDA KNOWLES,[52] BRIAN J. KOOPMAN,[53]
ARTHUR KOSOWSKY,[18] DARBY KRAMER,[54] ALEKSANDRA KUSIAK,[55, 6] ALEX LAGUË,[19] VICTORIA LAKEY,[56]
MASSIMILIANO LATTANZI,[15] EUNSEONG LEE,[19] YAQIONG LI,[33] ZACK LI,[39, 38] MICHELE LIMON,[19] MARTINE LOKKEN,[57]
THIBAUT LOUIS,[41] MARIUS LUNGU,[9] NIALL MACCRANN,[5, 6] AMANDA MACINNIS,[58] MATHEW S. MADHAVACHERIL,[19]
DIEGO MALDONADO,[36] FELIPE MALDONADO,[40] MAYA MALLABY-KAY,[49] GABRIELA A. MARQUES,[59, 60]
JOSHIWA VAN MARREWIJK,[61] FIONA MCCARTHY,[5, 6] JEFF MCMAHON,[60, 49, 9, 62] YOGESH MEHTA,[54] FELIPE MENANTEAU,[63, 64]
KAVILAN MOODLEY,[46] THOMAS W. MORRIS,[53, 65] TONY MROCZKOWSKI,[66] SIGURD NAESS,[67] TOSHIYA NAMIKAWA,[5, 6, 68]
FEDERICO NATI,[69] SIMRAN K. NERVAL,[47, 43] LAURA NEWBURGH,[53] ANDRINA NICOLA,[70] MICHAEL D. NIEMACK,[33, 16]
MICHAEL R. NOLTA,[22] JOHN ORLOWSKI-SCHERER,[19] LUCA PAGANO,[14, 15, 71] LYMAN A. PAGE,[8] SHIVAM PANDEY,[2]
BRUCE PARTRIDGE,[72] KAREN PEREZ SARMIENTO,[19] HEATHER PRINCE,[51] ROBERTO PUDDU,[23] FRANK J. QU,[27, 28, 6]
DAMIEN C. RAGAVAN,[45] BERNARDITA RIED GUACHALLA,[27, 28] KEIR K. ROGERS,[73, 43] FELIPE ROJAS,[23] TAI SAKUMA,[8]
EMMANUEL SCHAAN,[25, 28] BENJAMIN L. SCHMITT,[19] NEELIMA SEHGAL,[58] SHABBIR SHAIKH,[54] BLAKE D. SHERWIN,[5, 6]
CARLOS SIERRA,[9] JON SIEVERS,[74] CRISTÓBAL SIFÓN,[75] SARA SIMON,[59] RITA SONKA,[8] DAVID N. SPERGEL,[3]
SUZANNE T. STAGGS,[8] EMILIE STORER,[74, 8] KRISTEN SURRAO,[2] ERIC R. SWITZER,[29] NIKLAS TAMPIER,[36]
LEANDER THIELE,[76, 68] ROBERT THORNTON,[77, 19] HY TRAC,[78] CAROLE TUCKER,[1] JOEL ULLOM,[12] LEILA R. VALE,[12]
ALEXANDER VAN ENGELEN,[54] JEFF VAN LANEN,[12] CRISTIAN VARGAS,[50] EVE M. VAVAGIAKIS,[79, 33] KASEY WAGONER,[80, 8]
YUHAN WANG,[33] LUKAS WENZL,[16] EDWARD J. WOLLACK,[29] AND KAIWEN ZHENG[8]

(Affiliations can be found at the end of the document)

ABSTRACT

We use new cosmic microwave background (CMB) primary temperature and polarization anisotropy measurements from the Atacama Cosmology Telescope (ACT) Data Release 6 (DR6) to test foundational assumptions of the standard cosmological model, ΛCDM, and set constraints on extensions to it. We derive constraints from the ACT DR6 power spectra alone, as well as in combination with legacy data from the *Planck* mission. To break geometric degeneracies, we include ACT and *Planck* CMB lensing data and baryon acoustic oscillation data from DESI Year-1. To test the dependence of our results on non-ACT data, we also explore combinations replacing *Planck* with *WMAP* and DESI with BOSS, and further add supernovae measurements from Pantheon+ for models that affect the late-time expansion history. We verify the near-scale-invariance (running of the spectral index $dn_s/d\ln k = 0.0062 \pm 0.0052$) and adiabaticity of the primordial perturbations. Neutrino properties are consistent with Standard Model predictions: we find no evidence for new light, relativistic species that are free-streaming ($N_{\rm eff} = 2.86 \pm 0.13$, which combined with astrophysical measurements of primordial helium and deuterium abundances becomes $N_{\rm eff} = 2.89 \pm 0.11$), for non-zero neutrino masses ($\sum m_\nu < 0.082$ eV at 95% CL), or for neutrino self-interactions. We also find no evidence for self-interacting dark radiation ($N_{\rm idr} < 0.134$), or for early-universe variation of fundamental con-

stants, including the fine-structure constant ($\alpha_{\rm EM}/\alpha_{\rm EM,0} = 1.0043 \pm 0.0017$) and the electron mass ($m_e/m_{e,0} = 1.0063 \pm 0.0056$). Our data are consistent with standard big bang nucleosynthesis (we find $Y_p = 0.2312 \pm 0.0092$), the *COBE/FIRAS*-inferred CMB temperature (we find $T_{\rm CMB} = 2.698 \pm 0.016$ K), a dark matter component that is collisionless and with only a small fraction allowed as axion-like particles, a cosmological constant ($w = -0.986 \pm 0.025$), and the late-time growth rate predicted by general relativity ($\gamma = 0.663 \pm 0.052$). We find no statistically significant preference for a departure from the baseline ΛCDM model. In fits to models invoking early dark energy, primordial magnetic fields, or an arbitrary modified recombination history, we find $H_0 = 69.9^{+0.8}_{-1.5}$, 69.1 ± 0.5, or 69.6 ± 1.0 km/s/Mpc, respectively; using BOSS instead of DESI BAO data reduces the central values of these constraints by 1–1.5 km/s/Mpc while only slightly increasing the error bars. In general, models introduced to increase the Hubble constant or to decrease the amplitude of density fluctuations inferred from the primary CMB are not favored over ΛCDM by our data.

Contents

* Corresponding author: Erminia Calabrese, calabresee@cardiff.ac.uk
† Corresponding author: Colin Hill, jch2200@columbia.edu

1. INTRODUCTION

The Λ cold dark matter (ΛCDM) cosmological model has emerged as the standard model of cosmology over the past quarter-century, undergirded by precision measurements of the cosmic microwave background (CMB) primary anisotropy power spectra in both temperature and polarization (e.g., Spergel et al. 2003; Bennett et al. 2013; Planck Collaboration 2020c; Rosenberg et al. 2022; Tristram et al. 2024; Choi et al. 2020; Balkenhol et al. 2023; Chou et al. 2025, and upcoming South Pole Telescope results), the expansion history of the universe as probed by baryon acoustic oscillations (BAO; Eisenstein et al. 2005; Dawson et al. 2013; DESI Collaboration 2024a) and Type Ia supernovae measurements (SNIa; Riess et al. 1998; Perlmutter et al. 1999; Rubin et al. 2015, 2023; Scolnic et al. 2018, 2022; DES Collaboration 2024), the growth of structure from gravitational lensing and galaxy clustering measurements (e.g., Tegmark et al. 2004; Smith et al. 2007; Das et al. 2011; van Engelen et al. 2012; Planck Collaboration 2020d; Carron et al. 2022; Bianchini et al. 2020; Qu et al. 2024b; Ge et al. 2024; DES Collaboration 2022; Amon et al. 2022; Secco et al. 2022; Heymans et al. 2021; Asgari et al. 2021; More et al. 2023; Miyatake et al. 2023; Sugiyama et al. 2023; Dalal et al. 2023; Li et al. 2023a; Dark Energy Survey and Kilo-Degree Survey Collaboration 2023; Alam et al. 2017, 2021; Philcox & Ivanov 2022; DESI Collaboration 2024c), and a wide array of additional probes. However, there is strong motivation to further test the model and its underlying ingredients, particularly given our lack of microphysical knowledge of the dark sector. The CMB is a uniquely powerful probe of extensions to ΛCDM (e.g., Planck Collaboration 2020c; Aiola et al. 2020; Balkenhol et al. 2021), both because of the theoretical accuracy with which new signals can be predicted in the CMB and because the CMB is sensitive to weakly-coupled new physics that is often otherwise difficult to probe.

In this paper, we stress-test ΛCDM using a state-of-the-art CMB dataset built from the new Atacama Cosmology Telescope (ACT) Data Release 6 (DR6) measurements of the small-scale CMB temperature and polarization power spectra. A companion paper presents these data and combines them with the *Planck* mission legacy data (Planck Collaboration 2020a,b) to form the most statistically constraining CMB power spectrum dataset assembled to date (Louis et al. 2025). To validate constraints derived from the combination of ACT and *Planck* data, we also perform analyses combining ACT with legacy data from the *WMAP* mission (Bennett et al. 2013; Hinshaw et al. 2013). To assist in parameter degeneracy-breaking, we further add gravitational lensing measurements of the CMB from ACT DR6 and *Planck* (Qu et al. 2024b; Madhavacheril et al. 2024; Carron et al. 2022), as well as BAO distance measurements from the Dark Energy Spectroscopic Instrument (DESI; DESI Collaboration 2024a, 2025a) or the Baryon Oscillation Spectroscopic Survey (BOSS; Alam et al. 2017, 2021), and from the Pantheon+ supernovae compilation (Scolnic et al. 2022). Further low-redshift data are used in some analyses as well, where significant additional constraining power can be gained.

We test the cosmological model via both single-parameter extensions of ΛCDM and by relaxing its fundamental assumptions — for example, considering variations in the underlying particle physics, energy densities of various components, and gravitational and non-gravitational interactions between them. We constrain new physics operating at energy scales ranging from the inflationary epoch to the recombination epoch to the late-time universe, including models that have been constructed with the aim of increasing the value of the Hubble constant or decreasing the amplitude of late-time density fluctuations inferred from the primary CMB, as well as models motivated by more fundamental considerations in particle physics, such as the existence of new light species in the early universe.

This work builds on — and extends — previous cosmological explorations performed with ACT CMB power spectrum measurements (Dunkley et al. 2011; Sievers et al. 2013; Louis et al. 2017; Aiola et al. 2020; Thiele et al. 2021; Hill et al. 2022; An et al. 2022; Li et al. 2023c; Kreisch et al. 2024). The new ACT DR6 data provide higher sensitivity over a broad range of angular scales, allowing us to access potential signals that would previously have been hidden in the noise. In some cases (depending on the model extension), the ACT DR6 sensitivity is comparable to that achieved by the *Planck* legacy dataset (Planck Collaboration 2020c) and serves as a useful cross-check of the CMB response to a specific cosmological model. In other cases, because ACT DR6 provides constraining power in a different region of the power spectrum compared to *Planck* (particularly in polarization), the joint fit to both datasets surpasses bounds from *Planck* alone and thus represents a new state of the art.

Figure 1 highlights new leading results from ACT DR6 combined with other datasets on a wide range of benchmark single-parameter ΛCDM extensions that are studied in detail later in this paper. This figure is not ex-

haustive and shows only a small fraction of the extended models analyzed in this work. Figure 2 isolates the specific contributions from the new ACT DR6 data to the primary CMB-derived constraints, by comparing constraints from ACT alone, *Planck* alone, and their combination. It is evident that the new ACT DR6 data have reached a level of precision competitive with that of *Planck*; furthermore, due to the complementarity of the two datasets, their joint analysis yields significant gains over the sensitivity of *Planck* alone, as will be explored throughout this paper.

Across all model extensions studied in this work, we find no preference for departures from the baseline ΛCDM model. Accordingly, we set new limits on key fundamental physics parameters and theoretical models that deviate from the standard scenario, such as models featuring new particles or fields in the pre-recombination universe. Models introduced to increase the CMB-inferred Hubble constant or to decrease the CMB-inferred amplitude of density fluctuations are not favored by our data.

This paper is part of a suite of ACT DR6 papers, with companion papers describing the maps (Naess et al. 2025, N25 hereafter), and power spectra, likelihood, and baseline ΛCDM parameter constraints (Louis et al. 2025, L25 hereafter). Other papers report the power spectrum covariance matrix estimation (Atkins et al. 2024), beam measurements and modeling (Duivenvoorden et al. in prep), and foreground modeling for the power spectrum (Beringue et al. in prep). The broad set of ACT DR6 papers is summarized in N25 and also includes noise simulations (Atkins et al. 2023), CMB lensing maps and interpretation (Qu et al. 2024b; Madhavacheril et al. 2024; MacCrann et al. 2024), component-separated CMB temperature, CMB E-mode, and Compton y-maps (Coulton et al. 2024), studies of millimeter transients (Li et al. 2023b), and upcoming cluster and source catalogs.

The remainder of this paper is organized as follows. In §2 we summarize the main datasets used in our analysis. The theoretical framework and assumptions of our analyses are covered in §3, along with an overview of the various computational tools employed. §4-§7 contain the main set of constraints on numerous extensions of the standard cosmology, covering primordial perturbations and inflation constraints (§4), modifications of physics prior to and during recombination (§5), properties of known and hypothetical fundamental particles (§6), and modifications of gravity or other physics impacting cosmic evolution at late times (§7). We discuss model consistency and the resulting impact on cosmological parameter concordance in §8. In §9 we provide a brief summary, highlighting the consistency of the ACT and

Planck CMB power spectra with the standard ΛCDM cosmological model. A set of Appendices provides further technical details.

2. SUMMARY OF DATA
2.1. *CMB power spectra*

The ACT DR6 power spectra described in L25 are derived from maps made from five years of observations collected during 2017–2022, using detector arrays sensitive to three frequency bands: f090 ($77 - 112$ GHz), f150 ($124 - 172$ GHz), and f220 ($182 - 277$ GHz). The maps are described in N25. The array-band combinations and the multipole ranges that pass a comprehensive battery of null tests form the nominal DR6 dataset, comprising temperature-temperature power spectra (TT), temperature-E mode polarization power spectra (TE), and polarization-polarization power spectra (EE). These power spectra have white noise levels that improve over those of *Planck* by roughly a factor of three in polarization and a factor of two in temperature, with multi-frequency spectra measured over the multipole range $600 < \ell < 8500$ and the CMB signal extracted in the range $600 < \ell < 6500$. The spectra and their covariance matrix are used as inputs to a multi-frequency likelihood, `MFLike`, and a CMB-only (foreground-marginalized) likelihood, `ACT-lite`, also described in L25.

To leverage the full multipole range accessible with the CMB for cosmological analyses, we combine ACT with satellite data. A minimal addition used in all analyses of the ACT primary CMB (labeled ACT throughout) is a *Planck* measurement of the optical depth to reionization from the low-multipole EE power spectrum ($\ell < 30$) `Sroll2` likelihood (Pagano et al. 2020). In many cases we compress the information of `Sroll2` into a Gaussian prior on the optical depth, $\tau = 0.0566 \pm 0.0058$; for models that include parameters degenerate with primordial power spectrum parameters, we use the full likelihood shape. As described in L25, we use a baseline CMB combination, labeled P-ACT, which extends the combined dataset further with the inclusion of *Planck* data on large-to-intermediate scales — at $\ell < 1000$ in TT and $\ell < 600$ in TE/EE, truncating the multipole range of the `plik_lite` likelihood (Planck Collaboration 2020b) and generating a "*Planck*$_{\rm cut}$" likelihood. This combination is built to increase constraining power while minimizing the overlap between the two experiments and allowing us to neglect their covariance. In cases where it is useful to cross-check the results with a *Planck*-independent CMB combination, we replace *Planck* with *WMAP* data from the final 9-year release (Bennett et al. 2013; Hinshaw et al. 2013), with this combination labeled W-ACT.
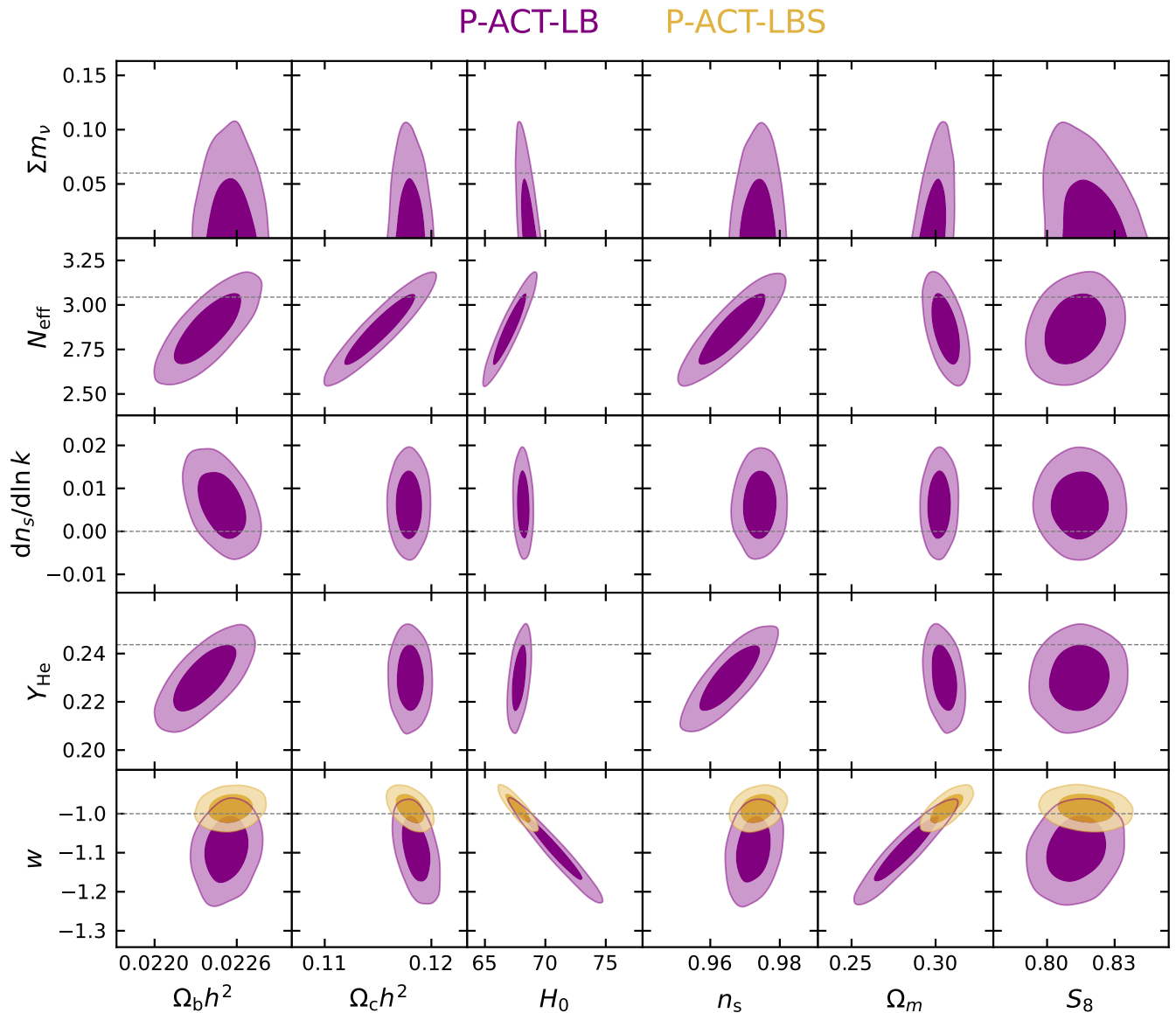
Figure 1. Constraints on single-parameter extensions to ΛCDM (vertical axis) versus key ΛCDM parameters (horizontal axis) from the combination of the new ACT DR6 power spectra with *Planck* legacy CMB spectra, CMB lensing from *Planck* and ACT, and BAO from DESI Year-1 data (purple; labeled P-ACT-LB, as defined in §2.5). We further add SNIa data from Pantheon+ (gold; with label P-ACT-LBS) for models that affect the late-time expansion history. The rows span over models varying neutrino physics (the summed mass and number of neutrinos with $\sum m_\nu$ and $N_{\rm eff}$ respectively, §6.1), variation of the primordial scalar perturbation spectral index with scale ($dn_s/d\ln k$, §4.1), the abundance of primordial helium ($Y_{\rm He}$, §6.2), and the dark energy equation of state (w, §7.2). These are shown across columns against ΛCDM parameters quantifying the baryon, cold dark matter, and total matter densities ($\Omega_b h^2$ and $\Omega_c h^2$ and Ω_m, respectively), the Hubble constant (H_0) in km/s/Mpc, the spectral index of primordial scalar perturbations (n_s), and the amplitude of density fluctuations (S_8). The contours show confidence levels at 68% and 95% (dark and light shade, respectively). The dashed gray lines mark the canonical values expected for these parameters in the standard models of cosmology and particle physics.
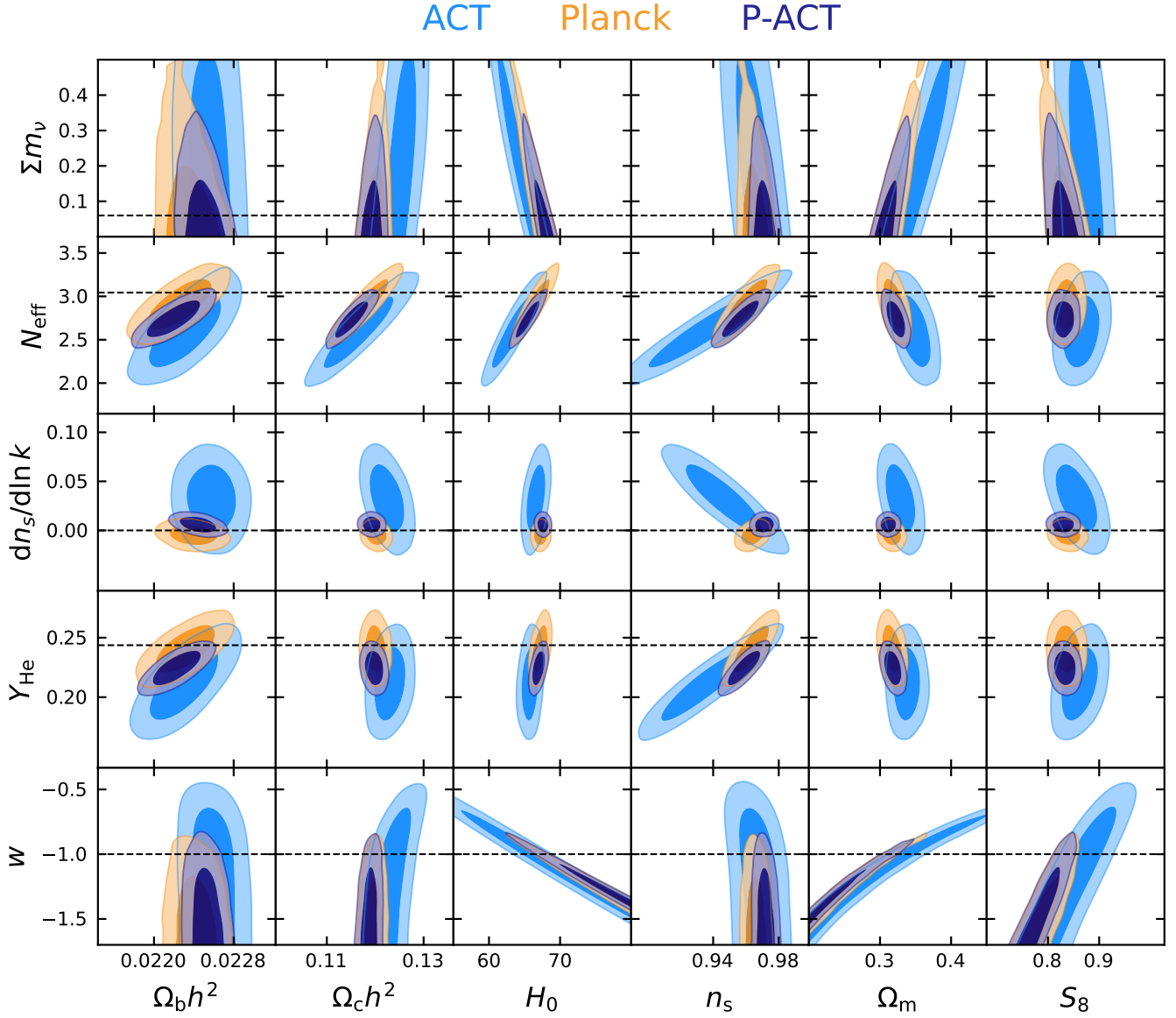
Figure 2. Similar to Fig. 1, but highlighting the specific constraints from the ACT DR6 CMB power spectra (light blue) compared to those from the *Planck* legacy CMB power spectra (orange) and those from a joint analysis of the two datasets (P-ACT, navy blue, as defined in §2.1), which breaks degeneracies and tightens the constraints.

In this case, we truncate the low-ℓ *WMAP* polarization likelihood, replacing it with the *Planck* `Sroll2` likelihood. We use a Python implementation of the *WMAP* likelihood, `pyWMAP`, which retains only the data in temperature (on all scales) and at $\ell > 23$ in polarization.

2.2. *CMB lensing*

Incorporating CMB lensing data into our cosmological constraints provides valuable complementary information to that obtained from the primary CMB power spectra. Gravitational lensing of the CMB probes large-scale structure across a wide range of cosmic history, with a broad peak at $z \approx 1$–2 and a tail extending to high redshift.

The ACT DR6 CMB lensing release provides the most precise detection of CMB lensing to date, with a 43σ (Qu et al. 2024b; Madhavacheril et al. 2024) measurement of the lensing power spectrum. Lensing is robustly measured across multipoles $40 < L < 763$, with extensive tests confirming stability against systematics and foreground contamination (MacCrann et al. 2024). The associated likelihood conservatively uses only this baseline range to minimize potential systematic impacts.

The *Planck* PR4 dataset provides a CMB lensing measurement comparable to ACT DR6 in signal-to-noise, achieving 42σ using the reprocessed NPIPE maps across multipole range $8 < L < 400$ (Carron et al. 2022). Combining *Planck* with ACT DR6 yields a state-of-the-art lensing power spectrum, with ACT adding high-precision data on smaller scales, $L > 400$.

Our analysis uses a Gaussian likelihood framework to combine the ACT DR6 and *Planck* PR4 bandpowers, which appropriately accounts for the small correlation between the two datasets (Qu et al. 2024b; Madhavacheril et al. 2024). The effective signal-to-noise ratio of the combined ACT DR6 + *Planck* NPIPE lensing spectrum, accounting for their joint covariance, corresponds to 58σ. Perturbative adjustments are also applied to correct for the weak dependence of the measurements on cosmological assumptions, following methods outlined in Planck Collaboration (2016b); Madhavacheril et al. (2024).[1]

2.3. *BAO*

BAO data measure the acoustic scale at ~ 150 Mpc in the clustering of galaxies in the late-time, $z \lesssim 4$,

---

[1] Although the ACT DR6 CMB lensing likelihood corrections have not been recomputed based on the improved knowledge of ACT maps and power spectra presented in this new suite of papers, we do not expect this to impact our results. We explicitly verify that even omitting these corrections altogether has negligible impact on our inferred parameter constraints.

universe. This feature allows one to constrain distance ratios parallel and perpendicular to the line of sight as a function of redshift. The BAO feature along the line-of-sight direction measures $D_H(z)/r_d$, the inverse-ratio between the sound horizon at the baryon drag epoch, r_d, and $D_H(z) \equiv c/H(z)$; when combined with a calibration of r_d (e.g., from CMB data), this allows a measurement of the Hubble parameter at redshift z. The BAO feature in the angular correlation function of galaxies at redshift z measures $D_M(z)/r_d$, the ratio between the comoving angular diameter distance and r_d, which thus allows inference of $D_M(z)$ when combined with a calibration of r_d. These quantities are often combined to report measurements of the angle-averaged distance $D_V(z)/r_d$, with $D_V(z) = (zD_M(z)^2 D_H(z))^{1/3}$. This has a strong dependence on the matter density and other parameters affecting the expansion history of the universe (see, e.g., Eisenstein 2005; Bassett & Hlozek 2010; Weinberg et al. 2013). Because the main signature is generated during a phase of linear evolution of matter density perturbations, BAO measurements have become the most common cosmological dataset used to break geometric degeneracies in CMB analyses.

Previous analyses used a compilation of BAO data at different redshifts from multiple surveys, such as the Baryon Oscillation Spectroscopic Survey (BOSS) (Alam et al. 2017) and the 6dF Galaxy Redshift Survey (Beutler et al. 2011). Here, we use the recent DESI Year-1 observations of the BAO feature in galaxy, quasar, and Lyman-α forest tracers (DESI Collaboration 2024a, 2025a,b) as our baseline BAO combination. This DESI dataset spans $0.1 < z < 4.2$ and includes twelve total data points, of which ten are pairs of $D_H(z)/r_d$ and $D_M(z)/r_d$, and two are combined $D_V(z)/r_d$ measurements, one each at the lowest and highest redshifts. To ensure that our results are not solely driven by DESI, and in light of the tension between some of the DESI luminous red galaxy (LRG) data points and previous measurements at the same redshifts, we also consider analyses with DESI replaced by BOSS/eBOSS BAO data, including both BOSS DR12 LRGs (Alam et al. 2017) and eBOSS DR16 LRGs (Alam et al. 2021). We primarily perform such analyses for models in which BAO data have a significant impact on the parameter constraints.

2.4. *SNIa*

Type Ia supernovae (SNIa) are powerful probes of cosmological distances in the modern universe (the last ten billion years). Using SNIa anchored to other cosmological distance indicators, supernovae constrain the luminosity distance across a range of redshifts; even in the absence of absolute calibration, SNIa precisely constrain

the relative expansion history of the universe at late times. SNIa are thus sensitive probes of the matter density and the equation of state of dark energy, as well as the spatial curvature when analyzed in tandem with the CMB. To maximize redshift coverage and ensure consistency of calibration of the SNIa, surveys from different groups are combined and re-calibrated, and released with a likelihood including systematic errors from fitting a model of supernova brightness, calibration offsets, and telescope systematics (e.g., Rubin et al. 2015, 2023; DES Collaboration 2024; Scolnic et al. 2018). Here we use the latest SNIa compilation from Pantheon+ (Scolnic et al. 2022; Brout et al. 2022), which brings together 18 samples comprising 1550 spectroscopically-confirmed SNIa spanning $0.001 < z < 2.26$. We primarily include Pantheon+ as an additional dataset when exploring models that affect the expansion history of the late-time universe, and do not explore other SNIa compilations.

2.5. *Glossary of data combinations and other additional datasets*

In this paper, we analyze the CMB primary anisotropy datasets introduced in §2.1 alone or combined with CMB lensing from §2.2, BAO data from §2.3, and SNIa data from §2.4. We report the resulting constraints with the label conventions for different dataset combinations summarized in Table 1. We present the constraints obtained with the most constraining data combination as our baseline results: depending on the model, this combination is either P-ACT-LB or P-ACT-LBS. We discuss and compare these results with those obtained from the primary CMB anisotropies — this is slightly different from the approach taken by the *Planck* collaboration, which focused primarily on comparisons between a joint CMB primary-anisotropy and lensing result versus results from the CMB combined with large-scale-structure (LSS) probes. We justify our ability to combine these data in §8.1, showing that the best-fit ΛCDM model to P-ACT CMB data gives excellent predictions for the low-redshift measurements, and furthermore that the ΛCDM model gives an excellent joint fit to all data.

Depending on the physical signature probed by each model, additional astrophysical and cosmological measurements (beyond CMB lensing, BAO, and SNIa data) can help to further tighten the parameter constraints. These are folded into specific analyses as described in each section of interest below.

As shown in L25, our baseline ΛCDM results confirm a discrepancy between the value of the Hubble constant, H_0, derived from the primary CMB and some measurements of this quantity from the local universe — see Freedman & Madore (2023); Verde et al. (2024) for rele-

Planck	$Planck^{\mathrm{TT/TE/EE}}$ + Sroll2
ACT	$\mathrm{ACT}^{\mathrm{TT/TE/EE}}$ + Sroll2
P-ACT	$\mathrm{ACT}^{\mathrm{TT/TE/EE}}$ + $Planck^{\mathrm{TT/TE/EE}}_{\mathrm{cut}}$ + Sroll2
W-ACT	$\mathrm{ACT}^{\mathrm{TT/TE/EE}}$ + $\mathrm{WMAP}^{\mathrm{TT/TE/EE}}$ + Sroll2
followed by	
-LB	when adding CMB lensing and BAO
-LS	when adding CMB lensing and SNIa
-LBS	when adding CMB lensing, BAO, and SNIa

Table 1. Dictionary listing the main dataset combinations analyzed in this work. Here, CMB lensing always refers to ACT DR6+*Planck* NPIPE lensing; BAO refers to the DESI Year-1 release unless explicitly stated otherwise (e.g., "B$_{\mathrm{BOSS}}$" referring to BOSS BAO); and SNIa refers to Pantheon+. All Planck results have been re-run to include an updated version of the Sroll2 likelihood compared to Planck Collaboration (2020c).

vant reviews. Specifically, the constraint on the Hubble constant using distance ladder methods with Cepheid-calibrated SNIa, from the SH0ES collaboration, $H_0 = 73.17 \pm 0.86$ km/s/Mpc (Riess et al. 2022; Breuval et al. 2024), is the most precise local measurement and also the most discrepant with the CMB estimate (L25). The latest value obtained by the CCHP program using tip of the red giant branch stars (TRGB) to calibrate SNIa distances is $H_0 = 70.39 \pm 1.94$ km/s/Mpc (Freedman et al. 2020, 2024), which is consistent with the CMB value (and with the SH0ES value), but less precise than the SH0ES constraint. Further recent results from direct measurements can be found in Verde et al. (2024). As a baseline choice, we do not combine our data with local measurements of H_0. However, we discuss in detail cases where a given model can accommodate a larger value of the Hubble constant compared to ΛCDM or where there are important parameter degeneracies that impact H_0.

Similarly, as shown in L25, our baseline ΛCDM results confirm the value of the fluctuation-amplitude parameter $S_8 \equiv \sigma_8 \sqrt{\Omega_m/0.3}$ (obtained from a combination of the amplitude of matter fluctuations on scales of $8\ h^{-1}$ Mpc, σ_8, and the total matter density, Ω_m) found in previous *Planck* analyses, which lies 2–3σ higher than values found in some weak lensing and galaxy clustering studies (see, e.g., Madhavacheril et al. 2024 for a collection of recent S_8 results from low-redshift probes). We emphasize that ACT and *Planck* CMB lensing data show no evidence of a low S_8 value (Madhavacheril et al. 2024; Planck Collaboration 2020d). As with H_0, as a baseline choice, we do not combine our data with low-redshift measurements of S_8. This choice is also motivated by the fact that some extended models alter the shape and/or redshift evolution of the matter power spectrum, and

thus a dedicated reanalysis of the relevant data within the context of each model would be necessary in order to derive valid constraints. Nevertheless, for some models it is appropriate to consider external priors on S_8 from low-redshift data; where this is useful and allowed by the parameter posteriors, we include in our analysis a prior from the joint analysis of DES and KIDS weak lensing data, $S_8 = 0.797 \pm 0.0155$ (Dark Energy Survey and Kilo-Degree Survey Collaboration 2023).[2]

3. ANALYSIS METHODOLOGY

We obtain cosmological parameter constraints using the ACT DR6 multi-frequency or CMB-only likelihood[3] coupled to Cobaya (Torrado & Lewis 2021), which itself is coupled to the Einstein-Boltzmann codes camb (Lewis et al. 2000) or class (Lesgourgues 2011; Blas et al. 2011), or to CosmoPower emulators of these codes (Spurio Mancini et al. 2022; Bolliet et al. 2024; Jense et al. 2025; Qu et al. 2024a), to compute the lensed theoretical CMB power spectra at high precision, as described in Appendix A. All codes exploring extended models requiring modifications to camb and class are benchmarked against the respective camb and class baseline ΛCDM results. In Table 4 in Appendix A, we provide a summary of the theory code and likelihood that are used for each model.

Unless explicitly mentioned otherwise, we compute all theory predictions using HyRec (Ali-Haïmoud & Hirata 2011) or CosmoRec (Chluba et al. 2010) (in class and camb, respectively), rather than Recfast (Seager et al. 1999), to obtain higher precision for recombination physics.[4] As a baseline choice, we compute Big Bang Nucleosynthesis (BBN) predictions using calculations of the primordial helium abundance from PRIMAT (Pitrou et al. 2018), but in §6.2 we explore other options and discuss in detail the impact of different helium and deu-

terium abundance calculations.[5] We also use the latest version of HMcode (Mead et al. 2021) (rather than Halofit, Smith et al. 2003; Takahashi et al. 2012) for modeling non-linear corrections to the matter power spectrum, unless explicitly stated otherwise. At ACT DR6 precision, the impact of non-linear corrections to CMB lensing are non-negligible even in the primary CMB power spectra (McCarthy et al. 2022). We adopt the dark-matter-only HMcode model for the non-linear matter power spectrum, with no baryonic feedback corrections.[6] We note that HMCode is not guaranteed to give accurate results when applied to models that alter late-time growth (e.g., models with interactions between dark matter and dark energy in the late universe, as in §7.3); in such cases, we use custom alternative models or restrict to linear scales. The vast majority of the new-physics models studied in this work alter physics in the early universe, and hence their impact on structure formation is generally captured in a change to the linear matter power spectrum at the onset of structure formation, which in most cases remains close to that in ΛCDM. These modeling choices are validated in Appendix A.

Our parameter set includes the six basic ΛCDM cosmological parameters: the physical baryon and cold dark matter densities, $\Omega_b h^2$ and $\Omega_c h^2$, the optical depth due to reionization, τ, the amplitude and spectral index of the power spectrum of primordial adiabatic scalar perturbations, A_s and n_s, both defined at a pivot scale $k_* = 0.05 \text{ Mpc}^{-1}$,[7] and a parameter that sets the absolute distance scale: (i) in camb, an approximation to the angular scale of the acoustic horizon at decoupling, θ_{MC}; (ii) in class, the angular size of the sound horizon at decoupling, θ_s; or (iii) the Hubble constant, H_0 in km/s/Mpc (note that the exact definition of the an-

---

[2] This is a symmetrized Gaussian approximation of the fixed-neutrino-mass result from Table 4 of Dark Energy Survey and Kilo-Degree Survey Collaboration (2023).

[3] As shown in L25, these two likelihoods yield cosmological parameters that agree within 0.1σ.

[4] The Recfast "fudge parameters" were tuned to provide sufficient accuracy for *Planck*, but are no longer sufficient for ACT DR6 sensitivity. We test the latest versions of HyRec and CosmoRec to ensure that they provide accurate recombination calculations when we compute the DR6 likelihood evaluation across the full parameter space, while also cross-checking the two codes against each other. We use both because the newest CosmoRec version is not yet available within class; thus we use CosmoRec in camb and HyRec in class.

[5] Differences in the exact helium abundance predicted by the most recent BBN codes have a negligible impact on the CMB primary anisotropy spectra and therefore on cosmological parameters inferred from them. We also note that PRIMAT-based BBN data were not present in class when our analyses were performed (although they now are), so we manually imported a PRIMAT-based table from camb to use in our class calculations. We take care to account for a small difference in the N_{eff} value assumed in the PRIMAT BBN table (3.044) and that assumed in the class BBN module (3.046).

[6] The latest HMcode model is not yet implemented in the main branch of class; we thank J. Lesgourgues for providing an updated version with this model implemented (developed from class v3.2.2).

[7] This pivot scale is the default choice in many CMB analyses, used by *Planck*, ACT, SPT, and other experiments. In some cases, following e.g., *WMAP*, *Planck*, and BICEP, results are also shown for $k_* = 0.002 \text{ Mpc}^{-1}$ — when for example it is important to look at larger scales. This is explicitly mentioned in the relevant sections.

gular scale varies between `camb` and `class` — see, e.g., the discussion in Bolliet et al. 2024).[8] We adopt broad, flat, uninformative priors on all ΛCDM parameters in every analysis in this paper (except when imposing an `Sroll2`-informed prior on τ in some ACT-only fits). Priors on extended-model parameters are described in each section, and are generally chosen to be uninformative as well. From the sampled parameters, we obtain several derived parameters, including the rms amplitude of linear density fluctuations at $z = 0$ on $8\ h^{-1}$Mpc scales, σ_8, the matter density fraction Ω_m, and $S_8 \equiv \sigma_8 \sqrt{\Omega_m/0.3}$. For models in which neutrino physics is not varied, we fix neutrino properties to comprise one massive and two massless particles, with total mass $\sum m_\nu = 0.06$ eV and effective number of neutrino species $N_{\mathrm{eff}} = 3.044$. Following *Planck* and the ACT DR6 CMB lensing analyses, we assume three massive eigenstates (zero massless) when analyzing models where the sum of the neutrino masses is a free parameter. Additional, model-specific parameters are added to the base ΛCDM set as explained in each subsection below.

Extra parameters are included in our theoretical model for astrophysical foregrounds, passband uncertainties, calibration, and polarization efficiency factors. These parameters are varied as described in L25 when using the `MFLike` likelihood, or reduced to a minimum set of two varying parameters for overall calibration and polarization efficiency when using the `ACT-lite` likelihood (also described in L25).

MCMC chains are run with theory predictions computed up to $\ell_{\max} = 9000$ and with the Gelman-Rubin convergence parameter, $R - 1$, reaching values $\sim O(10^{-2})$ and in nearly all cases smaller than 0.01. Parameter posteriors and statistical results are obtained with `GetDist` (Lewis 2019). Marginalized confidence intervals (for two-tailed limits) are calculated with the standard credible-interval approach, i.e., the interval between the two points with highest equal marginalized probability density.

Model comparisons are performed with respect to the benchmark ΛCDM results presented in L25. We determine the *maximum a posteriori* (MAP) point in parameter space for each model (note that the ACT DR6 likelihood includes informative priors on some nuisance parameters, and thus the MAP is used, rather than the maximum-likelihood point). The MAP for each model is then compared to the best-fit ΛCDM result for the relevant dataset combination. We take care to discard

---

[8] H_0 is expressed throughout this paper in km/s/Mpc; units are generally omitted for brevity.

contributions to the effective MAP χ^2 value arising from uninformative priors — the informative priors placed on nuisance parameters are always identical, and, as noted above, their contributions to the overall χ^2 are accounted for in the best-fit model determination. For reference, the best-fit P-ACT ΛCDM model yields MAP $\chi^2_{\Lambda\mathrm{CDM,MFLike}} = 2180.5$ and $\chi^2_{\Lambda\mathrm{CDM,ACT\text{-}lite}} = 781.9$ for the full P-ACT dataset (see also L25).

Constraints on parameters of the baseline ΛCDM model are presented in L25. In the following, we report constraints on a large suite of extended cosmological models, organized into four topical sections. In Fig. 3, we illustrate with a few examples how ACT data push constraints on these models beyond what has been achieved by *Planck*. Some models exhibit features on small scales ($\ell \gtrsim 2000$) not measured by *Planck*. In other cases, the integrated sensitivity over an extended range of multipoles on small scales, and the sensitive ACT DR6 measurements of TE and EE at intermediate scales, rule out models at high significance that would be allowed within the *Planck* bounds.

We also discuss how ACT DR6 improves on previous ACT releases, in particular for models that showed a hint of a preference over ΛCDM in the previous ACT DR4 dataset (Hill et al. 2022; Kreisch et al. 2024). Additional comparisons with the DR4 results are shown and discussed in Appendix B and Appendix E.

4. PRIMORDIAL PERTURBATIONS AND INFLATION

4.1. *Scale invariance of scalar perturbations*

One key prediction of the simplest single-field slow-roll inflation models is an almost scale-invariant spectrum of primordial scalar perturbations — the scalar spectral index n_s being close to, but crucially different from (and usually less than) unity (see, e.g., Peiris et al. 2003; Mukhanov 2007). Analyses of *Planck* CMB data have confirmed this prediction to high precision and shown its robustness across models (Planck Collaboration 2020c,e). The new constraints on n_s from ACT DR6 are presented and discussed in L25. Here, to test the inflation slow-roll approximation further, we take the common approach of expanding the power-law form of the primordial power spectrum of scalar curvature perturbations around a pivot scale k_* (Kosowsky & Turner 1995)

$$\mathcal{P}_{\mathcal{R}}(k) = A_s \left(\frac{k}{k_*}\right)^{n_s - 1\ +\ (1/2)\ (\mathrm{d}n_s/\mathrm{d}\ln k)\ \ln(k/k_*)}, \quad (1)$$

and constrain the running of the spectral index, $\mathrm{d}n_s/\mathrm{d}\ln k$ — i.e., the variation of n_s as function of
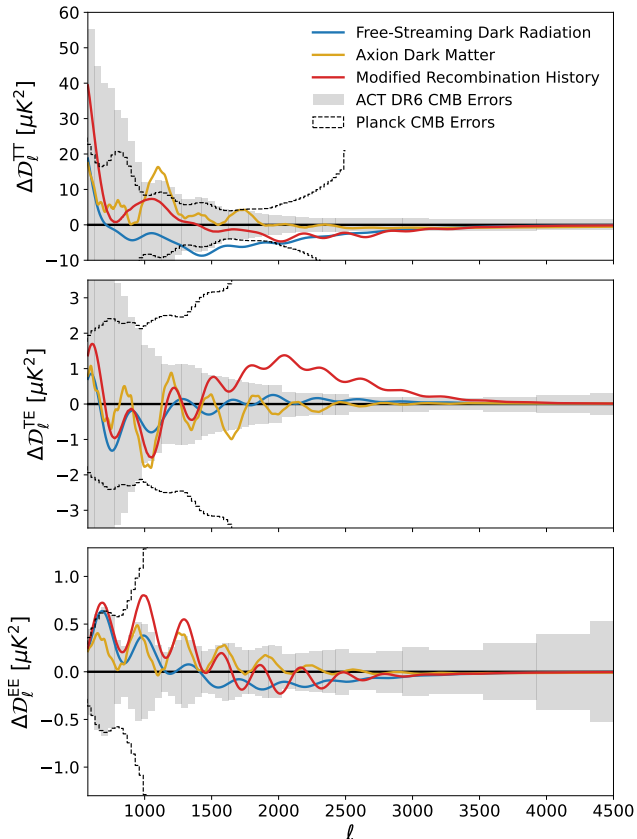
Figure 3. Models of free-streaming dark radiation (blue), axion dark matter (gold), and modified recombination history (red) that are allowed by *Planck* data show differences in TT, TE, and EE compared to the baseline ACT ΛCDM best-fit model (black line, L25), which are detectable by the new ACT data at high significance. We show theory differences for non-standard cosmologies consistent with existing *Planck* constraints relative to ACT's ΛCDM model, and compared to the sensitivity of ACT and *Planck* through their CMB-only bandpower errors. For free-streaming dark radiation we consider a model allowing for an effective number of relativistic species $N_{\rm eff} = 3.4$ (see §6.1);[a] for axion dark matter we take a model with 5% of the total dark matter density in the form of an axion of mass $m_{\rm ax} = 10^{-26}$ eV (see §6.3); for modified recombination history we show a model with a non-standard ionization fraction between redshift $z = 1000$ and 1500 (see §5.5).

[a] A self-interacting dark radiation model (§6.5.1) that fits *Planck* with excess radiation would look similar to the model shown here with a positive excess in $N_{\rm eff}$.

scale k, evaluated at $k_* = 0.05$ Mpc^{-1}. This is a single-parameter extension to ΛCDM, varied in the range $[-0.2, 0.2]$.

This parameter was found to be consistent with zero by *Planck*, with $\mathrm{d}n_s/\mathrm{d}\ln k = -0.0041 \pm 0.0067$ from combining *Planck* CMB, lensing, and BAO data (Planck Collaboration 2020c,e). With the addition of the new
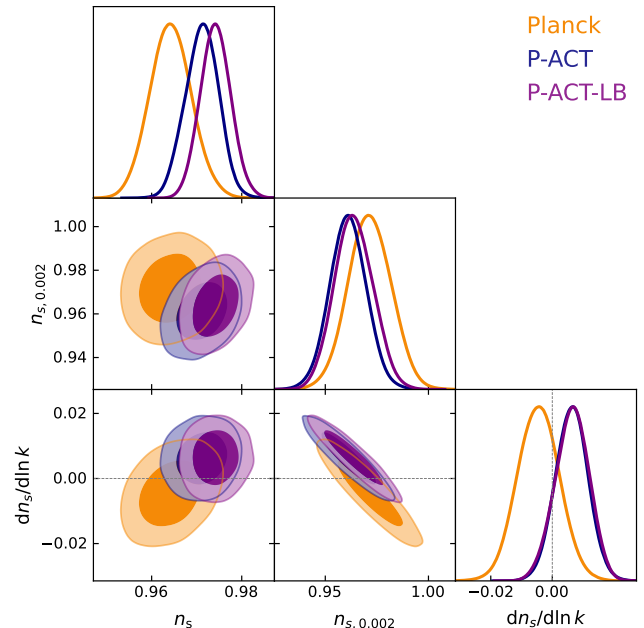

Figure 4. Constraints on parameters quantifying the scale invariance of primordial scalar perturbations: the scalar spectral index n_s and its running $\mathrm{d}n_s/\mathrm{d}\ln k$ at $k_* = 0.05$ Mpc^{-1}. Projections at larger scales (to facilitate comparisons with the *Planck* results) are shown with n_s at $k_* = 0.002$ Mpc^{-1} computed as a derived parameter. The new ACT CMB spectra move the *Planck*-alone constraint (orange) towards higher values of both n_s and $\mathrm{d}n_s/\mathrm{d}\ln k$, as shown by P-ACT (navy). The addition of lensing and BAO data shown in P-ACT-LB (purple) only shifts n_s slightly, leaving the running constraint unchanged. In all cases, we find consistency with the ΛCDM expectation (marked with gray dashed lines).

ACT DR6 spectra we confirm a vanishing running of the spectral index and tighten the error bar, finding

$$\mathrm{d}n_s/\mathrm{d}\ln k = 0.0060 \pm 0.0055 \quad (68\%, \text{P-ACT}),$$
$$= 0.0062 \pm 0.0052 \quad (68\%, \text{P-ACT-LB}). \quad (2)$$

Lacking the measurement of the first acoustic peak, and with both parameters acting to balance the tilt of the spectrum at small scales, ACT alone provides a looser bound on the combined $\mathrm{d}n_s/\mathrm{d}\ln k - n_s$ space compared to *Planck*, as shown in Fig. 2, giving $\mathrm{d}n_s/\mathrm{d}\ln k = 0.034 \pm 0.022$ (68%, ACT). With the P-ACT combination, n_s is firmly constrained and the error bar on the running is tightened by $\approx 20\%$. Adding additional datasets has a marginal impact here, with the constraints stabilizing around a vanishing running. Figure 4 shows the combined measurement of $\mathrm{d}n_s/\mathrm{d}\ln k - n_s$ and projections to *Planck*'s large scales, at $k_* = 0.002$ Mpc^{-1}. In Fig. 5 we report the same measurements in terms of the scalar primordial power spectrum using ACT, *Planck*,
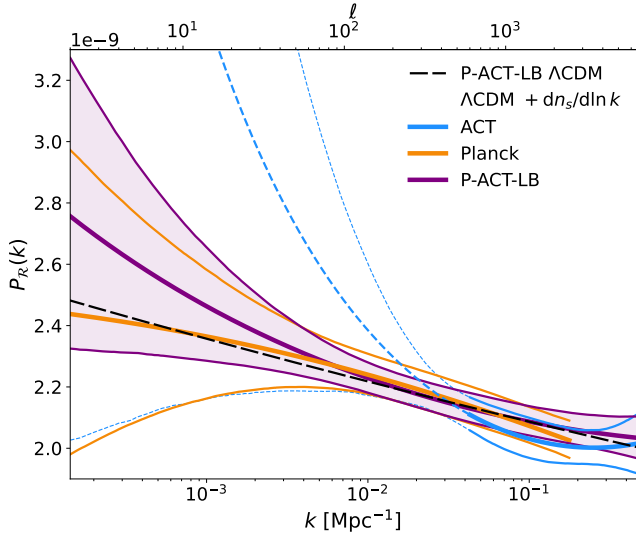
Figure 5. Inferred constraints on the primordial power spectrum of scalar curvature perturbations from ACT (blue), *Planck* (orange), and P-ACT-LB (purple), assuming a primordial power spectrum parameterized by an amplitude A_s, spectral index n_s, and running of the spectral index $\mathrm{d}n_s/\mathrm{d}\ln k$, each defined at a pivot scale $k_* = 0.05\,\mathrm{Mpc}^{-1}$. The constraints shown are the 95% CL allowed by the parametric constraints in Fig. 4, with the thick line being the mean and the thin lines the 95% limits. Each data combination is only plotted along the range of scales probed by the experiment, i.e., *Planck* is shown for $2 \leq \ell \leq 2508$, and ACT is shown with solid blue lines in the range $600 \leq \ell \leq 6500$ probed directly by DR6 and with dashed blue lines extrapolating this down to $\ell = 2 - 32$ probed by the inclusion of the Sroll2 data. The results are consistent with a vanishing running, as shown by the P-ACT-LB ΛCDM best-fit (long-dashed black line).

and P-ACT-LB. We infer $\mathcal{P}_{\mathcal{R}}(k)$ (using Eq. 1) by postprocessing the chains using the amplitude, spectral index, and running of the spectral index of our runs, and computing the 95% two-tailed confidence interval. All three datasets measure a similar amplitude and spectral index at the pivot scale, but the constraints from *Planck* prefer a slight negative running of the spectral index (due to needing to reconcile constraints from large and small scales — see the discussion in Planck Collaboration 2020c), indicated by the concave shape of the mean of the constraints, while ACT and the combination P-ACT-LB mildly prefer a slight positive running of the spectral index, changing the overall shape of $\mathcal{P}_{\mathcal{R}}(k)$ to convex.

Our constraints on $\mathrm{d}n_s/\mathrm{d}\ln k$ disfavor the moderate evidence for negative running of the spectral index seen in combined fits to Lyman-α forest and *Planck* data, $\mathrm{d}n_s/\mathrm{d}\ln k = -0.010 \pm 0.004$ (Palanque-Delabrouille et al. 2020). From CMB data alone (P-

ACT), we exclude $\mathrm{d}n_s/\mathrm{d}\ln k = -0.010$ at over 3σ significance.

4.2. *Primordial power spectrum*

In order to explore a broader range of deviations from a simple power-law primordial adiabatic power spectrum than those captured solely by the running of the scalar spectral index, we consider a more model-independent approach.

We reconstruct the primordial power spectrum of the scalar perturbations for wavenumber bins centered at $k = 10^{-4}, 10^{-3.5}, 10^{-3}, 10^{-2.5}$ and then 26 equally-spaced logarithmic bins from $0.011 \lesssim k\ /\mathrm{Mpc}^{-1} \lesssim 0.43$, where $k_{i+1} \simeq 1.16k_i$ (following previous similar analyses in Bridle et al. 2003; Guo et al. 2011; Hlozek et al. 2012; Aich et al. 2013; Hunt & Sarkar 2014; de Putter et al. 2014; Miranda et al. 2016; Hazra et al. 2016; Obied et al. 2017; Planck Collaboration 2020e; Raffaelli & Ballardini 2025). Given the degeneracy between the primordial power and the optical depth (often described in terms of the $A_s - \tau$ degeneracy), we sample the value of $e^{-2\tau}P_{\mathcal{R}}(k_i)$ for each ith bin. We use the cubic spline interpolation method implemented within `camb` to build the initial power spectrum from our binned values. For k values below our minimum-assumed wavenumber $k_{\min}$, we set the amplitude of the primordial power spectrum to $P_{\mathcal{R}}(k \leq k_{\min}) = P_{\mathcal{R}}(k_{\min})$. This approach removes the scalar spectral amplitude A_s and the scalar index n_s as sampled parameters, but adds the amplitudes within the 30 different bins as described above, leading to 28 additional parameters/degrees of freedom in this model as compared to ΛCDM. The prior ranges that we adopt for each k bin are given in Table 5 in Appendix C, and we use the `ACT-lite` likelihood to sample the extended parameter space.

In Fig. 6 we present constraints on the binned primordial power spectrum from ACT, *Planck*, P-ACT, and P-ACT-LB, compared to the P-ACT-LB best-fit ΛCDM power law. The constraints from P-ACT are improved over the *Planck*-alone measurements wherever ACT data are included (for $\ell \gtrsim 850$), with the ratio of P-ACT to *Planck* error bars ranging between 0.95 and 0.43 for wavenumbers between $0.063 < k\ \mathrm{Mpc}^{-1} < 0.15$ or $(880 \lesssim \ell \lesssim 2140)$. This range is chosen as $k = 0.063\,\mathrm{Mpc}^{-1}$ is the first wavenumber where P-ACT significantly improves over *Planck* and $k_\star = 0.15\,\mathrm{Mpc}^{-1}$ is the highest wavenumber where *Planck* has a two-sided marginalized posterior (rather than an upper limit). The correlations across bins can be very high and present either between direct neighbors or between more distant bins. In particular, we find correlations at the level of $\sim 30 - 40\%$, with a
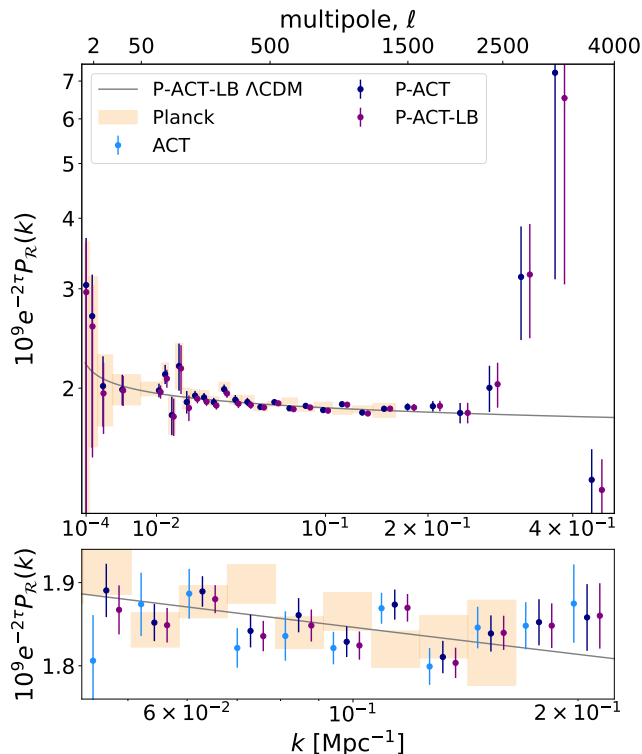
Figure 6. Binned reconstruction of the dimensionless primordial curvature power spectrum with 68% CL errors for different datasets. The new constraints are centered on the P-ACT measurement; the ACT (P-ACT-LB) wavenumbers on the x-axis are shifted to the left (right) by 4% in order to more easily see the values/errors for each dataset combination. *Planck* is plotted as shaded boxes for comparison up to $k = 0.15$ Mpc^{-1} — beyond this wavenumber, *Planck* alone gives unconstrained limits with the posteriors filling the whole prior range. The top panel shows the reconstruction over the full range of wavenumbers considered and highlights the improvement achieved with the addition of the ACT data (navy versus orange). For this panel, the x-axis is scaled as $k^{0.5}$ in order to best show the small scales. The bottom panel zooms into the region where ACT alone (light blue) becomes comparable and then overtakes *Planck* in constraining power. Adding lensing and BAO data (purple) has minimal impact. The binned measurement is consistent with the P-ACT-LB best-fit ΛCDM power-law spectrum shown in gray.

significant increase around $k = 0.01$ Mpc^{-1} where bins 6–9 are strongly anti-correlated reaching a level of 90%, and above $k = 0.1$ Mpc^{-1} where correlations increase again to reach $50 - 60\%$ at small scales.

In Fig. 7, we illustrate the improvement in constraining power for $k_\star = 0.15$ Mpc^{-1}. Above that wavenumber, the *Planck* constraints essentially fill the assumed prior range, while ACT constrains the amplitude of primordial power with a two-sided marginalized posterior up to $k = 0.32$ Mpc^{-1} and with a one-sided 95% CL to $k = 0.43$ Mpc^{-1}. The improvements come from the ACT
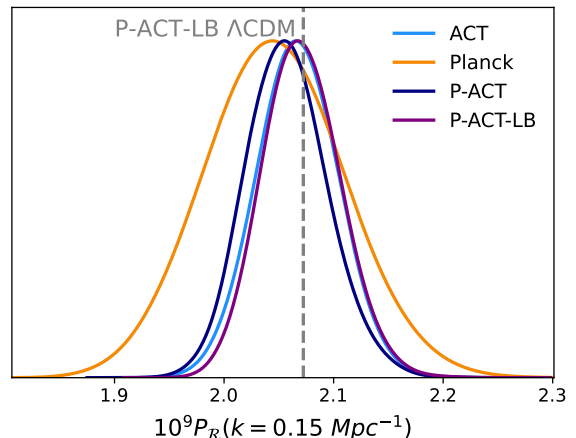

Figure 7. Marginalized posterior for the power at wavenumber $k_\star = 0.15$ Mpc^{-1}, showing the improvement brought by ACT over *Planck* and the limit achieved with P-ACT-LB. The results are consistent with the P-ACT-LB best-fit ΛCDM power-law model (dashed gray line). *Planck* cannot constrain the model above $k_\star$, while ACT continues to measure the amplitude of primordial power with a two-sided posterior up to $k = 0.32$ Mpc^{-1}.

sensitivity to smaller angular scales ($\ell > 2500$). In particular, at $k_\star$, we obtain a fractional error of 2.8% and 1.4% on $e^{-2\tau} P_\mathcal{R}(k)$ for *Planck* alone and ACT alone, respectively, and a fractional error of

$$\frac{\sigma(e^{-2\tau} P_\mathcal{R}(k_\star))}{e^{-2\tau} P_\mathcal{R}(k_\star)} = 1.2\% \quad (\text{P-ACT}),$$
$$= 1.1\% \quad (\text{P-ACT-LB}), \qquad (3)$$

with the individual fits consistent with ΛCDM. Our new constraints improve the range of k over which there are significant constraints by about a factor of three compared to *Planck*.

We map this measurement onto the linear matter power spectrum and compare with other measurements in Appendix C.

4.3. *Isocurvature perturbations*

Standard single-field inflation predicts purely adiabatic primordial perturbations, in the sense that all perturbations arise from a single degree of freedom (the local time at which inflation ends). This generally implies that fractional perturbations in the number density of all species are equal on super-horizon scales ($\delta n_i/n_i = \delta n_j/n_j$). In contrast, isocurvature perturbations — characterized by variations in the relative number densities or velocities of different species — can arise in a variety of early-universe scenarios, particularly if there are additional fields present around the time of inflation (Linde 1985; Mollerach 1990; Polarski & Starobinsky 1994; Garcia-Bellido & Wands 1996; Linde

& Mukhanov 1997; Lyth & Wands 2002; Kawasaki & Takahashi 2001; Lyth et al. 2003). Whereas current cosmological observations are consistent with purely adiabatic perturbations, and a pure isocurvature perturbation has been excluded since early measurements of the large-scale CMB anisotropies (Stompor et al. 1996; Enqvist et al. 2000, 2002), it is possible to have models with mixed adiabatic and isocurvature modes, as constrained in previous CMB anisotropy analyses (e.g., Bucher et al. 2004; Moodley et al. 2004; Bean et al. 2006; Planck Collaboration 2014, 2016c, 2020e). In this section, we place constraints on a range of scenarios consisting of a mixture of an adiabatic mode with a single (possibly correlated) isocurvature mode. We refer the reader to Table 6 in Appendix D for a detailed compilation of the isocurvature constraints derived in this work.

There are four possible non-decaying isocurvature modes: cold dark matter density (CDI), baryon density (BDI), neutrino density (NDI), and neutrino velocity (NVI) (Bucher et al. 2000). At linear order, BDI and CDI modes have an indistinguishable impact on the CMB power, differing only in amplitude; therefore, we do not analyze BDI modes directly.[9] Additionally, we do not consider NVI because it is less theoretically motivated than CDI and NDI. Consequently, we focus on two isocurvature modes: $\mathcal{I}_{\rm CDI}$ and $\mathcal{I}_{\rm NDI}$.

The primordial curvature and isocurvature fluctuations are described by the curvature power spectrum, $\mathcal{P}_{\mathcal{RR}}(k)$, the isocurvature power spectrum, $\mathcal{P}_{\mathcal{II}}(k)$, and their cross-power spectrum, $\mathcal{P}_{\mathcal{RI}}(k)$. Following *Planck* analyses of isocurvature (Planck Collaboration 2014, 2016c, 2020e), we assume power-law primordial power spectra defined in terms of their amplitudes at two scales, $k_1 = 0.002 \ {\rm Mpc}^{-1}$ and $k_2 = 0.1 \ {\rm Mpc}^{-1}$, hence

$$\mathcal{P}_{ab}(k) = \exp \left[\left(\frac{\ln(k) - \ln(k_2)}{\ln(k_1) - \ln(k_2)} \right) \ln \left(\mathcal{P}_{ab}^{(1)} \right) + \left(\frac{\ln(k) - \ln(k_1)}{\ln(k_2) - \ln(k_1)} \right) \ln \left(\mathcal{P}_{ab}^{(2)} \right) \right] \quad (4)$$

where $\mathcal{P}_{ab}^{(i)} \equiv \mathcal{P}_{ab}(k_i)$ and $a, b \in \{\mathcal{R}, \mathcal{I}\}$. The mixed adiabatic and isocurvature models are characterized by four new parameters: $\mathcal{P}_{\mathcal{RI}}^{(1)}, \mathcal{P}_{\mathcal{RI}}^{(2)}, \mathcal{P}_{\mathcal{II}}^{(1)}, \mathcal{P}_{\mathcal{II}}^{(2)}$.

For computational reasons, we focus on models where the adiabatic and isocurvature perturbations are either uncorrelated or fully (anti-)correlated, and thus $\mathcal{P}_{\mathcal{RI}}^{(i)}$ is a derived parameter. These are the most well-motivated isocurvature scenarios. We sample the adiabatic amplitudes $\mathcal{P}_{\mathcal{RR}}^{(1)}$ and $\mathcal{P}_{\mathcal{RR}}^{(2)}$ assuming uniform priors between

$[15, 40] \times 10^{-10}$ as a replacement of the amplitude and scalar spectral index of the baseline ΛCDM parameter set. For the isocurvature amplitudes, we sample $\mathcal{P}_{\mathcal{II}}^{(1)}$ and $\mathcal{P}_{\mathcal{II}}^{(2)}$ (for models where $n_{\mathcal{II}}$ is not fixed) assuming uniform priors between $[0, 100] \times 10^{-10}$. We sample the amplitudes at two scales instead of sampling a single amplitude and a spectral index to mitigate prior-volume effects that can arise if the data have no preference for isocurvature modes (Moodley et al. 2004).[10]

4.3.1. *Uncorrelated models*

We first present constraints on an uncorrelated ($\mathcal{P}_{\mathcal{RI}}^{(i)} = 0$) mixture of adiabatic perturbations with a single, possibly scale-invariant, CDI or NDI mode. Scale-invariant CDI perturbations can arise if there are axions or axion-like particles present during inflation (Turner et al. 1983; Axenides et al. 1983; Seckel & Turner 1985; Turner & Wilczek 1991; Linde 1991; Beltran et al. 2007; Hertzberg et al. 2008). Axions can also produce uncorrelated CDI with a blue spectral index (Kasuya & Kawasaki 2009).

For scale-invariant CDI and NDI modes, we vary $\mathcal{P}_{\mathcal{II}}^{(1)}$ and fix $\mathcal{P}_{\mathcal{II}}^{(2)} = \mathcal{P}_{\mathcal{II}}^{(1)}$. The P-ACT constraint on the amplitude of scale-invariant CDI perturbations is $10^{10} \mathcal{P}_{\mathcal{II}}^{(1)} < 1.1$ (95% CL). This is slightly weaker than the *Planck*-only bound of $10^{10} \mathcal{P}_{\mathcal{II}}^{(1)} < 0.9$ (95% CL), due to the positive correlation between the adiabatic spectral index ($n_{\mathcal{RR}}$) and the CDI amplitude. For NDI, the baseline P-ACT constraint on the isocurvature amplitude is $10^{10} \mathcal{P}_{\mathcal{II}}^{(1)} < 1.8$ at (95% CL), which is 15% tighter than the *Planck*-only bound, $10^{10} \mathcal{P}_{\mathcal{II}}^{(1)} < 2.1$ (95% CL). Neither of these constraints changes appreciably between P-ACT and P-ACT-LB.

Figure 8 shows the marginalized posterior distributions for the uncorrelated CDI model with a free spectral index. Combining ACT and *Planck*, we find

$$\left. \begin{array}{l} 10^{10} \mathcal{P}_{\mathcal{II}}^{(1)} < 0.7 \\ 10^{10} \mathcal{P}_{\mathcal{II}}^{(2)} < 26 \end{array} \right\} \quad \text{(one-tail 95\%, P-ACT).} \quad (5)$$

---

[9] Our CDI constraints can be converted to BDI constraints by applying the appropriate factors of Ω_c and Ω_b, as discussed in Planck Collaboration (2020e).

[10] We use `class` with the settings described in Appendix A to compute theoretical predictions for isocurvature models. Additionally, we set `hmcode_kmax_extra`=100 to address issues in the `HMCode` non-linear power spectrum calculation for blue-tilted isocurvature perturbations. Despite this, the non-linear evaluation can still fail for a small fraction ($< 1\%$) of samples in the *Planck*-only uncorrelated CDI constraints with a free spectral index. We exclude this subset of samples from our analysis, slightly affecting *Planck*-alone constraints for this model. The issues with the non-linear computation do not affect any of our constraints including ACT data, which already exclude such blue-tilted models.
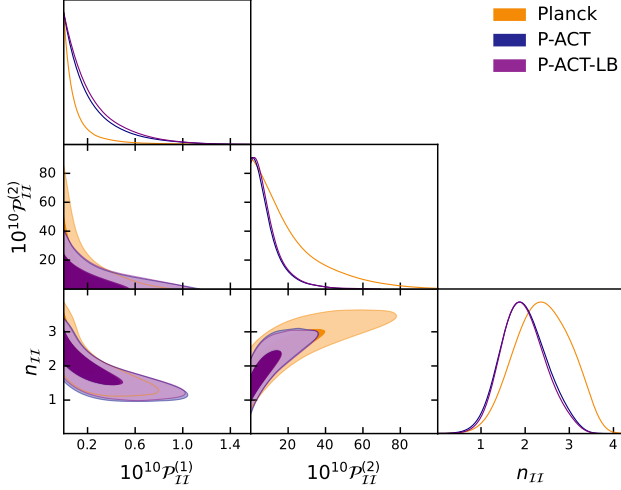
Figure 8. Constraints on the primordial isocurvature power spectrum parameters for a mixed adiabatic and uncorrelated CDI mode with a power-law power spectrum for several dataset combinations.
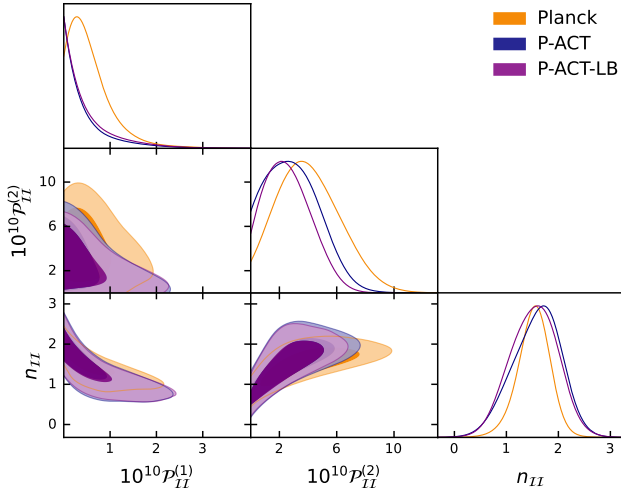

Figure 9. Same as Fig. 8 for a primordial isocurvature power spectrum with a mixed adiabatic and uncorrelated NDI mode.

The P-ACT constraint on $\mathcal{P}_{\mathcal{II}}^{(2)}$ is a significant improvement over the *Planck*-only constraint of $10^{10}\mathcal{P}_{\mathcal{II}}^{(2)} < 59$. Interestingly, the P-ACT constraint on $\mathcal{P}_{\mathcal{II}}^{(1)}$ is weaker than that from the *Planck* dataset alone. This is a consequence of the anti-correlation between $\mathcal{P}_{\mathcal{II}}^{(1)}$ and $\mathcal{P}_{\mathcal{II}}^{(2)}$, assuming a power-law spectrum. In other words, the large values of $\mathcal{P}_{\mathcal{II}}^{(2)}$ that are consistent with the *Planck* data, but not the P-ACT combination, drive the *Planck*-only marginalized posterior on $\mathcal{P}_{\mathcal{II}}^{(1)}$ towards zero. The addition of CMB lensing and BAO data does not significantly change the P-ACT constraints on this model.

Figure 9 presents the marginalized posteriors on the isocurvature amplitudes for an uncorrelated mixture of adiabatic and NDI modes assuming a free spectral index. Combining ACT and *Planck*, we find

$$\left.\begin{array}{l} 10^{10}\mathcal{P}_{\mathcal{II}}^{(1)} < 1.6 \\ 10^{10}\mathcal{P}_{\mathcal{II}}^{(2)} < 6.1 \end{array}\right\} \quad \text{(one-tail 95\%, P-ACT).} \quad (6)$$

Interestingly, although the *Planck* data alone showed a small, statistically insignificant peak in the posterior at non-zero values of $\mathcal{P}_{\mathcal{II}}^{(1)}$ and $\mathcal{P}_{\mathcal{II}}^{(2)}$, this feature disappears when ACT DR6 data are included. Finally, including CMB lensing and BAO data further improves the constraint on the amplitude of NDI perturbations at $k = 0.1$ Mpc^{-1} to $10^{10}\mathcal{P}_{\mathcal{II}}^{(2)} < 5.4$. In this case, the improvement from CMB lensing and BAO is predominately due to the anti-correlation between $n_{\mathcal{RR}}$ and $10^{10}\mathcal{P}_{\mathcal{II}}^{(2)}$, with P-ACT-LB preferring a slightly larger value of $n_{\mathcal{RR}}$ than P-ACT.

In summary, we find no evidence of uncorrelated CDI or NDI. Nevertheless, including ACT DR6 data leads to stringent bounds on the amplitude of small-scale isocurvature perturbations, highlighting the complementarity of large- and small-scale CMB observations.

4.3.2. *Correlated models*

We also present constraints on a correlated mixture of adiabatic and CDI perturbations. We consider the situation where the adiabatic and CDI modes are fully correlated, $\mathcal{P}_{\mathcal{RI}}(k) = \sqrt{\mathcal{P}_{\mathcal{RR}}(k)\mathcal{P}_{\mathcal{II}}(k)}$, as well as the fully anti-correlated scenario ($\mathcal{P}_{\mathcal{RI}}(k) = -\sqrt{\mathcal{P}_{\mathcal{RR}}(k)\mathcal{P}_{\mathcal{II}}(k)}$). In both cases, we vary only $\mathcal{P}_{\mathcal{II}}^{(1)}$ and fix $\mathcal{P}_{\mathcal{II}}^{(2)}$ assuming $n_{\mathcal{II}} = n_{\mathcal{RR}}$. While the high-resolution ACT DR6 spectra are unlikely to significantly improve upon the *Planck*-only constraints on these models as the transfer function for scale-invariant CDI perturbations is significantly suppressed at high multipoles, we explore correlated CDI models because they are theoretically well-motivated. For example, mixed adiabatic and CDI perturbations with large (anti-)correlations arise in the curvaton scenario (Mollerach 1990; Moroi & Takahashi 2001; Lyth & Wands 2002; Bartolo & Liddle 2002; Lyth et al. 2003).

For the fully correlated model, the P-ACT dataset constrains the isocurvature amplitude to $10^{10}\mathcal{P}_{\mathcal{II}}^{(1)} < 0.025$ (95% CL). Including CMB lensing and BAO data slightly relaxes this bound to $10^{10}\mathcal{P}_{\mathcal{II}}^{(1)} < 0.031$. For the fully anti-correlated model, P-ACT provides $10^{10}\mathcal{P}_{\mathcal{II}}^{(1)} < 0.027$, improving modestly on the *Planck*-only limit (< 0.031). P-ACT-LB leads to $10^{10}\mathcal{P}_{\mathcal{II}}^{(1)} < 0.015$ at 95% confidence.

Overall, we find no evidence of primordial isocurvature perturbations.

4.4. *Tensor modes and constraints on inflation models*

Tensor perturbations, for example in the form of primordial gravitational waves predicted by inflation models (see, e.g., Kamionkowski & Kovetz 2016 for a review), add power on very large scales in the CMB T/E angular power spectra and generate a unique large-scale B-mode polarization signal not measured by ACT. However, the full behavior of the primordial perturbations depends on the ratio/co-existence of tensor and scalar modes, with the latter measured by ACT small-scale data via n_s. Here, we study how the updated measurement of n_s presented in L25 affects constraints on inflation models.

The modeling of tensor perturbations is similar to that used for scalars, $\mathcal{P}_t(k) = A_t(k/k_*)^{n_t}$, and is usually quantified by the tensor-to-scalar ratio parameter, $r = \mathcal{P}_t(k_*)/\mathcal{P}_\mathcal{R}(k_*)$. Here we set n_t via the inflationary consistency relation, $n_t = -r/8$. Constraints on r and n_s can be directly related to the potential slow-roll parameters of inflation, ϵ_V and η_V, which are determined by the shape of the inflaton potential, as

$$\epsilon_V \equiv \frac{M_{Pl}{}^2}{2}\left(\frac{V_{,\phi}}{V}\right)^2,$$
$$\eta_V \equiv M_{Pl}{}^2\left(\frac{V_{,\phi\phi}}{V}\right), \qquad (7)$$

where M_{Pl} is the Planck mass, $V(\phi)$ is the inflaton potential, and $V_{,\phi}$ and $V_{,\phi\phi}$ are its first and second derivatives. These parameters respectively describe the steepness and curvature of the inflaton potential, and they relate to the power spectrum parameters as

$$r = 16\epsilon_V,$$
$$n_s - 1 = 2\eta_V - 6\epsilon_V. \qquad (8)$$

To derive new results in the $r - n_s$ plane presented in Fig. 10, we vary r in the range $[0, 1]$ and we include B-mode measurements from the BICEP and Keck telescopes at the South Pole, which have jointly accumulated more than fifteen years of observations of CMB polarization at degree scales. Their measurements of CMB B-modes are the most precise to date in the field (Ade et al. 2021, BK18) and completely drive the upper limit on r, which (combined with n_s from *Planck*) strongly excludes monomial inflation models with convex potentials. The inclusion of ACT data shows a preference for a slightly higher value of n_s, indicated by the purple contour shifting to the right of the orange contour in Fig. 10, and gives $r < 0.038$ (95%, P-ACT-LB-BK18). As a consequence, P-ACT can accommodate power-law inflation models with slightly higher power-law indices than those preferred by *Planck* alone (assuming 50–60 e-folds of inflation), i.e., power-law models that are closer
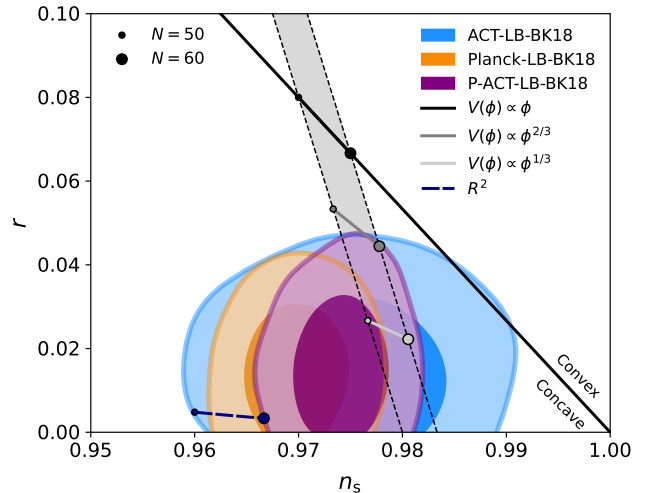

Figure 10. Constraints on the scalar and tensor primordial power spectra at $k_* = 0.05\,\mathrm{Mpc}^{-1}$, shown in the $r - n_s$ parameter space. The constraints on r are driven by the BK18 data, while the constraints on n_s are driven by *Planck* (orange), ACT (blue), or P-ACT (purple). The combined dataset also includes CMB lensing and BAO in all cases. The various circles and solid lines in between the gray band show predictions for different power-law potentials with the number of e-folds of inflation $50 < N < 60$, while the solid black line shows the separation between convex- and concave-shaped potentials. The Starobinsky R^2 model is also shown for 50-60 e-folds (dashed navy line); the P-ACT-LB measurement of n_s disfavors this model at $\gtrsim 2\sigma$, for $50 < N < 60$.

to a linear potential and hence possess a second derivative closer to zero. On the contrary, the Starobinsky R^2 inflation model (Starobinsky 1980; Starobinskij 1992), which predicts lower values of n_s, is more disfavored and lies on the 2σ boundary of P-ACT-LB.

The constraints on the slow-roll parameters are shown in Fig. 11, with BK18 determining ϵ_V and ACT adding to the constraint on η_V. The slight preference for a higher n_s value implies a value of η_V closer to zero,

$$\eta_V = (-95^{+23}_{-30}) \times 10^{-4} \quad (68\%, \text{P-ACT-LB-BK18}), \qquad (9)$$

and thus implies a preference for a slightly less concave inflaton potential.

The inclusion of running of the spectral index of scalar perturbations does not significantly change these results.

5. PRE- AND MODIFIED-RECOMBINATION PHYSICS

5.1. *Early dark energy*

The early dark energy (EDE) extension to ΛCDM introduces a new field that acts to accelerate the expansion of the universe prior to recombination, reducing
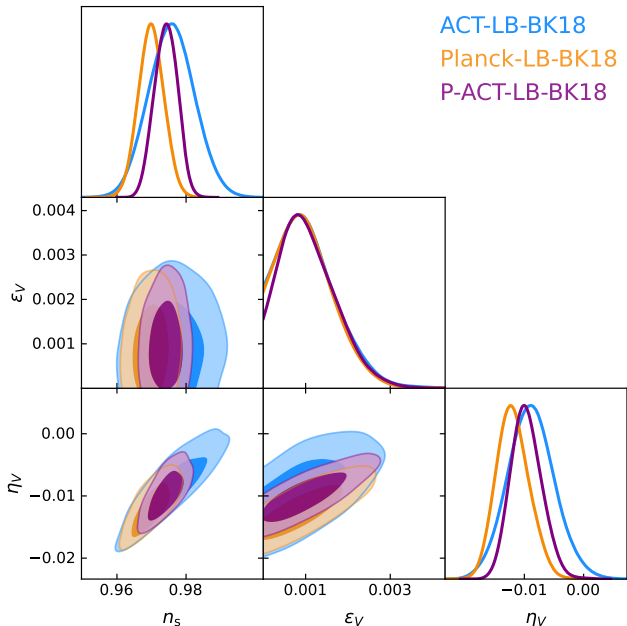
Figure 11. Constraints on the slow-roll parameters ϵ_V and η_V. The first parameter is driven by the BK18 limit on the tensor-to-scalar ratio, while η_V tracks the contribution to n_s from ACT (blue), *Planck* (orange), and P-ACT-LB (purple).

the sound horizon at last scattering and thus increasing the CMB-inferred Hubble constant (Poulin et al. 2019; Lin et al. 2019; Agrawal et al. 2023). Here, we consider an axion-like EDE model that has been widely studied in the literature, which is described by the potential (Poulin et al. 2019; Smith et al. 2020)

$$V(\phi) = m^2 f^2 (1 - \cos(\phi/f))^n \,, \tag{10}$$

where m is the mass of the field, f is the axion decay constant, and n is a power-law index. While $n = 1$ is excluded on phenomenological grounds — as the EDE would act as an additional contribution to dark matter at late times — values of $n \geq 2$ constitute viable models. Here, we consider as baseline the $n = 3$ model, as in previous literature (e.g., Hill et al. 2020; Ivanov et al. 2020b; D'Amico et al. 2021; La Posta et al. 2022; Hill et al. 2022), and discuss the $n = 2$ case below and in Appendix E.

Following previous works (Poulin et al. 2019; Smith et al. 2020; Hill et al. 2022), we adopt a phenomenological parametrization that introduces three additional parameters beyond those in ΛCDM: $f_{\rm EDE}$, z_c, and θ_i, where

$$f_{\rm EDE} = 8\pi G \rho_{\rm EDE}(z_c)/(3H^2(z_c)) \tag{11}$$

is the maximum fractional contribution of EDE to the cosmic energy budget, which is reached at "critical redshift" z_c, and the initial field displacement $\theta_i = \phi_i/f$.

The energy density $\rho_{\rm EDE}$ is given by

$$\rho_{\rm EDE}(z_c) = \frac{1}{2}\dot{\phi}(z_c)^2 + V(\phi(z_c)) \tag{12}$$

and the field ϕ evolves by the Klein-Gordon equation (dots here denote derivatives with respect to cosmic time)

$$\ddot{\phi} + 3H\dot{\phi} + \frac{dV}{d\phi} = 0 \,. \tag{13}$$

Initially the field is frozen due to Hubble friction. Around redshift z_c when $H \sim m$, the field begins to roll.

Several previous studies have constrained this model with various datasets (see, e.g., Kamionkowski & Riess 2023; Poulin et al. 2023b; McDonough et al. 2024 for reviews). Hill et al. (2020) found that *Planck* alone has no preference for EDE, with $f_{\rm EDE} < 0.087$ (95% CL) and $H_0 = 68.3 \pm 1.0$ (68% CL); these *Planck*-derived bounds were further tightened using NPIPE data in McDonough et al. (2024); Efstathiou et al. (2024). However, the ACT DR4 data showed a hint of a preference for the EDE model over ΛCDM at 2–3σ significance (Hill et al. 2022). The combination of ACT DR4, large-scale *Planck* TT, *Planck* CMB lensing, and BOSS BAO data yielded $f_{\rm EDE} = 0.091^{+0.020}_{-0.036}$ (68% CL) and $H_0 = 70.9^{+1.0}_{-2.0}$ km/s/Mpc (68% CL) (Hill et al. 2022) (see also Poulin et al. 2021; La Posta et al. 2022; Smith et al. 2022; Smith & Poulin 2024). However, the statistical weight of *Planck* was sufficiently large compared to DR4 that this mild preference disappeared when combining ACT DR4 with the full *Planck* data.

We re-evaluate here the preference for this model with the new ACT DR6 power spectra. Note that, in general, models with a significant EDE fraction leave imprints in the CMB power spectra on modes that are within (or entering) the horizon at redshifts around z_c. While some of these imprints can be absorbed by changes in other cosmological parameters, particularly $\Omega_c h^2$ and n_s (Hill et al. 2020), high-resolution polarization data are expected to break these degeneracies and yield strong sensitivity to EDE, should it be present (Smith et al. 2020; Hill et al. 2022; Smith & Poulin 2024). For models with $z_c \sim z_{\rm eq}$, unique features are imprinted in CMB power spectra at $\ell \sim 400 - 800$, as well as broader imprints extending to smaller angular scales. Indeed, the mild hint of EDE in the ACT DR4 analysis was largely driven by a fluctuation in the EE power spectrum at $\ell \sim 500$ and a broad trend in the joint ACT and *Planck* TE power spectrum (Hill et al. 2022). Our analysis of the new ACT DR6 spectra is a high-precision test as to whether these features were the first hints of a real signal, or simply a statistical fluctuation.

We sample the model parameters with uniform priors $f_{EDE} \in [0.001, 0.5]$, $\log_{10}(z_c) \in [3.0, 4.3]$, and $\theta_i \in [0.1, 3.1]$. We compute theoretical predictions using the EDE model implementation in `class`, which itself was merged from the modified version `class_ede` (Hill et al. 2020),[11] as well as using `CosmoPower`-based emulators of the `class` EDE predictions (described in Qu et al. 2024a). One important detail to note is that these emulators were trained on theory predictions computed assuming three massive neutrino species, which is different from our baseline convention in this paper of assuming one massive neutrino. This difference leads to very small shifts in the H_0 posteriors (< 0.1 km/s/Mpc), but otherwise leaves the parameter constraints unaffected, as we verify using full `class` runs. For calculations in the $n = 2$ EDE model, we compute theoretical predictions using the implementation in `camb`, as we find that calculations for this model are more numerically stable in `camb` than in `class` (for some extreme $n = 2$ scenarios, we find that `class` does not run successfully). As a test of the theory codes used for the EDE model, we verify that the χ^2_{ACT} values computed for a benchmark $n = 3$ EDE model with `camb` and `class` agree with one another to within 0.06, nearly as good as the ΛCDM agreement for these codes (see Appendix A).

Figures 12 and 13 show the marginalized posterior distributions for key parameters in the $n = 3$ EDE model, for different dataset combinations. With the new ACT DR6 spectra, we find

$$f_{EDE} < 0.088 \quad (95\%, \text{ACT}),$$
$$f_{EDE} < 0.12 \quad (95\%, \text{P-ACT}), \quad (14)$$

and

$$H_0 = 67.5^{+0.9}_{-1.7} \quad (68\%, \text{ACT}),$$
$$H_0 = 69.3^{+0.9}_{-1.5} \quad (68\%, \text{P-ACT}), \quad (15)$$

with the W-ACT case also shown in the figures to allow a *Planck*-independent assessment of the EDE constraints. We find that ACT alone shows essentially no shift in H_0 within the EDE model, compared to ΛCDM — the hint of non-zero EDE seen in the DR4 data is not seen in DR6 (comparisons between the DR4 and DR6 EDE constraints can be found in Appendix E). When combining with *Planck*, the H_0 posterior shifts upward, but when combining with *WMAP*, this is significantly lessened: we find $H_0 = 68.1^{+0.8}_{-1.6}$ (68%, W-ACT). As discussed below, the improvement in quality of fit in all cases is not statistically significant. When we also include CMB lensing
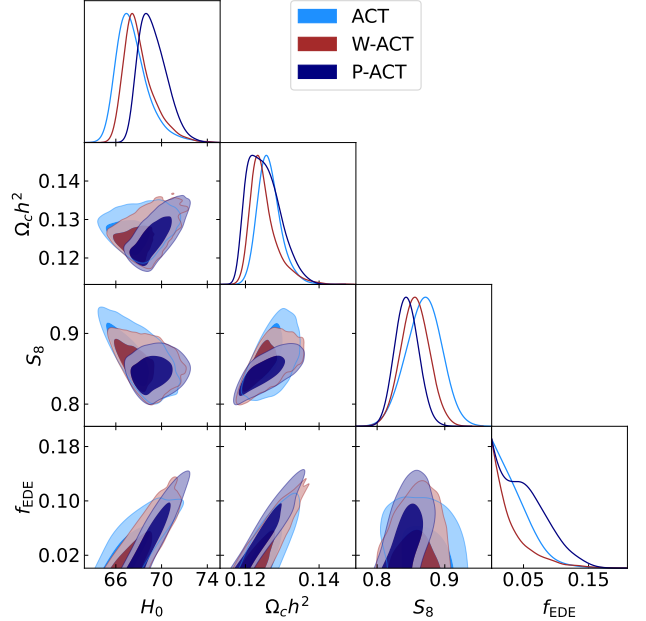
Figure 12. Marginalized contours at 68% and 95% confidence for the EDE fraction showing (well-known) positive correlations with H_0, $\Omega_c h^2$, and S_8 for different dataset combinations (ACT in blue, W-ACT in brown, and P-ACT in navy). The small bump in the marginalized f_{EDE} posterior for P-ACT is real and arises from the mild EDE improvement in χ^2 over ΛCDM in this model — see Table 2.

and BAO data, we obtain

$$f_{EDE} < 0.12 \quad (95\%, \text{P-ACT-LB})$$
$$H_0 = 69.9^{+0.8}_{-1.5} \quad (68\%, \text{P-ACT-LB}), \quad (16)$$

with W-ACT-LB giving similar results. For comparison, $H_0 = 68.2 \pm 0.4$ km/s/Mpc in ΛCDM for P-ACT-LB (L25). We also consider substituting BOSS BAO for DESI BAO data, which yields $f_{EDE} < 0.10$ (95%, P-ACT-LB$_{BOSS}$) and $H_0 = 69.2^{+0.7}_{-1.3}$ km/s/Mpc (68%, P-ACT-LB$_{BOSS}$), slightly decreasing H_0 and tightening the bound on f_{EDE} compared to P-ACT-LB.[12] We further verify that these results are essentially unchanged with the inclusion of SNIa data in the analysis.

We also obtain constraints for P-ACT-LB-S8,[13] which includes an external prior on S_8 from the joint analysis of DES-Y3 and KiDS-1000 cosmic shear data (Dark Energy Survey and Kilo-Degree Survey Collaboration 2023), as described in §2.5. Hill et al. (2020), who

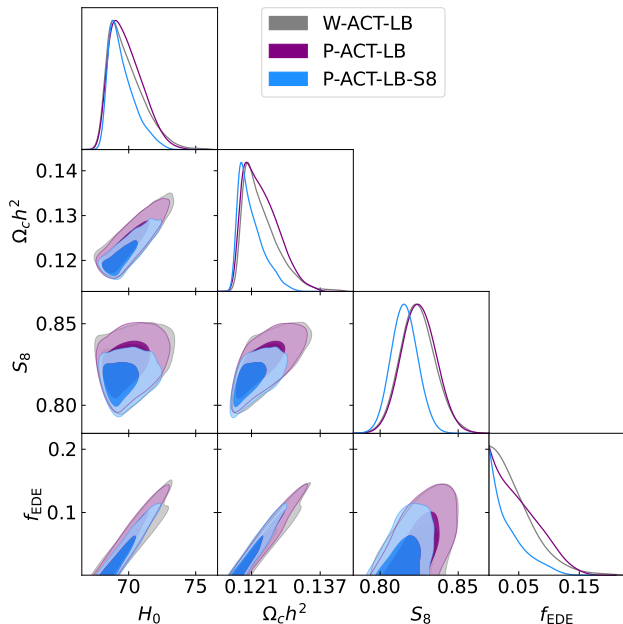**Figure 13.** Same as Fig. 12, tightening the limits with additional datasets (W-ACT-LB in gray, P-ACT-LB in purple, and P-ACT-LB-S8 in blue).

	$\Delta\chi^2$	Pref. in σ	$H_0^{(\text{EDE})}$	f_{EDE}	$\log_{10} z_c$
ACT	≈ 0.0	0.0	66.5	0.012	3.00
W-ACT	1.9	0.5	69.9	0.089	3.55
P-ACT	4.3	1.2	70.4	0.091	3.56
W-ACT-LB	2.9	0.8	70.2	0.070	3.52
P-ACT-LB	6.6	1.7	71.2	0.093	3.56

Table 2. The $\Delta\chi^2 = \chi^2_{\Lambda\text{CDM}} - \chi^2_{\text{EDE}}$ from the `MFLike` likelihood MAP points for the $n = 3$ EDE model compared to ΛCDM for each dataset combination, and preference (in units of σ) for EDE over ΛCDM using the likelihood-ratio test statistic. The values for H_0, f_{EDE}, and $\log_{10} z_c$ in the MAP EDE model are also reported. The data show no significant preference for non-zero EDE. For ACT alone, the MAP χ^2 for EDE is indistinguishable from that for ΛCDM within our numerical precision, indicating that adding EDE parameters does not improve the fit at all in this case.

also placed constraints on EDE, validated that a simple Gaussian prior on S_8 is a sufficiently accurate approximation to the inclusion of a full weak lensing likelihood in such joint analyses with CMB data (see their Appendix B). The inclusion of S_8 significantly tightens the upper limit on EDE (see Fig. 13), as positive f_{EDE} values increase this parameter above its ΛCDM value (the late-time matter power spectrum amplitude is increased due to increases in $\Omega_c h^2$ and n_s in the CMB fit), which is in the opposite direction to the preference in the DES and KiDS data (Hill et al. 2020).

Switching now to the $n = 2$ EDE model, for ACT alone, we obtain $f_{\text{EDE}} < 0.091$ (95%, ACT) with $H_0 = 67.5^{+0.9}_{-1.5}$ km/s/Mpc. Adding *Planck* yields $f_{\text{EDE}} < 0.11$ (95%, P-ACT) with $H_0 = 69.3^{+1.0}_{-1.5}$ km/s/Mpc. Finally, adding CMB lensing and BAO data yields $f_{\text{EDE}} < 0.11$ (95%, P-ACT-LB) with $H_0 = 70.1^{+0.9}_{-1.5}$ km/s/Mpc. These results are similar to the $n = 3$ case. A full comparison between the two models is discussed in Appendix E.

Some past studies (e.g., Herold et al. 2022; Herold & Ferreira 2023; Poulin et al. 2023b; Efstathiou et al. 2024) have discussed "projection effects," where, in the ΛCDM limit ($f_{\text{EDE}} \to 0$), the additional EDE-specific parameters (z_c and θ_i) have no impact. These can bias the Bayesian posterior for f_{EDE}. Additionally, the exact choice of the z_c prior range can have a significant effect on the final constraints in this model, as large values of

f_{EDE} are allowed if z_c is sufficiently high that no dynamical effects are imprinted on the CMB (i.e., the EDE is irrelevant by the recombination epoch, La Posta et al. 2022). Finally, the lower bound of $f_{\text{EDE}} = 0$ only allows the model fit to increase H_0 or leave it unchanged, not decrease it. Therefore, to evaluate whether the data have a meaningful preference for the EDE model, it is useful to compare the effective χ^2 value of the MAP EDE model to that of the ΛCDM model, rather than to solely inspect the Bayesian posteriors, as was done in Hill et al. (2022). To maximize the posterior, we use both `Cobaya` and `PROSPECT`, a profile likelihood code that can also be used for accurate global optimization (Brinch Holm et al. 2024).[14] We then take the global MAP from the different minimizer runs.

Performing this exercise, we find no preference for the EDE model from the DR6 data alone or combined with other datasets, as shown in Table 2 for the $n = 3$ EDE model. For ACT alone, we do not find an MAP point for the $n = 3$ EDE model with lower χ^2 than that found for ΛCDM, i.e., the additional parameters of the EDE model provide no meaningful improvement in goodness-of-fit to the ACT data within our numerical precision. The MAP model is nearly indistinguishable from ΛCDM, with $f_{\text{EDE}} = 0.012$ (very close to the ΛCDM edge of the parameter space) and $\log_{10} z_c = 3.00$, the lower edge of our prior, where the impact of EDE on the CMB is minimal. In the other cases, we note that in the EDE model there is a narrow degeneracy direction in the parameter space, where parameters may shift

---

[14] For the posterior maximization procedure, we use the full Boltzmann code `class` rather than the emulators, to obtain high numerical precision.

while having very similar effective χ^2 values. Nevertheless, in none of the cases do we find the improvement in goodness-of-fit over ΛCDM significant.

Using the $\Delta\chi^2$ values, we compute the equivalent preference in σ using the likelihood-ratio test as in Hill et al. (2022).[15] We find that in all cases the preference for EDE over ΛCDM is $< 2\sigma$. The $\Delta\chi^2$ values for the $n = 2$ case, shown in Appendix E, yield the same conclusion.

To further circumvent the problem of projection effects, some past works have used a profile likelihood approach (see, e.g., Lewis & Bridle 2002; Audren et al. 2013 for more detail). However, the $\Delta\chi^2$ values that we find between the EDE and ΛCDM MAP models are insignificant; as such, we see no evidence of preference for the EDE model in either a Bayesian or frequentist framework. Thus, we conclude that the significant computational expense of a full profile likelihood analysis is not justified, and is unlikely to affect the interpretation of these results.

5.2. *Varying fundamental constants*

The dynamics of recombination depends critically on the values of fundamental constants during the decoupling epoch, including the fine-structure constant $\alpha_{\rm EM}$ and the electron mass m_e. High-precision CMB observations thus allow for constraints on possible variations of these constants over vast scales in both distance and time (see, e.g., Sekiguchi & Takahashi 2021; Hart & Chluba 2020, 2018; Planck Collaboration 2015; Menegoni et al. 2012; Scóccola et al. 2009; Martins et al. 2004; Rocha et al. 2004; Battye et al. 2001; Avelino et al. 2001, 2000; Kaplinghat et al. 1999; Hannestad 1999). Furthermore, models featuring fundamental constant variations are amongst the few that have had some phenomenological success in increasing the CMB-inferred Hubble constant (Knox & Millea 2020; Sekiguchi & Takahashi 2021; Schöneberg et al. 2022). However, we emphasize that these models are not physical, in the sense that the fundamental constant variation is not driven dynamically by a new field or interaction; we simply assume that $\alpha_{\rm EM}$ or m_e can take a different value in the early universe than it does today, which opens degeneracies in the CMB. Recently, Baryakhtar et al. (2024) have found that a first-principles implementation of varying-constant models can yield rather different conclusions than crude phenomenological models, due to (for example) the impact of perturbations in the field driving

the constant-variation, as well as its contribution to the cosmic energy budget. However, for simplicity, here we stick to a phenomenological approach in which $\alpha_{\rm EM}$ or m_e are simply allowed to vary, thus testing their values at the CMB epoch as compared to today.

We use the new ACT DR6 power spectra to place updated bounds on possible variation of $\alpha_{\rm EM}$ and m_e (considered individually). For simplicity, we assume that the value of $\alpha_{\rm EM}$ (or m_e) undergoes an instantaneous, step-function transition well after recombination is completed, but well before the reionization epoch (specifically, we choose $z = 50$ for the redshift of this transition). The value of the constant after the transition is fixed to the laboratory-measured value (Particle Data Group 2024), while the value before the transition is taken to be a free parameter. The relevant physical effects on the recombination dynamics are treated via the implementation in `HyRec` (Ali-Haïmoud & Hirata 2011), as incorporated in `class` (note that `CosmoRec` (Chluba et al. 2010) includes a similarly accurate treatment of these effects). The dominant physical effects are due to changes in the Thomson scattering cross-section, with $\sigma_{\rm T} \propto \alpha_{\rm EM}^2 m_e^{-2}$, and changes in the energy levels of atomic hydrogen, with $E \propto \alpha_{\rm EM}^2 m_e$. Many additional, subtle effects arise due to the non-equilibrium nature of cosmological recombination — see, e.g., Hart & Chluba (2018); Chluba & Ali-Haïmoud (2016); Planck Collaboration (2015) for a thorough discussion. In general, variations of $\alpha_{\rm EM}$ or m_e change the timing of recombination, with higher values of these constants associated with earlier recombination. Thus, such variations change the physical scales imprinted in the CMB power spectrum, including the damping scale. The new ACT DR6 spectra allow tests of these effects in a qualitatively new regime, deep into the damping tail in TT and across a wide range of scales in TE and EE.

As pointed out in Sekiguchi & Takahashi (2021), a joint variation of m_e and the spatial curvature Ω_k opens up a particularly significant degeneracy with H_0 and other cosmological parameters. In principle, such a model has sufficient freedom to accommodate an increased value of H_0 while providing a good fit to not only CMB data, but also late-time measurements of the distance-redshift relation from BAO and SNIa data. Here, we revisit this scenario. In addition, we also consider a model in which both $\alpha_{\rm EM}$ and Ω_k are allowed to vary.

5.2.1. *Electron mass*

We parametrize a possible deviation of the electron mass from its present-day value by introducing a free parameter $m_e/m_{e,0}$, where m_e ($m_{e,0}$) is the mass at

---

[15] Because the ΛCDM model is a subset of the EDE model (with $f_{\rm EDE} = 0$), the $\Delta\chi^2$ between the best-fit EDE and best-fit ΛCDM models follows a chi-squared distribution with three degrees of freedom, corresponding to the three additional free parameters of the EDE model.

$z > 50$ ($z < 50$, including today). We adopt a flat, uninformative prior: $m_e/m_{e,0} \in [0.3, 1.7]$. Combining ACT and *Planck*, we find

$$m_e/m_{e,0} = 0.856^{+0.060}_{-0.073} \quad (68\%, \text{P-ACT}), \qquad (17)$$

whereas *Planck* alone yields $m_e/m_{e,0} = 0.880^{+0.068}_{-0.080}$. While the P-ACT result lies 2.4σ below unity, we find that this is driven mostly by the *Planck* data: ACT alone yields $m_e/m_{e,0} = 1.02^{+0.11}_{-0.15}$, while combining ACT with *WMAP* yields

$$m_e/m_{e,0} = 0.921 \pm 0.083 \quad (68\%, \text{W-ACT}). \quad (18)$$

Interpreting the P-ACT result as a statistical fluctuation, we further include CMB lensing and DESI BAO data to obtain

$$\left.\begin{array}{rl} m_e/m_{e,0} = & 1.0096 \pm 0.0060 \\ H_0 = & 69.8 \pm 1.1 \end{array}\right\} \quad (68\%, \text{P-ACT-LB}). \tag{19}$$

Further adding SNIa data slightly tightens the constraints while moving them closer to ΛCDM, giving $m_e/m_{e,0} = 1.0063 \pm 0.0056$ and $H_0 = 69.1 \pm 1.0$ (68%, P-ACT-LBS).

These bounds represent the tightest constraints to date on the value of the electron mass at the recombination epoch, now approaching the half-percent level. Here, the BAO data are crucial in breaking severe geometric degeneracies that arise in the primary CMB when the electron mass is allowed to vary (see, e.g., Hart & Chluba 2018 and Sekiguchi & Takahashi 2021 for detailed discussion). These severe degeneracies also allow much more freedom in the Hubble constant, which increases compared to the value found in ΛCDM when fitting these datasets. Nevertheless, we emphasize again that this model is not physical: no dynamical field has been introduced that drives the evolution of m_e.

5.2.2. *Electron mass and spatial curvature*

Sekiguchi & Takahashi (2021) noted that variation of the electron mass has the unique property of allowing multiple scales in the CMB to be preserved (in combination with other ΛCDM parameters changing), including the acoustic scale and the damping scale. However, this variation will change the late-time expansion history, which is why the inclusion of BAO data plays a key role in the constraints above. This observation motivates further extending the model to allow freedom to adjust the late-time distance-redshift relation. Sekiguchi & Takahashi (2021) considered scenarios in which either the spatial curvature or the dark energy equation of state were allowed to vary in addition to m_e. They found
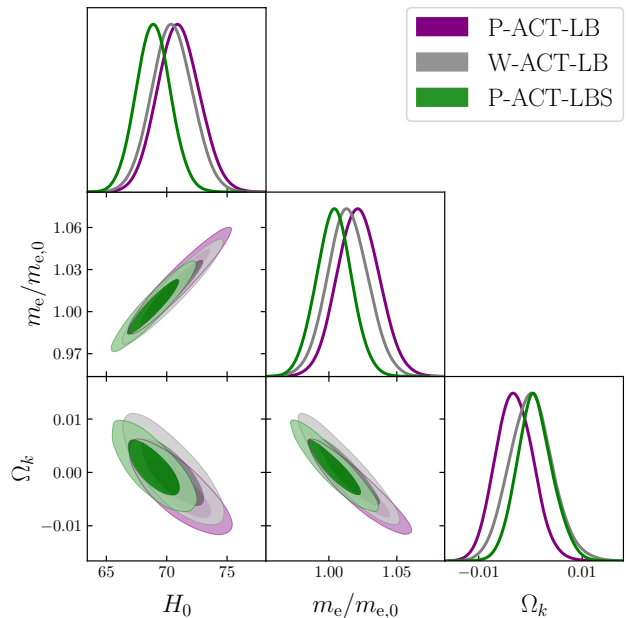

Figure 14. Constraints on a (non-physical) model with time variation of the electron mass and non-zero spatial curvature. This model opens up significant degeneracies in the CMB (and BAO) data. A joint fit to P-ACT-LB yields a higher value of H_0 than in ΛCDM, but with a much larger error bar; the same behavior is seen for W-ACT-LB, indicating that the results are not specific to *Planck*. However, inclusion of SNIa data (P-ACT-LBS, green) pushes the results toward ΛCDM, disfavoring this approach for increasing the cosmologically-inferred value of H_0.

spatial curvature to yield surprising success in accommodating significant variation of m_e (and hence H_0) in fits to *Planck* CMB and BOSS BAO data, a result that was further validated in Schöneberg et al. (2022).

Here, we revisit this model with the new ACT DR6 spectra. We adopt a uniform prior $\Omega_k \in [-0.6, 0.6]$ and the same prior on m_e used above. We compute theoretical predictions using `class`.

We find that this two-parameter extension of ΛCDM is highly unconstrained in fits to CMB data alone. We thus focus solely on joint analyses of CMB and late-time data here, with results shown in Fig. 14. Our baseline dataset combination yields

$$\left.\begin{array}{rl} m_e/m_{e,0} = & 1.022 \pm 0.016 \\ \Omega_k = & -0.0031 \pm 0.0037 \\ H_0 = & 71.0 \pm 1.7 \end{array}\right\} \quad (68\%, \text{P-ACT-LB}). \tag{20}$$

While neither non-standard m_e or non-flat Ω_k are detected on their own in this fit, their combined impact allows H_0 to take on higher values, consistent with earlier results from Sekiguchi & Takahashi (2021); Schöneberg et al. (2022). To assess the additional constraining

power contributed by ACT, note that the error bar on H_0 in our P-ACT-LB analysis is roughly 20% smaller than that found for the same model using *Planck* and BOSS BAO data ($H_0 = 69.29 \pm 2.11$, Schöneberg et al. 2022). We verify that these results are not driven by the high CMB lensing amplitude in *Planck* by replacing *Planck* with *WMAP* in the dataset combination, finding

$$
\left.\begin{aligned}
m_e/m_{e,0} &= 1.014 \pm 0.015 \\
\Omega_k &= 0.0001 \pm 0.0042 \\
H_0 &= 70.4 \pm 1.7
\end{aligned}\right\} \quad (68\%,\ \text{W-ACT-LB}).
$$
(21)

The parameter posteriors in these fits are significantly broadened compared to those obtained in ΛCDM (cf. $H_0 = 68.22 \pm 0.36$ for P-ACT-LB in L25) or ΛCDM$+\Omega_k$. For comparison, we find $\Omega_k = 0.0019 \pm 0.0015$ for P-ACT-LB in §7.1; this bound is weakened by more than a factor of two in the model studied here. Although the central values of some parameters shift compared to ΛCDM, the significance of the shifts is counteracted by the increased error bars, and we find that this model does not yield a significant improvement in goodness-of-fit over ΛCDM. For the MAP model obtained for P-ACT-LB (W-ACT-LB), we find $\Delta\chi^2 = -2.4$ (-1.5) with respect to ΛCDM, with two additional free parameters. These values correspond to a 1.0σ or 0.7σ preference over ΛCDM, respectively, neither of which is significant.

It is also worth noting that the DESI BAO data play an important role in the central value of the H_0 posterior here (and in other models studied in this work). Due to the computational expense of running MCMC chains for this model (which is extremely slow to evaluate in `class`), we use importance-sampling with an approximate version of the BOSS BAO likelihoods to assess how the results would shift if DESI were replaced with BOSS. We find that the central value of the H_0 posterior shifts downward by 1–1.5 km/s/Mpc, while the electron mass and spatial curvature shift closer to their ΛCDM values. The error bars on all quantities increase only slightly. Thus, we conclude that the central values of the above parameter constraints are partially driven by the DESI BAO data.

Furthermore, we find that a joint analysis with Pantheon+ SNIa data pulls all parameters toward their ΛCDM values, while tightening the error bars compared to the P-ACT-LB results:

$$
\left.\begin{aligned}
m_e/m_{e,0} &= 1.004 \pm 0.013 \\
\Omega_k &= 0.0008^{+0.0032}_{-0.0036} \\
H_0 &= 68.9 \pm 1.4
\end{aligned}\right\} \quad (68\%,\ \text{P-ACT-LBS}).
$$
(22)

Notably, the H_0 value in this fit is fully consistent with its ΛCDM value. From the joint analysis of P-ACT-LBS and the insignificant improvement in quality of fit to P-ACT-LB, we conclude that there is no evidence for a scenario with spatial curvature and a non-standard electron mass at recombination. The possibility of obtaining a high value of H_0 from cosmological data in this model is significantly reduced by these new results.

5.2.3. *Fine-structure constant*

As done above for the electron mass, we parametrize possible deviation of the fine-structure constant from its present-day value by introducing a free parameter $\alpha_{\rm EM}/\alpha_{\rm EM,0}$, where $\alpha_{\rm EM}$ ($\alpha_{\rm EM,0}$) is the value at $z > 50$ ($z < 50$, including today). We adopt a flat, uninformative prior: $\alpha_{\rm EM}/\alpha_{\rm EM,0} \in [0.6, 1.4]$. Combining ACT and *Planck*, we find

$$
\alpha_{\rm EM}/\alpha_{\rm EM,0} = 1.0037 \pm 0.0017 \quad (68\%,\ \text{P-ACT}), \quad (23)
$$

representing a 30% reduction in the error bar compared to that from *Planck* alone, which yields $\alpha_{\rm EM}/\alpha_{\rm EM,0} = 1.0005 \pm 0.0025$ (consistent with Hart & Chluba 2020). ACT alone yields $\alpha_{\rm EM}/\alpha_{\rm EM,0} = 1.0046 \pm 0.0035$.

Further including CMB lensing and DESI BAO data yields

$$
\alpha_{\rm EM}/\alpha_{\rm EM,0} = 1.0043 \pm 0.0017 \quad (68\%,\ \text{P-ACT-LB}), \quad (24)
$$

thus fluctuating $\approx 2.5\sigma$ above unity. Inclusion of SNIa data has negligible effect on this result. As higher $\alpha_{\rm EM}$ corresponds to earlier recombination, this result also yields a moderate increase in the Hubble constant, with $H_0 = 69.27 \pm 0.54$ km/s/Mpc. Interpreting this result as a statistical fluctuation, these bounds represent the tightest constraints to date on the value of the fine-structure constant at the recombination epoch, approaching the per-mille level.

5.2.4. *Fine-structure constant and spatial curvature*

Unlike the electron mass, variation of the fine-structure constant (in combination with other parameters) can not simultaneously preserve all of the relevant physical scales in the CMB power spectrum; this is largely why the constraints on $\alpha_{\rm EM}$ above are tighter than those on m_e. This is also why the Hubble constant cannot increase as significantly when varying $\alpha_{\rm EM}$ as when varying m_e (Sekiguchi & Takahashi 2021). For completeness, and to better understand the results found above for the $m_e+\Omega_k$ model, here we consider extending the varying-$\alpha_{\rm EM}$ model to also allow the spatial curvature to vary. This allows further freedom in the late-time expansion history, allowing wider range of parameter variations to be accommodated in fits to CMB and BAO data.

As above, we compute theoretical predictions for this model using `class`. We adopt an uninformative prior $\Omega_k \in [-0.6, 0.6]$, while allowing α_{EM} to vary as in our previous analysis.

As expected, we find that this two-parameter extension is far less degenerate than the $m_e + \Omega_k$ model studied above. Focusing for simplicity solely on the P-ACT-LB dataset combination, we find

$$\left.\begin{array}{rl} \alpha_{\text{EM}}/\alpha_{\text{EM},0} = & 1.0041 \pm 0.0017 \\ \Omega_k = & 0.0007 \pm 0.0015 \\ H_0 = & 69.4 \pm 0.6 \end{array}\right\} \quad (68\%, \text{P-ACT-LB}).$$

(25)

Comparing to the results above, it is evident that the constraint on α_{EM} is essentially unchanged by the opening of the spatial curvature, which itself is also tightly constrained near zero. Likewise, H_0 hardly changes, with the analogous result for fixed spatial curvature yielding $H_0 = 69.3 \pm 0.5$ km/s/Mpc.

Contrasting the varying-α_{EM} results with the varying-electron-mass case, we find that the degeneracy structure of the two models is remarkably different, with the electron mass possessing much more flexibility in accommodating a wide range of parameter space than the fine-structure constant, consistent with Hart & Chluba (2018, 2020); Sekiguchi & Takahashi (2021).[16] Nevertheless, we note again that all of the varying-constant models studied here are not physical, but rather simply crude phenomenological approximations. These results may be a useful guide in constructing physical models that can achieve similar flexibility in accommodating a wide range of data.

5.3. *Primordial magnetic fields*

The existence of primordial magnetic fields (PMFs) is a compelling possibility. Such PMFs could cause inhomogeneities in the baryon distribution around recombination. Thus, the PMF model is an example of a slightly more generic scenario known as "baryon clumping" (Jedamzik & Abel 2013; Jedamzik & Saveliev 2019). Primordial magnetic fields with a blue-tilted power spectrum can naturally have kpc-scale correlation lengths. Once the photon gas dynamically decouples from the baryon fluid on small scales, the magnetic force causes efficient growth of baryon density perturbations to potentially $\mathcal{O}(1)$ contrasts. These kpc-scale perturbations are not directly resolvable in CMB observations, but they cause accelerated recombination due to

the quadratic source term in the equation describing the recombination rate (Peebles 1968). The corresponding decrease in the sound horizon could then partially reconcile CMB-based determinations of the Hubble constant with local universe measurements (Jedamzik & Pogosian 2020). As magnetic fields are part of the standard model and their generation during early-universe phase transitions is conceivable, PMFs (or baryon clumping models in general) are a well-motivated scenario to potentially increase the CMB-inferred Hubble constant.[17]

Baryon clumping induces changes in the Silk damping tail in addition to the leading-order geometric effect described above. Two counteracting effects are at play (Jedamzik & Abel 2013): shortened photon diffusion due to accelerated hydrogen recombination suppresses Silk damping, but the previously accelerated helium recombination decreases the ionization fraction and thus increases the damping. These two effects do not generally cancel, and empirically the first one appears to be dominant (e.g., Thiele et al. 2021). Thus, the high-resolution ACT DR6 data with good signal-to-noise in the damping tail enable stringent constraints on baryon clumping scenarios.

Theoretical modeling of PMF-induced baryon clumping is non-trivial. We adopt a simplified model used in earlier works (Jedamzik & Pogosian 2020; Thiele et al. 2021; Rashkovetskyi et al. 2021; Galli et al. 2022; Jedamzik & Pogosian 2023). The baryon density distribution function is sampled by three zones in each of which the baryon density is taken as a constant. Taking the zones as indexed by $i = 1, 2, 3$, each zone carries a volume fraction f_i and a baryon density $\Delta_i \equiv \rho_{b,i}/\langle\rho_b\rangle$. Volume and mass conservation imply the constraints $\sum f_i = \sum f_i \Delta_i = 1$. For each zone, the recombination history is computed separately and the thermal history is then taken as the volume-weighted average over the three zones. This treatment neglects Lyα photon mixing (Jedamzik et al. 2025).

Within the three-zone model, we choose to work with the "M1" scenario of Jedamzik & Pogosian (2020): $f_2 = 1/3$, $\Delta_1 = 0.1$, $\Delta_2 = 1$. After applying the constraints described above, the model thus has only a single free parameter, the variance b of the small-scale baryon density fluctuations

$$1 + b \equiv \sum_i f_i \Delta_i^2.$$

(26)

---

[16] A similar result is found for the small-scale baryon clumping scenario studied in §5.3 — allowing Ω_k to vary also has little degeneracy with the clumping parameter constraint.

[17] Note that effects due to Faraday rotation (e.g., Cai & Guan 2022) are not considered here and are expected to yield weaker constraints on such models (Pogosian et al. 2019).
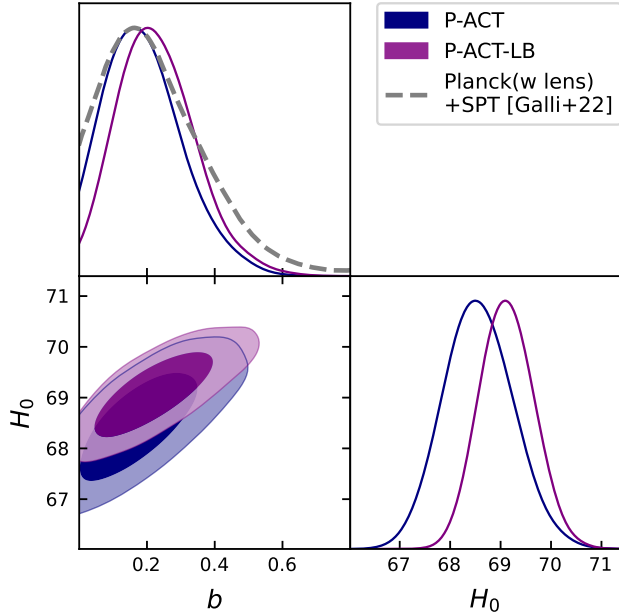
Figure 15. Constraints on the variance b of the small-scale baryon density distribution at recombination from P-ACT (navy) and P-ACT-LB (purple), compared with the latest results from *Planck* (including CMB lensing) combined with SPT small-scale polarization (gray dashed line). Primordial magnetic fields would induce baryon clumping on small scales, and hence $b > 0$. No evidence of clumping is seen in our analysis.

Recent perturbative and simulation-based works have suggested refinements of this simplified treatment (Lee & Ali-Haïmoud 2021; Jedamzik et al. 2025). Jedamzik et al. (2025) recently presented constraints on primordial magnetic fields using a simulation-informed model for the recombination history. Where comparisons can be made between this method and our three-zone model, there is a remarkably close agreement between the two approaches. In particular, the posteriors for H_0 in Jedamzik et al. (2025) are similar to results found for the three zone-model.

In the absence of a more accurate publicly available model and in order to facilitate comparison with previous constraints, we choose to continue working with the three-zone model. However, we stress that our constraints are to be interpreted in the context of this model and further work will be needed to evaluate the viability of baryon clumping scenarios more generally. Nevertheless, previous work has indicated that increasing the flexibility of the model does not substantially alter the constraint on b or H_0 (Thiele et al. 2021).

Figure 15 shows our constraints on the clumping parameter and the Hubble constant, from primary CMB data alone and in combination with CMB lensing and BAO data. We find that the constraint on b is tightened

compared to previous analyses:

$$b < 0.41 \ (95\%, \text{P-ACT}),$$
$$< 0.44 \ (95\%, \text{P-ACT-LB}). \tag{27}$$

For comparison, the *Planck* primary CMB alone constrains $b < 0.51$, and the combination of *Planck* (including CMB lensing) plus SPT-3G gives results consistent with our P-ACT measurement (Galli et al. 2022). If we combine all three datasets (ACT, *Planck*, and the public SPT-3G data), there is only a marginal improvement on P-ACT.

Note that the posteriors including ACT data peak at non-zero b; thus the improvement in constraining power is larger than what is suggested by comparing the upper limits. As quantified by the standard deviation in b, adding ACT improves upon the *Planck*-only constraint by about 30%. We find no detection of baryon clumping and hence further restrict this model's ability to increase the CMB-inferred H_0 value: we find $H_0 = 68.6 \pm 0.7$ km/s/Mpc and $H_0 = 69.1 \pm 0.5$ km/s/Mpc for P-ACT and P-ACT-LB in this model, respectively.

In contrast to the seemingly similar model with varying electron mass, we find that the inclusion of spatial curvature as a free parameter does not appreciably change the H_0 posterior in the P-ACT-LB data combination (see §5.2.2 for contrasting results in the varying-electron-mass case). The non-trivial small-scale effects in the baryon clumping model constrain b beyond the information contained in the geometric sound-horizon modification.

5.4. *Temperature of the CMB*

Several studies (e.g., Ivanov et al. 2020a; Wen et al. 2021; Hill & Bolliet 2023) have explored the possibility of increasing the CMB-anisotropy-inferred value of the Hubble constant by changing the CMB monopole temperature, T_{CMB}. In particular, Ivanov et al. (2020a) highlighted a strong negative degeneracy in the H_0-T_{CMB} plane when the monopole temperature is left free in analyses of *Planck* data. Setting a SH0ES prior on H_0 would then yield a temperature measurement 3σ lower than the combined measurement of $T_{\text{CMB}} = 2.72548 \pm 0.00057$ K (Fixsen 2009) from *COBE/FIRAS* and other data.[18]

Obtaining a higher value of H_0 via a decrease in the monopole CMB temperature is difficult. Models with some level of post-recombination reheating can have an

---

[18] Note that the error bar on T_{CMB} from Fixsen (2009) is sufficiently small that this value is taken as a fixed constant in analyses of ΛCDM (and the extended models studied in this paper).

impact by allowing a lower value of the monopole temperature in the early universe (e.g., Hill & Bolliet 2023 propose to convert a fraction of DM into photons during the dark ages). However, although such a process is straightforward to implement in a phenomenological way, it is hard to find a well-grounded physical mechanism to motivate it such that the blackbody spectrum is preserved (see, e.g., Chluba 2014).

Nevertheless, these studies have led to the realization that current CMB anisotropy data in combination with BAO data provide, on their own, a powerful probe of the amount of radiation in the universe.[19] A single-parameter extension to the ΛCDM model, where T_{CMB} is left free, is well constrained. Ivanov et al. (2020a) combine *Planck* 2018 CMB anisotropy and lensing data with BOSS DR12 BAO data (eBOSS Collaboration 2018) and find $T_{\mathrm{CMB}} = 2.706^{+0.019}_{-0.020}$ K (68% CL). Updating this *Planck* result including BAO from DESI, we find a slightly tighter constraint, $T_{\mathrm{CMB}} = 2.696 \pm 0.017$ K. With the addition of the new ACT DR6 spectra, we find a similar constraint

$$T_{\mathrm{CMB}} = 2.698 \pm 0.016 \, \mathrm{K} \quad (68\%, \mathsf{P\text{-}ACT\text{-}LB}). \quad (28)$$

This 0.6% measurement of T_{CMB} is consistent with the direct *COBE/FIRAS* monopole measurement. The corresponding constraint on H_0 is consistent with the result in ΛCDM, as shown in Fig. 16.

5.5. *Modified recombination history*

In this subsection, we present a non-parametric reconstruction of the cosmological recombination history, including ACT DR6 data. Modifications to the standard recombination history have been extensively studied, both as a powerful test of the standard cosmological model and as a potential avenue to increase the value of the Hubble constant inferred from CMB observations (e.g., Lee et al. 2023; Lynch et al. 2024b,a; Pogosian et al. 2024; Mirpoorian et al. 2024). To investigate such modifications, we use the `ModRec` model developed in Lynch et al. (2024b), which parametrizes departures in the ionization fraction, $X_{\mathrm{e}}(z) \equiv n_{\mathrm{e}}(z)/n_{\mathrm{H}}(z)$, from the standard recombination history, where $n_{\mathrm{e}}(z)$ and $n_{\mathrm{H}}(z) = n_{\mathrm{HI}}(z) + n_{\mathrm{HII}}(z)$ are the number densities of free electrons and hydrogen nuclei, respectively. While phenomenological, the flexible parametrization employed by `ModRec` effectively captures a broad range of physical scenarios, including the effects of primordial magnetic fields, time-varying electron mass, and dark
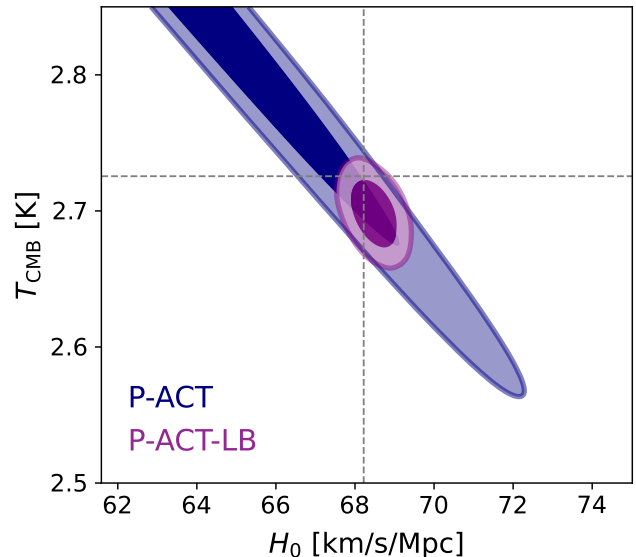
---

[19] Note that it is important to self-consistently vary the calibration of the CMB anisotropy data in such analyses, as explained in Ivanov et al. (2020a).


Figure 16. Constraints on the CMB monopole temperature (T_{CMB}) and H_0. The P-ACT-LB combination (purple) effectively breaks the degeneracy between these two parameters present in CMB-only analyses (navy) and gives a tight measurement of both parameters, similar to that achieved with CMB data from *Planck* in previous literature. The results are consistent with the ΛCDM case, in which T_{CMB} is fixed to the *COBE/FIRAS* value (gray dashed lines).

matter annihilation (Lynch et al. 2024b), all of which are also studied separately elsewhere in this paper.

Following Lynch et al. (2024b), we parameterize departures from the standard ionization fraction $\Delta X_{\mathrm{e}}(z) = X_{\mathrm{e}}(z) - X_{\mathrm{e}}^{\mathrm{std}}(z)$ at seven control points spanning $z = 533$ to 1600, leaving reionization and helium recombination unchanged. These control points are interpolated using a cubic spline that enforces physical bounds, $0 \leq X_{\mathrm{e}}(z) \leq X_{\mathrm{e}}^{\mathrm{max}}$, where $X_{\mathrm{e}}^{\mathrm{max}}$ is the maximum allowed ionization fraction. We compute all theoretical predictions using the `class` implementation of `ModRec`, with precision parameters and settings described in Appendix A. Our control points and their priors are identical to those used in Lynch et al. (2024a,b).

We present constraints on the `ModRec` model using the Planck-LB and P-ACT-LB datasets — we do not show or discuss discuss P-ACT alone as BAO data are essential for breaking degeneracies between the modified recombination parameters and standard cosmological parameters (Lynch et al. 2024b). We show results for both DESI and BOSS BAO datasets, as the choice of BAO data impacts the reconstructed $X_e(z)$ due to differences in the inferred values of $r_d H_0$ and Ω_m between BOSS and DESI measurements, assuming ΛCDM (Lynch et al. 2024a; Pogosian et al. 2024).
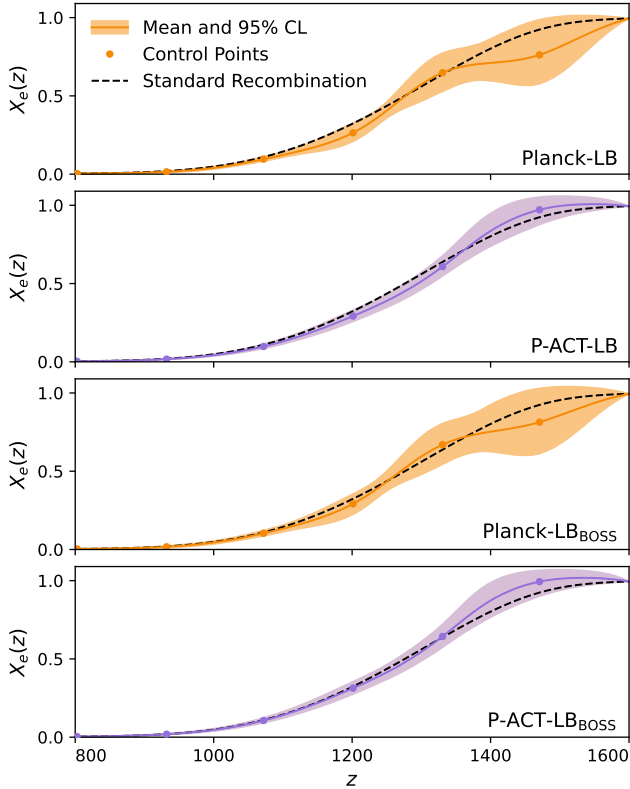
Figure 17. Reconstructed ionization fraction as a function of redshift using the `ModRec` model. The shaded region shows the mean and 95% two-tailed CL. The circles indicate the mean ionization fraction at the control points used in the reconstruction. The top (bottom) two panels use DESI (BOSS) BAO; the orange and purple colors distinguish between using *Planck*-alone or P-ACT CMB data. The black dashed line shows the evolution of the ionization fraction for the standard recombination scenario assuming the P-ACT-LB best-fit ΛCDM parameters. We see no evidence of a deviation from the standard recombination history.

Figure 17 shows the mean and 95% two-tailed CL constraints on the reconstructed ionization fraction as a function of redshift. Including ACT DR6 data significantly improves the constraints on $X_e(z)$, with a factor of two reduction in the uncertainty of the highest redshift ($z \approx 1467$) control point.[20] This improvement arises because modifications to the ionization fraction impact the polarization and damping tail of the CMB (Hadzhiyska & Spergel 2019; Lynch et al. 2024b). The reconstructed recombination histories are consistent

---

[20] The modified recombination history cosmology in Fig. 3 is obtained by selecting a sample from the Planck-LB chain that has at least a 20% difference in the highest-redshift ionization fraction relative to the standard recombination history and a $\Delta\chi^2 < 1$ compared to the chain's best-fit cosmology.
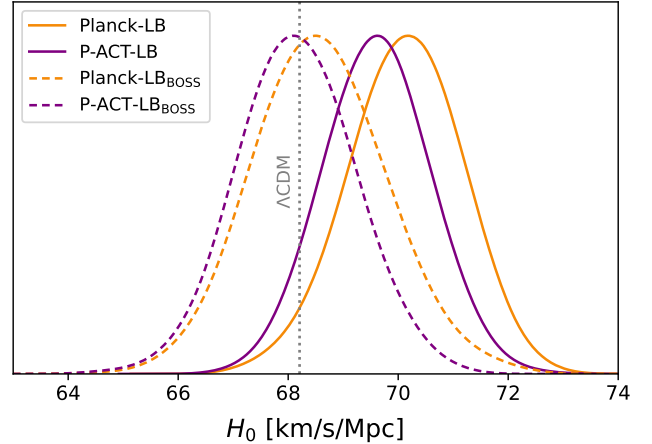
Figure 18. Marginalized constraints on H_0 from the `ModRec` analysis for the P-ACT-LB (purple) and Planck-LB (orange) datasets. The solid (dashed) lines use DESI (BOSS) BAO. The vertical gray line denotes the best-fit ΛCDM value of H_0 from the P-ACT-LB (DESI) dataset.

with the standard recombination scenario (black dashed lines).[21]

Notably, the mean ionization fraction from the P-ACT-LB$_{\text{BOSS}}$ reconstruction is nearly indistinguishable from the standard recombination scenario across all redshifts analyzed, with all sampled control points agreeing with the standard recombination history within 1σ, except for the highest redshift control point ($z = 1467$), where the ACT data favor a slightly higher (1.5σ) ionization fraction than the standard model. This is driven by ACT's mild preference for less damping compared to *Planck*, as a larger value of X_e at high redshifts leads to a decrease in damping (Lynch et al. 2024b). This mild preference for a higher X_e at high redshifts is in the opposite direction of what is generally required by modified recombination models that aim to increase the value of H_0 inferred from the primary CMB. Finally, with respect to the MAP ΛCDM model, we find $\Delta\chi^2 = -11.6$ (-8.4) for the P-ACT-LB (P-ACT-LB$_{\text{BOSS}}$) datasets, for a model with seven additional free parameters. These values correspond to a preference of 1.6σ and 1.0σ over ΛCDM, respectively, and hence are not statistically significant. We present the full set of constraints on the control points in Appendix F.

In Fig. 18 we present the marginalized constraints on H_0 from the `ModRec` analysis. Including ACT data shifts H_0 closer to its ΛCDM value for both BAO datasets,

---

[21] The standard recombination history is computed using the best-fit ΛCDM parameters from the P-ACT-LB dataset. Using the best-fit parameters from other datasets considered in this work has negligible impact on the predicted $X_e(z)$.

consistent with our findings that ACT data support the standard recombination history. We find

$$H_0 = 69.6 \pm 1.0 \ (68\%, \text{P-ACT-LB}),$$
$$= 68.1 \pm 1.1 \ (68\%, \text{P-ACT-LB}_{\text{BOSS}}). \quad (29)$$

For comparison, $H_0 = 70.1 \pm 1.1 \ (68.6 \pm 1.2)$ km/s/Mpc for the Planck-LB (Planck-LB$_{\text{BOSS}}$) dataset combinations. Additionally, we find that the choice of BAO data can lead to a shift of ~ 1.5 km/s/Mpc in the posterior mean of H_0. These findings are consistent with previous studies of the ModRec model (Lynch et al. 2024a,b) and are representative of a more general trend where the H_0 value inferred from models that modify the (pre)-recombination era physics depends sensitively on the BAO data.

Finally, given that Lynch et al. (2024b) found that ModRec constraints on Ω_m including DESI BAO data prefer a lower value than recent Ω_m constraints from supernova surveys, we comment on the Ω_m constraints for the ModRec model. For P-ACT-LB (Planck-LB), we find $\Omega_m = 0.296 \pm 0.007 \ (0.295 \pm 0.007)$. Therefore, including ACT data has a negligible impact on the inferred value of Ω_m for the ModRec model.

6. PARTICLE ASTROPHYSICS

6.1. *Neutrinos*

The CMB is sensitive to a cosmological background of neutrinos produced in the early universe that contribute a significant fraction ($\sim 41\%$) of the radiation density. In the Standard Model (SM) of particle physics, these neutrinos are expected to be three flavors of massless active particles that interact weakly with other SM particles but, as explained below, they are known to have non-zero masses.

6.1.1. *Number and mass*

The exact number of neutrinos and their total mass are two key parameters of the cosmological model, and can point to beyond-Standard-Model (BSM) physics.

Neutrino number

The effective number of relativistic species quantifies the contribution to the radiation density of neutrinos, or other light particles, during their relativistic phase (including during the BBN epoch and the CMB decoupling epoch), $N_{\text{eff}} \equiv (8/7)(11/4)^{4/3} \rho_\nu / \rho_\gamma$, where ρ_ν and ρ_γ are respectively the neutrino and photon energy densities. Three neutrino species undergoing a non-instantaneous decoupling from the primordial plasma correspond to $N_{\text{eff}} = 3.044$ (Bennett et al. 2021; Froustey et al. 2020; Akita & Yamaguchi 2020; Drewes

et al. 2024), accounting for energy-dependent interactions in the early universe. Numbers greater than this value might indicate the existence of additional light particles or extra free-streaming (dark) radiation — as postulated by many BSM theories (e.g., Weinberg 1978; Essig et al. 2013; Brust et al. 2013; Abazajian et al. 2012; Weinberg 2013; Kawasaki et al. 2015; Baumann et al. 2016b). Values of N_{eff} smaller than 3.044 are also possible in scenarios where radiation is affected not by the existence of extra particles but by non-standard properties of neutrinos or changes to the standard thermal history. In low-reheating temperature scenarios, for example, the late-time entropy production associated with the decay of a massive particle might delay the beginning of the radiation-dominated era down to a temperature of a few MeV, thus preventing the full thermalization of neutrinos (see, e.g., Kawasaki et al. 1999, 2000; Giudice et al. 2001; Tegmark & Zaldarriaga 2002; Ichikawa et al. 2005, 2007; De Bernardis et al. 2008; de Salas et al. 2015; Hasegawa et al. 2019; Barbieri et al. 2025). Entropy production occurring after neutrino decoupling might also reduce N_{eff} below its standard value by increasing the photon temperature relative to neutrinos (see, e.g., Steigman 2013, and also Cadamuro & Redondo 2012, for a scenario involving the decay of an axion-like particle). A reduction of the effective number of neutrino species might also be the signature of sterile neutrinos with strong self-interactions (Mirizzi et al. 2015).

The CMB is able to constrain N_{eff} because its value affects the expansion rate of the universe, especially during the radiation-dominated phase, thereby altering the expansion history just before recombination and the predicted abundances of primordial light elements (Bashinsky & Seljak 2004; Hou et al. 2013; Abazajian et al. 2015; Pan et al. 2016; Baumann et al. 2016a). At the perturbative level, N_{eff} alters the damping tail (high-ℓ region) of the TT/TE/EE spectra, both because the change to the expansion history alters the timescale for diffusion damping and because the free-streaming nature of the radiation damps the growth of perturbations, with the latter also inducing a characteristic phase shift in the acoustic peaks (Bashinsky & Seljak 2004). Combining the *Planck* legacy CMB with *Planck* CMB lensing and BOSS BAO, the neutrino number is measured to be $N_{\text{eff}} = 2.99 \pm 0.17$ at 68% CL (Planck Collaboration 2020c), or $N_{\text{eff}} = 3.06 \pm 0.17$ at 68% CL when we evaluate this estimate using Planck-LB.

With the new ACT DR6 spectra we find $N_{\text{eff}} = 2.60^{+0.21}_{-0.29}$ at 68% CL, combining into

$$N_{\text{eff}} = 2.73 \pm 0.14 \quad (68\%, \text{P-ACT}),$$
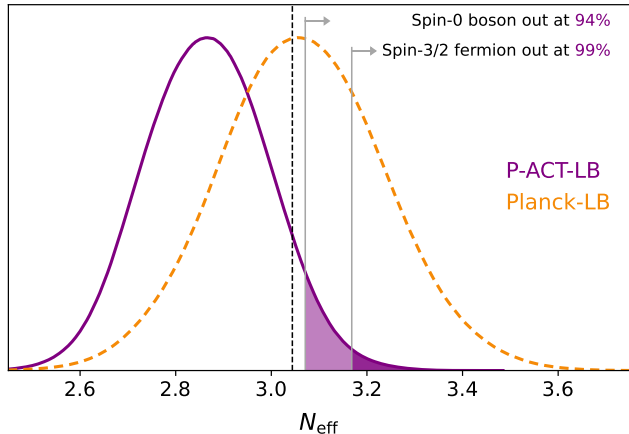$$= 2.86 \pm 0.13 \quad (68\%, \text{P-ACT-LB}), \quad (30)$$

Figure 19. Constraints on the effective number of relativistic species, N_{eff}. With the addition of the ACT DR6 spectra (purple) the constraint is more precise than the measurement from *Planck* combined with CMB lensing and BAO (orange) by $\sim 25\%$. The constraint is consistent with the SM expectation of $N_{\text{eff}} = 3.044$ for three light active neutrinos marked by the dashed vertical line. The purple bands show the region excluding a minimum contribution in extra radiation from another thermalized relativistic species, disfavoring $N_{\text{eff}} = 3.044 + 0.027$ from a spin-0 boson at 94% confidence (light purple), and the most stringent bound on the existence of another species, disfavoring $N_{\text{eff}} = 3.044 + 0.095$ from a spin-3/2 fermion at 99% confidence (dark purple) — see also Fig. 20.

and giving

$$N_{\text{eff}} < 3.08 \quad (\text{one-tail } 95\%, \text{P-ACT-LB}). \quad (31)$$

This measurement is consistent with SM predictions for three relativistic neutrinos and disfavors the existence of another thermalized particle (irrespective of its spin or decoupling time) at 94% confidence, as calculated from the likelihood of having a minimal additional contribution of 0.027 from a scalar boson (see below) beyond the expected value of 3.044, as shown in Fig. 19. Higher-spin particles are disfavored at higher significance. A strong contribution to this new limit comes from the peak of the ACT N_{eff} distribution shifting to lower values compared to the *Planck* measurement because, as shown in Fig. 3, the new ACT data prefer somewhat less damping than the *Planck* best-fit model.

While our constraints are consistent with the SM expectation — and the shift is not statistically significant enough to draw strong conclusions — it is interesting to consider physical models that could yield values of $N_{\text{eff}} < 3.044$. Recalling that N_{eff} depends on the neutrino-to-photon energy density ratio, a simple possibility to decrease N_{eff} is an injection of energy into the photon-baryon plasma after neutrino decoupling, but before last scattering (note that this would thus

lead to different values for N_{eff} at the BBN and CMB epochs). Taking the central value of our P-ACT (P-ACT-LB) posterior, the photon energy density would need to be increased by 12% (6%) between neutrino decoupling and last scattering. If this energy injection takes place between redshifts $5 \times 10^4 < z < 2 \times 10^6$, a μ distortion will be produced in the CMB monopole energy spectrum; if it takes place at lower redshifts $z < 5 \times 10^4$, a y-type distortion will be produced. Using standard formulae for the distortion amplitudes (e.g., Chluba & Sunyaev 2012), the P-ACT (P-ACT-LB) energy-injection values would yield $\mu = 0.16$ or $y = 0.03$ ($\mu = 0.09$ or $y = 0.02$). Such large spectral distortions are strongly excluded already by the *COBE/FIRAS* data (Fixsen et al. 1996; Bianchini & Fabbian 2022).[22] Nevertheless, a low N_{eff} value could still be obtained via energy injection into the photon bath at $2 \times 10^6 < z < 10^9$, by cooling the neutrinos via a BSM interaction, or by other, more exotic mechanisms as discussed above.

If we instead start by assuming the existence of the three SM neutrinos and add new, specific light relic particles with mass $\lesssim$ eV — i.e., only looking at regions of parameter space with $N_{\text{eff}} > 3.044$ — then we can set limits on the new species' nature by exploiting the fact that the excess in N_{eff} that they generate depends on the spin of the particle and on the temperature at which they decoupled from the thermal bath in the early universe, as shown in Fig. 20 (with predictions from Borsanyi et al. 2016 for different species as adopted in previous CMB literature, including Planck Collaboration 2016a, 2020c; CMB-S4 Collaboration 2016; Simons Observatory Collaboration 2019). We do this by fitting for the positive ΔN_{eff} that such new species would contribute to N_{eff}. We find $\Delta N_{\text{eff}} < 0.32$ at 95% CL from ACT, which becomes

$$\begin{aligned} \Delta N_{\text{eff}} &< 0.14 \quad (95\%, \text{P-ACT}), \\ &< 0.17 \quad (95\%, \text{P-ACT-LB}), \quad (32) \end{aligned}$$

where lensing and BAO data relax the bound by moving the overall N_{eff} posterior to higher values as previously. The same limit using Planck-LB is $\Delta N_{\text{eff}} < 0.36$ at 95% confidence. Our P-ACT-LB combination excludes at 95% CL any light particle of spin 0 or 1/2 that decoupled after the start of the QCD phase transition at temperatures $\lesssim 200$ MeV and all light particles with spin 3/2 that decoupled at temperatures $\lesssim 1$ GeV. These are the strongest constraints to date on the possible ex-

---

[22] The *COBE/FIRAS* spectral distortion bounds are sufficiently tight that only very small increases in the photon energy density are allowed during the μ and y epochs, corresponding roughly to $\Delta N_{\text{eff}} = -0.0002$ (for both the μ and y limits).
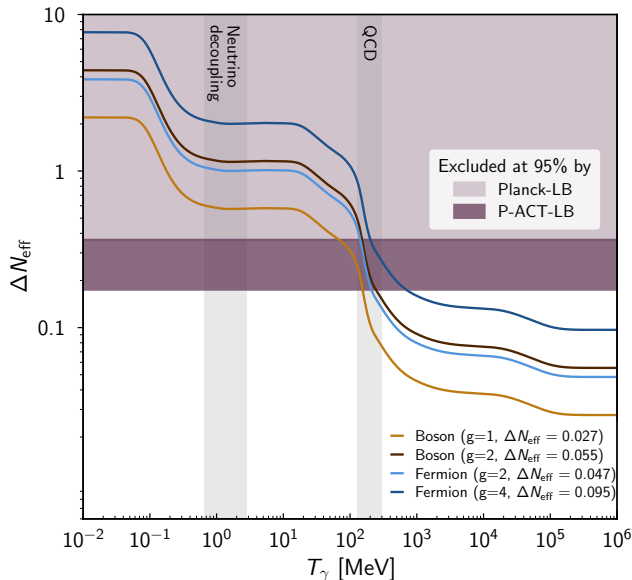
Figure 20. Excess in the contribution to radiation, $\Delta N_{\rm eff}$, caused by the existence of additional relativistic species with g independent spin states s (with $g = 2s + 1$) as a function of the temperature at which they decouple from the thermal bath. Particles decoupling after the QCD phase transition are excluded by our constraints; in particular, light particles of spin 0 and 1/2 must decouple at temperatures $\gtrsim 200$ MeV and all light particles of spin 3/2 must decouple at temperatures $\gtrsim 1$ GeV. The figure is adapted from the versions in Planck Collaboration (2020c) and Simons Observatory Collaboration (2019) but, differently from those versions, this figure is based on the fit of a positive excess rather than from the tail of the full $N_{\rm eff}$ posterior, i.e., we assume the existence of another species in addition to the three SM neutrinos (varying only $\Delta N_{\rm eff} > 0$).

istence of light, weakly coupled particles in the early universe.

As shown in Figs. 1 and 2, the region of parameter space preferred by ACT is in the low H_0 corner of the $N_{\rm eff} - H_0$ correlation — we find $H_0 = 67.00 \pm 0.91$ km/s/Mpc (68%, P-ACT-LB) when varying $N_{\rm eff}$. This is driven by ACT's preference for values of $N_{\rm eff}$ below 3.044, while values higher than the SM expectation would be necessary to increase the expansion rate. Therefore, this model extension is no longer viable to move the CMB-inferred Hubble constant toward the local SH0ES estimate. On the contrary, the P-ACT-LB constraint is well within the CCHP measurement of H_0. If we import this latter measurement as a prior on H_0, we find a small pull of the central value of $N_{\rm eff}$ to higher values and negligible tightening of the error bar.

Including also a prior on S_8 (as described in §2.5) leaves the constraint essentially unchanged. In fact, including all state-of-the-art non-CMB data has limited
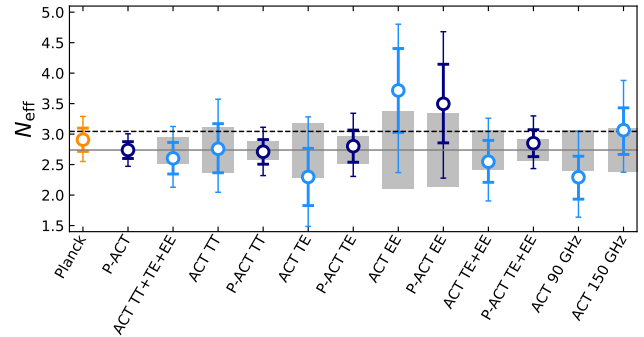
Figure 21. Robustness tests of the ACT measurement of $N_{\rm eff}$. The P-ACT value used as a reference and marked with the solid gray line is compared with the *Planck* estimate (orange), with individual TT, TE, and EE probes within P-ACT (navy points) and with different subsets of ACT data (light blue points). All measurements are reported with 1 and 2σ uncertainties (thicker and thinner colored error bars, respectively) and the SM prediction of $N_{\rm eff} = 3.044$ is shown with the dashed black horizontal line. The gray bands show the expected statistical fluctuation incurred when looking only at a subset of the data — calculated as the σ difference between the full dataset and the nested subset of data used for each point (Gratton & Challinor 2020).

impact on the precision of this measurement, which is dominated by P-ACT.

$N_{\rm eff}$ is often used as a proxy parameter to explore the sensitivity of small-scale CMB data to physics that impacts the damping tail; conclusions drawn for $N_{\rm eff}$ in fact speak more broadly about patterns in — and robustness of — results from small scales. As such, we perform a number of tests to look at the stability of the $N_{\rm eff}$ measurement. In Fig. 21, we report the variation in the constraint when comparing our baseline ACT and P-ACT datasets with only a subset of the data.[23] The results are stable across probes, frequencies, and combinations with *Planck*. The overall constraint is dominated by the ACT TT and TE spectra.

Neutrino mass

The total mass of all neutrino species is parametrized by $\sum m_\nu$. Measurements of flavor oscillations between neutrinos have provided evidence for a non-zero mass (Super-Kamiokande Collaboration 1998; SNO Collaboration 2002) and set a lower limit on the value of $\sum m_\nu$. Depending on the hierarchy (ordering) between mass eigenstates, $\sum m_\nu \gtrsim 60$ meV for the normal hierarchy and $\sum m_\nu \gtrsim 100$ meV for the inverted hierar-

---

[23] To allow fair comparisons across values, all these runs are performed with the ACT multi-frequency likelihood; the ACT TE- and EE-only runs allow the polarization efficiencies to vary freely within a 20% uniform prior.
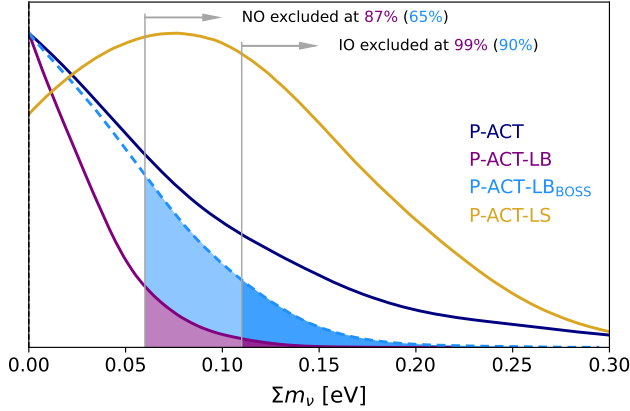
Figure 22. Upper limits on the sum of the neutrino masses, Σm_ν, within the ΛCDM model. The gray lines mark the lower bounds coming from neutrino oscillation experiments, assuming a Normal Ordering (NO, $\Sigma m_\nu > 0.06$ eV) or Inverted Ordering (IO, $\Sigma m_\nu > 0.10$ eV), respectively, and the colored bands show the exclusion regions coming from cosmology for each scenario. The most stringent bound is given by P-ACT-LB (purple), with a significant contribution coming from DESI BAO. For this data combination, and within the assumption of the ΛCDM model, the IO scenario is disfavored at 99% confidence. The limits get more relaxed but still competitive when replacing DESI BAO with BOSS/eBOSS BAO (light blue) or when using SNIa (gold).

chy (e.g., Particle Data Group 2024). The absolute value of the total mass is still unknown but, given that massive neutrinos with masses at sub-eV scales cannot be explained with the mass-generation mechanisms of the SM of particle physics, we already know that new physics is at play. Cosmology and laboratory experiments are highly complementary probes of the neutrino mass scale, being sensitive to different combinations of individual neutrino masses and mixing parameters, and relying on different assumptions in the derivation of the constraints (see, e.g., Gerbino et al. 2023).

Neutrino mass impacts the growth of structures in the universe after the neutrinos become non-relativistic (e.g., Lesgourgues & Pastor 2006; Dvorkin et al. 2019), suppressing growth at the level of a few percent. This in turn affects the amplitude of density perturbations measurable in the lensing of the CMB temperature and polarization anisotropies. Planck-LB gives $\sum m_\nu < 0.077$ eV at 95% confidence (DESI Collaboration 2025b), with a significant contribution from the CMB lensing data. With the new ACT DR6 spectra we find

$$\sum m_\nu < 0.082 \text{ eV} \quad (95\%, \text{P-ACT-LB}),$$
$$< 0.083 \text{ eV} \quad (95\%, \text{W-ACT-LB}). \quad (33)$$
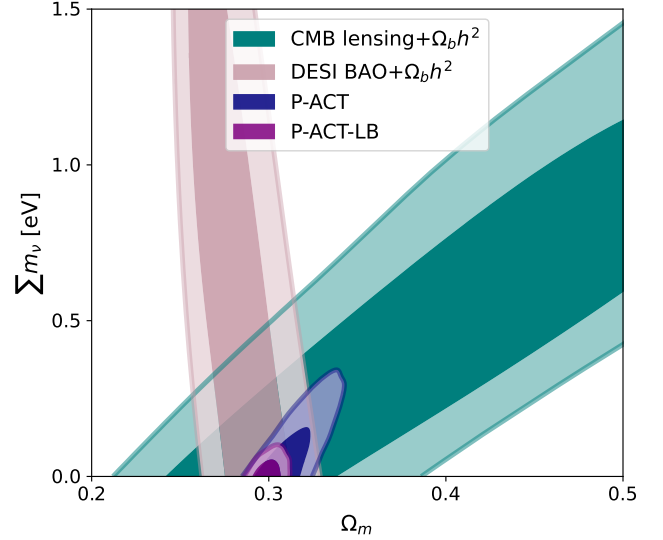
Figure 23. 2D marginalized posteriors at 68% and 95% CL highlighting different degeneracy directions between the neutrino mass and the matter density for different cosmological probes. The BAO data (pink) are mostly insensitive to how matter is distributed across different components and only bound the total matter density. CMB lensing (teal) breaks this degeneracy, separating out the neutrinos from other matter components, once the baryon density is anchored by BBN constraints. Together with CMB anisotropies (purple), the combination of these data sets a stringent limit on the sum of the neutrino masses.

The addition of ACT DR6 to *Planck* leaves the bounds almost unchanged. However, the neutrino mass constraints from *Planck* correlate with the high fluctuation of the lensing-like smearing effect in the *Planck* CMB spectra (measured by the A_{lens} parameter, Calabrese et al. 2008) so the ACT dataset serves here as a useful cross-check of the result. The impact of extra lensing is mitigated in the P-ACT combination by the cut in ℓ that we introduce in *Planck* temperature and is completely avoided in the W-ACT combination — since, as shown in L25, ACT DR6 measures A_{lens} consistent with ΛCDM predictions. Once CMB lensing and BAO data are included, the CMB power spectra contribution to the bound is sub-dominant and the same across experiments. The conclusion that extra lensing-like smearing in the power spectra is not the primary contributor to the very tight bounds on $\sum m_\nu$ was also reached by Green & Meyers (2024), who delve into all the different pieces of data contributing to a neutrino mass constraint (see also Escudero & Abazajian 2025).

As shown in Figs. 22 and 23, neutrino mass measurements from cosmology need different datasets to come together to disentangle the effect of neutrinos on the geometry of the universe and growth of structure from the late-time expansion effects (for a recent review see,

e.g., Loverde & Weiner 2024). In particular, DESI's constraint on the total matter density, through measuring the BAO and inferring cosmic distances, plays a large role in these neutrino mass limits, as shown in Fig. 23. The CMB lensing measurement then breaks the degeneracy between the total density in matter and in neutrinos, due to the unique effect of the neutrino on suppressing the clustering at smaller scales. The addition of ACT DR6 spectra confirms the tight limit that DESI Collaboration (2025b) found with *Planck*. The combination of P-ACT-LB disfavors at $\sim 99\%$ confidence the inverted ordering scenario. This conclusion holds also for an independent-of-*Planck* combination, with W-ACT-LB giving very similar results.

Given the strong impact on these constraints from BAO, we explore other dataset combinations that can help the CMB for neutrino mass constraints. We replace DESI with BOSS BAO and obtain a bound of

$$\sum m_\nu < 0.13 \text{ eV } (95\%, \text{P-ACT-LB}_{\text{BOSS}}), \quad (34)$$

which is unchanged when replacing *Planck* with *WMAP*. We also exclude BAO completely and instead exploit the information on the matter density coming from SNIa measurements, finding

$$\sum m_\nu < 0.24 \text{ eV } (95\%, \text{P-ACT-LS}). \quad (35)$$

In both cases, the limits become weaker and raise the likelihood of the inverted ordering (see Fig. 22). The broadening of the bound in P-ACT-LS is due to the preference of a larger value of the matter density exhibited by the supernovae measurements, as described in Loverde & Weiner (2024).

In Fig. 24, we compare our P-ACT-LB bounds with constraints on the effective Majorana mass $m_{\beta\beta}$ from the neutrinoless double-beta decay ($0\nu2\beta$) experiment KamLAND-Zen (KamLAND-Zen Collaboration 2024) (comparable constraints — not shown here — have also been obtained by the GERDA collaboration, GERDA Collaboration 2020). The viable parameter space, represented by the two colored bands for the two neutrino mass orderings, is cut by the combination of cosmology and $0\nu2\beta$ results within ΛCDM. Assuming that the neutrino mass mechanism leads to the $0\nu2\beta$ process (which thus assumes neutrinos are Majorana particles), KamLAND-Zen is able to exclude almost entirely the inverted ordering region. Cosmology further excludes the still-allowed IO region and a large fraction of the normal ordering. This sets a challenging target for next-generation $0\nu2\beta$ searches to probe the region of $m_{\beta\beta} < 18 \text{ meV}$ (the lowest value for the Majorana effective mass in the inverted ordering when considering measurements from neutrino oscillation experiments, i.e.,
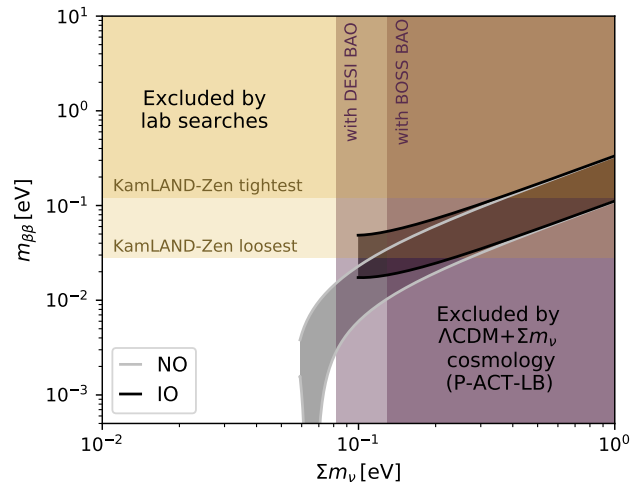
Figure 24. Neutrino oscillation experiments require that the neutrino mass scale parameters live in one of the two bands for normal ordering (NO, grey) or inverted ordering (IO, black), with the width of the bands reflecting the lack of knowledge of the Majorana phases (Particle Data Group 2020). Cosmology helps distinguish between the two scenarios, disfavoring at 95% CL the vertical band in purple, within the ΛCDM model. The dark purple region is disfavored when including BOSS BAO data, while when using DESI BAO data more parameter space is excluded, as shown by the light purple band. Neutrinoless double-beta decay results at 90% CL from KamLAND-Zen (KamLAND-Zen Collaboration 2024) exclude the horizontal gold bands (these account for the uncertainty in the calculation of the nuclear matrix elements when translating the bounds on the xenon half life from KamLAND-Zen to a bound on the effective Majorana mass $m_{\beta\beta}$). The still viable parameter space is within the colored bands for the two neutrino mass orderings. The new cosmology results presented here reduce the allowed parameter space compared to $0\nu2\beta$ by excluding within the ΛCDM$+\sum m_\nu$ model the inverted ordering region and a large fraction of the normal ordering region. This result however strongly depends on the use of DESI BAO data; with BOSS BAO the limits are more relaxed.

the lowest value at the bottom of the black IO band in Fig. 24). However, as discussed in, e.g., DESI Collaboration (2025b); Shao et al. (2024), these limits are model-dependent: for example, extended models with time-varying dark energy will relax the bounds on neutrino mass and bring the IO back into the allowed region. Cosmological bounds also assume that neutrinos are long-lived particles with a Fermi-Dirac distribution function. Models that deviate from these assumptions, such as scenarios featuring decaying neutrinos or neutrinos with average momenta larger than that of a thermal distribution (e.g., Dvali & Funcke 2016; Lorenz et al. 2019; Oldengott et al. 2019; Chacko et al. 2020, 2021; Barenboim et al. 2021; Alvey et al. 2022a,b; Chen et al.

2022a; Abellán et al. 2022), would likely still be compatible with masses in the IO band.

The constraints on both $N_{\rm eff}$ and $\sum m_\nu$ remain stable when varying both parameters at the same time, with

$$\left.\begin{array}{c} N_{\rm eff} = 2.85 \pm 0.25 \\[1ex] \sum m_\nu < 0.073 \text{ eV} \end{array}\right\} \quad (95\%, \text{ P-ACT-LB}) \quad (36)$$

and little correlation in the joint parameter region.

While the constraint on $N_{\rm eff}$ agrees with SM predictions, the most probable value for $\sum m_\nu$ from cosmology is currently zero, in contrast with oscillation measurements. If this difference were to become significant with more precise data, it would imply a tension between our constraints on neutrino properties in the early universe versus neutrino measurements in the laboratory. Fortunately, with the increasing sensitivity of future CMB and BAO measurements, we can hope to determine the sum of neutrino masses to 0.02–0.03 eV precision (e.g., CMB-S4 Collaboration 2016; Simons Observatory Collaboration 2019; Eisenstein & DESI Collaboration 2015; Abitbol et al. 2025).

6.1.2. *Neutrino self-interactions*

Neutrino self-interactions can arise in a class of BSM models, for example in models where Majorana neutrinos interact through a (pseudo)scalar, the Majoron ϕ, related to the breaking of lepton number and to the generation of small neutrino masses (Chikashige et al. 1980, 1981; Schechter & Valle 1982). In a wide class of models, the neutrino-Majoron coupling constant g, controlling the strength of neutrino self-interactions, is proportional to m_ν/v_L, where m_ν is the neutrino mass and v_L is the scale of the new physics that breaks lepton number. In general, a signature of neutrino self-interactions in cosmological observations might point to BSM physics. Here, we study the CMB phenomenology related to neutrino self-interactions arising from neutrino–neutrino scattering processes, which is mostly independent of the spin and parity properties of the mediator. The symbol ϕ in the following will denote a generic mediator, including the Majoron, unless otherwise stated. We consider interactions among the three active neutrinos that do not couple different mass eigenstates, and with eigenstate-independent strength (in other words, the matrix of couplings is proportional to the identity matrix in the mass basis).

Self-interactions affect the evolution of perturbations by making neutrinos behave, at certain times, as a collisional fluid and not as free-streaming particles. Acoustic oscillations will then propagate in the neutrino fluid and enhance, through gravity, the amplitude of photon fluctuations. Collisions will also cancel the characteristic phase shift imprinted on photon and matter perturbations by neutrino free streaming. These effects are relevant during the radiation-dominated era, when neutrinos provide a non-negligible contribution to the total energy density, and are imprinted at the time when perturbation modes re-enter the horizon. The range of scales affected thus also depends on the energy dependence of the scattering rate, which simplifies in the two limiting scenarios considered in the following: a very light ("massless") or very heavy mediator.

Heavy mediator

We consider first the case where the mass m_ϕ of the mediator is much larger than the neutrino temperature at all times directly probed by CMB anisotropies (Cyr-Racine & Sigurdson 2014). In this case, the neutrino interaction is effectively a four-fermion vertex controlled by a dimensional coupling constant $G_{\rm eff} = g^2/m_\phi^2$, i.e., the effective low-energy Lagrangian is $\mathcal{L}_{\rm eff} = G_{\rm eff}\bar\nu\nu\bar\nu\nu$. This is analogous to the low-energy behavior of standard weak interactions, just with $G_{\rm eff}$ taking the place of the Fermi constant $G_{\rm F} \simeq 1.17 \times 10^{-5} \text{ GeV}^{-2}$. This low-energy limit does not depend on the nature of the mediator, so the analysis here naturally encompasses both the scalar and vector cases. The Boltzmann hierarchy for neutrino perturbations including the collision term $\mathcal{L}_{\rm eff}$ generated by the interaction has been derived by Kreisch et al. (2020).

In this scenario, neutrino free-streaming does not start at the time of weak decoupling, but is instead delayed until $T_{\rm fs} = T_{\nu,\rm dec}(G_F/G_{\rm eff})^{2/3}$, where $T_{\nu,\rm dec} \simeq 1\,\rm MeV$ is the neutrino decoupling temperature. Neutrino self-interactions through a heavy mediator leave an imprint at angular scales $\theta \lesssim \theta_{\rm fs}$ (assuming $\theta_{\rm fs} < \theta_{\rm eq}$), where $\theta_{\rm fs}$ is the scale entering the horizon at $T = T_{\rm fs}$.

Previous analyses have shown that CMB and BAO data are compatible with, and in some cases prefer, neutrino self-interactions with $G_{\rm eff} \gg G_F$ (Cyr-Racine & Sigurdson 2014; Archidiacono & Hannestad 2014; Lancaster et al. 2017; Oldengott et al. 2017; Park et al. 2019; Kreisch et al. 2020; Barenboim et al. 2019; Brinckmann et al. 2021; Das & Ghosh 2021; Mazumdar et al. 2022; Roy Choudhury et al. 2021; Poudou et al. 2025). In fact, the posterior for $G_{\rm eff}$ has been found to be bimodal, with probability being concentrated in two distinct regions: a moderately interacting (MIν) mode, compatible with no self-interactions, and a strongly interacting (SIν) mode. The analysis of ACT DR4 data showed a slight preference for neutrino self-interactions at the $2-3\sigma$ level, finding $G_{\rm eff} \lesssim 10^{-3}\,\rm MeV^{-2}$ for MIν, and $G_{\rm eff} \simeq 10^{-1.5}\,\rm MeV^{-2}$ for SIν (Kreisch et al. 2024).

	ACT	P-ACT	P-ACT-LB
$\Delta\chi^2_{\mathrm{MI}\nu}$	-0.2	2.9	3.1
$\Delta\chi^2_{\mathrm{SI}\nu}$	-3.2	-10.6	-7.3
$\sigma_{\mathrm{MI}\nu}$	$-$	1.7	1.8
$\sigma_{\mathrm{SI}\nu}$	$-$	$-$	$-$

Table 3. $\Delta\chi^2 \equiv \chi^2_{\Lambda\mathrm{CDM}} - \chi^2_{\Lambda\mathrm{CDM}+G_{\mathrm{eff}}}$ from the MAP points of the MIν and SIν regions for different data combinations. When self-interacting neutrino models yield an improvement of the fit over ΛCDM we also report the preference for the model in units of σ. We find no statistically significant preference for neutrino self-interactions.

We start by considering a one-parameter extension of ΛCDM, including G_{eff} as an extra parameter and keeping fixed $\sum m_\nu = 0.06\,\mathrm{eV}$ and $N_{\mathrm{eff}} = 3.044$. To check if the bimodal behavior persists with the ACT DR6 spectra, we split the parameter space in two regions, $G_{\mathrm{eff}} < 10^{-2}\,\mathrm{MeV}^{-2}$ (MIν) and $G_{\mathrm{eff}} > 10^{-2}\,\mathrm{MeV}^{-2}$ (SIν), and perform separate MCMC runs with flat priors on $\log_{10}\left(G_{\mathrm{eff}}\,\mathrm{MeV}^2\right)$: $-8 \leq \log_{10}\left(G_{\mathrm{eff}}\,\mathrm{MeV}^2\right) \leq -2$ (MIν) and $-2 \leq \log_{10}\left(G_{\mathrm{eff}}\,\mathrm{MeV}^2\right) \leq 0$ (SIν). The logarithmic prior allows us to explore a wide range of values of G_{eff}, spanning several orders of magnitude.

In the MIν region, the P-ACT and P-ACT-LB combinations are compatible with $G_{\mathrm{eff}} = 0$, but show a mild preference for $\log_{10}\left(G_{\mathrm{eff}}\,\mathrm{MeV}^2\right) \simeq -3$. In contrast, in the SI$\nu$ region, the posteriors for the same dataset combinations peak at the lower edge of the prior range, i.e., at $\log_{10}\left(G_{\mathrm{eff}}\,\mathrm{MeV}^2\right) = -2.0$. We show the two posteriors in Fig. 25. Since we are performing separate parameter estimation runs for MIν and SIν, we cannot use the distributions to assess the relative probability of the two scenarios. Instead we compare the effective χ^2 of MAP models in the two regions to that of the ΛCDM model, as reported in Table 3. We find that the SIν model is never preferred over ΛCDM. The MIν model yields basically no improvement to the goodness-of-fit for the ACT DR6 data alone with respect to ΛCDM, while it gives marginal improvement for P-ACT and P-ACT-LB. Specifically, we find $\Delta\chi^2_{\mathrm{MI}\nu} = 2.9$ (P-ACT) and $\Delta\chi^2_{\mathrm{MI}\nu} = 3.1$ (P-ACT-LB), corresponding respectively to a mild 1.7σ and 1.8σ preference over ΛCDM, as computed using the likelihood-ratio test.

Since $G_{\mathrm{eff}} = 0$ is compatible with the data, the posterior for the MIν scenario ideally extends with non-zero probability down to $\log_{10}\left(G_{\mathrm{eff}}\mathrm{MeV}^2\right) \to -\infty$. The posterior is therefore ill-defined with a diverging integrated probability. This prevents the computation of meaningful Bayesian credible intervals. Previous analyses chose to arbitrarily cut the distribution at some lower bound and reported credible intervals depending on this choice.
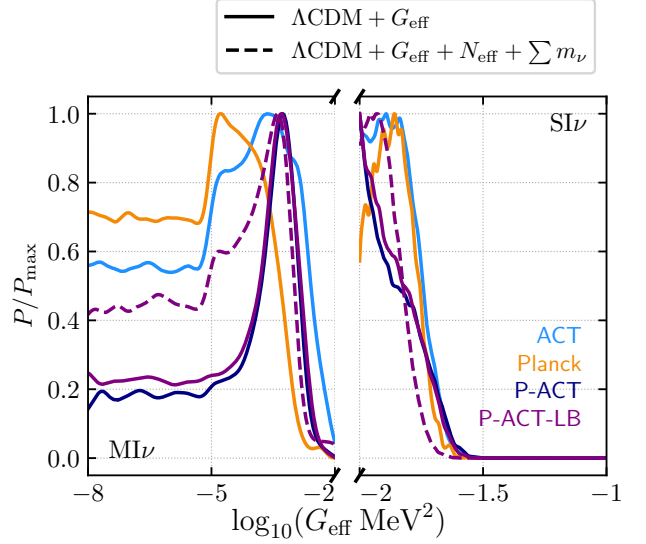
Figure 25. Posterior distribution of the neutrino self-interaction effective coupling constant, G_{eff}, for various datasets within the ΛCDM $+ G_{\mathrm{eff}}$ model (solid lines) and the more extended case of ΛCDM $+ G_{\mathrm{eff}} + N_{\mathrm{eff}} + \sum m_\nu$ (dashed line). The posterior is presented in two distinct regions of parameter space, corresponding to the MIν and SIν modes, each independently normalized due to separate sampling. Analysis of the MAP models in the two regions shows that neutrino self-interactions are not preferred over ΛCDM (corresponding to $G_{\mathrm{eff}} = 0$), for any dataset combination. In the ΛCDM $+ G_{\mathrm{eff}}$ model, for P-ACT-LB we find the MIν at 1.8σ and no peak for SIν; a similar behavior is also found for the more extended model. Minimal smoothing is applied to the plot to preserve the features of the distribution.

Here, we take a different approach; once the information about the position of the peaks has been acquired from the runs with a logarithmic prior, the proposal density of the MCMC can be correspondingly tuned and we repeat the runs using a uniform prior on G^2_{eff}, namely $0 \leq G^2_{\mathrm{eff}} \leq (10^{-2}\,\mathrm{MeV}^{-2})^2$, ensuring a proper posterior. We choose a uniform prior on G^2_{eff} rather than on G_{eff} because the former amounts to a uniform prior on the scattering rate $\Gamma \propto G^2_{\mathrm{eff}}$. Adopting this strategy, we find

$$G_{\mathrm{eff}}\ (\mathrm{MI}\nu) < 7.9 \times 10^{-3}\,\mathrm{MeV}^{-2}\ (95\%, \mathsf{P\text{-}ACT\text{-}LB}). \tag{37}$$

We repeat the analysis for a model in which only one of the three neutrino families is self-interacting. In this case, we find that both P-ACT and P-ACT-LB yield a posterior with a well-defined peak in the SI region; in particular, $\log_{10}\left(G_{\mathrm{eff}}\,\mathrm{MeV}^2\right) = -1.33^{+0.21}_{-0.14}$ (68% P-ACT-LB). The posterior in the MI region is instead qualitatively similar to the one found in the scenario with three interacting neutrinos. Both these single interacting-neutrino models are however not significantly preferred over ΛCDM, with $\Delta\chi^2_{\mathrm{MI}\nu} = -1.2$ and

$\Delta\chi^2_{\mathrm{SI}\nu} = -5.5$ (P-ACT-LB), corresponding respectively to a 1.1σ (MIν) and 2.3σ (SIν) preference over ΛCDM.

We further consider a 9-parameter extended model with three interacting neutrinos in which, in addition to the base ΛCDM parameters and G_{eff}, also N_{eff} and $\sum m_\nu$ are allowed to vary. As in Kreisch et al. (2024), N_{eff} is used to rescale the neutrino temperature. We find results similar to those for the ΛCDM+G_{eff} model with three interacting neutrinos (see Fig. 25). In particular, we do not find a peak in the posterior in the SI region, in contrast to the mild preference for such a model seen in the analysis of the ACT DR4 data (Kreisch et al. 2024). The mild hint of SIν in the DR4 analysis was largely driven by a high fluctuation in the EE power spectrum at intermediate scales, $700 < \ell < 1000$, which is no longer present in the DR6 spectra (see Appendix B).

To summarize, we find that limits on interacting neutrino models are sensitive to the underlying assumptions used to describe the broader physics in the neutrino sector. However, neutrino self-interactions are not detected in any scenario that we consider and not preferred over ΛCDM.

This lack of evidence also limits the ability of this model to increase the value of the Hubble constant. For example, a heavy mediator in the MIν scenario gives $H_0 = 68.2 \pm 0.4$ km/s/Mpc (ΛCDM+G_{eff}) and $H_0 = 67.5 \pm 1.0$ km/s/Mpc (ΛCDM+G_{eff}+N_{eff}+$\sum m_\nu$) using P-ACT-LB. In general, we find no significant shift compared to ΛCDM for the ΛCDM+G_{eff} model. In the extended case of ΛCDM+G_{eff} + N_{eff} + $\sum m_\nu$, the H_0 distribution shifts lower by ~ 1 km/s/Mpc and has a twice larger uncertainty. This is driven by the $N_{\mathrm{eff}} - H_0$ correlation and by ACT's preference for $N_{\mathrm{eff}} < 3.044$ found in ΛCDM+N_{eff} (see §6.1.1), which persists in this model. In the SIν scenario, we find instead $H_0 = 69.0 \pm 0.4$ km/s/Mpc (ΛCDM+G_{eff}) and $H_0 = 67.0 \pm 0.9$ km/s/Mpc (ΛCDM+G_{eff}+N_{eff}+$\sum m_\nu$) for P-ACT-LB. The ~ 1 km/s/Mpc upward shift in H_0 in the ΛCDM+G_{eff} model is induced by the positive correlation between G_{eff} and θ_s. In the ΛCDM+G_{eff} + N_{eff} + $\sum m_\nu$ model, this effect is countered by a lower value of N_{eff}, resulting in a lower value of H_0 with respect to the corresponding MIν scenario.

Laboratory searches, especially double-β decay experiments and observations of meson and lepton decays, severely constrain the coupling of neutrinos with a new light boson (Blinov et al. 2019). Taken at face value, the values of G_{eff} in the SIν region, as well as those corresponding to the MIν peak, are excluded by these searches as shown in Fig. 26, unless the new scalar couples almost exclusively to τ neutrinos.
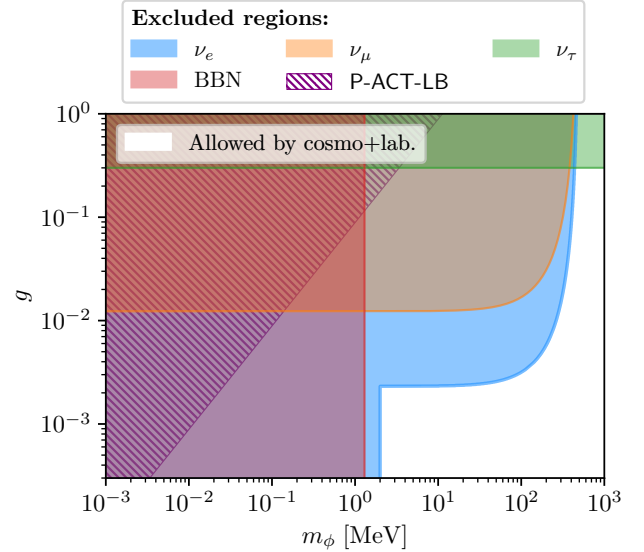
Figure 26. Cosmological and laboratory limits on neutrino couplings with a new scalar ϕ. The purple band with hatches in the upper left corner corresponds to the region excluded by P-ACT-LB accounting for both MI and SI neutrinos. The other overlaid color bands are excluded by particle physics and BBN limits. The shaded blue region refers to scalars coupling to electron neutrinos and is excluded by neutrinoless double β decay searches (Blum et al. 2018; Kharusi et al. 2021; NEMO-3 Collaboration 2014; GERDA Collaboration 2020) and measurements of the ratio $\mathrm{Br}(K^+ \to e^+\nu_e)/\mathrm{Br}(K^+ \to \mu^+\nu_\mu)$ (Lessa & Peres 2007; NA48/2 Collaboration 2007). The orange shaded region is excluded by laboratory constraints on the decay $K^+ \to \mu^+\nu_\mu\phi$ (Particle Data Group 2024) that apply to scalars coupling to μ neutrinos. The green shaded region is excluded by laboratory constraints on the decay $\tau^- \to \ell_\alpha^+ \bar\nu_\alpha \nu_\tau \phi$ (Lessa & Peres 2007), applying to scalars coupling to τ neutrinos. The red-shaded region is excluded by BBN constraints on N_{eff} (Blinov et al. 2019). Together, cosmology and laboratory measurements allow the parameter space remaining in the right bottom corner (in white).

Light mediator

In this scenario the mediator mass is much smaller than the average neutrino momentum at all times of interest and the scattering rate $\Gamma \propto g^4 T$, so that the ratio between the scattering and Hubble rates increases with time. Neutrinos will then start free streaming at weak decoupling as usual, and become collisional again at later times (Archidiacono & Hannestad 2014; Forastieri et al. 2015, 2019). The effects of collisions are confined to scales between θ_{coll}, the scale entering the horizon when neutrinos stop free streaming at late times, and θ_{eq}. These correspond to intermediate angular scales in the CMB power spectra (larger scales compared to those affected by a heavy mediator) and so we expect less contribution to this limit from ACT DR6.

We write the thermally averaged cross section $\langle\sigma v\rangle = \xi g^4/T^2 \equiv g_{\rm eff}^4/T^2$, where the coefficient ξ depends on the details of the interaction, including the nature of the mediator. We consider a one-parameter extension of ΛCDM, varying $g_{\rm eff}^4$ with a flat prior. As in the heavy mediator case, this is equivalent to a flat prior on the neutrino interaction rate $\Gamma \propto g^4$. We follow the approach of Forastieri et al. (2015, 2019) where the collision term is approximated using the thermally-averaged scattering rate in the relaxation time approximation. From *Planck* CMB data, we find $g_{\rm eff}^4 < 1.5 \times 10^{-27}$ at 95% CL. The new ACT DR6 spectra alone give a limit about three times weaker, with $g_{\rm eff}^4 < 5.2 \times 10^{-27}$ at 95% CL. Combining the two datasets gives a $\sim 20\%$ improvement on *Planck* alone, with

$$g_{\rm eff}^4 < 1.2 \times 10^{-27} \quad (95\%, \text{P-ACT}),$$
$$< 1.3 \times 10^{-27} \quad (95\%, \text{P-ACT-LB}), \qquad (38)$$

or $|g_{\rm eff}| < 1.1 \times 10^{-7}$.

Neutrino couplings with a light scalar can be constrained from $0\nu2\beta$ experiments and from supernovae explosions. These constraints are expressed in terms of the couplings $g_{\alpha\beta}$ in the basis of the eigenstates of the weak interaction, with $\alpha, \beta = e, \mu, \tau$, as opposed to the mass basis used in our analysis. The two bases are related through the neutrino mixing matrix. Currently, EXO-200 provides the most stringent laboratory limits on the electron neutrino-Majoron coupling: $|g_{ee}| < (0.4 - 0.9) \times 10^{-5}$ (Kharusi et al. 2021), where the range expresses the uncertainty due to nuclear matrix elements. Supernova data can also be used to constrain neutrino-Majoron couplings. In particular, scalar emission might overly shorten the observed neutrino signal from SN1987A. This luminosity argument excludes the range of couplings $3 \times 10^{-7} < |g_{\alpha\beta}| < 2 \times 10^{-5}$ (Kachelriess et al. 2000). In most of the neutrino parameter space allowed by oscillation experiments, $\max(|g_{\alpha\beta}|) \sim g_{\rm eff}$ and P-ACT yields the strongest constraints on neutrino interactions with a light (pseudo)scalar. In Fig. 27, we show the posterior distribution for $g_{\rm eff}^4$ for various data combinations, and compare with the limit from the luminosity argument. In the same figure we also show the mild correlation between $g_{\rm eff}$ and the scalar spectral index n_s, which we interpret as the result of the additional power at intermediate scales (i.e., on the left of the pivot scale k_*) for $g_{\rm eff} > 0$.

6.2. *Helium and deuterium abundances*

Light elements formed in the early universe during BBN, with abundances depending on the baryon-to-photon density ratio, $\eta_{\rm b} \equiv n_{\rm b}/n_\gamma$, and the number of
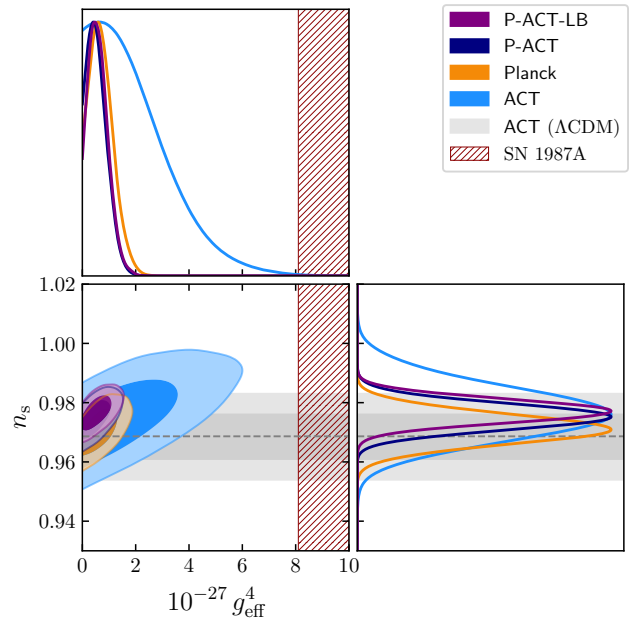
Figure 27. Constraints on the effective neutrino self-coupling, $g_{\rm eff}^4$, in the light mediator limit from multiple data combinations. The hatched area is excluded by a luminosity argument applied to SN1987A (Kachelriess et al. 2000). The shaded gray region shows the 68% and 95% credible intervals for n_s in the ΛCDM model (L25). The degeneracy with n_s stems from the fact that large $g_{\rm eff}$ increases power at scales typically larger than the pivot scale $k_* = 0.05\,{\rm Mpc}^{-1}$, while increasing the slope of the primordial spectrum reduces the power at those scales. The inclusion of ACT shifts the contours to larger values of n_s, consistent with what is reported in §4.1, and mildly tightens the bounds on $g_{\rm eff}$ compared to *Planck* alone.

relativistic degrees of freedom, $N_{\rm eff}$. Throughout this section we assume no leptonic asymmetry in the electron neutrino sector, i.e., a vanishing chemical potential of electron neutrinos. Given the photon temperature today (Fixsen 2009), $\eta_{\rm b}$ can be related to the physical baryon density $\omega_b \equiv \Omega_b h^2$.

To compute primordial abundances of light elements as a function of $\Omega_b h^2$ and $N_{\rm eff}$ we can use various computational codes, each built upon different underlying assumptions. In this paper we make use of the `PRIMAT` (Pitrou et al. 2018) and `PRyMordial` (Burns et al. 2024) codes in three configurations:

(a) `PRIMAT_2021`: this is the default BBN computation used in `camb` version 1.5, but it was not present in the public version of `class` at the time our analyses were performed.[24] We use `PRIMAT`

---

[24] We manually import `PRIMAT`-based tables from `camb` to use in `class`, as described in §3. As of writing, `PRIMAT` has recently been included in the public version of `class`.

as the baseline BBN code in all analyses presented in this paper. It implements tabulated reaction rates based on theoretical ab-initio calculations (see Pitrou et al. 2018 and references therein for details) and assumes a neutron lifetime value $\tau_N = (879.4 \pm 0.6)$ s, i.e., the average provided in `PDG 2020` (Particle Data Group 2020);

(b) `PRIMAT_2024`: uses the same rates as `PRIMAT_2021`, with an updated value of $\tau_N = (878.4 \pm 0.5)$ s from `PDG 2024` (Particle Data Group 2024);

(c) `PRyMordial`: uses a modified version of the `NACRE II` database (Xu et al. 2013) for the thermonuclear rates (see Burns et al. 2024 and references therein for details) and the same value of the neutron lifetime used by `PRIMAT_2024`, i.e., $\tau_N = (878.4 \pm 0.5)$ s.

These different BBN calculations return the same cosmological parameters and only affect the prediction of BBN abundances, so a distinction and detailed discussion is only required in this section. We focus on BBN predictions for the primordial helium abundance, expressed as the nucleon number density fraction, $Y_p \equiv n_{He}/n_b$ — rather than the mass fraction parameter Y_{He} normally used in CMB calculations — and the primordial deuterium abundance, $D/H \equiv D/H|_p \times 10^5$. Astrophysical determinations of the helium abundance are primarily derived from observations of low-metallicity extragalactic HII regions, whereas deuterium abundances are measured from high-redshift quasar absorption systems. The latest determinations are summarized in `PDG 2024` which also provides average estimates for both elements[25], namely $Y_p = 0.245 \pm 0.003$ (Aver et al. 2021, 2022; Valerdi et al. 2019, 2021; Fernández et al. 2019; Kurichin et al. 2021; Hsyu et al. 2020) and $D/H = 2.547 \pm 0.029$ (Cooke et al. 2014, 2016; Riemer-Sørensen et al. 2015; Balashev et al. 2016; Riemer-Sørensen et al. 2017). We do not discuss here abundances of other light elements, such as tritium, ^{3}He, and ^{7}Li; these elements are more uncertain in both their determination and their interpretation (Fields 2011; Iliadis & Coc 2020; Particle Data Group 2024).

6.2.1. *Abundances assuming standard BBN*

Fixing the radiation density to its standard value ($N_{eff} = 3.044$), the baryon density in the baseline

---

ΛCDM model can be directly related to the helium fraction. L25 shows that with the new ACT data the baryon density is measured to 0.5% uncertainty; for the three configurations listed above, this leads to[26]

$$
\left.
\begin{aligned}
&\text{(a) } Y_p = 0.24727 \\
&\qquad \pm 0.000046 \ (0.000131) \\
&\text{(b) } Y_p = 0.24707 \\
&\qquad \pm 0.000046 \ (0.000118) \\
&\text{(c) } Y_p = 0.24691 \\
&\qquad \pm 0.000049 \ (0.000153)
\end{aligned}
\right\} \quad (68\%, \text{ P-ACT-LB}),
$$

(39)

where the first set of errors reflect only the uncertainty on $\Omega_b h^2$ and the second in parentheses includes the theoretical BBN uncertainty added in quadrature. The shift between (a) and (b) is mainly driven by the different value adopted for the neutron lifetime, while the shift between (b) and (c) reflects the different treatment of the reaction rates and nuclear cross-sections between `PRIMAT` and `PRyMordial`; see Schöneberg (2024) for an exhaustive comparison. However, all these shifts are within the theoretical errors provided by the different codes, and encompassed by the `PDG` average of the observational bounds, which shows an order of magnitude larger error bar; see the upper panel of Fig. 28.

We find that relaxing the assumptions on the radiation density by varying N_{eff} weakens the constraints on the helium fraction, substantially absorbing all the discrepancies between different BBN codes:

$$
\left.
\begin{aligned}
&\text{(a) } Y_p = 0.2448 \pm 0.0019 \\
&\text{(b) } Y_p = 0.2446 \pm 0.0018 \\
&\text{(c) } Y_p = 0.2445 \pm 0.0018
\end{aligned}
\right\} \quad (68\%, \text{ P-ACT-LB}).
$$

(40)

Here the error is dominated by the uncertainty on $\Omega_b h^2$ and N_{eff}, and the shift with respect to the $N_{eff} = 3.044$ case is driven by the shift of $\Omega_b h^2$ between ΛCDM and ΛCDM+N_{eff} models.

Following the same approach, we can predict the deuterium abundance under the assumption of standard BBN. In the baseline ΛCDM model the baryon density translates into

$$
\left.
\begin{aligned}
&\text{(a) } D/H = 2.415 \pm 0.019 \ (0.036) \\
&\text{(b) } D/H = 2.413 \pm 0.019 \ (0.033) \\
&\text{(c) } D/H = 2.480 \pm 0.020 \ (0.104)
\end{aligned}
\right\} \quad (68\%, \text{ P-ACT-LB}).
$$

(41)

For deuterium, the neutron lifetime value has a negligible impact (Grohs & Fuller 2022) and the shift is

---

[25] Section 24.3 of Particle Data Group (2024) details the averaging procedure. The `PDG 2024` average helium abundance does not incorporate the recent measurements from the EMPRESS survey performed on the Subaru telescope (Matsumoto et al. 2022), which indicate a helium abundance, $Y_p = 0.2370 \pm 0.0034$, $\approx 2.4\sigma$ lower than the `PDG` value.

[26] Note that Y_p is only logarithmically sensitive to the baryon density, which leads to the small error bars here.
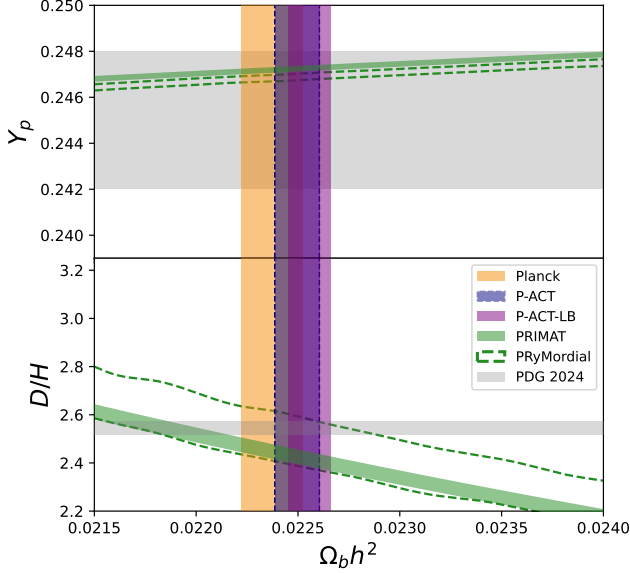
Figure 28. Comparison of the constraints at 68% confidence on the baryon density $\Omega_b h^2$ from *Planck* (orange), P-ACT (navy), and P-ACT-LB (purple), versus the measured primordial helium fraction Y_p (top panel) and deuterium fraction D/H (bottom panel). The green bands show the 1σ predicted relations between the parameters according to `PRIMAT` 2021 (filled) and `PRyMordial` (empty dashed). The gray bands are the average 68% confidence levels of the astrophysical measurements of these fractions, according to `PDG 2024` (Particle Data Group 2024).

substantially caused by differences between `PRIMAT` and `PRyMordial` calculations, and mainly driven by the different choices made for the reaction rates. Theoretical errors also reflect the different choices made in the marginalization procedure by `PRIMAT` and `PRyMordial` — see again Schöneberg (2024) for an exhaustive comparison. When compared to direct measurements of the deuterium abundance, estimations based on `PRIMAT` exhibit a mild tension, ranging between 2 and 3σ. In contrast, the inferred values obtained using the `PRyMordial` computation are consistent with the `PDG` average, regardless of whether theoretical uncertainties are included; see the lower panel of Fig. 28.

In the ΛCDM+$N_{\rm eff}$ model, the scenario remains unchanged, with all constraints being shifted downward due to the higher baryon abundance found in this model

$$
\left.
\begin{aligned}
&\text{(a) D/H} = 2.384 \pm 0.029\ (0.042) \\
&\text{(b) D/H} = 2.383 \pm 0.029\ (0.040) \\
&\text{(c) D/H} = 2.455 \pm 0.028\ (0.099)
\end{aligned}
\right\}
\ (68\%,\ \text{P-ACT-LB}).
$$

$$(42)$$

Again, the deuterium abundance inferred assuming `PRyMordial` is consistent with astrophysical measure-
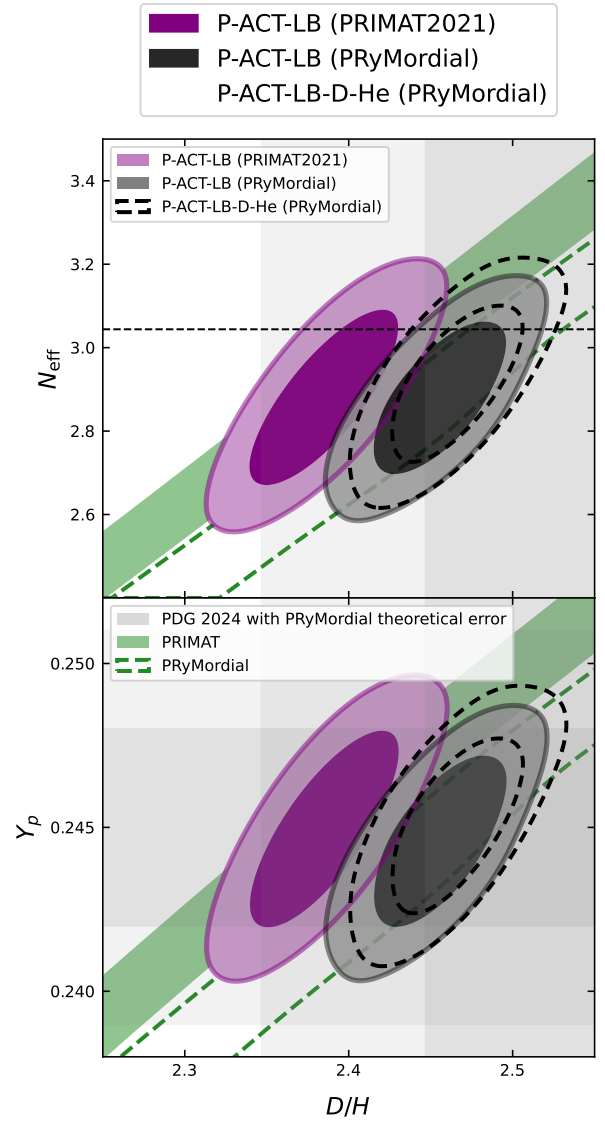
Figure 29. Constraints on the plane $N_{\rm eff}$–D/H (upper panel) and Y_p–D/H (lower panel) from P-ACT-LB assuming `PRIMAT` 2021 as BBN consistency (purple), P-ACT-LB assuming `PRyMordial` (filled black), and P-ACT-LB-D-He again assuming `PRyMordial` (dashed empty black). The green bands show predicted relations between the parameters according to `PRIMAT` 2021 (filled) and `PRyMordial` (empty dashed), assuming 1σ error on $\Omega_b h^2$ from P-ACT-LB in the ΛCDM model. The gray bands show the `PDG` averages with 68% and 95% errors obtained combining in quadrature the observational error and the `PRyMordial` theoretical error.

ments while both `PRIMAT`-based estimates are in mild tension ($\sim 3\sigma$).

Given these results, we combine direct deuterium measurements, accounting for both observational and theoretical uncertainties, with the posterior distribution of $(\Omega_b h^2, N_{\rm eff})$ only under the assumption of `PRyMordial` BBN calculations. This approach yields joint CMB+BBN predictions. After marginalizing over $\Omega_b h^2$, we obtain

$$
N_{\rm eff} = 2.87 \pm 0.13 \quad (68\%,\ \text{P-ACT-LB-D}). \tag{43}
$$
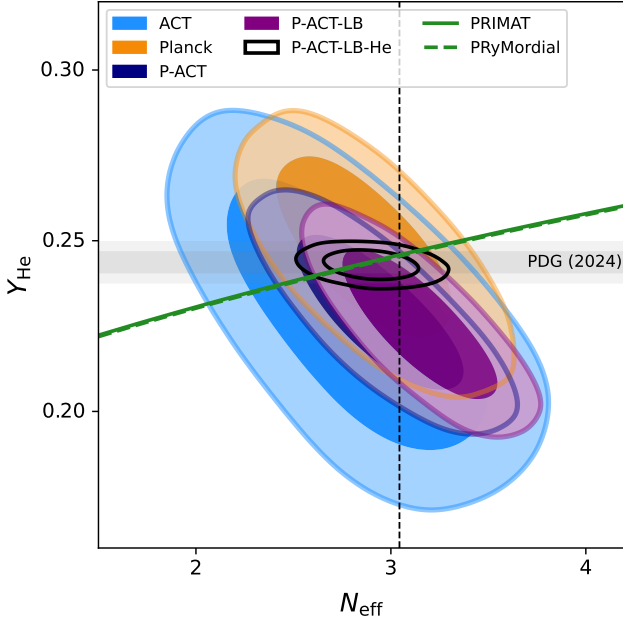
Figure 30. Constraints on the helium abundance, $Y_{\rm He}$, and number of effective neutrino species, $N_{\rm eff}$, with both parameters varying freely, for different data combinations. The horizontal bands are the `PDG` average of observational bounds with 68% and 95% errors. The green curves show the predicted relations between the parameters according to `PRIMAT` and `PRyMordial`, assuming the best-fit of `P-ACT-LB`, and the dashed black line marks the SM prediction of $N_{\rm eff} = 3.044$.

The uncertainty on $N_{\rm eff}$ remains substantially unchanged compared to the limit from `P-ACT-LB` (§6.1), as the theoretical error on deuterium dominates. The mean of the distribution is shifted towards slightly higher values, driven by the higher astrophysical measurement of the deuterium abundance as shown in Fig. 29.

We also expand this to include helium. In this case, the total uncertainty is dominated by the astrophysical measurement, which is only 50% larger than the CMB determination (see Eq. 40). Combining the CMB data with the `PDG` averages we get

$$N_{\rm eff} = 2.89 \pm 0.11 \quad (68\%, \textsf{P-ACT-LB-D-He}), \quad (44)$$

which represents the tightest limit on $N_{\rm eff}$ to date.

By assuming the `PDG` averages for helium and deuterium abundances and employing `PRyMordial` as the BBN calculator, we can also derive a pure BBN constraint on $N_{\rm eff}$, finding $N_{\rm eff} = 2.93 \pm 0.21$ (68%, `D-He`) after marginalizing over $\eta_{\rm b}$. This estimate shows that the number of neutrinos at BBN and at the CMB recombination epoch are in very good agreement.

6.2.2. Model-independent bounds on the helium fraction

Instead of deriving the primordial helium abundance from BBN codes using constraints on $(\Omega_b h^2, N_{\rm eff})$, we

can measure it directly with the CMB. Variations in $Y_{\rm He}$ alter the density of free electrons between helium and hydrogen recombination, thereby affecting the damping tail of the CMB anisotropies. By sampling the ΛCDM+$Y_{\rm He}$ model and converting the helium mass fraction into the helium nucleon fraction, we find

$$Y_p = 0.2312 \pm 0.0092 \quad (68\%, \textsf{P-ACT-LB}), \quad (45)$$

in good agreement with the astrophysical helium abundance measurements. Since both the helium abundance and the number of relativistic degrees of freedom influence the CMB damping tail, allowing both to vary simultaneously leads to weaker constraints

$$\left. \begin{array}{l} Y_p = 0.227 \pm 0.014 \\ N_{\rm eff} = 3.14 \pm 0.25 \end{array} \right\} \quad (68\%, \textsf{P-ACT-LB}). \quad (46)$$

This is still consistent with direct helium abundance measurements and with the expected number of neutrinos, but with larger errors. The relatively low values of Y_p in this case have the same origin as the low value of $N_{\rm eff}$ in the ΛCDM+$N_{\rm eff}$ model, since lower values of both of these parameters reduce the damping, which is preferred by the ACT data. The joint constraints in the $N_{\rm eff} - Y_{\rm He}$ plane are shown in Fig. 30, where the anti-correlation between these two parameters is clearly evident.

Considering the `PDG` collection of helium abundance measurements as an external dataset, it is possible to sample the ΛCDM+$N_{\rm eff}$+$Y_{\rm He}$ model imposing a prior on Y_p, which leads to

$$\left. \begin{array}{l} Y_p = 0.2444 \pm 0.0029 \\ N_{\rm eff} = 2.86 \pm 0.14 \end{array} \right\} \quad (68\%, \textsf{P-ACT-LB-He}), \quad (47)$$

where the degeneracy between $N_{\rm eff}$ and $Y_{\rm He}$ is efficiently broken by helium measurements (see Fig. 30) and the retrieved $N_{\rm eff}$ constraint is consistent with the one obtained in the ΛCDM+$N_{\rm eff}$ model.

6.3. Axion-like particles

We constrain contributions to the total dark-sector content from ultralight axion-like particles (with masses between $10^{-28} < m_{\rm ax}$ /eV $< 10^{-24}$). This ultralight pseudo-scalar dark matter model is well-motivated by high-energy physics, as axions can generically arise from a variety of broken symmetries or compactified extra dimensions, the so-called "axiverse" (Arvanitaki et al. 2010; Duffy & van Bibber 2009). These ultralight axions suppress structure formation below their de Broglie wavelength, which manifests on astrophysical scales. The axion Jeans scale λ_J, below which structure is

smoothed out, depends on the axion mass: $\lambda_J \propto m_{\mathrm{ax}}^{-1/2}$ (Amendola & Barbieri 2006; Duffy & van Bibber 2009; Arvanitaki et al. 2010; Park et al. 2022; Hlozek et al. 2015; Marsh 2016; Hui et al. 2017; Laguë et al. 2021; O'Hare 2024). The dynamics of the axion are described through the Klein-Gordon equation

$$\phi'' + 2\mathcal{H}\phi' + a^2 \frac{dV}{d\phi} = 0. \tag{48}$$

Here ϕ is the axion field, with ϕ_0 indicating its homogeneous component, and primes denote derivatives with respect to conformal time. In the simplest case with a quadratic axion potential, this simplifies to

$$\phi'' + 2\mathcal{H}\phi' + a^2 m_{\mathrm{ax}}^2 \phi = 0, \tag{49}$$

where $\mathcal{H} \equiv a'/a = aH$ is the conformal Hubble parameter, which acts as a friction term in the oscillator equation governing the axion dynamics. When the Hubble term drops (as the universe cools) to near the axion mass $m_{\mathrm{ax}} \simeq 3H(a_{\mathrm{osc}})$, the axion field begins to coherently oscillate, and begins to behave as a dark matter component (with $\rho_{\mathrm{ax}} \propto a^{-3}$), whereas it behaves as a frozen-in "dark-energy-like" component at earlier times. This links the axion mass directly to its observational impact on the CMB and large-scale structure clustering. We solve for the relic axion density by solving the field equations given that

$$\Omega_{\mathrm{ax}} = \left[\frac{1}{2}\left(\frac{\phi_0'}{a}\right)^2 + \frac{m_{\mathrm{ax}}^2}{2}\phi_0^2 \right]_{m_{\mathrm{ax}}=3H} \frac{a_{\mathrm{osc}}^3}{\rho_{\mathrm{crit}}}, \tag{50}$$

where ρ_{crit} is the critical density at $z = 0$. We model the effects of axions via the `axionCAMB` Boltzmann solver,[27] which has been used in several previous analyses of the impacts of axions on the CMB and LSS (e.g., Hlozek et al. 2015; Hložek et al. 2018; Rogers et al. 2023; Laguë et al. 2021). There have been several improvements in the full Boltzmann solution (e.g., Liu et al. 2024) that are particularly relevant in extreme ranges of parameter space that we do not consider here. We leave a full comparison between codes for future work.

In order to correctly model the power on small scales (and to not introduce spurious signals of axion physics, see Hložek et al. 2017; Dentler et al. 2022), we use a modified halo model including mixed dark matter (Vogt et al. 2023). The computational cost of both the halo model code and `axionCAMB` requires using an emulator for efficient computation. We employ the `axionEmu`
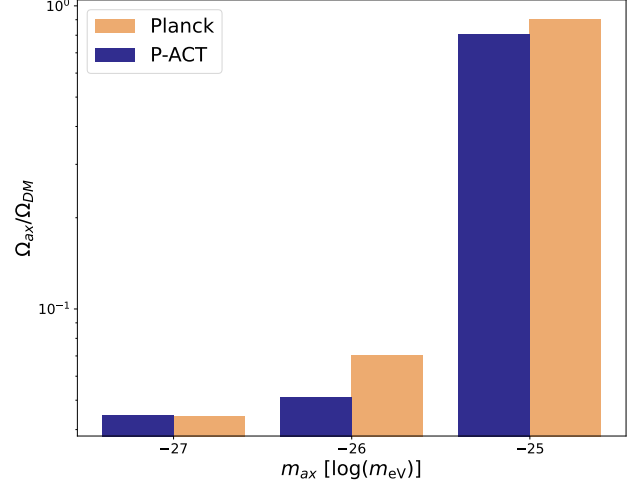
Figure 31. Constraints on the axion fraction using P-ACT (navy) compared to *Planck* alone (orange). Combining ACT with *Planck* significantly improves the constraints on the axion fraction compared to *Planck* alone for the axion mass of $m_{\mathrm{ax}} = 10^{-26}$ eV. For lighter masses the axion starts to roll in its potential at later times, leading to changes on scales where *Planck* has the majority of the constraining power.

emulator,[28] which is based on a modified version of `CosmoPower`.

We present our constraints on the allowed fraction of the dark matter density that is comprised of axions in Fig. 31. For the lightest axion species $m_{\mathrm{ax}} \lesssim 10^{-28}$ eV (not studied here, but see, e.g., Hlozek et al. 2015) this represents a limit on how axions can constitute the dark energy. For the $m_{\mathrm{ax}} \gtrsim 10^{-27}$ eV axions that we consider here, constraints on the axion fraction reflect a disentangling of axion effects from standard cold dark matter in large-scale clustering.

Using the primary CMB spectra from *Planck* alone or P-ACT, we find

$$m_{\mathrm{ax}} = 10^{-26} \text{ eV} :$$
$$\Omega_{\mathrm{ax}}/(\Omega_{\mathrm{ax}} + \Omega_c) < 0.070 \quad (95\%, \text{ Planck})$$
$$< 0.052 \quad (95\%, \text{ P-ACT}). \tag{51}$$

The upper limits for $m_{\mathrm{ax}} = 10^{-27}$ eV are comparable between *Planck* and P-ACT at 4.5%, while P-ACT reduces the allowed fraction of axion-like dark matter to roughly 5% (95% CL) for the mass $m_{\mathrm{ax}} = 10^{-26}$ eV. For masses lighter than $m_{\mathrm{ax}} < 10^{-26}$, the axion starts to roll in its potential at later times, leading to changes in the primary CMB spectra on scales where *Planck* is most constraining. Some of the improvement in the con-

---

straints comes from the degeneracy between the axion density and the scalar spectral index. As the preferred value of n_s slightly increases between *Planck* and P-ACT, the limits on the axion density also tighten. The impact of increased sensitivity in the temperature and polarization power spectra is more pronounced for the CMB lensing deflection power spectrum, particularly for $m_{ax} \geq 10^{-25}$ eV. A full presentation of axion constraints including the ACT DR6 lensing power spectrum, and detailed modeling of the nonlinear clustering that impacts the lensing deflection on small scales, will be provided in a future paper (Laguë et al. in prep).

6.4. Dark matter

Many compelling dark matter (DM) models can be tested with cosmological probes, including scenarios where DM interacts with baryons or annihilates into photons as described in this section, and scenarios where DM interacts with dark radiation (§6.5) or with dark energy (§7.3).

6.4.1. DM-baryon interactions

Dark matter models beyond the standard paradigm of cold, collisionless DM (CDM) include scenarios in which DM interacts with baryons (Cushman et al. 2013; Battaglieri et al. 2017; Gluscevic et al. 2019; Akerib et al. 2022). As done in previous ACT analyses (Li et al. 2023c), we consider the specific case in which DM elastically scatters with protons (Gluscevic & Boddy 2018; Boddy & Gluscevic 2018) through a contact interaction. These models were previously explored using both linear cosmology (Boehm & Schaeffer 2005; Sigurdson et al. 2004; Dvorkin et al. 2014; Gluscevic & Boddy 2018; Boddy & Gluscevic 2018; Boddy et al. 2018; Nguyen et al. 2021; Rogers et al. 2022; Li et al. 2023c; Slatyer & Wu 2018; Buen-Abad et al. 2022; Hooper et al. 2022; Becker et al. 2021) and near-field cosmology (Maamari et al. 2021; Nadler et al. 2019, 2021; Gluscevic et al. 2019). In a DM-baryon scattering scenario, the two corresponding cosmological fluids exchange heat and momentum, leading to collisional damping of small-scale perturbations in the early universe. The strength of the interaction is quantified with the momentum-transfer cross-section $\sigma_{MT} = \sigma_0 (v/c)^n$, where v is the relative particle velocity (sourced primarily by thermal velocities at the redshifts of interest), n is the power-law index determined by the interaction theory, and the cross-section normalization σ_0 is a free parameter of the model.

We consider models with $n = -4$, 0, and 2 and fix the DM particle mass to $m_\chi = 1$ MeV. We choose a sub-proton mass because direct detection experiments probe values of m_χ greater than 1 GeV, and constraints from N_{eff} exclude thermal-relic DM with masses lower than $\sim$

1 MeV (Lewin & Smith 1996; An et al. 2022). The choice of $m_\chi = 1$ MeV allows us to explore the extreme end of what direct detection does not reach. We then choose to explore the set of n values that correspond to the most salient DM-baryon scattering models: millicharged DM ($n = -4$), a velocity-independent and spin-independent contact interaction ($n = 0$), and DM with a velocity-dependent contact interaction ($n = 2$) (Dvorkin et al. 2014). We use a modified version of class (Gluscevic & Boddy 2018; Boddy et al. 2018) that incorporates the effect of DM-baryon scattering in the linear-theory Einstein-Boltzmann equations. We assume a broad, flat, positive prior on σ_0 for each value of n. Each interaction model is thus a single-parameter extension of ΛCDM, for a given n and DM particle mass.

We present constraints corresponding to the three interaction scenarios in Fig. 32. For $n = -4$, we find that ACT data do not improve on *Planck* constraints, giving $\sigma_0(n = -4) < 6.1 \times 10^{-42}$ cm^2 (95%, P-ACT); similarly, the addition of CMB lensing and BAO data has a negligible impact on the constraint. This is because the $n = -4$ model produces a scale-independent suppression at high ℓ, and the high-multipole measurements from ACT do not add significantly to the signal-to-noise for this scenario. On the other hand, the $n = 0$ model produces a strong ℓ-dependent power suppression in both temperature and polarization (e.g., He et al. 2025), and thus ACT alone has comparable constraining power to *Planck*, leading to an upper bound of $\sigma_0(n = 0) < 1.7 \times 10^{-26}$ cm^2 (95%, ACT). A combined analysis of ACT and *Planck* data leads to a factor of two improvement in the upper bounds,

$$\sigma_0(n = 0) < 9.9 \times 10^{-27} \text{ cm}^2 \ (95\%, \text{P-ACT}),$$
$$< 8.5 \times 10^{-27} \text{ cm}^2 \ (95\%, \text{P-ACT-LB}). (52)$$

For $n = 2$, ACT only marginally improves on *Planck* constraints, giving $\sigma_0(n = 2) < 1.5 \times 10^{-21}$ cm^2 (95%, P-ACT). The addition of CMB lensing and BAO data again has a minimal impact, giving $\sigma_0(n = 2) < 1.2 \times 10^{-21}$ cm^2 (95%, P-ACT-LB). As ACT data are particularly sensitive to power suppression on small scales, the difference in constraining power for $n = 0$ and $n = 2$ stems from the baryon-loading-like effect occurring in the $n = 2$ model, which leads to an enhancement of power at intermediate multipoles, rather than a strong suppression seen in the $n = 0$ case (Boddy et al. 2018).

The limits presented here are the tightest bounds on DM-baryon interactions obtained to date from linear cosmology. In particular, these bounds are consistent with and comparable to the results of joint analyses of *Planck*, BOSS, and DES data (He et al. 2023; He et al. 2025). Meanwhile, the bounds obtained from highly
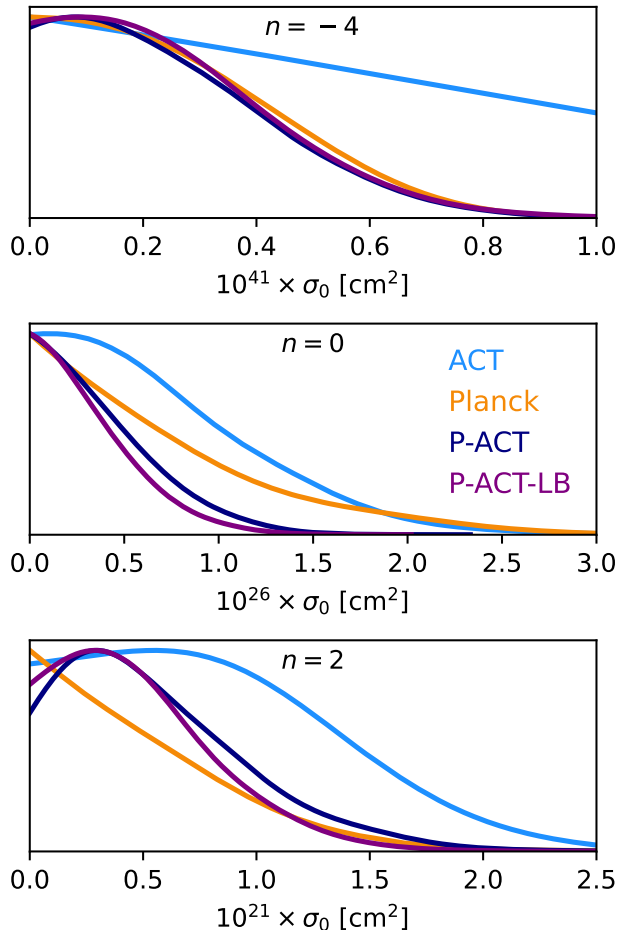
Figure 32. Constraints on the normalization of the momentum-transfer cross-section σ_0 for DM-proton elastic scattering are shown as 1D marginalized posterior probability distributions for three models: $n = -4$ (top), $n = 0$ (middle), and $n = 2$ (bottom). In the top and bottom cases, the addition of ACT does not alter the constraint from *Planck* (compare navy and orange lines). In the case of $n = 0$, ACT data (light blue) have similar constraining power to *Planck*, leading to a factor of two improvement in the upper bound when the two data sets are analyzed jointly. In all cases, the addition of lensing and BAO data only marginally affects the bounds.

nonlinear systems, such as the Milky Way satellite galaxy population, are stronger for all models that produce strong scale-dependent suppression (in this case, $n = 0, 2$), as they lead to a notable decrement of small halos in the late universe (Maamari et al. 2021; Nadler et al. 2019; Nadler et al. 2024). However, the non-linear modeling required for satellite analyses does not yet allow the exploration of the full cosmological parameter space, and the bounds obtained from near-field cosmology are thus not an apples-to-apples comparison to the present results. Moreover, mixed DM with a subcompo-

nent interacting through velocity-independent ($n = 0$) scattering was also found to yield a lower value of S_8, by suppressing the linear matter power spectrum on semi-nonlinear scales (He et al. 2023; He et al. 2025). The ACT DR6 analysis results presented here are consistent with the preferred parameter space of interacting DM that reduces S_8 by a non-negligible amount, for the case where all DM interacts with protons. However, models that are most interesting in this context feature mixed DM and dedicated analyses of these scenarios are left for future work.

6.4.2. *DM annihilation*

If DM annihilates into Standard Model particles, energy released by the annihilation process is injected into the photon-baryon plasma around the time of recombination. This energy injection affects the CMB by altering the ionization history so as to broaden the width of the last-scattering surface and introducing a unique signature in matter clustering. The main observational signatures in the CMB power spectra are: (i) damping of high-ℓ power in both temperature and polarization; (ii) enhancement of the polarization power spectrum at $\ell \lesssim 400$; (iii) shifts of the low-ℓ acoustic peaks in polarization (e.g., Padmanabhan & Finkbeiner 2005; Madhavacheril et al. 2014; Green et al. 2019). The high-ℓ signature is degenerate with other parameters that alter the damping tail, such as n_s; thus, most of the constraining power beyond *Planck* for this model is anticipated to come from large-scale polarization measurements. Because of this, we do not expect major improvements in the constraints for this model from ACT DR6, given the scales probed by our data.

We follow earlier literature (Finkbeiner et al. 2012; Madhavacheril et al. 2014) and constrain the annihilation parameter

$$p_{\mathrm{ann}} = f_{\mathrm{eff}} \frac{\langle \sigma v \rangle}{m_\chi} \qquad (53)$$

where m_χ is the DM particle mass, $\langle \sigma v \rangle$ is the thermally-averaged annihilation cross-section, and f_{eff} is the fraction of the energy due to annihilation that is injected into the plasma (Planck Collaboration 2020c). The transferred energy fraction $f(z)$ is indeed redshift-dependent, but this redshift dependence only weakly impacts the CMB and can thus be approximated by a constant fraction $f(z) \approx f_{\mathrm{eff}}$ (Slatyer 2016a,b). Thus, f_{eff} corresponds to the energy transferred to the plasma around the redshifts at which the CMB is most sensitive to DM annihilation ($z \approx 500 - 600$) (Finkbeiner et al. 2012). We assume that this energy from DM annihilation is transferred to the plasma immediately, known as the "on-the-spot approximation" (Planck Collabo-
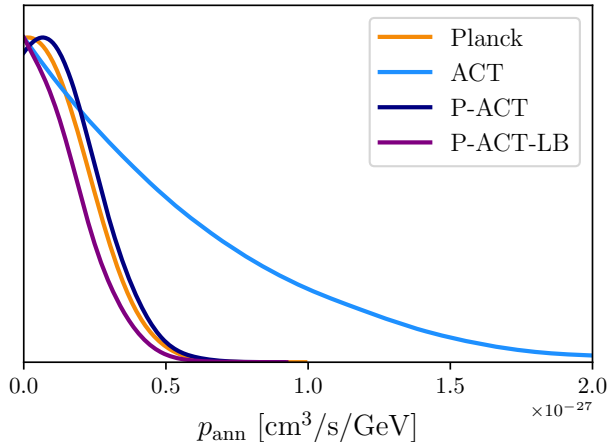
Figure 33. Constraints on DM annihilation (see Eq. (53)). The posterior peak shifts slightly away from zero when combining ACT and *Planck* data, leading to a slightly weaker upper limit than that from *Planck* alone. Including CMB lensing and DESI BAO data pushes the peak back to zero and yields an upper bound slightly tighter than that found with *Planck*.

ration 2020c). We set a broad, flat prior on $p_{\mathrm{ann}} \in [0, 10^{-26} \mathrm{~cm}^3/\mathrm{s}/\mathrm{GeV}]$ and use the implementation of this model in the current standard version of `class`.

The results of this analysis are summarized in Fig. 33. We find no evidence of DM annihilation from the new ACT DR6 spectra, with $p_{\mathrm{ann}} < 1.4 \times 10^{-27} \mathrm{~cm}^3/\mathrm{s}/\mathrm{GeV}$ (95%, ACT). When combining with *Planck*, we find that the joint upper limit does not improve upon the *Planck*-only constraint of $p_{\mathrm{ann}} < 3.9 \times 10^{-28} \mathrm{~cm}^3/\mathrm{s}/\mathrm{GeV}$ (95%),[29] but this is primarily due to the peak of the posterior for p_{ann} shifting slightly away from zero, as can be seen in Fig. 33. The joint constraint gives $p_{\mathrm{ann}} < 4.1 \times 10^{-28} \mathrm{~cm}^3/\mathrm{s}/\mathrm{GeV}$ (95%, P-ACT). The addition of CMB lensing and BAO data helps to tighten the constraints and pushes the peak of the posterior back to zero, yielding $p_{\mathrm{ann}} < 3.6 \times 10^{-28} \mathrm{~cm}^3/\mathrm{s}/\mathrm{GeV}$ (95%, P-ACT-LB). Further addition of SNIa data does not tighten this limit. While the ACT DR6 data do not significantly improve constraints on p_{ann} beyond those from *Planck*, future improvements from large-scale CMB polarization data are expected (see, e.g., Madhavacheril et al. 2014; Green et al. 2019).

6.5. *Interacting dark radiation*

6.5.1. *Self-interacting DR*

A wide range of dark radiation (DR) models have been constructed, beyond the simple free-streaming case parameterized by N_{eff} (e.g., Jeong & Takahashi 2013; Buen-Abad et al. 2015; Cyr-Racine et al. 2016; Lesgourgues et al. 2016; Aloni et al. 2022; Joseph et al. 2023; Buen-Abad et al. 2023; Rubira et al. 2023; Schöneberg et al. 2023; Zhou & Weiner 2024). These models generically involve self-interactions amongst the DR, interactions between the DR and (a subset of) the DM, or combinations thereof, potentially with non-trivial time-dependence (e.g., due to the temperature of the DR-DM sector falling below the mass of a massive mediator particle). As a first step toward investigating these scenarios, we consider a simple model of (strongly) self-interacting DR (SIDR), for example due to a new gauge interaction in the dark sector. At the background level, this model is identical to N_{eff}, with a free parameter $N_{\mathrm{idr}} \geq 0$ describing the number of additional relativistic species (and hence the additional DR energy density). However, the SIDR and free-streaming DR models differ at the perturbative level: the SIDR forms a perfect relativistic fluid with $w = 1/3 = c_s^2$, with interactions sufficiently strong that no anisotropic stress (or higher-order Boltzmann moments) can be supported. Thus, the perturbative dynamics are characterized fully by the continuity and Euler equations. Unlike free-streaming DR, SIDR can cluster on small scales, thus reducing the impact of Silk damping on the high-ℓ power spectra (at fixed DR energy density). In addition, SIDR generates a smaller phase shift in the power spectra. Thus, CMB fits to the SIDR model can accommodate larger amounts of DR than the free-streaming DR model, which can thus allow higher values of H_0 (e.g., Aloni et al. 2022; Schöneberg et al. 2022; Allali et al. 2024).

We consider a simple SIDR model parameterized solely by N_{idr}, with $N_{\mathrm{idr}} \geq 0$. We assume no interactions between the SIDR and the DM. We use the implementation of this model in `class`[30] and we adopt a flat, uninformative prior $N_{\mathrm{idr}} \in [0, 6]$. We assume that the SM neutrino sector consists of one massive state carrying 0.06 eV and two massless states, with $N_{\mathrm{eff}} = 3.044$.

Constraints on this model are presented in Fig. 34. From the ACT DR6 primary CMB power spectra alone, we find

$$N_{\mathrm{idr}} < 0.339 \qquad (95\%, \mathsf{ACT})$$
$$H_0 = 66.85^{+0.85}_{-1.0} \qquad (68\%, \mathsf{ACT}). \qquad (54)$$

---

[29] We find a slightly weaker bound for *Planck* alone than that in Eq. (89a) of Planck Collaboration (2020c); this may be due to a slight shift of the central value arising from our use of `Sroll2` for the low-ℓ EE data, which is particularly important in constraining this model.

[30] We set `idm_dr_tight_coupling_trigger_tau_c_over_tau_h = 0.005` and `idm_dr_tight_coupling_trigger_tau_c_over_tau_k = 0.008` to ensure high accuracy, identical to the values we use for the analogous `class` accuracy parameters in the SM sector (see Appendix A).
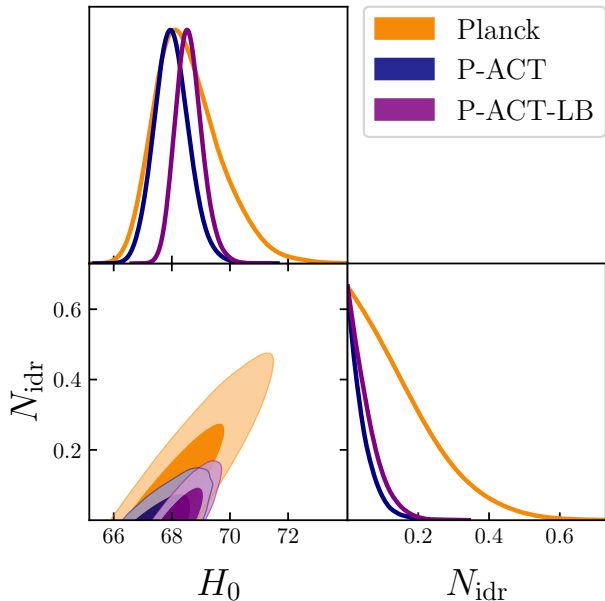
Figure 34. Constraints on the number of strongly self-interacting dark relativistic species, $N_{\rm idr}$. The addition of ACT DR6 spectra improves the constraint from *Planck* by more than a factor of three (navy versus orange) and notably disfavors values of H_0 above 70 km/s/Mpc that are allowed by *Planck* alone. Inclusion of CMB lensing and DESI BAO data (purple) slightly weakens the SIDR upper limit due to small shifts in the best-fit model parameters, but nevertheless further tightens the H_0 posterior. These are the tightest bounds on SIDR obtained to date.

Including *Planck* primary CMB power spectra, we obtain

$$N_{\rm idr} < 0.114 \qquad (95\%,\ \textsf{P-ACT})$$
$$H_0 = 68.00^{+0.55}_{-0.63} \quad (68\%,\ \textsf{P-ACT}). \qquad (55)$$

The joint P-ACT constraint represents more than a factor-of-three improvement over the constraint from *Planck* alone, for which we find $N_{\rm idr} < 0.379$ at 95% confidence. The origin of this tight constraint is the lack of preference for excess high-ℓ damping in the DR6 power spectra; since SIDR can only increase damping (due to the physical bound $N_{\rm idr} > 0$), its existence is thus disfavored by the data. From the primary CMB, we thus see no evidence of additional SIDR species, extending our results for the free-streaming DR case ($N_{\rm eff}$) to a very different physical regime.

Including additional low-redshift datasets does not significantly tighten the bound on $N_{\rm idr}$, but further tightens the error bar on H_0 and other cosmological parameters. From the combination of ACT and *Planck* CMB spectra, ACT and *Planck* CMB lensing, and DESI

BAO, we obtain

$$N_{\rm idr} < 0.134 \qquad (95\%,\ \textsf{P-ACT-LB})$$
$$H_0 = 68.59^{+0.41}_{-0.50} \quad (68\%,\ \textsf{P-ACT-LB}). \qquad (56)$$

The upper limit on $N_{\rm idr}$ weakens slightly compared to that found for P-ACT above, due to small shifts in the best-fit parameter values. Further including SNIa data in the analysis yields negligible changes to these constraints.

The MAP SIDR model found for P-ACT, as well as that found for P-ACT-LB, yields negligible improvement in the quality of fit over ΛCDM — in fact, we find that the MAP SIDR model lies at the ΛCDM limit of the parameter space in both cases, i.e., with $N_{\rm idr} = 0$, indicating no preference for this model extension. We emphasize again that this lack of preference arises from the lack of excess damping seen at high-ℓ in ACT: because SIDR can only increase damping over that in ΛCDM, the model cannot accommodate decreased damping (unlike $N_{\rm eff}$, which can do so via a value of $N_{\rm eff} < 3.044$).

These are the tightest bounds on SIDR presented to date. The ability of this model to increase the value of H_0 inferred from cosmological data is strongly limited by these observations, with the new ACT DR6 spectra playing a crucial role in significantly tightening the constraints compared to those from *Planck*.

6.5.2. *Interacting DR-DM*

A wide range of dark sector models have been considered in the literature, featuring various types of interactions between dark radiation and dark matter species (e.g., Cyr-Racine et al. 2016; Buen-Abad et al. 2015; Lesgourgues et al. 2016). As a first step in probing this space of models, here we consider the fiducial scenario studied in Rubira et al. (2023), in which an SIDR fluid (identical to that studied above) interacts with all of the DM via an interaction with a momentum transfer rate $\Gamma(a) = \Gamma_{0,\rm nadm} a^{-2}$ between the DM and the DR (Buen-Abad et al. 2018). Microphysically, such an interaction can be realized in dark-sector models featuring non-Abelian gauge bosons (hence the "nadm" subscript) that mediate interactions between Dirac fermion DM particles (Buen-Abad et al. 2015; Lesgourgues et al. 2016). In this particular model, Γ has a redshift (or temperature) dependence that matches that of the Hubble rate during radiation domination — see Buen-Abad et al. (2015) for an explicit calculation of the momentum transfer rate in the "nadm" model. As a consequence, the interaction between the DR and the DM is relevant while modes covering a broad range of scales enter the horizon (essentially during all of radiation domination), which leads to a roughly scale-
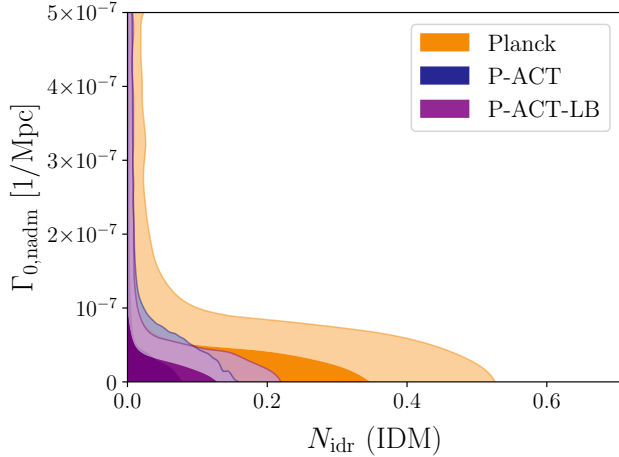
Figure 35. Constraints on the IDR-IDM model. Here the interaction strength $\Gamma_{0,\mathrm{nadm}}$ is given in 1/Mpc. The inclusion of ACT DR6 spectra (navy) significantly improves the constraints from *Planck* alone (orange). Inclusion of CMB lensing and DESI BAO data (purple) slightly weakens the N_{idr} upper limit due to small shifts in the best-fit model parameters, but further tightens the constraint on $\Gamma_{0,\mathrm{nadm}}$. The notation N_{idr} (IDM) indicates that the IDR in the model constrained here is interacting with the DM, unlike that in Fig. 34.

invariant suppression of power for such modes. This makes the model a promising candidate to decrease the CMB-inferred value of S_8 (Buen-Abad et al. 2015; Rubira et al. 2023). The SIDR abundance (set by N_{idr}) determines the scale where power is suppressed, while the interaction strength $\Gamma_{0,\mathrm{nadm}}$ determines the amount of suppression (Buen-Abad et al. 2015).[31]

We use the implementation of this interacting DR – interacting DM (IDR-IDM) model in `class` (Lesgourgues et al. 2016; Archidiacono et al. 2019). The model contains two additional free parameters beyond those of base ΛCDM: N_{idr} (as in the SIDR model above) and $\Gamma_{0,\mathrm{nadm}}$. We adopt the same priors and model assumptions as for the SIDR scenario for all common parameters, while for $\Gamma_{0,\mathrm{nadm}}$, we adopt an uninformative, uniform prior $\Gamma_{0,\mathrm{nadm}}/(\mathrm{Mpc}^{-1}) \in \left[0.0, 5.0 \times 10^{-7}\right]$.

We find no preference for the IDR-IDM scenario in the ACT DR6 spectra. Constraints on this model are shown in Fig. 35. Joint analysis of ACT and *Planck* yields

$$\left.\begin{array}{l} N_{\mathrm{idr}} < 0.0977 \\ \Gamma_{0,\mathrm{nadm}} < 4.45 \times 10^{-7}\ \mathrm{Mpc}^{-1} \end{array}\right\} \quad (95\%,\ \mathsf{P\text{-}ACT}). \tag{57}$$

---

[31] Note that the IDR-IDM interaction studied here is not relevant in the late universe, and thus late-time growth is not affected; modifications to structure formation are captured by the change in the linear matter power spectrum.

This is a significant improvement over analogous results from *Planck* alone, for which we find $N_{\mathrm{idr}} < 0.367$ at 95% CL and no bound on $\Gamma_{0,\mathrm{nadm}}$ (at 95% CL). We find negligible reduction in S_8 in the P-ACT fit to the IDR-IDM model, with $S_8 = 0.814^{+0.023}_{-0.015}$ at 68% CL. Inclusion of CMB lensing and DESI BAO data in the combined dataset yields:

$$\left.\begin{array}{l} N_{\mathrm{idr}} < 0.135 \\ \Gamma_{0,\mathrm{nadm}} < 4.09 \times 10^{-7}\ \mathrm{Mpc}^{-1} \end{array}\right\} \quad (95\%,\ \mathsf{P\text{-}ACT\text{-}LB}). \tag{58}$$

The bound on S_8 tightens considerably compared to P-ACT, with $S_8 = 0.808^{+0.013}_{-0.0095}$ at 68% CL, further limiting this model's ability to yield low values of this parameter.

We note that Bayesian constraints on the IDR-IDM model can suffer from volume effects, since $\Gamma_{0,\mathrm{nadm}}$ becomes degenerate in the $N_{\mathrm{idr}} \to 0$ limit. We thus confirm that the best-fit IDR-IDM model to P-ACT or P-ACT-LB does not yield a significantly better fit to these data than ΛCDM. In fact, as found for SIDR, we find that the MAP model in the IDR-IDM scenario for both P-ACT and P-ACT-LB is indistinguishable from ΛCDM within our numerical precision. Overall, we see no evidence of extended dark-sector physics in this analysis.

7. GRAVITY AND LATE-TIME PHYSICS

7.1. *Geometry: spatial curvature*

In the inflationary scenario, at the end of inflation the universe is predicted to emerge in a state very close to spatially flat (Linde 1982; Albrecht & Steinhardt 1982). This hypothesis is tested empirically by allowing the curvature density parameter, Ω_k, which is fixed to zero in the baseline ΛCDM model, to be a free parameter. As discussed in L25, the new ACT DR6 power spectra alone prefer a flat geometry, breaking degeneracies via lensing effects in the power spectra; in a joint fit with *Planck*, ACT DR6 moves the *Planck* contours toward vanishing curvature. When adding BAO and CMB lensing data to the primary CMB, the degeneracy with the matter density is more effectively broken, as shown in Fig. 36, and the constraints tighten significantly, yielding

$$\Omega_k = 0.0019 \pm 0.0015 \quad (68\%,\ \mathsf{P\text{-}ACT\text{-}LB}), \tag{59}$$

similar to $\Omega_k = 0.0022 \pm 0.0015$ (68%, Planck-LB). These limits derived from the combination of CMB and low-redshift data tightly constrain the universe's spatial geometry, and are fully consistent with spatial flatness.

This result can be converted into a new limit on the present-day radius of spatial curvature of the universe, $R_k = c/H_0/\sqrt{(|\Omega_{\mathrm{tot}} - 1|)}$ where Ω_{tot} is the total cosmic
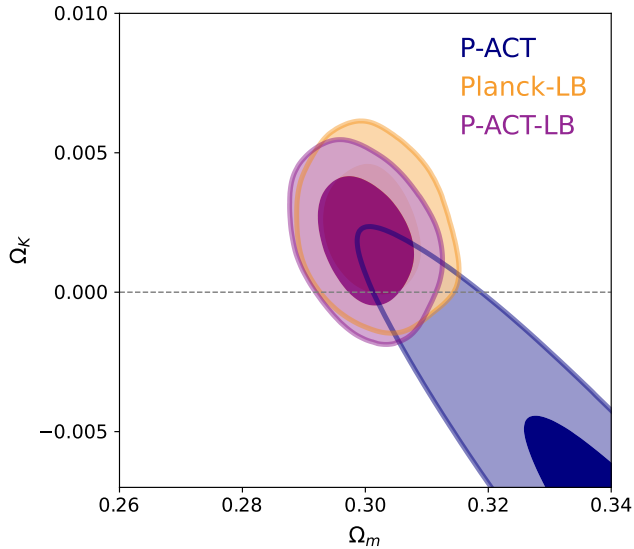
Figure 36. Curvature can be measured from the CMB alone due to lensing effects in the primary CMB; the new ACT DR6 spectra are consistent with a flat universe (dashed line) both alone and in combination with *Planck*, as described in L25 and as shown by the navy contour. The P-ACT-LB combination (purple) tightens the constraint around zero curvature, further breaking the degeneracy with the matter density and improving on Planck-LB (orange).

energy density, such that $\Omega_k = 1 - \Omega_{\text{tot}}$. With P-ACT-LB we find at 95% confidence $R_k > 105$ Gpc or equivalently $R_k > 343$ billion light-years for a closed universe ($\Omega_{\text{tot}} > 1$ or $\Omega_k < 0$) and $R_k > 66$ Gpc or $R_k > 215$ billion light-years for an open universe ($\Omega_{\text{tot}} < 1$ or $\Omega_k > 0$).

7.2. *Late-time dark energy*

Within the ΛCDM model, the dark energy density is constant over time, described by a cosmological constant Λ with an equation of state $w \equiv -1$ at all times. A common way of exploring the dark energy component is to relax the assumption on its equation of state, considering a time evolution of the pressure-density ratio $P/\rho = w(a)$ with (Chevallier & Polarski 2001; Linder 2003)[32]

$$w(a) = w_0 + w_a(1 - a). \tag{60}$$

This is equivalent to a cosmological constant Λ when setting today's value of the equation of state to $w_0 = -1$ and its time dependence to $w_a = 0$. This expansion can then be used for explorations varying either only w_0 or both w_0 and w_a, as we do below. Opening these degrees of freedom in the dark energy component causes strong degeneracies between parameters when using only CMB

---

[32] See, e.g., Shlivko & Steinhardt (2024) for consideration of time-evolving dark energy beyond the (w_0, w_a) parametrization.

---

data and therefore we mostly report results for combinations with CMB lensing and external probes of the expansion history, including both BAO and SNIa. In particular, as shown in DESI Collaboration (2025b) in fits to models with additional degrees of freedom in the dark energy equation of state, SNIa are essential to break degeneracies with H_0 and the matter density. We do not expect significant improvements from the new ACT power spectra for late-time dark energy, but we report constraints here given interest in this model following the DESI Year-1 results.

When $w \equiv w_0$ is free to vary as a single-parameter extension to ΛCDM (without time dependence — $w_a = 0$ — and imposing a flat prior $w_0 \in [-3, 1]$)[33], we obtain the contours shown in Fig. 1 for P-ACT-LB. Adding also SNIa data, we find

$$w_0 = -0.986 \pm 0.025 \ (68\%, \text{P-ACT-LBS}), \tag{61}$$

in good agreement with the ΛCDM expectation, and with the same error bar as previous measurements using CMB from *Planck* ($w_0 = -0.997 \pm 0.025$, DESI Collaboration 2025b).

When we expand the model further, with both w_0 and w_a varying (with a flat prior $w_a \in [-3, 2]$), we find

$$\left. \begin{array}{l} w_0 = -0.837 \pm 0.061 \\ w_a = -0.66^{+0.27}_{-0.24} \end{array} \right\} \ (68\%, \text{P-ACT-LBS}), \tag{62}$$

with marginalized posteriors shown in Fig. 37. We see a moderate preference for the $w_0 w_a$CDM model over ΛCDM, similar to what was reported in DESI Collaboration (2025b) using CMB data from *Planck* ($w_0 = -0.827 \pm 0.063$, $w_a = -0.75^{+0.29}_{-0.25}$).[34] This result is driven partially by the DESI data and partially by the SNIa data. Substituting the BAO dataset with BOSS BAO, the posteriors are consistent with the cosmological constant scenario. The specific CMB dataset used for this analysis has essentially no impact: *Planck* alone, P-ACT, or W-ACT yield similar results.

With the combined P-ACT-LBS dataset, we find a well-constrained value of $H_0 = 67.73 \pm 0.68$ km/s/Mpc and $H_0 = 68.02 \pm 0.72$ km/s/Mpc for the w_0 and $w_0 - w_a$ extensions, respectively. Similarly to DESI Collaboration (2025b), we also find that SNIa reduce by a factor of ~ 2 the uncertainty on H_0 and shift the mean to lower values by ~ 3 km/s/Mpc (see Fig. 1).

---

[33] To get theory predictions for this model we use `camb` with the Parametrized Post-Friedmann approach (Fang et al. 2008) to compute dark energy perturbations (`dark_energy_model=DarkEnergyPPF`).

[34] Quantitatively, comparing the MAP $w_0 w_a$CDM and ΛCDM models, we find $\Delta\chi^2 = -7.0$ (2.2σ) for P-ACT-LBS, while DESI Collaboration (2025b) find $\Delta\chi^2 = -8.7$ (2.5σ) for Planck-LBS.
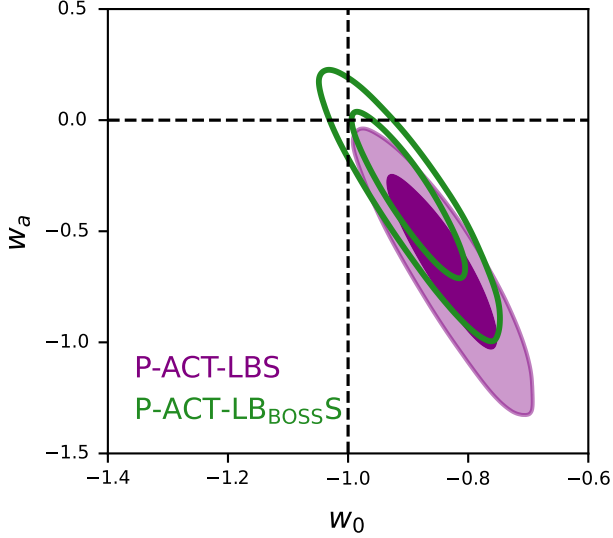
Figure 37. Constraints on the dark energy equation of state parameters, varying both today's value, w_0, and its time variation, w_a. Similar to other studies, we find that DESI drives a preference for time-varying dark energy (compared to the dashed ΛCDM line), which is relaxed when considering BOSS BAO instead (green contours). The CMB contribution to this measurement is sub-dominant, apart from breaking parameter degeneracies, with Planck, W-ACT, and P-ACT giving similar results.

7.3. *Interacting DE-DM*

An extension of ΛCDM with kinetic interactions between the DM and DE fluids was initially considered in Simpson (2010). This model introduces a coupling constant, Γ_{DMDE}, describing pure momentum transfer between the DM and DE. This coupling leaves the homogeneous background cosmological evolution unchanged, but alters the dark sector perturbation evolution equations as follows (Simpson 2010):

$$\delta'_{\mathrm{DM}} = -\theta_{\mathrm{DM}} + 3\phi', \tag{63}$$

$$\delta'_{\mathrm{DE}} = -\left[(1+w) + 9\frac{\mathcal{H}^2}{k^2}\left(1-w^2\right)\right]\theta_{\mathrm{DE}}$$
$$+ 3(1+w)\phi' - 3\mathcal{H}(1-w)\delta_{\mathrm{DE}}, \tag{64}$$

$$\theta'_{\mathrm{DM}} = -\mathcal{H}\theta_{\mathrm{DM}} - k^2\phi + \frac{a\Gamma_{\mathrm{DMDE}}}{\bar{\rho}_{\mathrm{DM}}}\Delta\theta, \tag{65}$$

$$\theta'_{\mathrm{DE}} = 2\mathcal{H}\theta_{\mathrm{DE}} + \frac{k^2}{(1+w)}\delta_{\mathrm{DE}} + k^2\phi - \frac{a\Gamma_{\mathrm{DMDE}}}{(1+w)\bar{\rho}_{\mathrm{DE}}}\Delta\theta, \tag{66}$$

where w is the DE equation of state, $\delta \equiv \rho/\bar{\rho} - 1$ is the energy density contrast, $\theta \equiv \nabla \cdot \mathbf{v}$ is the velocity divergence, $\Delta\theta \equiv \theta_{\mathrm{DE}} - \theta_{\mathrm{DM}}$, $\mathcal{H}$ is the conformal Hubble factor ($\mathcal{H} = aH$), ϕ is the Newtonian gravitational potential, and $'$ denotes differentiation with respect to conformal time.

This type of interaction leads to slower structure growth, and this idea was revisited in Poulin et al. (2023a) as a potential way to reduce the value of S_8 inferred from CMB and LSS data. The coupling strength needed to appreciably reduce S_8 is around $\Gamma_{\mathrm{DMDE}}/(H_0\rho_c) \sim 1$ (where ρ_c is the critical density). While previous work assumed linear theory, Laguë et al. (2024) developed a halo-model approach to characterize the behavior of DM with non-zero Γ_{DMDE} on semi-linear scales. This model is an adapted version of HMcode (still assuming dark matter only) and accounts for changes in halo formation resulting from DE-DM interactions using modified fitting functions for the critical and virial overdensities. A combination of CMB lensing from ACT DR6 and *Planck*, BAO from SDSS/BOSS, and CMB primary anisotropy measurements from *Planck* constrains the contribution of $\Gamma_{\mathrm{DMDE}}/H_0\rho_c < 2.76$ at the 95% CL using this prescription (Laguë et al. 2024).

Here, we enlarge the dataset to include the new ACT DR6 primary CMB power spectra, and we replace the BAO likelihood with that of DESI.[35] We study two configurations for this model. We first fix the dark energy equation of state to three different values of $w \in \{-0.999, -0.975, -0.95\}$, allowing Γ_{DMDE} to vary (the model is thus a two-parameter extension of ΛCDM with only one additional degree of freedom). We avoid $w = -1$ due to a divergence that arises in Eq. (66) in this case. We then also jointly sample both parameters, but we find that Metropolis-Hastings sampling performs poorly when varying both w and Γ_{DMDE}. This occurs because w can take a very wide range of values when Γ_{DMDE} goes to 0.[36] We adopt a flat prior $\Gamma_{\mathrm{DMDE}}/(H_0\rho_c) \in [10^{-8}, 50]$. We compute theoretical predictions for this scenario using the modified version of class from Laguë et al. (2024).[37]

We show the parameter posterior distributions for a subset of the runs in Fig. 38. Given the large degeneracies present in this model when using only CMB data, we focus on results for the data combinations P-ACT-LB and P-ACT-LBS. For fixed values of w, we find that the limit on $\Gamma_{\mathrm{DMDE}}/(H_0\rho_c)$ gets tighter moving away from the $w = -1$ boundary: $\Gamma_{\mathrm{DMDE}}/(H_0\rho_c)_{w=-0.999} < 3.10$, $\Gamma_{\mathrm{DMDE}}/(H_0\rho_c)_{w=-0.975} < 1.64$, and

---

[35] We note here that the interacting DE-DM model is the only case in this paper for which we use the *extended* setting for the ACT DR6 + *Planck* CMB lensing data. To constrain Γ_{DMDE}, we make use of the full CMB lensing likelihood up to $L = 1250$ (Madhavacheril et al. 2024; Qu et al. 2024b).

[36] In this case, due to the computational expense in this model, we stop the chains at a Gelman-Rubin statistic of $R-1 < 0.05$; thus, slight variations in the final bounds are expected.

[37] https://github.com/fmccarthy/Class_DMDE
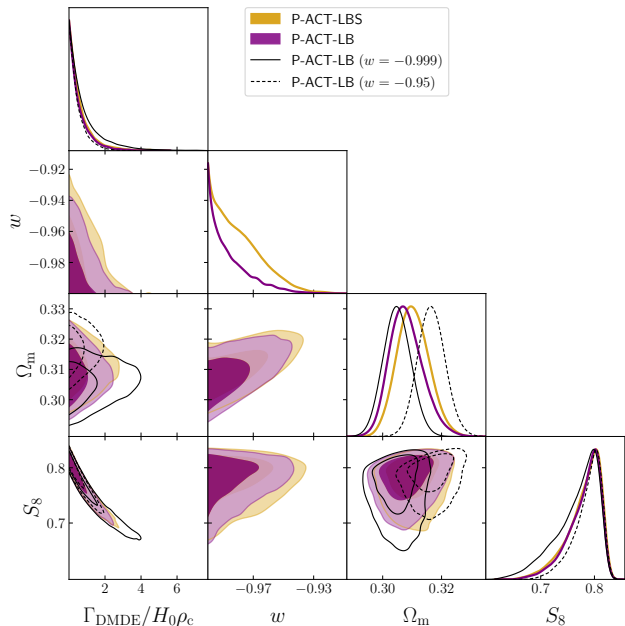
Figure 38. Constraints on the strength of the DM-DE interaction rate for the data combinations P-ACT-LB and P-ACT-LBS, for varying equation of state (filled contours) and two fixed values of w (empty contours and black lines). The preferred parameters are in agreement with the ΛCDM values of $w = -1$ and $\Gamma_{\mathrm{DMDE}} = 0$ (no coupling between DM and DE).

$\Gamma_{\mathrm{DMDE}}/(H_0\rho_{\mathrm{c}})_{w=-0.95} < 1.64$ (all at 95% CL from P-ACT-LB). Similarly, the S_8 limit gets tighter, with the low-end tail of the distribution being more excluded (see Fig. 38). When varying w and $\Gamma_{\mathrm{DMDE}}/(H_0\rho_{\mathrm{c}})$ simultaneously, we find

$$\Gamma_{\mathrm{DMDE}}/(H_0\rho_{\mathrm{c}}) < 1.9 \ (95\%, \mathsf{P\text{-}ACT\text{-}LB}),$$
$$S_8 = 0.781^{+0.04}_{-0.02} \qquad (68\%, \mathsf{P\text{-}ACT\text{-}LB}), \qquad (67)$$

and when including SNIa data from Pantheon+

$$\Gamma_{\mathrm{DMDE}}/(H_0\rho_{\mathrm{c}}) < 2.1 \ (95\%, \mathsf{P\text{-}ACT\text{-}LBS}),$$
$$S_8 = 0.780^{+0.04}_{-0.02} \qquad (68\%, \mathsf{P\text{-}ACT\text{-}LBS}). \qquad (68)$$

We also perform the same analyses with BOSS BAO data used in place of DESI, finding similar constraints on S_8 (with error bars 10-30% larger) and somewhat weaker bounds on Γ_{DMDE} (roughly 20-50% larger upper limits). We see no preference for this model over ΛCDM for any dataset combination considered here, with the best-fit model lying at the $\Gamma_{\mathrm{DMDE}} = 0$ edge of the parameter space (note that there are no projection effects in the Bayesian posteriors in the cases where we fix w to specific values). The inclusion of the ACT DR6 and DESI data tightens the upper limit on Γ_{DMDE} by 33% compared to the bounds from Laguë et al. (2024) when

varying both w and Γ_{DMDE} using the P-ACT-LB dataset. The improvement in constraining power comes mainly from using the DESI BAO dataset instead of BOSS and the improved bounds on Ω_m from the primary CMB in ACT DR6. The addition of SNIa data from Pantheon+ does not improve our bounds.

As observed in previous work, the coupling between the DM and DE leads to reduced values of S_8, significantly broadening the marginalized posterior for this parameter. When $-w$ approaches unity, the effects of the coupling are delayed to lower redshifts. This makes CMB lensing, which is sensitive to redshifts around $z \sim 1-2$, less constraining for this model. For this reason, we find a more extended posterior for $\Gamma_{\mathrm{DMDE}}/(H_0\rho_{\mathrm{c}})$ when w is near -1, as shown in Fig. 38. In general, we find that this model allows values of S_8 from P-ACT-LB that are consistent with values found in galaxy weak lensing surveys, but we caution that a joint analysis with such datasets would require a full model for the nonlinear matter power spectrum in this scenario.

7.4. *Modified gravity*

The growth rate of large-scale structure $f(a) \equiv d\ln D(a)/d\ln a$, where $D(a)$ is the linear growth factor and a is the scale factor, can be accurately approximated in the matter- or dark energy-dominated eras as

$$f(a) = \Omega_m^\gamma(a), \qquad (69)$$

where γ is the growth index, which takes a canonical value of 0.55 in general relativity (GR) with a flat ΛCDM cosmology (Fry 1985; Wang & Steinhardt 1998; Linder 2005). This simple model with values of γ differing from 0.55 is part of a broader class of modified gravity theories, which generically predict modifications to the growth of structure. Various studies have considered and constrained different prescriptions for the growth and geometry (e.g., Wang et al. 2007; Guzzo et al. 2008; Dossett et al. 2010; Hudson & Turnbull 2012; Rapetti et al. 2013; Pouri et al. 2014; Ruiz & Huterer 2015; Bernal et al. 2016; Johnson et al. 2016; Alam et al. 2016; Moresco & Marulli 2017; Basilakos & Anagnostopoulos 2020; DES Collaboration 2021; García-García et al. 2021; Ruiz-Zapatero et al. 2021, 2022; White et al. 2022; Andrade et al. 2021; Chen et al. 2022b; DES Collaboration 2023). Some studies have found evidence for suppression of the growth of structure, while others have not. One of the most sensitive datasets for such theories is the combination $f\sigma_8(z)$ (the product of $f(z)$ and $\sigma_8(z)$) which is constrained by various redshift-space distortion (RSD) and peculiar velocity surveys. RSD surveys measure the growth rate of structure via the imprint of peculiar velocities on the quadrupole of redshift-space galaxy clustering measurements (e.g., Kaiser 1987;

Hamilton 1998; Percival & White 2009; Song & Percival 2009). Surveys of the peculiar velocities of individual galaxies can be performed at low-to-moderate redshifts, when an estimate of the absolute distance to each galaxy is available (e.g., from Cepheid, TRGB, or SNIa observations), thus allowing the cosmological contribution to the observed redshift to be isolated from the peculiar-velocity contribution (e.g., Miller & Branch 1992; Riess et al. 1998; Turnbull et al. 2012; Tully et al. 2016; Stahl et al. 2021). CMB data also contribute constraining power via lensing effects (e.g., Calabrese et al. 2009).

A recent analysis by Nguyen et al. (2023) found moderate evidence of a potential deviation from the GR prediction for γ. They considered measurements of peculiar velocities from Boruah et al. (2020), Huterer et al. (2017), Turner et al. (2022), and Said et al. (2020), and measurements of RSD from Beutler et al. (2012), Howlett et al. (2015), Blake et al. (2012), Blake et al. (2013), Pezzotta et al. (2017), Alam et al. (2021), and Okumura et al. (2016). Combining these with data from *Planck*, they found evidence for suppression of the growth of structure at 3.7σ significance, with $\gamma = 0.639^{+0.024}_{-0.025}$. This suppression both significantly reduced S_8 and eliminated *Planck*'s (mild) preference for positive spatial curvature.

Here, we study the impact of including the new ACT DR6 spectra on these results, following the approach of Nguyen et al. (2023). Since Eq. (69) is only valid for sub-horizon perturbations, this approach leaves the unlensed primary CMB perturbations unchanged, but modifies the CMB lensing potential and other late-time observables self-consistently. We use all measurements considered by Nguyen et al. (2023) to form a $f\sigma_8$ likelihood, consisting of a simple Gaussian likelihood for each survey's constraint on $f\sigma_8$. DESI also recently released $f\sigma_8$ measurements (DESI Collaboration 2024b) which we do not include here to facilitate comparison with Nguyen et al. (2023), but we discuss them in §8.1. In combination with ACT and other datasets, we use the $f\sigma_8$ likelihood to constrain the growth index γ as a single-parameter extension to ΛCDM, varied with a uniform prior $\gamma \in [0, 2]$. To perform the theoretical calculations, we use the modified version of `camb` released by Nguyen et al. (2023).[38]

With the new DR6 spectra, we find the growth index to be $\gamma = 0.560 \pm 0.110$, with $S_8 = 0.872 \pm 0.042$ (68%, ACT). Combining with *Planck*, these limits tighten significantly, yielding $\gamma = 0.688 \pm 0.071$ and $S_8 = 0.812 \pm 0.017$ (68%, P-ACT). Further adding CMB

[38] https://github.com/MinhMPA/CAMB_GammaPrime_Growth
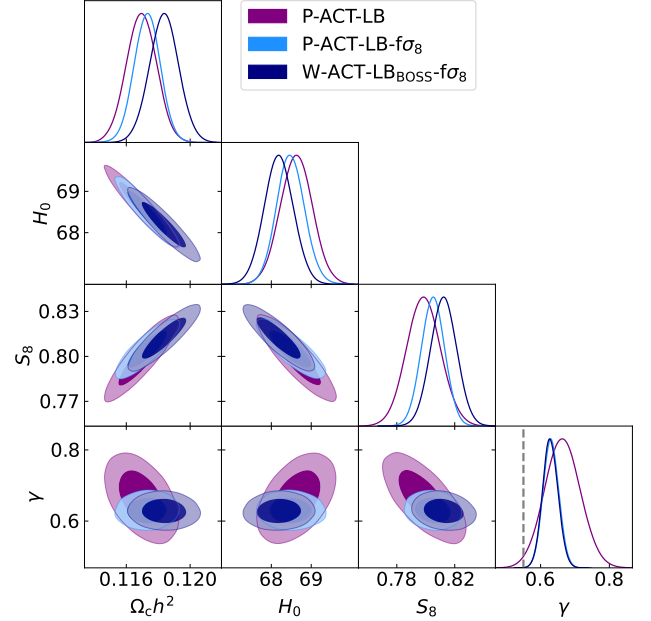
Figure 39. Constraints on a modified growth of structure model in which the growth index γ is allowed to vary, for different dataset combinations (P-ACT-LB in purple, P-ACT-LB-$f\sigma_8$ in light blue, and W-ACT-LB$_{\rm BOSS}$-$f\sigma_8$ in navy). The addition of $f\sigma_8$ measurements effectively breaks degeneracies between γ and other parameters, but moves the constraint away from the GR prediction of $\gamma = 0.55$ (marked by the gray dashed line) at $> 3\sigma$. The consistency between P-ACT-LB-$f\sigma_8$ and W-ACT-LB$_{\rm BOSS}$-$f\sigma_8$ indicates that the γ result is not driven strongly by the preference for high $A_{\rm lens}$ in *Planck*, or by DESI BAO.

lensing and DESI BAO data, we obtain

$$\left.\begin{array}{ll} \gamma = & 0.663 \pm 0.052 \\ S_8 = & 0.799 \pm 0.012 \end{array}\right\} \quad (68\%, \text{P-ACT-LB}). \quad (70)$$

This value of γ lies 2.2σ above the GR prediction, but is nevertheless consistent with it (as shown in Fig. 39). When replacing the DESI BAO data with BOSS BAO data, we obtain $\gamma = 0.635 \pm 0.053$ and $S_8 = 0.812 \pm 0.013$ (68%, P-ACT-LB$_{\rm BOSS}$), which is consistent with the P-ACT-LB result but moves closer to the GR expectation. Including now the $f\sigma_8$ measurements, we obtain[39]

[39] We note that when including $f\sigma_8$ measurements, for the BOSS likelihood we use a likelihood that combines BAO and RSD data from BOSS DR12 and eBOSS DR16, as described in eBOSS Collaboration (2021). When we refer to P-ACT-LB$_{\rm BOSS}$-$f\sigma_8$ or W-ACT-LB$_{\rm BOSS}$-$f\sigma_8$, this is the BOSS likelihood that is used.

$$\left.\begin{array}{rl} \gamma = & 0.630 \pm 0.023 \\ S_8 = & 0.8050 \pm 0.0081 \end{array}\right\} \quad (68\%, \text{ P-ACT-LB-f}\sigma_8). \tag{71}$$

Replacing DESI BAO data with BOSS has minimal impact, giving $\gamma = 0.634 \pm 0.024$ and $S_8 = 0.8121 \pm 0.0084$ (68%, P-ACT-LB$_{\text{BOSS}}$-fσ_8). The central values of γ in these constraints deviate from GR at 3.5σ. The data driving this result are those from RSD and peculiar velocity surveys, but the central values are consistent with those found in our analyses without these data.

Note that values of $\gamma > 0.55$ can improve concordance between CMB-derived and LSS-derived constraints on S_8, compared to those in ΛCDM. For example, our P-ACT result in the modified-growth model ($S_8 = 0.812 \pm 0.017$) is lower than that in ΛCDM ($S_8 = 0.830 \pm 0.014$, L25). We do not run constraints using non-CMB data on their own, but Nguyen et al. (2023) find that the combination of $f\sigma_8$, DES-Y1 3×2-point, and pre-DESI BAO data yields $S_8 = 0.784^{+0.017}_{-0.016}$ in this model. This agrees with the P-ACT S_8 result at 1.2σ, whereas in ΛCDM, the same comparison is discrepant at 3.0σ. The moderate tension is reduced in the modified-growth model both by $\sim 1\sigma$ shifts in the central S_8 values and small increases in the error bars.

The effects of varying γ on the lensed CMB power spectrum are similar to those from the phenomenological lensing amplitude parameter, A_{lens} (Nguyen et al. 2023), for which $Planck$ has a moderate preference for a value $A_{\text{lens}} > 1$ (Planck Collaboration 2020c). To assess whether it is the $Planck$ A_{lens} behavior driving the evidence for a high growth index, we swap in $WMAP$ for $Planck$ data. For the CMB-only combination, we find $\gamma = 0.621 \pm 0.087$ and $S_8 = 0.840 \pm 0.028$ (68%, W-ACT). Adding CMB lensing, BOSS BAO, and the $f\sigma_8$ data yields

$$\left.\begin{array}{rl} \gamma = & 0.628 \pm 0.022 \\ S_8 = & 0.8122 \pm 0.0091 \end{array}\right\} \quad (68\%, \text{ W-ACT-LB}_{\text{BOSS}}\text{-f}\sigma_8), \tag{72}$$

still finding a 3.5σ deviation from the GR value of γ. This shows that the current evidence for a non-standard growth index is not driven by $Planck$'s preference for a high CMB lensing amplitude or by DESI BAO data. The precision on this result is driven strongly by the $f\sigma_8$ data. We discuss in more detail how this $f\sigma_8$ dataset compares with ΛCDM in §8.1. Any preference for this model appears to be largely driven by the $f\sigma_8$ data (in fact, by just two of these data points) rather than the ACT data or other CMB data, as discussed further in §8.1.

8. CONSISTENCY WITH LOW-REDSHIFT DATA AND IMPACT ON COSMOLOGICAL CONCORDANCE

8.1. ΛCDM *consistency with low-redshift observations*

Given our findings that no model is significantly preferred over ΛCDM, we confirm the consistency of our baseline ΛCDM model (described in L25) with the main low-redshift datasets used here in combination with P-ACT. The agreement between the predictions of the best-fit P-ACT ΛCDM model and direct measurements of the CMB lensing power spectrum, BAO distances, and SNIa distances provides a powerful consistency test of the cosmological model and justifies our joint inclusion of these datasets in ΛCDM and extended model fits.

In Fig. 40, we show predictions for the two main datasets we combine with: ACT DR6+$Planck$ NPIPE CMB lensing and DESI BAO. We find that the P-ACT ΛCDM best-fit model predicts these observations well, and slightly improves the agreement with the DESI data, compared to that seen for the ΛCDM model determined by $Planck$ alone. The same figure also shows the combined P-ACT-LB ΛCDM fit to all datasets, including residuals and the probability to exceed (PTE) for CMB lensing and BAO.[40] We find here and in L25 that the jointly-derived ΛCDM model is a good fit to all datasets. The residuals and best-fit PTE for $Planck$ and ACT primary CMB power spectra are discussed in L25.

Figure 41 shows the equivalent comparison for the Pantheon+ SNIa compilation. We show the usual Hubble diagram of the distance modulus (corrected apparent magnitude) of all SNIa in the compilation as a function of redshift, and compare it with ΛCDM predictions from the CMB and the joint best-fit model. Differently from Brout et al. (2022), we do not normalize the distance modulus using the SH0ES calibration. Instead, we separately obtain and correct for the absolute magnitude calibration from the Planck and P-ACT cosmology. The fit of the joint P-ACT-S dataset marginalizes over this calibration while sampling the cosmological parameters. We find that all ΛCDM solutions are in good agreement with the whole sample, recovering maximum-likelihood values similar to those reported in the Pantheon+ public chains.

Figure 42 shows the data used in the $f\sigma_8$ likelihood from §7.4, compared with the theoretical predictions in

---

[40] The three models give very similar PTEs for CMB lensing — 34.7%, 35.3%, 35.3% for $Planck$, P-ACT, and P-ACT-LB, respectively — which round to the same number when reporting only two significant figures.
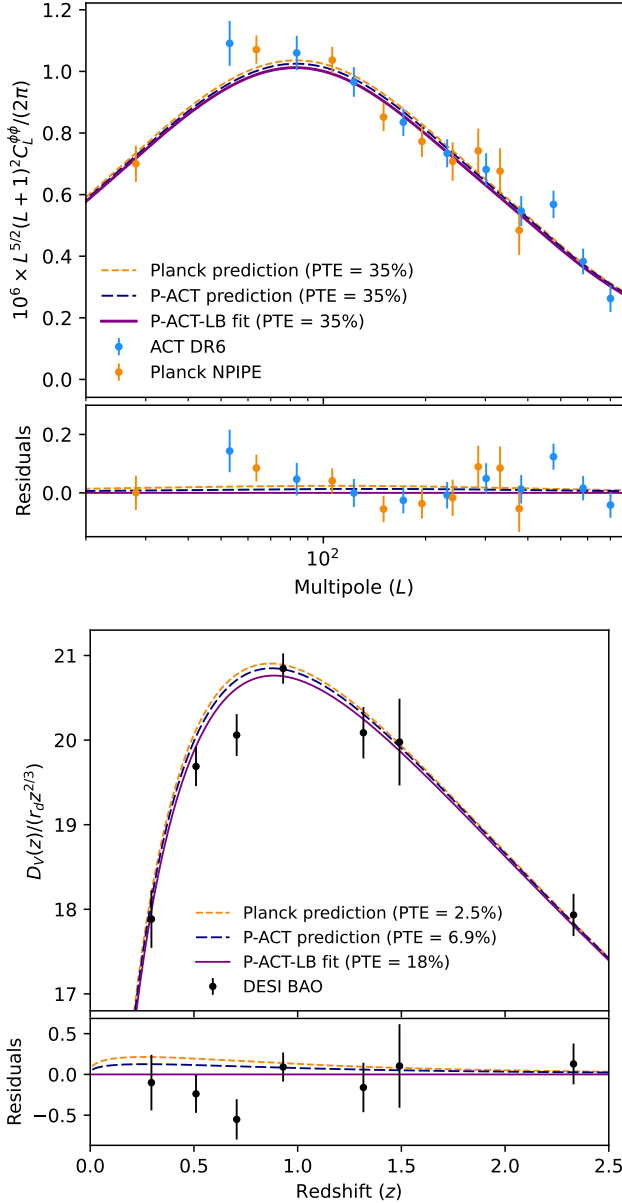
Figure 40. The ACT DR6 and *Planck* NPIPE CMB lensing power spectra (top panel) and the DESI BAO distance-redshift relation (bottom panel) are compared to ΛCDM predictions from primary CMB anisotropy data (*Planck* in orange and P-ACT in navy). The joint P-ACT-LB ΛCDM best-fit model is shown in purple. For CMB lensing, we show only the bandpowers used in the baseline likelihood described in §2.2. The DESI dataset is described in §2.3 and includes twelve total data points; of these twelve points, five pairs of $D_H(z)/r_d$ and $D_M(z)/r_d$ are combined into five different $D_V(z)/r_d$ measurements leading to a total of seven data points in this figure. The PTEs are calculated approximating the number of degrees of freedom to be equal to the number of data points and without propagating uncertainties in theory predictions.
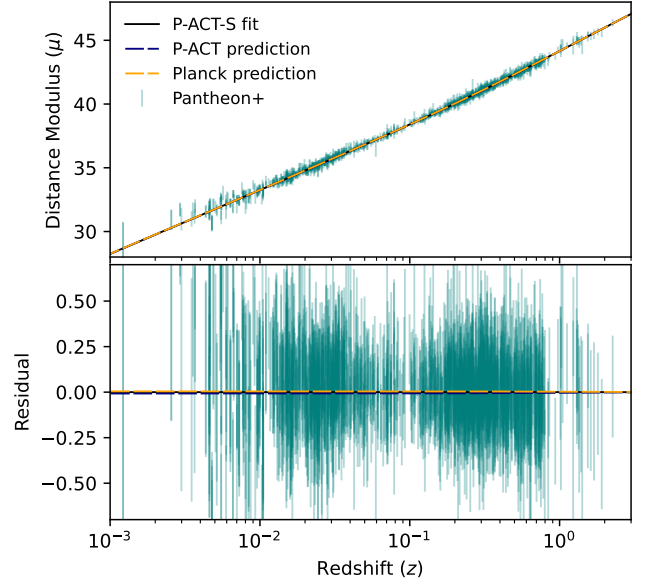
Figure 41. The SNIa Hubble diagram, showing the distance modulus μ as a function of redshift for the Pantheon+ compilation. The full SNIa sample is compared with the CMB anisotropy best-fit ΛCDM model predictions (from either *Planck* or P-ACT), and with the joint P-ACT CMB plus SNIa ΛCDM best-fit (P-ACT-S in black). The distance modulus has been calibrated relative to each ΛCDM best-fit cosmology (rather than using SH0ES, as done in Brout et al. 2022).

ΛCDM for $f\sigma_8(z)$ from the 68% CL constraints for P-ACT and W-ACT (L25). It appears that the hint of deviation from ΛCDM found in §7.4 is driven by low-z points in the $f\sigma_8$ dataset that have small error bars and lie below the CMB expectation for $f\sigma_8(z)$. To assess the difference between the CMB-predicted $f\sigma_8(z)$ and the data points from RSD and peculiar velocity surveys, we compute the χ^2 between them, finding $\chi^2 = 28.0$ with respect to the P-ACT prediction and $\chi^2 = 37.3$ with respect to the W-ACT prediction, both for 20 degrees of freedom, indicating some discordance (note, however, that these χ^2 values do not propagate the theoretical uncertainty on the CMB predictions). These χ^2 values decrease significantly if we omit two of the low-z peculiar velocity data points that have the lowest $f\sigma_8$ values. These points are at redshifts $z = 0.025$ (from Turner et al. 2022, with $f\sigma_8 = 0.357 \pm 0.071$) and $z = 0.035$ (from Said et al. 2020 with $f\sigma_8 = 0.338 \pm 0.027$). Omitting these points, we find $\chi^2 = 14.4$ for the P-ACT prediction and $\chi^2 = 19.1$ for W-ACT, both for 18 degrees of freedom, illustrating no tension. Because of the significant χ^2 reduction that results from removing the lowest two redshift points, we conclude that deviations from ΛCDM when including $f\sigma_8$ data in §7.4 are largely driven by those points. In theory, one could redo
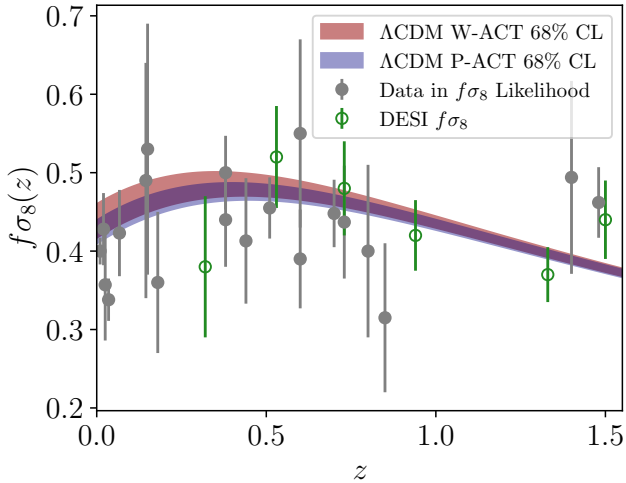
Figure 42. Measurements of $f\sigma_8$ used in our likelihood analysis of the modified gravity model (§7.4) with 1σ error bars (gray). The navy band shows the theoretically-predicted $f\sigma_8(z)$ with the 68% confidence interval for the best-fit ΛCDM cosmology to P-ACT, with the brown band representing the same for W-ACT. We also show $f\sigma_8$ measurements from DESI (DESI Collaboration 2024b) in green, but note that these are not used in our $f\sigma_8$ likelihood analysis and are only shown for comparison.

the analysis omitting those points from the likelihood. However, we do not perform this exercise here since it is not the ACT DR6 data driving these deviations.

Figure 42 also shows recent $f\sigma_8$ measurements from DESI (DESI Collaboration 2024b), though these points are not used in our joint likelihood analysis. Assuming a diagonal covariance matrix, we find that the DESI measurements have $\chi^2 = 4.0$ with respect to the P-ACT ΛCDM prediction and $\chi^2 = 4.2$ with respect to the W-ACT ΛCDM prediction, both for 6 degrees of freedom. Thus, the DESI RSD data are in good agreement with ΛCDM, further suggesting that the two outlying $f\sigma_8$ points at very low-z are not indicative of new physics.

8.2. Cosmological concordance

Many of the models studied in this paper impact the value of the Hubble constant inferred from the primary CMB power spectra, and the precision of the H_0 measurement changes because of parameter degeneracies in these scenarios. In some cases, such as in models with variations in the particle physics content and/or particle interactions, the degeneracies are due to changes in the ingredients of the universe affecting the expansion history at early times. In other cases, for example for the early dark energy model, the physics prior to or at recombination is changed significantly to reduce the sound horizon and this increases the Hubble constant at the expense of additional degrees of freedom

in the cosmological model correlating with H_0. While no robust detection of any of these extended models has been made in previous CMB or LSS data, some of these models have previously had non-negligible success in shifting the CMB-derived H_0 value toward the local distance ladder estimate from SH0ES. In this work, we have shown that this is generally no longer the case when including the new ACT data. ACT DR6 contributes to limiting the allowed region of parameter space to $66.1 < H_0 < 71.0$ km/s/Mpc within all of the models studied here. This range is calculated as the minimum and maximum value at 68% CL of all the P-ACT-LB and P-ACT-LBS results (whichever yields higher precision) from all models explored in this work; the neutrino self-interaction result from §6.1.2 sets the lower end of the allowed range and the early dark energy result from §5.1 sets the upper end. This range of values is in agreement with the CCHP measurement (Freedman et al. 2024), but lies below the latest SH0ES measurement (Breuval et al. 2024).

These results are summarized in Fig. 43. Figure 44 provides more details on the full suite of H_0 constraints for the three classes of models that have a non-negligible impact on H_0. Figure 45 breaks this result further down into the specific behavior of H_0 versus key model parameters in many extended models of interest, and shows that both the CMB-only dataset, P-ACT, and its combination with CMB lensing and BAO, P-ACT-LB, are inconsistent with the SH0ES estimate. Because of correlations with the inferred value of the total matter density Ω_m,[41] BAO data play an important role in determining the central value of H_0 in many extended models. Notably, as shown in many of the analyses in §5–§7, using BOSS BAO instead of DESI data reduces the central value of H_0 by 1–1.5 km/s/Mpc — hence moving constraints in the opposite direction of SH0ES — while only slightly increasing the error bars. Upcoming DESI data will be instrumental in further clarifying this situation.

From a more model-independent perspective, the consistency of the inferred physical matter density $\Omega_m h^2$ from *Planck* and ACT (as well as their combination; L25) within ΛCDM provides a strong indication that the ΛCDM model accurately describes physics just prior to recombination. As noted in Knox & Millea (2020), the shape of the radiation-driving envelope in the CMB power spectra is directly tied to the physics operat-

---

[41] Note that the primary CMB most directly constrains a degenerate combination of Ω_m and H_0, roughly $\Omega_m h^3$, with the exact value of the exponent depending on the range of angular scales measured, due to the different physical effects at play (e.g., Percival et al. 2002; Kable et al. 2019).
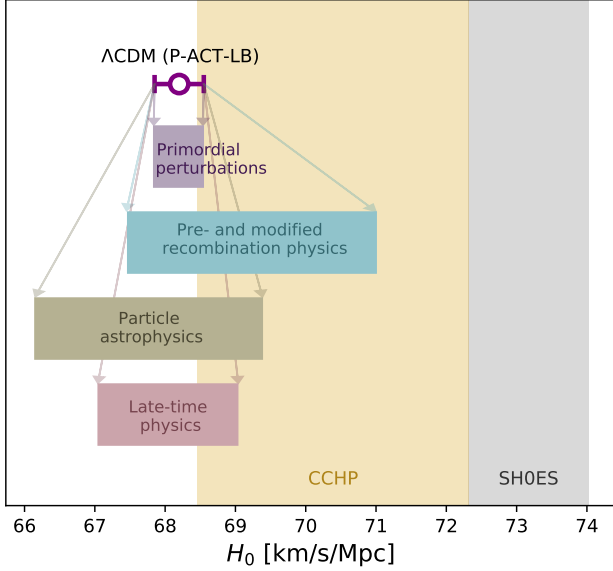
Figure 43. Inferred measurements of the Hubble constant across classes of models from P-ACT primary CMB combined with low-redshift data. Each box captures the range of H_0 allowed by all models explored in this paper within that class (§4-§7) — drawing from the 68% limits obtained with the most stringent data combination for that model, P-ACT-LB or P-ACT-LBS depending on the model (see also Fig. 44) — and marks shifts and broadening with respect to the 68% CL estimate in ΛCDM from P-ACT-LB (purple bar, L25). All estimates are statistically consistent with the CCHP measurement (68% CL from Freedman et al. 2024, gold band), but no class of extensions fully meets the bounds from SH0ES (68% CL from Breuval et al. 2024, gray band). See also Verde et al. 2024 for additional direct H_0 measurements.

ing around matter-radiation equality. If new physics were present at this epoch, a generic expectation is that ΛCDM-based inferences of $\Omega_m h^2$ should exhibit deviations when inferred on different angular scale ranges, due to different scales probing $H(z)$ at different times via radiation driving. We see no such evidence of such deviations in $\Omega_m h^2$ (L25), thus providing a strong validation of the physics of ΛCDM in this important redshift range.

We also find that models that alter the growth of structure are not preferred by our data. In particular, we do not find evidence in any extended model for a significant shift in the CMB-inferred S_8 value toward lower late-universe estimates, for example from cosmic shear surveys, as summarized in Fig. 46. Our results generally lie on the upper end of the limits from DES+KiDS (Dark Energy Survey and Kilo-Degree Survey Collaboration 2023), although it is important to note that the S_8 value in ΛCDM is already consistent between P-ACT-LB and this result. Also in this case the matter density
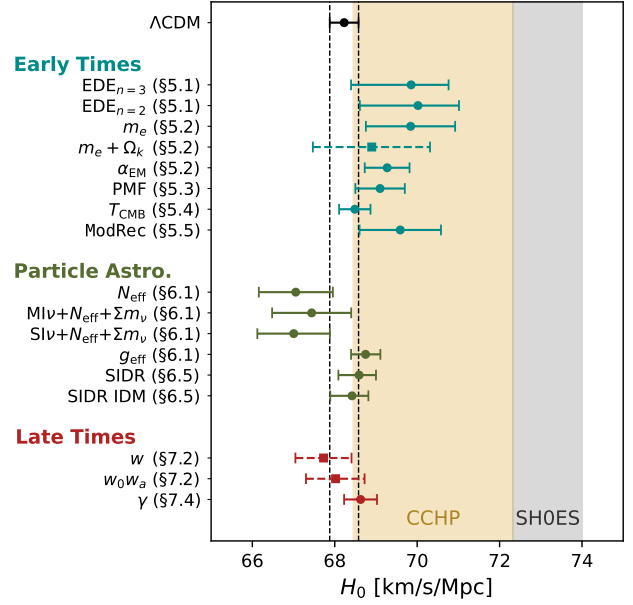
Figure 44. The three classes of models shown in Fig. 43 that have an impact on the inferred value of H_0 — changes in early-time physics before or at recombination (teal), new particle astrophysics (olive green), and new physics impacting the late-time expansion of the universe (dark red) — are broken down here into the constraints for specific models within each class. Solid (dashed) bars are constraints at 68% confidence derived from P-ACT-LB (P-ACT-LBS).

inferred via DESI BAO will contribute to the location of the maximum-likelihood point. For all models tested, using BOSS instead of DESI BAO data yields qualitatively similar conclusions. In addition, it is important to note that the inference of S_8 itself from galaxy weak lensing or other late-time data will generally change in the presence of the new physics shown in these models (e.g., non-GR values of γ or non-zero $\Gamma_{\rm DMDE}$), and thus one should take the comparison shown here with a grain of salt. For a high-precision comparison, constraints from late-time data should be self-consistently derived in these extended models, which we leave to future, dedicated analyses.

9. SUMMARY

In this paper, we have used a state-of-the-art CMB primary anisotropy dataset built from new ACT DR6 power spectra combined with large-scale data from the *Planck* satellite to set constraints on a large suite of extended cosmological models, both testing foundational assumptions made in the standard ΛCDM model and constraining more complex scenarios. We show that the new ACT DR6 data have reached a level of precision competitive with that of *Planck* for the primary CMB contribution to the constraints, and because of the
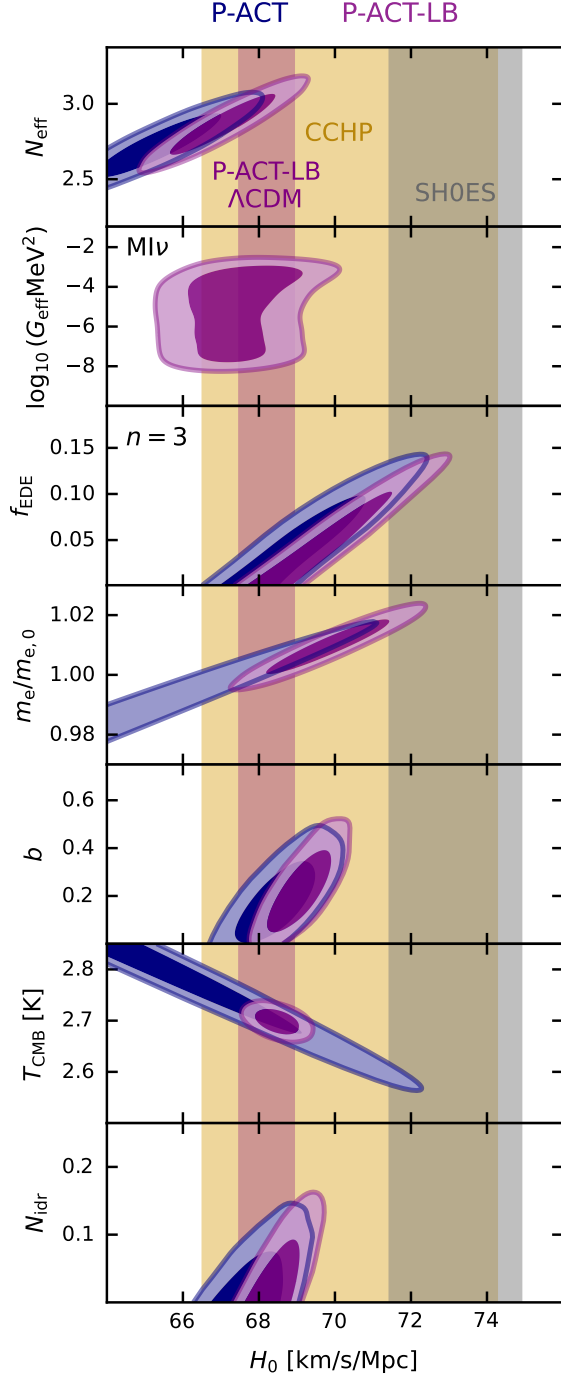
Figure 45. Constraints at 68% and 95% confidence on H_0 in select extended models from P-ACT (navy) and P-ACT-LB (purple), with the vertical bands indicating the 2σ limits for the latter data combination within ΛCDM. Degeneracies with extended-model parameters do not move the P-ACT or P-ACT-LB limits into agreement with the SH0ES constraints (2σ region from Breuval et al. 2024 shown as a gray band), but the constraints are in agreement with the CCHP measurement (2σ region from Freedman et al. 2024 shown as a gold band). Note that the MIν model shown in the second panel also includes varying $N_{\rm eff}$ and $\sum m_\nu$.
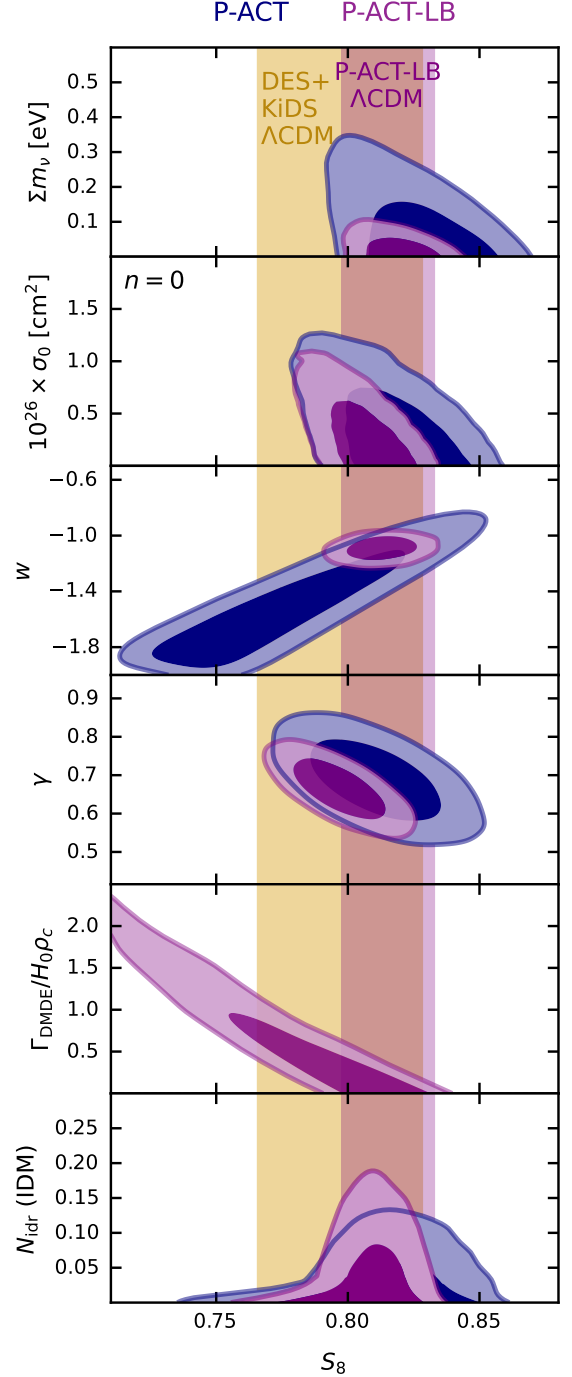
Figure 46. Constraints at 68% and 95% confidence on S_8 in select extended models from P-ACT (navy) and P-ACT-LB (purple) compared to the DES-Y3+KiDS cosmic shear limit (2σ region from the ΛCDM case with fixed neutrino mass from Dark Energy Survey and Kilo-Degree Survey Collaboration 2023 shown as a gold band). The P-ACT-LB ΛCDM constraint (2σ purple vertical band) is already in statistical agreement with DES-Y3+KiDS (see L25). Degeneracies with extended-model parameters do not generally move the P-ACT-LB central values to even lower S_8 values at the center of the DES-Y3+KiDS posterior.

complementarity of the two datasets — particularly at $\ell > 2000$ in TT and on essentially all scales measured by ACT in TE and EE — their joint analysis yields significant gains over the sensitivity of *Planck* alone. We further include ACT and *Planck* CMB lensing data, BAO data from DESI and SNIa from Pantheon+ to obtain the tightest limits to date on many fundamental physics parameters and cosmological models. To validate the results, we also explore combinations replacing *Planck* with *WMAP* large-scale CMB data, and DESI with BAO data from BOSS.

Key takeaways from this work include:

- We test predictions for the early-universe inflationary epoch, verifying the near-scale-invariance and adiabaticity of the primordial scalar perturbations, and restricting the parameter space for inflation models;

- We tightly bound the presence of early dark energy, or primordial magnetic fields that would impact the pre-recombination period, as well as variations in fundamental constants or in the monopole temperature of the CMB or the standard recombination history;

- We measure the properties of neutrinos and find no evidence for new light, relativistic species that are free-streaming, no evidence for non-zero neutrino masses, and no evidence for neutrino self-interactions. We also set limits on primordial helium and deuterium abundances that are consistent with standard BBN predictions and with astrophysical measurements;

- Dark matter is consistent with the standard collisionless CDM assumption, with no evidence for annihilation or interactions with baryons. We also limit the contribution to DM from ultralight axion-like particles to be no more than 5% at axion masses of 10^{-26} eV;

- We find no evidence for interactions in the dark sector, either within a single dark radiation component, between dark radiation and dark matter components, or between dark matter and dark energy;

- Dark energy and late-time gravity generally behave as expected in the standard model ($w = -1$ and $\gamma = 0.55$), although we find a moderate hint for time-evolving dark energy with P-ACT-LBS, consistent with (and driven by the BAO and SNIa data from) DESI Collaboration (2025b). Upcoming BAO and SNIa data are expected to clarify the robustness of this hint.

Assessing the preference for each extended model over ΛCDM via the marginalized posterior for the extended-model parameter (in the case of 1D extensions) or via comparison of the MAP model to that in ΛCDM (in the case of multi-parameter extensions), we find that no extended model is preferred over ΛCDM. This conclusion includes a wide range of extended models constructed with the aim of increasing the value of the Hubble constant or decreasing the amplitude of density fluctuations inferred from the primary CMB. With these results providing stringent tests in new observational regimes, the footing of the standard model of cosmology is further solidified.

This work paves the way for further, higher-precision tests of the cosmological model in the coming decade with even more sensitive CMB polarization data, including that expected from the Simons Observatory (Simons Observatory Collaboration 2019; Abitbol et al. 2025), CMB-S4 (CMB-S4 Collaboration 2016; Abazajian et al. 2019), LiteBIRD (LiteBIRD Collaboration et al. 2023), and other experiments. The noise levels of these surveys will push nearly an order of magnitude below those of ACT DR6 over the next 10-15 years, enabling precise searches for new physics, including not only the models studied in this work, but also new scenarios yet to be constructed.

REFERENCES

Abazajian, K., et al. 2019, arXiv:1907.04473, arXiv e-prints, arXiv:1907.04473, CMB-S4 Science Case, Reference Design, and Project Plan

Abazajian, K. N., et al. 2012, arXiv:1204.5379, arXiv e-prints, arXiv:1204.5379, Light Sterile Neutrinos: A White Paper

—. 2015, arXiv:1309.5383, Astroparticle Physics, 63, 66, Neutrino physics from the cosmic microwave background and large scale structure

Abellán, G. F., Chacko, Z., Dev, A., Du, P., Poulin, V., & Tsai, Y. 2022, arXiv:2112.13862, Journal of High Energy Physics, 2022, 76, Improved cosmological constraints on the neutrino mass and lifetime

Abitbol, M., et al. 2025, arXiv:2503.00636, arXiv e-prints, arXiv:2503.00636, The Simons Observatory: Science Goals and Forecasts for the Enhanced Large Aperture Telescope

Abolfathi, B., et al. 2018, arXiv:1707.09322, ApJS, 235, 42, The Fourteenth Data Release of the Sloan Digital Sky Survey: First Spectroscopic Data from the Extended Baryon Oscillation Spectroscopic Survey and from the Second Phase of the Apache Point Observatory Galactic Evolution Experiment

Ade, P. A. R., et al. 2021, arXiv:2110.00483, Phys. Rev. Lett., 127, 151301, Improved Constraints on Primordial Gravitational Waves using Planck, WMAP, and BICEP/Keck Observations through the 2018 Observing Season

Agrawal, P., Cyr-Racine, F.-Y., Pinner, D., & Randall, L. 2023, arXiv:1904.01016, Phys. Dark Univ., 42, 101347, Rock 'n' roll solutions to the Hubble tension

Aich, M., Hazra, D. K., Sriramkumar, L., & Souradeep, T. 2013, arXiv:1106.2798, Phys. Rev. D, 87, 083526, Oscillations in the inflaton potential: Complete numerical treatment and comparison with the recent and forthcoming CMB datasets

Aiola, S., et al. 2020, arXiv:2007.07288, J. Cosmology Astropart. Phys., 2020, 047, The Atacama Cosmology Telescope: DR4 maps and cosmological parameters

Akerib, D. S., et al. 2022, arXiv:2203.08084, Snowmass2021 Cosmic Frontier Dark Matter Direct Detection to the Neutrino Fog

Akita, K. & Yamaguchi, M. 2020, arXiv:2005.07047, J. Cosmology Astropart. Phys., 2020, 012, A precision calculation of relic neutrino decoupling

Alam, S., Ho, S., & Silvestri, A. 2016, arXiv:1509.05034, Mon. Not. Roy. Astron. Soc., 456, 3743, Testing deviations from ΛCDM with growth rate measurements from six large-scale structure surveys at $z = 0.06$–1

Alam, S., et al. 2017, arXiv:1607.03155, MNRAS, 470, 2617, The clustering of galaxies in the completed SDSS-III Baryon Oscillation Spectroscopic Survey: cosmological analysis of the DR12 galaxy sample

—. 2021, arXiv:2007.08991, Phys. Rev. D, 103, 083533, Completed SDSS-IV extended Baryon Oscillation Spectroscopic Survey: Cosmological implications from two decades of spectroscopic surveys at the Apache Point Observatory

Albrecht, A. & Steinhardt, P. J. 1982, Phys. Rev. Lett., 48, 1220, Cosmology for Grand Unified Theories with Radiatively Induced Symmetry Breaking, https://link.aps.org/doi/10.1103/PhysRevLett.48.1220

Ali-Haïmoud, Y. & Hirata, C. M. 2011, arXiv:1011.3758, Phys. Rev. D, 83, 043513, HyRec: A fast and highly accurate primordial hydrogen and helium recombination code

Allali, I. J., Notari, A., & Rompineve, F. 2024, arXiv:2404.15220, arXiv e-prints, arXiv:2404.15220, Dark Radiation with Baryon Acoustic Oscillations from DESI 2024 and the H_0 tension

Aloni, D., Berlin, A., Joseph, M., Schmaltz, M., & Weiner, N. 2022, arXiv:2111.00014, Phys. Rev. D, 105, 123516, A Step in understanding the Hubble tension

Alvey, J., Escudero, M., & Sabti, N. 2022a, arXiv:2111.12726, J. Cosmology Astropart. Phys., 2022, 037, What can CMB observations tell us about the neutrino distribution function?

Alvey, J., Escudero, M., Sabti, N., & Schwetz, T. 2022b, arXiv:2111.14870, Phys. Rev. D, 105, 063501, Cosmic neutrino background detection in large-neutrino-mass cosmologies

Amendola, L. & Barbieri, R. 2006, hep-ph/0509257, Physics Letters B, 642, 192, Dark matter from an ultra-light pseudo-Goldsone-boson

Amon, A., et al. 2022, arXiv:2105.13543, Phys. Rev. D, 105, 023514, Dark Energy Survey Year 3 results: Cosmology from cosmic shear and robustness to data calibration

An, R., Gluscevic, V., Calabrese, E., & Hill, J. C. 2022, arXiv:2202.03515, J. Cosmology Astropart. Phys., 2022, 002, What does cosmology tell us about the mass of thermal-relic dark matter?

Andrade, U., Anbajagane, D., von Marttens, R., Huterer, D., & Alcaniz, J. 2021, arXiv:2107.07538, JCAP, 11, 014, A test of the standard cosmological model with geometry and growth

Archidiacono, M. & Hannestad, S. 2014, arXiv:1311.3873, JCAP, 07, 046, Updated constraints on non-standard neutrino interactions from Planck

58

Archidiacono, M., Hooper, D. C., Murgia, R., Bohr, S., Lesgourgues, J., & Viel, M. 2019, arXiv:1907.01496, J. Cosmology Astropart. Phys., 2019, 055, Constraining Dark Matter-Dark Radiation interactions with CMB, BAO, and Lyman-α

Arvanitaki, A., Dimopoulos, S., Dubovsky, S., Kaloper, N., & March-Russell, J. 2010, arXiv:0905.4720, Phys. Rev. D, 81, 123530, String Axiverse

Asgari, M., et al. 2021, arXiv:2007.15633, A&A, 645, A104, KiDS-1000 cosmology: Cosmic shear constraints and comparison between two point statistics

Atkins, Z., et al. 2023, arXiv:2303.04180, J. Cosmology Astropart. Phys., 2023, 073, The Atacama Cosmology Telescope: map-based noise simulations for DR6

—. 2024, arXiv:2412.07068, arXiv e-prints, arXiv:2412.07068, The Atacama Cosmology Telescope: Semi-Analytic Covariance Matrices for the DR6 CMB Power Spectra, https://ui.adsabs.harvard.edu/abs/2024arXiv241207068A

Audren, B., Lesgourgues, J., Benabed, K., & Prunet, S. 2013, arXiv:1210.7183, J. Cosmology Astropart. Phys., 2013, 001, Conservative constraints on early cosmology with MONTE PYTHON

Avelino, P. P., Martins, C. J. A. P., Rocha, G., & Viana, P. 2000, astro-ph/0008446, Phys. Rev. D, 62, 123508, Looking for a varying α in the cosmic microwave background

Avelino, P. P., et al. 2001, astro-ph/0102144, Phys. Rev. D, 64, 103505, Early-universe constraints on a time-varying fine structure constant

Aver, E., Berg, D. A., Hirschauer, A. S., Olive, K. A., Pogge, R. W., Rogers, N. S. J., Salzer, J. J., & Skillman, E. D. 2022, arXiv:2109.00178, MNRAS, 510, 373, A comprehensive chemical abundance analysis of the extremely metal poor Leoncino Dwarf galaxy (AGC 198691)

Aver, E., Berg, D. A., Olive, K. A., Pogge, R. W., Salzer, J. J., & Skillman, E. D. 2021, arXiv:2010.04180, J. Cosmology Astropart. Phys., 2021, 027, Improving helium abundance determinations with Leo P as a case study

Axenides, M., Brandenberger, R. H., & Turner, M. S. 1983, Phys. Lett. B, 126, 178, Development of Axion Perturbations in an Axion Dominated Universe

Balashev, S. A., Zavarygin, E. O., Ivanchik, A. V., Telikova, K. N., & Varshalovich, D. A. 2016, arXiv:1511.01797, MNRAS, 458, 2188, The primordial deuterium abundance: subDLA system at $z_{abs} = 2.437$ towards the QSO J 1444+2919

Balkenhol, L. et al. 2021, arXiv:2103.13618, Phys. Rev. D, 104, 083509, Constraints on ΛCDM extensions from the SPT-3G 2018 EE and TE power spectra

Balkenhol, L., et al. 2023, arXiv:2212.05642, Phys. Rev. D, 108, 023510, Measurement of the CMB temperature power spectrum and constraints on cosmology from the SPT-3G 2018 TT, TE, and EE dataset

Barbieri, N., Brinckmann, T., Gariazzo, S., Lattanzi, M., Pastor, S., & Pisanti, O. 2025, arXiv:2501.01369, Current constraints on cosmological scenarios with very low reheating temperatures

Barenboim, G., Chen, J. Z., Hannestad, S., Oldengott, I. M., Tram, T., & Wong, Y. Y. Y. 2021, arXiv:2011.01502, J. Cosmology Astropart. Phys., 2021, 087, Invisible neutrino decay in precision cosmology

Barenboim, G., Denton, P. B., & Oldengott, I. M. 2019, arXiv:1903.02036, Phys. Rev. D, 99, 083515, Constraints on inflation with an extended neutrino sector

Bartolo, N. & Liddle, A. R. 2002, astro-ph/0203076, Phys. Rev. D, 65, 121301, The Simplest curvaton model

Baryakhtar, M., Simon, O., & Weiner, Z. J. 2024, arXiv:2405.10358, Phys. Rev. D, 110, 083505, Cosmology with varying fundamental constants from hyperlight, coupled scalars

Bashinsky, S. & Seljak, U. 2004, astro-ph/0310198, Phys. Rev. D, 69, 083002, Signatures of relativistic neutrinos in CMB anisotropy and matter clustering

Basilakos, S. & Anagnostopoulos, F. K. 2020, arXiv:1903.10758, Eur. Phys. J. C, 80, 212, Growth index of matter perturbations in the light of Dark Energy Survey

Bassett, B. & Hlozek, R. 2010, in Dark Energy: Observational and Theoretical Approaches, ed. P. Ruiz-Lapuente, 246

Battaglieri, M., et al. 2017, arXiv:1707.04591, US Cosmic Visions: New Ideas in Dark Matter 2017: Community Report

Battye, R. A., Crittenden, R., & Weller, J. 2001, astro-ph/0008265, Phys. Rev. D, 63, 043505, Cosmic concordance and the fine structure constant

Baumann, D., Green, D., Meyers, J., & Wallisch, B. 2016a, arXiv:1508.06342, J. Cosmology Astropart. Phys., 2016, 007, Phases of new physics in the CMB

Baumann, D., Green, D., & Wallisch, B. 2016b, arXiv:1604.08614, Phys. Rev. Lett., 117, 171301, New Target for Cosmic Axion Searches

Bean, R., Dunkley, J., & Pierpaoli, E. 2006, astro-ph/0606685, Phys. Rev. D, 74, 063503, Constraining isocurvature initial conditions with WMAP 3-year data

Becker, N., Hooper, D. C., Kahlhoefer, F., Lesgourgues, J., & Schöneberg, N. 2021, Journal of Cosmology and Astroparticle Physics, 2021, 019, Cosmological constraints on multi-interacting dark matter, https://doi.org/10.1088%2F1475-7516%2F2021%2F02%2F019

Beltran, M., Garcia-Bellido, J., & Lesgourgues, J. 2007, hep-ph/0606107, Phys. Rev. D, 75, 103507, Isocurvature bounds on axions revisited

Bennett, C. L., et al. 2013, arXiv:1212.5225, ApJS, 208, 20, Nine-year Wilkinson Microwave Anisotropy Probe (WMAP) Observations: Final Maps and Results

Bennett, J. J., Buldgen, G., de Salas, P. F., Drewes, M., Gariazzo, S., Pastor, S., & Wong, Y. Y. Y. 2021, arXiv:2012.02726, J. Cosmology Astropart. Phys., 2021, 073, Towards a precision calculation of the effective number of neutrinos N_{eff} in the Standard Model. Part II. Neutrino decoupling in the presence of flavour oscillations and finite-temperature QED

Beringue, B., Surrao, K., Hill, J. C., et al. in prep

Bernal, J. L., Verde, L., & Cuesta, A. J. 2016, arXiv:1511.03049, JCAP, 02, 059, Parameter splitting in dark energy: is dark energy the same in the background and in the cosmic structures?

Beutler, F., et al. 2011, arXiv:1106.3366, MNRAS, 416, 3017, The 6dF Galaxy Survey: baryon acoustic oscillations and the local Hubble constant

—. 2012, arXiv:1204.4725, MNRAS, 423, 3430, The 6dF Galaxy Survey: z≈ 0 measurements of the growth rate and σ_8

Bianchini, F. & Fabbian, G. 2022, arXiv:2206.02762, Phys. Rev. D, 106, 063527, CMB spectral distortions revisited: A new take on μ distortions and primordial non-Gaussianities from FIRAS data

Bianchini, F., et al. 2020, arXiv:1910.07157, ApJ, 888, 119, Constraints on Cosmological Parameters from the 500 deg^2 SPTPOL Lensing Power Spectrum

Blake, C., et al. 2012, arXiv:1204.3674, MNRAS, 425, 405, The WiggleZ Dark Energy Survey: joint measurements of the expansion and growth history at z ¡ 1

Blake, C. et al. 2013, arXiv:1309.5556, Mon. Not. Roy. Astron. Soc., 436, 3089, Galaxy And Mass Assembly (GAMA): improved cosmic growth measurements using multiple tracers of large-scale structure

Blas, D., Lesgourgues, J., & Tram, T. 2011, arXiv:1104.2933, J. Cosmology Astropart. Phys., 2011, 034, The Cosmic Linear Anisotropy Solving System (CLASS). Part II: Approximation schemes

Blinov, N., Kelly, K. J., Krnjaic, G. Z., & McDermott, S. D. 2019, arXiv:1905.02727, Phys. Rev. Lett., 123, 191102, Constraining the Self-Interacting Neutrino Interpretation of the Hubble Tension

Blum, K., Nir, Y., & Shavit, M. 2018, arXiv:1802.08019, Phys. Lett. B, 785, 354, Neutrinoless double-beta decay with massive scalar emission

Boddy, K. K. & Gluscevic, V. 2018, Physical Review D, 98, First cosmological constraint on the effective theory of dark matter-proton interactions, https://doi.org/10.1103%2Fphysrevd.98.083510

Boddy, K. K., Gluscevic, V., Poulin, V., Kovetz, E. D., Kamionkowski, M., & Barkana, R. 2018, Phys. Rev. D, 98, 123506, Critical assessment of CMB limits on dark matter-baryon scattering: New treatment of the relative bulk velocity, https://link.aps.org/doi/10.1103/PhysRevD.98.123506

Boehm, C. & Schaeffer, R. 2005, Astronomy & Astrophysics, 438, 419, Constraints on Dark Matter interactions from structure formation: damping lengths, https://doi.org/10.1051%2F0004-6361%3A20042238

Bolliet, B., Spurio Mancini, A., Hill, J. C., Madhavacheril, M., Jense, H. T., Calabrese, E., & Dunkley, J. 2024, arXiv:2303.01591, MNRAS, 531, 1351, High-accuracy emulators for observables in ΛCDM, N_{eff}, Σm_ν, and w cosmologies

Borsanyi, S., et al. 2016, arXiv:1606.07494, arXiv e-prints, arXiv:1606.07494, Lattice QCD for Cosmology

Boruah, S. S., Hudson, M. J., & Lavaux, G. 2020, arXiv:1912.09383, Mon. Not. Roy. Astron. Soc., 498, 2703, Cosmic flows in the nearby Universe: new peculiar velocities from SNe and cosmological constraints

Breuval, L., et al. 2024, arXiv:2404.08038, Astrophys. J., 973, 30, Small Magellanic Cloud Cepheids Observed with the Hubble Space Telescope Provide a New Anchor for the SH0ES Distance Ladder

Bridle, S. L., Lewis, A. M., Weller, J., & Efstathiou, G. 2003, astro-ph/0302306, MNRAS, 342, L72, Reconstructing the primordial power spectrum

Brinch Holm, E., Nygaard, A., Dakin, J., Hannestad, S., & Tram, T. 2024, arXiv:2312.02972, MNRAS, 535, 3686, PROSPECT: a profile likelihood code for frequentist cosmological parameter inference

Brinckmann, T., Chang, J. H., & LoVerde, M. 2021, arXiv:2012.11830, Phys. Rev. D, 104, 063523, Self-interacting neutrinos, the Hubble parameter tension, and the cosmic microwave background

Brout, D., et al. 2022, arXiv:2202.04077, ApJ, 938, 110, The Pantheon+ Analysis: Cosmological Constraints

60

Brust, C., Kaplan, D. E., & Walters, M. T. 2013, arXiv:1303.5379, Journal of High Energy Physics, 2013, 58, New light species and the CMB

Bucher, M., Dunkley, J., Ferreira, P. G., Moodley, K., & Skordis, C. 2004, astro-ph/0401417, Phys. Rev. Lett., 93, 081301, Initial Conditions of the Universe: How Much Isocurvature is Allowed?

Bucher, M., Moodley, K., & Turok, N. 2000, astro-ph/9904231, Phys. Rev. D, 62, 083508, The General primordial cosmic perturbation

Buen-Abad, M. A., Chacko, Z., Kilic, C., Marques-Tavares, G., & Youn, T. 2023, arXiv:2208.05984, Journal of High Energy Physics, 2023, 12, Stepped partially acoustic dark matter, large scale structure, and the Hubble tension

Buen-Abad, M. A., Essig, R., McKeen, D., & Zhong, Y.-M. 2022, Physics Reports, 961, 1, Cosmological constraints on dark matter interactions with ordinary matter, https://doi.org/10.1016%2Fj.physrep.2022.02.006

Buen-Abad, M. A., Marques-Tavares, G., & Schmaltz, M. 2015, arXiv:1505.03542, Phys. Rev. D, 92, 023531, Non-Abelian dark matter and dark radiation

Buen-Abad, M. A., Schmaltz, M., Lesgourgues, J., & Brinckmann, T. 2018, arXiv:1708.09406, J. Cosmology Astropart. Phys., 2018, 008, Interacting dark sector and precision cosmology

Burns, A.-K., Tait, T. M. P., & Valli, M. 2024, arXiv:2307.07061, European Physical Journal C, 84, 86, PRyMordial: the first three minutes, within and beyond the standard model

Cadamuro, D. & Redondo, J. 2012, arXiv:1110.2895, JCAP, 02, 032, Cosmological bounds on pseudo Nambu-Goldstone bosons

Cai, H. & Guan, Y. 2022, arXiv:2111.14199, Phys. Rev. D, 105, 063536, Computing microwave background polarization power spectra from cosmic birefringence

Calabrese, E., Cooray, A., Martinelli, M., Melchiorri, A., Pagano, L., Slosar, A., & Smoot, G. F. 2009, arXiv:0908.1585, Phys. Rev. D, 80, 103516, CMB lensing constraints on dark energy and modified gravity scenarios

Calabrese, E., Slosar, A., Melchiorri, A., Smoot, G. F., & Zahn, O. 2008, arXiv:0803.2309, Phys. Rev. D, 77, 123531, Cosmic microwave weak lensing data as a test for the dark universe

Carron, J., Mirmelstein, M., & Lewis, A. 2022, arXiv:2206.07773, J. Cosmology Astropart. Phys., 2022, 039, CMB lensing from Planck PR4 maps

Chabanier, S., Millea, M., & Palanque-Delabrouille, N. 2019, arXiv:1905.08103, MNRAS, 489, 2247, Matter power spectrum: from Ly α forest to CMB scales

Chacko, Z., Dev, A., Du, P., Poulin, V., & Tsai, Y. 2020, arXiv:1909.05275, Journal of High Energy Physics, 2020, 20, Cosmological limits on the neutrino mass and lifetime

—. 2021, arXiv:2002.08401, Phys. Rev. D, 103, 043519, Determining the neutrino lifetime from cosmology

Chen, J. Z., Oldengott, I. M., Pierobon, G., & Wong, Y. Y. Y. 2022a, arXiv:2203.09075, Eur. Phys. J. C, 82, 640, Weaker yet again: mass spectrum-consistent cosmological constraints on the neutrino lifetime

Chen, S.-F., White, M., DeRose, J., & Kokron, N. 2022b, arXiv:2204.10392, JCAP, 07, 041, Cosmological analysis of three-dimensional BOSS galaxy clustering and Planck CMB lensing cross correlations via Lagrangian perturbation theory

Chevallier, M. & Polarski, D. 2001, gr-qc/0009008, International Journal of Modern Physics D, 10, 213, Accelerating Universes with Scaling Dark Matter

Chikashige, Y., Mohapatra, R. N., & Peccei, R. D. 1980, Phys. Rev. Lett., 45, 1926, Spontaneously Broken Lepton Number and Cosmological Constraints on the Neutrino Mass Spectrum

—. 1981, Phys. Lett. B, 98, 265, Are There Real Goldstone Bosons Associated with Broken Lepton Number?

Chluba, J. 2014, arXiv:1405.1277, MNRAS, 443, 1881, Tests of the CMB temperature-redshift relation, CMB spectral distortions and why adiabatic photon production is hard

Chluba, J. & Ali-Haïmoud, Y. 2016, arXiv:1510.03877, MNRAS, 456, 3494, COSMOSPEC: fast and detailed computation of the cosmological recombination radiation from hydrogen and helium

Chluba, J., Fung, J., & Switzer, E. R. 2012, arXiv:1110.0247, MNRAS, 423, 3227, Radiative transfer effects during primordial helium recombination

Chluba, J. & Sunyaev, R. A. 2012, arXiv:1109.6552, MNRAS, 419, 1294, The evolution of CMB spectral distortions in the early Universe

Chluba, J., Vasil, G. M., & Dursi, L. J. 2010, arXiv:1003.4928, MNRAS, 407, 599, Recombinations to the Rydberg states of hydrogen and their effect during the cosmological recombination epoch

Choi, S. K., et al. 2020, arXiv:2007.07289, J. Cosmology Astropart. Phys., 2020, 045, The Atacama Cosmology Telescope: a measurement of the Cosmic Microwave Background power spectra at 98 and 150 GHz

Chou, T. L., et al. 2025, arXiv:2501.06890, arXiv e-prints, arXiv:2501.06890, Measurements of the Temperature and E-mode Polarization of the Cosmic Microwave Background from the Full 500-square-degree SPTpol Dataset

CMB-S4 Collaboration. 2016, arXiv:1610.02743, arXiv e-prints, arXiv:1610.02743, CMB-S4 Science Book, First Edition

Cooke, R. J., Pettini, M., Jorgenson, R. A., Murphy, M. T., & Steidel, C. C. 2014, arXiv:1308.3240, ApJ, 781, 31, Precision Measures of the Primordial Abundance of Deuterium

Cooke, R. J., Pettini, M., Nollett, K. M., & Jorgenson, R. 2016, arXiv:1607.03900, ApJ, 830, 148, The Primordial Deuterium Abundance of the Most Metal-poor Damped Lyman-α System

Coulton, W., et al. 2024, arXiv:2307.01258, Phys. Rev. D, 109, 063530, Atacama Cosmology Telescope: High-resolution component-separated maps across one third of the sky

Cushman, P., et al. 2013, Snowmass CF1 Summary: WIMP Dark Matter Direct Detection, https://arxiv.org/abs/1310.8327

Cyr-Racine, F.-Y. & Sigurdson, K. 2014, arXiv:1306.1536, Phys. Rev. D, 90, 123533, Limits on Neutrino-Neutrino Scattering in the Early Universe

Cyr-Racine, F.-Y., Sigurdson, K., Zavala, J., Bringmann, T., Vogelsberger, M., & Pfrommer, C. 2016, arXiv:1512.05344, Phys. Rev. D, 93, 123527, ETHOS—an effective theory of structure formation: From dark particle physics to the matter distribution of the Universe

Dalal, R., et al. 2023, arXiv:2304.00701, Phys. Rev. D, 108, 123519, Hyper Suprime-Cam Year 3 results: Cosmology from cosmic shear power spectra

D'Amico, G., Senatore, L., Zhang, P., & Zheng, H. 2021, arXiv:2006.12420, JCAP, 05, 072, The Hubble Tension in Light of the Full-Shape Analysis of Large-Scale Structure Data

Dark Energy Survey and Kilo-Degree Survey Collaboration. 2023, arXiv:2305.17173, The Open Journal of Astrophysics, 6, 36, DES Y3 + KiDS-1000: Consistent cosmology combining cosmic shear surveys

Das, A. & Ghosh, S. 2021, arXiv:2011.12315, JCAP, 07, 038, Flavor-specific interaction favors strong neutrino self-coupling in the early universe

Das, S., et al. 2011, arXiv:1103.2124, Phys. Rev. Lett., 107, 021301, Detection of the Power Spectrum of Cosmic Microwave Background Lensing by the Atacama Cosmology Telescope

Dawson, K. S., et al. 2013, arXiv:1208.0022, AJ, 145, 10, The Baryon Oscillation Spectroscopic Survey of SDSS-III

De Bernardis, F., Pagano, L., & Melchiorri, A. 2008, Astropart. Phys., 30, 192, New constraints on the reheating temperature of the universe after WMAP-5

de Putter, R., Linder, E. V., & Mishra, A. 2014, arXiv:1401.7022, Phys. Rev. D, 89, 103502, Inflationary freedom and cosmological neutrino constraints

de Salas, P. F., Lattanzi, M., Mangano, G., Miele, G., Pastor, S., & Pisanti, O. 2015, arXiv:1511.00672, Phys. Rev. D, 92, 123534, Bounds on very low reheating scenarios after Planck

Dentler, M., Marsh, D. J. E., Hložek, R., Laguë, A., Rogers, K. K., & Grin, D. 2022, arXiv:2111.01199, MNRAS, 515, 5646, Fuzzy dark matter and the Dark Energy Survey Year 1 data

DES Collaboration. 2021, arXiv:2010.05924, Phys. Rev. D, 103, 023528, DES Y1 results: Splitting growth and geometry to test ΛCDM

—. 2022, arXiv:2105.13549, Phys. Rev. D, 105, 023520, Dark Energy Survey Year 3 results: Cosmological constraints from galaxy clustering and weak lensing

—. 2023, arXiv:2207.05766, Phys. Rev. D, 107, 083504, Dark Energy Survey Year 3 results: Constraints on extensions to ΛCDM with weak lensing and galaxy clustering

—. 2024, arXiv:2401.02929, ApJ, 973, L14, The Dark Energy Survey: Cosmology Results with $\sim$1500 New High-redshift Type Ia Supernovae Using the Full 5 yr Data Set

DESI Collaboration. 2024a, arXiv:2404.03000, arXiv e-prints, arXiv:2404.03000, DESI 2024 III: Baryon Acoustic Oscillations from Galaxies and Quasars

—. 2024b, arXiv:2411.12021, arXiv e-prints, arXiv:2411.12021, DESI 2024 V: Full-Shape Galaxy Clustering from Galaxies and Quasars

—. 2024c, arXiv:2411.12022, arXiv e-prints, arXiv:2411.12022, DESI 2024 VII: Cosmological Constraints from the Full-Shape Modeling of Clustering Measurements

—. 2025a, arXiv:2404.03001, J. Cosmology Astropart. Phys., 2025, 124, DESI 2024 IV: Baryon Acoustic Oscillations from the Lyman alpha forest

—. 2025b, arXiv:2404.03002, J. Cosmology Astropart. Phys., 2025, 021, DESI 2024 VI: cosmological constraints from the measurements of baryon acoustic oscillations

Dossett, J., Ishak, M., Moldenhauer, J., Gong, Y., Wang, A., & Gong, Y. 2010, arXiv:1004.3086, JCAP, 04, 022, Constraints on growth index parameters from current and future observations

62

Drewes, M., Georis, Y., Klasen, M., Wiggering, L. P., &
Wong, Y. Y. Y. 2024, arXiv:2402.18481, J. Cosmology
Astropart. Phys., 2024, 032, Towards a precision
calculation of N $_{eff}$ in the Standard Model. Part III.
Improved estimate of NLO contributions to the collision
integral

Duffy, L. D. & van Bibber, K. 2009, arXiv:0904.3346, New
J. Phys., 11, 105008, Axions as Dark Matter Particles

Duivenvoorden, A. et al. in prep

Dunkley, J., et al. 2011, arXiv:1009.0866, ApJ, 739, 52, The
Atacama Cosmology Telescope: Cosmological Parameters
from the 2008 Power Spectrum

Dvali, G. & Funcke, L. 2016, arXiv:1602.03191,
Phys. Rev. D, 93, 113002, Small neutrino masses from
gravitational θ -term

Dvorkin, C., Blum, K., & Kamionkowski, M. 2014, Phys.
Rev. D, 89, 023519, Constraining dark matter-baryon
scattering with linear cosmology,
https://link.aps.org/doi/10.1103/PhysRevD.89.023519

Dvorkin, C., et al. 2019, arXiv:1903.03689, BAAS, 51, 64,
Neutrino Mass from Cosmology: Probing Physics Beyond
the Standard Model

eBOSS Collaboration. 2018, arXiv:1705.06373, Mon. Not.
Roy. Astron. Soc., 473, 4773, The clustering of the
SDSS-IV extended Baryon Oscillation Spectroscopic
Survey DR14 quasar sample: first measurement of baryon
acoustic oscillations between redshift 0.8 and 2.2

—. 2021, arXiv:2007.08991, Phys. Rev. D, 103, 083533,
Completed SDSS-IV extended Baryon Oscillation
Spectroscopic Survey: Cosmological implications from
two decades of spectroscopic surveys at the Apache Point
Observatory

Efstathiou, G., Rosenberg, E., & Poulin, V. 2024,
arXiv:2311.00524, Phys. Rev. Lett., 132, 221002,
Improved Planck Constraints on Axionlike Early Dark
Energy as a Resolution of the Hubble Tension

Eisenstein, D. 2005, New Astronomy Reviews, 49, 360,
wide-Field Imaging from Space, Dark energy and cosmic
sound, https://www.sciencedirect.com/science/article/
pii/S1387647305000850

Eisenstein, D. & DESI Collaboration. 2015, in American
Astronomical Society Meeting Abstracts, Vol. 225,
American Astronomical Society Meeting Abstracts #225,
336.05

Eisenstein, D. J., et al. 2005, astro-ph/0501171, ApJ, 633,
560, Detection of the Baryon Acoustic Peak in the
Large-Scale Correlation Function of SDSS Luminous Red
Galaxies

Enqvist, K., Kurki-Suonio, H., & Valiviita, J. 2000,
astro-ph/0006429, Phys. Rev. D, 62, 103003, Limits on
isocurvature fluctuations from boomerang and MAXIMA

—. 2002, astro-ph/0108422, Phys. Rev. D, 65, 043002,
Open and closed CDM isocurvature models contrasted
with the CMB data

Escudero, H. G. & Abazajian, K. N. 2025,
arXiv:2412.05451, Phys. Rev. D, 111, 043520, Status of
neutrino cosmology: Standard ΛCDM, extensions, and
tensions

Essig, R., et al. 2013, arXiv:1311.0029, arXiv e-prints,
arXiv:1311.0029, Dark Sectors and New, Light,
Weakly-Coupled Particles

Fang, W., Hu, W., & Lewis, A. 2008, arXiv:0808.3125,
Phys. Rev. D, 78, 087303, Crossing the phantom divide
with parametrized post-Friedmann dark energy

Fernández, V., Terlevich, E., Díaz, A. I., & Terlevich, R.
2019, arXiv:1905.09215, MNRAS, 487, 3221, A Bayesian
direct method implementation to fit emission line
spectra: application to the primordial He abundance
determination

Fields, B. D. 2011, arXiv:1203.3551, Annual Review of
Nuclear and Particle Science, 61, 47, The Primordial
Lithium Problem

Finkbeiner, D. P., Galli, S., Lin, T., & Slatyer, T. R. 2012,
Physical Review D, 85, Searching for dark matter in the
CMB: A compact parametrization of energy injection
from new physics,
http://dx.doi.org/10.1103/PhysRevD.85.043522

Fixsen, D. J. 2009, arXiv:0911.1955, ApJ, 707, 916, The
Temperature of the Cosmic Microwave Background

Fixsen, D. J., Cheng, E. S., Gales, J. M., Mather, J. C.,
Shafer, R. A., & Wright, E. L. 1996, astro-ph/9605054,
ApJ, 473, 576, The Cosmic Microwave Background
Spectrum from the Full COBE FIRAS Data Set

Forastieri, F., Lattanzi, M., & Natoli, P. 2015,
arXiv:1504.04999, JCAP, 07, 014, Constraints on secret
neutrino interactions after Planck

—. 2019, arXiv:1904.07810, Phys. Rev. D, 100, 103526,
Cosmological constraints on neutrino self-interactions
with a light mediator

Freedman, W. L. & Madore, B. F. 2023, arXiv:2309.05618,
J. Cosmology Astropart. Phys., 2023, 050, Progress in
direct measurements of the Hubble constant

Freedman, W. L., Madore, B. F., Jang, I. S., Hoyt, T. J.,
Lee, A. J., & Owens, K. A. 2024, arXiv:2408.06153,
arXiv e-prints, arXiv:2408.06153, Status Report on the
Chicago-Carnegie Hubble Program (CCHP):
Measurement of the Hubble Constant Using the Hubble
and James Webb Space Telescope

Freedman, W. L., et al. 2020, arXiv:2002.01550, ApJ, 891, 57, Calibration of the Tip of the Red Giant Branch

Froustey, J., Pitrou, C., & Volpe, M. C. 2020, arXiv:2008.01074, J. Cosmology Astropart. Phys., 2020, 015, Neutrino decoupling including flavour oscillations and primordial nucleosynthesis

Fry, J. 1985, Physics Letters B, 158, 211, Dynamical measures of density in exotic cosmologies

Galli, S., Pogosian, L., Jedamzik, K., & Balkenhol, L. 2022, arXiv:2109.03816, Phys. Rev. D, 105, 023513, Consistency of Planck, ACT, and SPT constraints on magnetically assisted recombination and forecasts for future experiments

Garcia-Bellido, J. & Wands, D. 1996, astro-ph/9511029, Phys. Rev. D, 53, 5437, Metric perturbations in two field inflation

García-García, C., Zapatero, J. R., Alonso, D., Bellini, E., Ferreira, P. G., Mueller, E.-M., Nicola, A., & Ruiz-Lapuente, P. 2021, arXiv:2105.12108, JCAP, 10, 030, The growth of density perturbations in the last ∼10 billion years from tomographic large-scale structure data

Ge, F., et al. 2024, arXiv:2411.06000, arXiv e-prints, arXiv:2411.06000, Cosmology From CMB Lensing and Delensed EE Power Spectra Using 2019-2020 SPT-3G Polarization Data

Gerbino, M., et al. 2023, arXiv:2203.07377, Physics of the Dark Universe, 42, 101333, Synergy between cosmological and laboratory searches in neutrino physics

GERDA Collaboration. 2020, Phys. Rev. Lett., 125, 252502, Final Results of GERDA on the Search for Neutrinoless Double-β Decay, https://link.aps.org/doi/10.1103/PhysRevLett.125.252502

Giudice, G. F., Kolb, E. W., & Riotto, A. 2001, hep-ph/0005123, Phys. Rev. D, 64, 023508, Largest temperature of the radiation era and its cosmological implications

Gluscevic, V. & Boddy, K. K. 2018, Physical Review Letters, 121, Constraints on Scattering of keV–TeV Dark Matter with Protons in the Early Universe, https://doi.org/10.1103%2Fphysrevlett.121.081301

Gluscevic, V., et al. 2019, Cosmological Probes of Dark Matter Interactions: The Next Decade, https://arxiv.org/abs/1903.05140

Gratton, S. & Challinor, A. 2020, arXiv:1911.07754, MNRAS, 499, 3410, Understanding parameter differences between analyses employing nested data subsets

Green, D., Meerburg, P. D., & Meyers, J. 2019, arXiv:1804.01055, J. Cosmology Astropart. Phys., 2019, 025, Aspects of dark matter annihilation in cosmology

Green, D. & Meyers, J. 2024, arXiv:2407.07878, arXiv e-prints, arXiv:2407.07878, The Cosmological Preference for Negative Neutrino Mass

Grohs, E. & Fuller, G. M. 2022, in Handbook of Nuclear Physics, 127

Guo, Z.-K., Schwarz, D. J., & Zhang, Y.-Z. 2011, arXiv:1105.5916, J. Cosmology Astropart. Phys., 2011, 031, Reconstruction of the primordial power spectrum from CMB data

Guzzo, L. et al. 2008, arXiv:0802.1944, Nature, 451, 541, A test of the nature of cosmic acceleration using galaxy redshift distortions

Hadzhiyska, B. & Spergel, D. N. 2019, arXiv:1808.04083, Phys. Rev. D, 99, 043537, Measuring the Duration of Last Scattering

Hamilton, A. J. S. 1998, astro-ph/9708102, in Astrophysics and Space Science Library, Vol. 231, The Evolving Universe, ed. D. Hamilton, 185

Hannestad, S. 1999, astro-ph/9810102, Phys. Rev. D, 60, 023515, Possible constraints on the time variation of the fine structure constant from cosmic microwave background data

Harris, C. R., et al. 2020, arXiv:2006.10256, Nature, 585, 357, Array programming with NumPy

Hart, L. & Chluba, J. 2018, arXiv:1705.03925, MNRAS, 474, 1850, New constraints on time-dependent variations of fundamental constants using Planck data

—. 2020, arXiv:1912.03986, MNRAS, 493, 3255, Updated fundamental constant constraints from Planck 2018 data and possible relations to the Hubble tension

Hasegawa, T., Hiroshima, N., Kohri, K., Hansen, R. S. L., Tram, T., & Hannestad, S. 2019, arXiv:1908.10189, JCAP, 12, 012, MeV-scale reheating temperature and thermalization of oscillating neutrinos by radiative and hadronic decays of massive particles

Hazra, D. K., Shafieloo, A., Smoot, G. F., & Starobinsky, A. A. 2016, arXiv:1605.02106, J. Cosmology Astropart. Phys., 2016, 009, Primordial features and Planck polarization

He, A., Ivanov, M. M., An, R., Driskell, T., & Gluscevic, V. 2025, arXiv:2502.02636, Bounds on Velocity-Dependent Dark Matter-Baryon Scattering from Large-Scale Structure, https://arxiv.org/abs/2502.02636

He, A., Ivanov, M. M., An, R., & Gluscevic, V. 2023, arXiv:2301.08260, ApJ, 954, L8, S_8 Tension in the Context of Dark Matter-Baryon Scattering

Herold, L. & Ferreira, E. G. M. 2023, arXiv:2210.16296, Phys. Rev. D, 108, 043513, Resolving the Hubble tension with early dark energy

64

Herold, L., Ferreira, E. G. M., & Komatsu, E. 2022, arXiv:2112.12140, Astrophys. J. Lett., 929, L16, New Constraint on Early Dark Energy from Planck and BOSS Data Using the Profile Likelihood

Hertzberg, M. P., Tegmark, M., & Wilczek, F. 2008, arXiv:0807.1726, Phys. Rev. D, 78, 083507, Axion Cosmology and the Energy Scale of Inflation

Heymans, C., et al. 2021, arXiv:2007.15632, A&A, 646, A140, KiDS-1000 Cosmology: Multi-probe weak gravitational lensing and spectroscopic galaxy clustering constraints

Hill, J. C. & Bolliet, B. 2023, arXiv:2304.03750, arXiv e-prints, arXiv:2304.03750, Did the Universe Reheat After Recombination?

Hill, J. C., McDonough, E., Toomey, M. W., & Alexander, S. 2020, Physical Review D, 102, Early dark energy does not restore cosmological concordance

Hill, J. C., et al. 2022, arXiv:2109.04451, Phys. Rev. D, 105, 123536, Atacama Cosmology Telescope: Constraints on prerecombination early dark energy

Hinshaw, G., et al. 2013, arXiv:1212.5226, ApJS, 208, 19, Nine-year Wilkinson Microwave Anisotropy Probe (WMAP) Observations: Cosmological Parameter Results

Hložek, R., Marsh, D. J. E., & Grin, D. 2018, arXiv:1708.05681, MNRAS, 476, 3063, Using the full power of the cosmic microwave background to probe axion dark matter

Hložek, R., Marsh, D. J. E., Grin, D., Allison, R., Dunkley, J., & Calabrese, E. 2017, arXiv:1607.08208, Phys. Rev. D, 95, 123511, Future CMB tests of dark matter: Ultralight axions and massive neutrinos

Hlozek, R., Grin, D., Marsh, D. J. E., & Ferreira, P. G. 2015, arXiv:1410.2896, Phys. Rev. D, 91, 103512, A search for ultralight axions using precision cosmological data

Hlozek, R., et al. 2012, arXiv:1105.4887, ApJ, 749, 90, The Atacama Cosmology Telescope: A Measurement of the Primordial Power Spectrum

Hooper, D. C., Schöneberg, N., Murgia, R., Archidiacono, M., Lesgourgues, J., & Viel, M. 2022, Journal of Cosmology and Astroparticle Physics, 2022, 032, One likelihood to bind them all: Lyman-α constraints on non-standard dark matter, https://doi.org/10.1088%2F1475-7516%2F2022%2F10%2F032

Hou, Z., Keisler, R., Knox, L., Millea, M., & Reichardt, C. 2013, arXiv:1104.2333, Phys. Rev. D, 87, 083008, How massless neutrinos affect the cosmic microwave background damping tail

Howlett, C., Ross, A., Samushia, L., Percival, W., & Manera, M. 2015, arXiv:1409.3238, Mon. Not. Roy. Astron. Soc., 449, 848, The clustering of the SDSS main galaxy sample – II. Mock galaxy catalogues and a measurement of the growth of structure from redshift space distortions at $z = 0.15$

Hsyu, T., Cooke, R. J., Prochaska, J. X., & Bolte, M. 2020, arXiv:2005.12290, ApJ, 896, 77, The PHLEK Survey: A New Determination of the Primordial Helium Abundance

Hudson, M. J. & Turnbull, S. J. 2012, arXiv:1203.4814, ApJ, 751, L30, The Growth Rate of Cosmic Structure from Peculiar Velocities at Low and High Redshifts

Hui, L., Ostriker, J. P., Tremaine, S., & Witten, E. 2017, arXiv:1610.08297, Phys. Rev. D, 95, 043541, Ultralight scalars as cosmological dark matter

Hunt, P. & Sarkar, S. 2014, arXiv:1308.2317, J. Cosmology Astropart. Phys., 2014, 025, Reconstruction of the primordial power spectrum of curvature perturbations using multiple data sets

Hunter, J. D. 2007, Computing in Science & Engineering, 9, 90, Matplotlib: A 2D graphics environment

Huterer, D., Shafer, D., Scolnic, D., & Schmidt, F. 2017, arXiv:1611.09862, JCAP, 05, 015, Testing ΛCDM at the lowest redshifts with SN Ia and galaxy velocities

Ichikawa, K., Kawasaki, M., & Takahashi, F. 2005, astro-ph/0505395, Phys. Rev. D, 72, 043522, The Oscillation effects on thermalization of the neutrinos in the Universe with low reheating temperature

—. 2007, astro-ph/0611784, JCAP, 05, 007, Constraint on the effective number of neutrino species from the WMAP and SDSS LRG power spectra

Iliadis, C. & Coc, A. 2020, arXiv:2008.12200, ApJ, 901, 127, Thermonuclear Reaction Rates and Primordial Nucleosynthesis

Ivanov, M. M., Ali-Haïmoud, Y., & Lesgourgues, J. 2020a, arXiv:2005.10656, Phys. Rev. D, 102, 063515, H0 tension or T0 tension?

Ivanov, M. M., McDonough, E., Hill, J. C., Simonović, M., Toomey, M. W., Alexander, S., & Zaldarriaga, M. 2020b, arXiv:2006.11235, Phys. Rev. D, 102, 103502, Constraining Early Dark Energy with Large-Scale Structure

Jedamzik, K. & Abel, T. 2013, Journal of Cosmology and Astroparticle Physics, 2013, 050, Small-scale primordial magnetic fields and anisotropies in the cosmic microwave background radiation, https://dx.doi.org/10.1088/1475-7516/2013/10/050

Jedamzik, K., Abel, T., & Ali-Haimoud, Y. 2025, arXiv:2312.11448, JCAP, 03, 012, Cosmic recombination in the presence of primordial magnetic fields

Jedamzik, K. & Pogosian, L. 2020, arXiv:2004.09487, Phys. Rev. Lett., 125, 181302, Relieving the Hubble Tension with Primordial Magnetic Fields

—. 2023, arXiv:2307.05475, arXiv e-prints, arXiv:2307.05475, Primordial magnetic fields and the Hubble tension

Jedamzik, K., Pogosian, L., & Abel, T. 2025, arXiv:2503.09599, arXiv e-prints, arXiv:2503.09599, Hints of Primordial Magnetic Fields at Recombination and Implications for the Hubble Tension

Jedamzik, K. & Saveliev, A. 2019, arXiv:1804.06115, Phys. Rev. Lett., 123, 021301, Stringent Limit on Primordial Magnetic Fields from the Cosmic Microwave Background Radiation

Jense, H. T., Harrison, I., Calabrese, E., Spurio Mancini, A., Bolliet, B., Dunkley, J., & Hill, J. C. 2025, arXiv:2405.07903, RAS Techniques and Instruments, 4, rzaf002, A complete framework for cosmological emulation and inference with CosmoPower

Jeong, K. S. & Takahashi, F. 2013, arXiv:1305.6521, Physics Letters B, 725, 134, Self-interacting dark radiation

Johnson, A., Blake, C., Dossett, J., Koda, J., Parkinson, D., & Joudaki, S. 2016, arXiv:1504.06885, Mon. Not. Roy. Astron. Soc., 458, 2725, Searching for Modified Gravity: Scale and Redshift Dependent Constraints from Galaxy Peculiar Velocities

Joseph, M., Aloni, D., Schmaltz, M., Sivarajan, E. N., & Weiner, N. 2023, arXiv:2207.03500, Phys. Rev. D, 108, 023520, A Step in understanding the S_8 tension

Kable, J. A., Addison, G. E., & Bennett, C. L. 2019, arXiv:1809.03983, ApJ, 871, 77, Quantifying the CMB Degeneracy between the Matter Density and Hubble Constant in Current Experiments

Kachelriess, M., Tomas, R., & Valle, J. W. F. 2000, hep-ph/0001039, Phys. Rev. D, 62, 023004, Supernova bounds on Majoron emitting decays of light neutrinos

Kaiser, N. 1987, MNRAS, 227, 1, Clustering in real space and in redshift space

Kamionkowski, M. & Kovetz, E. D. 2016, arXiv:1510.06042, ARA&A, 54, 227, The Quest for B Modes from Inflationary Gravitational Waves

Kamionkowski, M. & Riess, A. G. 2023, arXiv:2211.04492, Ann. Rev. Nucl. Part. Sci., 73, 153, The Hubble Tension and Early Dark Energy

KamLAND-Zen Collaboration. 2024, arXiv:2406.11438, Search for Majorana Neutrinos with the Complete KamLAND-Zen Dataset

Kaplinghat, M., Scherrer, R. J., & Turner, M. S. 1999, astro-ph/9810133, Phys. Rev. D, 60, 023516, Constraining variations in the fine-structure constant with the cosmic microwave background

Kasuya, S. & Kawasaki, M. 2009, arXiv:0904.3800, Phys. Rev. D, 80, 023516, Axion isocurvature fluctuations with extremely blue spectrum

Kawasaki, M., Kohri, K., & Sugiyama, N. 1999, astro-ph/9811437, Phys. Rev. Lett., 82, 4168, Cosmological constraints on late time entropy production

—. 2000, astro-ph/0002127, Phys. Rev. D, 62, 023506, MeV scale reheating temperature and thermalization of neutrino background

Kawasaki, M. & Takahashi, F. 2001, hep-ph/0105134, Phys. Lett. B, 516, 388, Adiabatic and isocurvature fluctuations of Affleck-Dine field in D term inflation model

Kawasaki, M., Yamada, M., & Yanagida, T. T. 2015, arXiv:1504.04126, Phys. Rev. D, 91, 125018, Observable dark radiation from a cosmologically safe QCD axion

Kharusi, S. A. et al. 2021, arXiv:2109.01327, Phys. Rev. D, 104, 112002, Search for Majoron-emitting modes of ^{136}Xe double beta decay with the complete EXO-200 dataset

Knox, L. & Millea, M. 2020, arXiv:1908.03663, Phys. Rev. D, 101, 043533, Hubble constant hunter's guide

Kosowsky, A. & Turner, M. S. 1995, astro-ph/9504071, Phys. Rev. D, 52, R1739, CBR anisotropy and the running of the scalar spectral index

Kou, R. & Lewis, A. 2025, arXiv:2410.16185, J. Cosmology Astropart. Phys., 2025, 033, A flexible parameterization to test early physics solutions to the Hubble tension with future CMB data

Kreisch, C. D., Cyr-Racine, F.-Y., & Doré, O. 2020, arXiv:1902.00534, Phys. Rev. D, 101, 123505, Neutrino puzzle: Anomalies, interactions, and cosmological tensions

Kreisch, C. D., et al. 2024, arXiv:2207.03164, Phys. Rev. D, 109, 043501, Atacama Cosmology Telescope: The persistence of neutrino self-interaction in cosmological measurements

Kurichin, O. A., Kislitsyn, P. A., Klimenko, V. V., Balashev, S. A., & Ivanchik, A. V. 2021, arXiv:2101.09127, MNRAS, 502, 3045, A new determination of the primordial helium abundance using the analyses of H II region spectra from SDSS

La Posta, A., Louis, T., Garrido, X., & Hill, J. C. 2022, arXiv:2112.10754, Phys. Rev. D, 105, 083519, Constraints on prerecombination early dark energy from SPT-3G public data

66

Laguë, A., Bond, J. R., Hložek, R., Marsh, D. J. E., & Söding, L. 2021, arXiv:2004.08482, MNRAS, 504, 2391, Evolving ultralight scalars into non-linearity with Lagrangian perturbation theory

Laguë, A., McCarthy, F., Madhavacheril, M., Hill, J. C., & Qu, F. J. 2024, arXiv:2402.08149, Phys. Rev. D, 110, 023536, Constraints on dark matter-dark energy scattering from ACT DR6 CMB lensing measurements

Laguë, A. et al. in prep

Lancaster, L., Cyr-Racine, F.-Y., Knox, L., & Pan, Z. 2017, arXiv:1704.06657, JCAP, 07, 033, A tale of two modes: Neutrino free-streaming in the early universe

Lee, N. & Ali-Haïmoud, Y. 2021, arXiv:2108.07798, Phys. Rev. D, 104, 103509, Probing small-scale baryon and dark matter isocurvature perturbations with cosmic microwave background anisotropies

Lee, N., Ali-Haïmoud, Y., Schöneberg, N., & Poulin, V. 2023, arXiv:2212.04494, Phys. Rev. Lett., 130, 161003, What It Takes to Solve the Hubble Tension through Modifications of Cosmological Recombination

Lesgourgues, J. 2011, arXiv:1104.2932, arXiv e-prints, arXiv:1104.2932, The Cosmic Linear Anisotropy Solving System (CLASS) I: Overview

Lesgourgues, J., Marques-Tavares, G., & Schmaltz, M. 2016, arXiv:1507.04351, J. Cosmology Astropart. Phys., 2016, 037, Evidence for dark matter interactions in cosmological precision data?

Lesgourgues, J. & Pastor, S. 2006, astro-ph/0603494, Phys. Rep., 429, 307, Massive neutrinos and cosmology

Lessa, A. P. & Peres, O. L. G. 2007, hep-ph/0701068, Phys. Rev. D, 75, 094001, Revising limits on neutrino-Majoron couplings

Lewin, J. & Smith, P. 1996, Astroparticle Physics, 6, 87, Review of mathematics, numerical factors, and corrections for dark matter experiments based on elastic nuclear recoil, https://www.sciencedirect.com/science/article/pii/S0927650596000473

Lewis, A. 2019, arXiv:1910.13970, arXiv e-prints, arXiv:1910.13970, GetDist: a Python package for analysing Monte Carlo samples

Lewis, A. & Bridle, S. 2002, astro-ph/0205436, Phys. Rev. D, 66, 103511, Cosmological parameters from CMB and other data: A Monte Carlo approach

Lewis, A., Challinor, A., & Lasenby, A. 2000, astro-ph/9911177, ApJ, 538, 473, Efficient Computation of Cosmic Microwave Background Anisotropies in Closed Friedmann-Robertson-Walker Models

Li, X., et al. 2023a, arXiv:2304.00702, Phys. Rev. D, 108, 123518, Hyper Suprime-Cam Year 3 results: Cosmology from cosmic shear two-point correlation functions

Li, Y., et al. 2023b, arXiv:2303.04767, ApJ, 956, 36, The Atacama Cosmology Telescope: Systematic Transient Search of 3 Day Maps

Li, Z., et al. 2023c, arXiv:2208.08985, J. Cosmology Astropart. Phys., 2023, 046, The Atacama Cosmology Telescope: limits on dark matter-baryon interactions from DR4 power spectra

Lin, M.-X., Benevento, G., Hu, W., & Raveri, M. 2019, arXiv:1905.12618, Phys. Rev. D, 100, 063542, Acoustic Dark Energy: Potential Conversion of the Hubble Tension

Linde, A. 1982, Physics Letters B, 108, 389, A new inflationary universe scenario: A possible solution of the horizon, flatness, homogeneity, isotropy and primordial monopole problems, https://www.sciencedirect.com/science/article/pii/0370269382912199

Linde, A. D. 1985, Phys. Lett. B, 158, 375, Generation of Isothermal Density Perturbations in the Inflationary Universe

—. 1991, Phys. Lett. B, 259, 38, Axions in inflationary cosmology

Linde, A. D. & Mukhanov, V. F. 1997, astro-ph/9610219, Phys. Rev. D, 56, R535, Nongaussian isocurvature perturbations from inflation

Linder, E. V. 2003, astro-ph/0208512, Phys. Rev. Lett., 90, 091301, Exploring the Expansion History of the Universe

Linder, E. V. 2005, Physical Review D, 72, Cosmic growth history and expansion history

LiteBIRD Collaboration, et al. 2023, arXiv:2202.02773, Progress of Theoretical and Experimental Physics, 2023, 042F01, Probing cosmic inflation with the LiteBIRD cosmic microwave background polarization survey

Liu, R., Hu, W., & Grin, D. 2024, arXiv:2412.15192, arXiv e-prints, arXiv:2412.15192, Accurate method for ultralight axion CMB and matter power spectra

Lorenz, C. S., Funcke, L., Calabrese, E., & Hannestad, S. 2019, arXiv:1811.01991, Phys. Rev. D, 99, 023501, Time-varying neutrino mass from a supercooled phase transition: Current cosmological constraints and impact on the Ω_m-σ_8 plane

Louis, T., La Posta, A., Atkins, Z., Jense, H., et al. 2025, The Atacama Cosmology Telescope: DR6 Power Spectra, Likelihoods and ΛCDM Parameters

Louis, T., et al. 2017, arXiv:1610.02360, J. Cosmology Astropart. Phys., 2017, 031, The Atacama Cosmology Telescope: two-season ACTPol spectra and parameters

Loverde, M. & Weiner, Z. J. 2024, arXiv:2410.00090, J. Cosmology Astropart. Phys., 2024, 048, Massive neutrinos and cosmic composition

Lynch, G. P., Knox, L., & Chluba, J. 2024a, arXiv:2406.10202, Phys. Rev. D, 110, 083538, DESI observations and the Hubble tension in light of modified recombination

—. 2024b, arXiv:2404.05715, Phys. Rev. D, 110, 063518, Reconstructing the recombination history by combining early and late cosmological probes

Lyth, D. H., Ungarelli, C., & Wands, D. 2003, astro-ph/0208055, Phys. Rev. D, 67, 023503, The Primordial density perturbation in the curvaton scenario

Lyth, D. H. & Wands, D. 2002, hep-ph/0110002, Phys. Lett. B, 524, 5, Generating the curvature perturbation without an inflaton

Maamari, K., Gluscevic, V., Boddy, K. K., Nadler, E. O., & Wechsler, R. H. 2021, The Astrophysical Journal Letters, 907, L46, Bounds on Velocity-dependent Dark Matter–Proton Scattering from Milky Way Satellite Abundance, https://doi.org/10.3847%2F2041-8213%2Fabd807

MacCrann, N., et al. 2024, arXiv:2405.01188, MNRAS, 532, 4247, The Atacama Cosmology Telescope: Reionization kSZ trispectrum methodology and limits

Madhavacheril, M. S., Sehgal, N., & Slatyer, T. R. 2014, Phys. Rev. D, 89, 103508, Current dark matter annihilation constraints from CMB and low-redshift data, https://link.aps.org/doi/10.1103/PhysRevD.89.103508

Madhavacheril, M. S., et al. 2024, The Astrophysical Journal, 962, 113, The Atacama Cosmology Telescope: DR6 Gravitational Lensing Map and Cosmological Parameters, http://dx.doi.org/10.3847/1538-4357/acff5f

Marsh, D. J. E. 2016, arXiv:1510.07633, Phys. Rept., 643, 1, Axion Cosmology

Martins, C. J. A. P., Melchiorri, A., Rocha, G., Trotta, R., Avelino, P. P., & Viana, P. T. P. 2004, astro-ph/0302295, Physics Letters B, 585, 29, WMAP constraints on varying α and the promise of reionization

Matsumoto, A., et al. 2022, arXiv:2203.09617, ApJ, 941, 167, EMPRESS. VIII. A New Determination of Primordial He Abundance with Extremely Metal-poor Galaxies: A Suggestion of the Lepton Asymmetry and Implications for the Hubble Tension

Mazumdar, A., Mohanty, S., & Parashari, P. 2022, arXiv:2011.13685, JCAP, 10, 011, Flavour specific neutrino self-interaction: H_0 tension and IceCube

McCarthy, F., Hill, J. C., & Madhavacheril, M. S. 2022, arXiv:2103.05582, Phys. Rev. D, 105, 023517, Baryonic feedback biases on fundamental physics from lensed CMB power spectra

McDonough, E., Hill, J. C., Ivanov, M. M., La Posta, A., & Toomey, M. W. 2024, arXiv:2310.19899, International Journal of Modern Physics D, 33, 2430003, Observational constraints on early dark energy

Mead, A. J., Brieden, S., Tröster, T., & Heymans, C. 2021, arXiv:2009.01858, MNRAS, 502, 1401, HMCODE-2020: improved modelling of non-linear cosmological power spectra with baryonic feedback

Menegoni, E., Archidiacono, M., Calabrese, E., Galli, S., Martins, C. J. A. P., & Melchiorri, A. 2012, arXiv:1202.1476, Phys. Rev. D, 85, 107301, Fine structure constant and the CMB damping scale

Miller, D. L. & Branch, D. 1992, AJ, 103, 379, Type 1a Supernovae and Cosmic Peculiar Velocities

Miranda, V., Hu, W., He, C., & Motohashi, H. 2016, arXiv:1510.07580, Phys. Rev. D, 93, 023504, Nonlinear excitations in inflationary power spectra

Mirizzi, A., Mangano, G., Pisanti, O., & Saviano, N. 2015, arXiv:1410.1385, Phys. Rev. D, 91, 025019, Collisional production of sterile neutrinos via secret interactions and cosmological implications

Mirpoorian, S. H., Jedamzik, K., & Pogosian, L. 2024, arXiv:2411.16678, Modified recombination and the Hubble tension

Miyatake, H., et al. 2023, arXiv:2304.00704, Phys. Rev. D, 108, 123517, Hyper Suprime-Cam Year 3 results: Cosmology from galaxy clustering and weak lensing with HSC and SDSS using the emulator based halo model

Mollerach, S. 1990, Phys. Rev. D, 42, 313, Isocurvature Baryon Perturbations and Inflation

Moodley, K., Bucher, M., Dunkley, J., Ferreira, P. G., & Skordis, C. 2004, astro-ph/0407304, Phys. Rev. D, 70, 103520, Constraints on isocurvature models from the WMAP first-year data

More, S., et al. 2023, arXiv:2304.00703, Phys. Rev. D, 108, 123520, Hyper Suprime-Cam Year 3 results: Measurements of clustering of SDSS-BOSS galaxies, galaxy-galaxy lensing, and cosmic shear

Moresco, M. & Marulli, F. 2017, arXiv:1705.07903, Mon. Not. Roy. Astron. Soc., 471, L82, Cosmological constraints from a joint analysis of cosmic growth and expansion

Moroi, T. & Takahashi, T. 2001, hep-ph/0110096, Phys. Lett. B, 522, 215, [Erratum: Phys.Lett.B 539, 303–303 (2002)], Effects of cosmological moduli fields on cosmic microwave background

Mukhanov, S. 2007, Journal of Physics A: Mathematical and Theoretical, 40, 6561, Cosmological perturbations from inflation, https://dx.doi.org/10.1088/1751-8113/40/25/S01

NA48/2 Collaboration. 2007, Nucl. Phys. B Proc. Suppl., 169, 205, Testing LFV measuring the ratio R(K) between the branching ratio of K+- —> e+- nu (gamma) and K+- —> mu+- nu (gamma) in NA48/2 experiment: Measurement and perspectives

Nadler, E., et al. 2021, Physical Review Letters, 126, Constraints on Dark Matter Properties from Observations of Milky Way Satellite Galaxies, https://doi.org/10.1103%2Fphysrevlett.126.091101

Nadler, E. O., An, R., Gluscevic, V., Benson, A., & Du, X. 2024, arXiv:2410.03635, arXiv e-prints, arXiv:2410.03635, COZMIC. I. Cosmological Zoom-in Simulations with Initial Conditions Beyond CDM

Nadler, E. O., Gluscevic, V., Boddy, K. K., & Wechsler, R. H. 2019, The Astrophysical Journal, 878, L32, Constraints on Dark Matter Microphysics from the Milky Way Satellite Population, https://doi.org/10.3847%2F2041-8213%2Fab1eb2

Naess, S., Guan, Y., Duivenvoorden, A., Hasselfield, M., et al. 2025, The Atacama Cosmology Telescope: DR6 Maps

NEMO-3 Collaboration. 2014, arXiv:1311.5695, Phys. Rev. D, 89, 111101, Search for neutrinoless double-beta decay of ^{100}Mo with the NEMO-3 detector

Nguyen, D. V., Sarnaaik, D., Boddy, K. K., Nadler, E. O., & Gluscevic, V. 2021, Phys. Rev. D, 104, 103521, Observational constraints on dark matter scattering with electrons, https://link.aps.org/doi/10.1103/PhysRevD.104.103521

Nguyen, N.-M., Huterer, D., & Wen, Y. 2023, arXiv:2302.01331, Phys. Rev. Lett., 131, 111001, Evidence for Suppression of Structure Growth in the Concordance Cosmological Model

Obied, G., Dvorkin, C., Heinrich, C., Hu, W., & Miranda, V. 2017, arXiv:1706.09412, Phys. Rev. D, 96, 083526, Inflationary features and shifts in cosmological parameters from Planck 2015 data

O'Hare, C. A. J. 2024, arXiv:2403.17697, PoS, COSMICWISPers, 040, Cosmology of axion dark matter

Okumura, T. et al. 2016, arXiv:1511.08083, Publ. Astron. Soc. Jap., 68, 38, The Subaru FMOS galaxy redshift survey (FastSound). IV. New constraint on gravity theory from redshift space distortions at $z \sim 1.4$

Oldengott, I. M., Barenboim, G., Kahlen, S., Salvado, J., & Schwarz, D. J. 2019, arXiv:1901.04352, J. Cosmology Astropart. Phys., 2019, 049, How to relax the cosmological neutrino mass bound

Oldengott, I. M., Tram, T., Rampf, C., & Wong, Y. Y. Y. 2017, arXiv:1706.02123, JCAP, 11, 027, Interacting neutrinos in cosmology: exact description and constraints

Padmanabhan, N. & Finkbeiner, D. P. 2005, astro-ph/0503486, Phys. Rev. D, 72, 023508, Detecting dark matter annihilation with CMB polarization: Signatures and experimental prospects

Pagano, L., Delouis, J. M., Mottet, S., Puget, J. L., & Vibert, L. 2020, arXiv:1908.09856, A&A, 635, A99, Reionization optical depth determination from Planck HFI data with ten percent accuracy

Palanque-Delabrouille, N., Yèche, C., Schöneberg, N., Lesgourgues, J., Walther, M., Chabanier, S., & Armengaud, E. 2020, arXiv:1911.09073, J. Cosmology Astropart. Phys., 2020, 038, Hints, neutrino bounds, and WDM constraints from SDSS DR14 Lyman-α and Planck full-survey data

Pan, Z., Knox, L., Mulroe, B., & Narimani, A. 2016, arXiv:1603.03091, MNRAS, 459, 2513, Cosmic microwave background acoustic peak locations

Park, M., Kreisch, C. D., Dunkley, J., Hadzhiyska, B., & Cyr-Racine, F.-Y. 2019, arXiv:1904.02625, Phys. Rev. D, 100, 063524, ΛCDM or self-interacting neutrinos: How CMB data can tell the two models apart

Park, S., Bak, D., Lee, J.-W., & Park, I. 2022, arXiv:2207.07192, J. Cosmology Astropart. Phys., 2022, 033, Analyzing planar galactic halo distributions with fuzzy/cold dark matter models

Particle Data Group. 2020, Progress of Theoretical and Experimental Physics, 2020, 083C01, Review of Particle Physics

—. 2024, Phys. Rev. D, 110, 030001, Review of particle physics

Peebles, P. J. E. 1968, ApJ, 153, 1, Recombination of the Primeval Plasma

Peiris, H. V., et al. 2003, astro-ph/0302225, ApJS, 148, 213, First-Year Wilkinson Microwave Anisotropy Probe (WMAP) Observations: Implications For Inflation

Percival, W. J. & White, M. 2009, arXiv:0808.0003, MNRAS, 393, 297, Testing cosmological structure formation using redshift-space distortions

Percival, W. J., et al. 2002, astro-ph/0206256, MNRAS, 337, 1068, Parameter constraints for flat cosmologies from cosmic microwave background and 2dFGRS power spectra

Perlmutter, S., et al. 1999, astro-ph/9812133, ApJ, 517, 565, Measurements of Ω and Λ from 42 High-Redshift Supernovae

Pezzotta, A. et al. 2017, arXiv:1612.05645, Astron. Astrophys., 604, A33, The VIMOS Public Extragalactic Redshift Survey (VIPERS): The growth of structure at $0.5 < z < 1.2$ from redshift-space distortions in the clustering of the PDR-2 final sample

Philcox, O. H. E. & Ivanov, M. M. 2022, arXiv:2112.04515, Phys. Rev. D, 105, 043517, BOSS DR12 full-shape cosmology: Λ CDM constraints from the large-scale galaxy power spectrum and bispectrum monopole

Pitrou, C., Coc, A., Uzan, J.-P., & Vangioni, E. 2018, arXiv:1801.08023, Phys. Rep., 754, 1, Precision big bang nucleosynthesis with improved Helium-4 predictions

Planck Collaboration. 2014, arXiv:1303.5076, A&A, 571, A16, Planck 2013 results. XVI. Cosmological parameters

—. 2015, arXiv:1406.7482, A&A, 580, A22, Planck intermediate results. XXIV. Constraints on variations in fundamental constants

—. 2016a, arXiv:1502.01589, A&A, 594, A13, Planck 2015 results. XIII. Cosmological parameters

—. 2016b, arXiv:1502.01591, A&A, 594, A15, Planck 2015 results. XV. Gravitational lensing

—. 2016c, arXiv:1502.02114, A&A, 594, A20, Planck 2015 results. XX. Constraints on inflation

—. 2020a, arXiv:1807.06205, A&A, 641, A1, Planck 2018 results. I. Overview and the cosmological legacy of Planck

—. 2020b, arXiv:1907.12875, A&A, 641, A5, Planck 2018 results. V. CMB power spectra and likelihoods

—. 2020c, arXiv:1807.06209, A&A, 641, A6, Planck 2018 results. VI. Cosmological parameters

—. 2020d, arXiv:1807.06210, A&A, 641, A8, Planck 2018 results. VIII. Gravitational lensing

—. 2020e, arXiv:1807.06211, A&A, 641, A10, Planck 2018 results. X. Constraints on inflation

Pogosian, L., Shimon, M., Mewes, M., & Keating, B. 2019, arXiv:1904.07855, Phys. Rev. D, 100, 023507, Future CMB constraints on cosmic birefringence and implications for fundamental physics

Pogosian, L., Zhao, G.-B., & Jedamzik, K. 2024, arXiv:2405.20306, Astrophys. J. Lett., 973, L13, A Consistency Test of the Cosmological Model at the Epoch of Recombination Using DESI Baryonic Acoustic Oscillation and Planck Measurements

Polarski, D. & Starobinsky, A. A. 1994, astro-ph/9404061, Phys. Rev. D, 50, 6123, Isocurvature perturbations in multiple inflationary models

Poudou, A., Simon, T., Montandon, T., Teixeira, E. M., & Poulin, V. 2025, arXiv:2503.10485, arXiv e-prints, arXiv:2503.10485, Self-interacting neutrinos in light of recent CMB and LSS data

Poulin, V., Bernal, J. L., Kovetz, E. D., & Kamionkowski, M. 2023a, arXiv:2209.06217, Phys. Rev. D, 107, 123538, Sigma-8 tension is a drag

Poulin, V., Smith, T. L., & Bartlett, A. 2021, arXiv:2109.06229, Phys. Rev. D, 104, 123550, Dark energy at early times and ACT data: A larger Hubble constant without late-time priors

Poulin, V., Smith, T. L., Grin, D., Karwal, T., & Kamionkowski, M. 2018, arXiv:1806.10608, Phys. Rev. D, 98, 083525, Cosmological implications of ultralight axionlike fields

Poulin, V., Smith, T. L., & Karwal, T. 2023b, arXiv:2302.09032, Physics of the Dark Universe, 42, 101348, The Ups and Downs of Early Dark Energy solutions to the Hubble tension: A review of models, hints and constraints circa 2023

Poulin, V., Smith, T. L., Karwal, T., & Kamionkowski, M. 2019, Phys. Rev. Lett., 122, 221301, Early Dark Energy can Resolve the Hubble Tension

Pouri, A., Basilakos, S., & Plionis, M. 2014, arXiv:1402.0964, JCAP, 08, 042, Precision growth index using the clustering of cosmic structures and growth data

Qu, F. J., Surrao, K. M., Bolliet, B., Hill, J. C., Sherwin, B. D., & Jense, H. T. 2024a, arXiv:2404.16805, arXiv e-prints, arXiv:2404.16805, Accelerated inference on accelerated cosmic expansion: New constraints on axion-like early dark energy with DESI BAO and ACT DR6 CMB lensing

Qu, F. J., et al. 2024b, arXiv:2304.05202, ApJ, 962, 112, The Atacama Cosmology Telescope: A Measurement of the DR6 CMB Lensing Power Spectrum and Its Implications for Structure Growth

Raffaelli, A. & Ballardini, M. 2025, arXiv:2503.10609, arXiv e-prints, arXiv:2503.10609, Knot reconstruction of the scalar primordial power spectrum with Planck, ACT, and SPT CMB data

Rapetti, D., Blake, C., Allen, S. W., Mantz, A., Parkinson, D., & Beutler, F. 2013, arXiv:1205.4679, Mon. Not. Roy. Astron. Soc., 432, 973, A combined measurement of cosmic growth and expansion from clusters of galaxies, the CMB and galaxy clustering

Rashkovetskyi, M., Muñoz, J. B., Eisenstein, D. J., & Dvorkin, C. 2021, arXiv:2108.02747, Phys. Rev. D, 104, 103517, Small-scale clumping at recombination and the Hubble tension

Reid, B. A., et al. 2010, arXiv:0907.1659, MNRAS, 404, 60, Cosmological constraints from the clustering of the Sloan Digital Sky Survey DR7 luminous red galaxies

Riemer-Sørensen, S., Kotuš, S., Webb, J. K., Ali, K., Dumont, V., Murphy, M. T., & Carswell, R. F. 2017, arXiv:1703.06656, MNRAS, 468, 3239, A precise deuterium abundance: remeasurement of the z = 3.572 absorption system towards the quasar PKS1937-101

Riemer-Sørensen, S., et al. 2015, arXiv:1412.4043, MNRAS, 447, 2925, A robust deuterium abundance; re-measurement of the z = 3.256 absorption system towards the quasar PKS 1937-101

Riess, A. G., et al. 1998, astro-ph/9805201, AJ, 116, 1009, Observational Evidence from Supernovae for an Accelerating Universe and a Cosmological Constant

—. 2022, arXiv:2112.04510, ApJ, 934, L7, A Comprehensive Measurement of the Local Value of the Hubble Constant with 1 km s^{-1} Mpc^{-1} Uncertainty from the Hubble Space Telescope and the SH0ES Team

Rocha, G., Trotta, R., Martins, C. J. A. P., Melchiorri, A., Avelino, P. P., Bean, R., & Viana, P. T. P. 2004, astro-ph/0309211, MNRAS, 352, 20, Measuring α in the early Universe: cosmic microwave background polarization, re-ionization and the Fisher matrix analysis

Rogers, K. K., Dvorkin, C., & Peiris, H. V. 2022, Physical Review Letters, 128, Limits on the Light Dark Matter–Proton Cross Section from Cosmic Large-Scale Structure, https://doi.org/10.1103%2Fphysrevlett.128.171301

Rogers, K. K., Hložek, R., Laguë, A., Ivanov, M. M., Philcox, O. H. E., Cabass, G., Akitsu, K., & Marsh, D. J. E. 2023, arXiv:2301.08361, J. Cosmology Astropart. Phys., 2023, 023, Ultra-light axions and the S$_8$ tension: joint constraints from the cosmic microwave background and galaxy clustering

Rosenberg, E., Gratton, S., & Efstathiou, G. 2022, arXiv:2205.10869, MNRAS, 517, 4620, CMB power spectra and cosmological parameters from Planck PR4 with CamSpec

Roy Choudhury, S., Hannestad, S., & Tram, T. 2021, arXiv:2012.07519, JCAP, 03, 084, Updated constraints on massive neutrino self-interactions from cosmology in light of the H_0 tension

Rubin, D., et al. 2015, in American Astronomical Society Meeting Abstracts, Vol. 225, American Astronomical Society Meeting Abstracts #225, 255.12

Rubin, D., et al. 2023, arXiv:2311.12098, arXiv e-prints, arXiv:2311.12098, Union Through UNITY: Cosmology with 2,000 SNe Using a Unified Bayesian Framework

Rubira, H., Mazoun, A., & Garny, M. 2023, arXiv:2209.03974, J. Cosmology Astropart. Phys., 2023, 034, Full-shape BOSS constraints on dark matter interacting with dark radiation and lifting the S$_8$ tension

Ruiz, E. J. & Huterer, D. 2015, arXiv:1410.5832, Phys. Rev. D, 91, 063009, Testing the dark energy consistency with geometry and growth

Ruiz-Zapatero, J., García-García, C., Alonso, D., Ferreira, P. G., & Grumitt, R. D. P. 2022, arXiv:2201.07025, Mon. Not. Roy. Astron. Soc., 512, 1967, Model-independent constraints on Ωm and H(z) from the link between geometry and growth

Ruiz-Zapatero, J. et al. 2021, arXiv:2105.09545, Astron. Astrophys., 655, A11, Geometry versus growth - Internal consistency of the flat ΛCDM model with KiDS-1000

Sabti, N., Muñoz, J. B., & Blas, D. 2022, arXiv:2110.13161, ApJ, 928, L20, New Roads to the Small-scale Universe: Measurements of the Clustering of Matter with the High-redshift UV Galaxy Luminosity Function

Said, K., Colless, M., Magoulas, C., Lucey, J. R., & Hudson, M. J. 2020, arXiv:2007.04993, Mon. Not. Roy. Astron. Soc., 497, 1275, Joint analysis of 6dFGS and SDSS peculiar velocities for the growth rate of cosmic structure and tests of gravity

Schechter, J. & Valle, J. W. F. 1982, Phys. Rev. D, 25, 774, Neutrino Decay and Spontaneous Violation of Lepton Number

Schöneberg, N. 2024, arXiv:2401.15054, J. Cosmology Astropart. Phys., 2024, 006, The 2024 BBN baryon abundance update

Schöneberg, N., Abellán, G. F., Sánchez, A. P., Witte, S. J., Poulin, V., & Lesgourgues, J. 2022, arXiv:2107.10291, Phys. Rep., 984, 1, The H$_0$ Olympics: A fair ranking of proposed models

Schöneberg, N., Abellán, G. F., Simon, T., Bartlett, A., Patel, Y., & Smith, T. L. 2023, arXiv:2306.12469, Phys. Rev. D, 108, 123513, Comparative analysis of interacting stepped dark radiation

Scóccola, C. G., Landau, S. J., & Vucetich, H. 2009, arXiv:0910.1083, Mem. Soc. Astron. Italiana, 80, 814, WMAP 5-year constraints on time variation of α and m_e

Scolnic, D., et al. 2022, arXiv:2112.03863, ApJ, 938, 113, The Pantheon+ Analysis: The Full Data Set and Light-curve Release

Scolnic, D. M., et al. 2018, arXiv:1710.00845, ApJ, 859, 101, The Complete Light-curve Sample of Spectroscopically Confirmed SNe Ia from Pan-STARRS1 and Cosmological Constraints from the Combined Pantheon Sample

Seager, S., Sasselov, D. D., & Scott, D. 1999, astro-ph/9909275, ApJ, 523, L1, A New Calculation of the Recombination Epoch

Secco, L. F., et al. 2022, arXiv:2105.13544, Phys. Rev. D, 105, 023515, Dark Energy Survey Year 3 results: Cosmology from cosmic shear and robustness to modeling uncertainty

Seckel, D. & Turner, M. S. 1985, Phys. Rev. D, 32, 3178, Isothermal Density Perturbations in an Axion Dominated Inflationary Universe

Sekiguchi, T. & Takahashi, T. 2021, arXiv:2007.03381, Phys. Rev. D, 103, 083507, Early recombination as a solution to the H_0 tension

Shao, H., Givans, J. J., Dunkley, J., Madhavacheril, M., Qu, F., Farren, G., & Sherwin, B. 2024, arXiv:2409.02295, arXiv e-prints, arXiv:2409.02295, Cosmological limits on the neutrino mass sum for beyond-ΛCDM models

Shlivko, D. & Steinhardt, P. J. 2024, arXiv:2405.03933, Physics Letters B, 855, 138826, Assessing observational constraints on dark energy

Sievers, J. L., et al. 2013, arXiv:1301.0824, J. Cosmology Astropart. Phys., 2013, 060, The Atacama Cosmology Telescope: cosmological parameters from three seasons of data

Sigurdson, K., Doran, M., Kurylov, A., Caldwell, R. R., & Kamionkowski, M. 2004, Phys. Rev. D, 70, 083501, Dark-matter electric and magnetic dipole moments, https://link.aps.org/doi/10.1103/PhysRevD.70.083501

Simons Observatory Collaboration. 2019, arXiv:1808.07445, J. Cosmology Astropart. Phys., 2019, 056, The Simons Observatory: science goals and forecasts

Simpson, F. 2010, arXiv:1007.1034, Phys. Rev. D, 82, 083505, Scattering of dark matter and dark energy

Slatyer, T. R. 2016a, arXiv:1506.03811, Phys. Rev. D, 93, 023527, Indirect dark matter signatures in the cosmic dark ages. I. Generalizing the bound on s -wave dark matter annihilation from Planck results

—. 2016b, arXiv:1506.03812, Phys. Rev. D, 93, 023521, Indirect dark matter signatures in the cosmic dark ages. II. Ionization, heating, and photon production from arbitrary energy injections

Slatyer, T. R. & Wu, C.-L. 2018, Physical Review D, 98, Early-Universe constraints on dark matter-baryon scattering and their implications for a global 21 cm signal, https://doi.org/10.1103%2Fphysrevd.98.023013

Smith, K. M., Zahn, O., & Doré, O. 2007, arXiv:0705.3980, Phys. Rev. D, 76, 043510, Detection of gravitational lensing in the cosmic microwave background

Smith, R. E., et al. 2003, astro-ph/0207664, MNRAS, 341, 1311, Stable clustering, the halo model and non-linear cosmological power spectra

Smith, T. L., Lucca, M., Poulin, V., Abellan, G. F., Balkenhol, L., Benabed, K., Galli, S., & Murgia, R. 2022, arXiv:2202.09379, Phys. Rev. D, 106, 043526, Hints of early dark energy in Planck, SPT, and ACT data: New physics or systematics?

Smith, T. L. & Poulin, V. 2024, arXiv:2309.03265, Phys. Rev. D, 109, 103506, Current small-scale CMB constraints to axionlike early dark energy

Smith, T. L., Poulin, V., & Amin, M. A. 2020, arXiv:1908.06995, Phys. Rev. D, 101, 063523, Oscillating scalar fields and the Hubble tension: a resolution with novel signatures

SNO Collaboration. 2002, nucl-ex/0204008, Phys. Rev. Lett., 89, 011301, Direct Evidence for Neutrino Flavor Transformation from Neutral-Current Interactions in the Sudbury Neutrino Observatory

Song, Y.-S. & Percival, W. J. 2009, arXiv:0807.0810, J. Cosmology Astropart. Phys., 2009, 004, Reconstructing the history of structure formation using redshift distortions

Spergel, D. N., et al. 2003, astro-ph/0302209, ApJS, 148, 175, First-Year Wilkinson Microwave Anisotropy Probe (WMAP) Observations: Determination of Cosmological Parameters

Spurio Mancini, A., Piras, D., Alsing, J., Joachimi, B., & Hobson, M. P. 2022, arXiv:2106.03846, MNRAS, 511, 1771, COSMOPOWER: emulating cosmological power spectra for accelerated Bayesian inference from next-generation surveys

Stahl, B. E., de Jaeger, T., Boruah, S. S., Zheng, W., Filippenko, A. V., & Hudson, M. J. 2021, arXiv:2105.05185, MNRAS, 505, 2349, Peculiar-velocity cosmology with Types Ia and II supernovae

Starobinskij, A. A. 1992, Soviet Journal of Experimental and Theoretical Physics Letters, 55, 489, Spectrum of adiabatic perturbations in the universe when there are singularities in the inflationary potential.

Starobinsky, A. A. 1980, Physics Letters B, 91, 99, A new type of isotropic cosmological models without singularity

Steigman, G. 2013, arXiv:1303.0049, Phys. Rev. D, 87, 103517, Equivalent neutrinos, light WIMPs, and the chimera of dark radiation

Stompor, R., Banday, A. J., & Gorski, K. M. 1996, astro-ph/9511087, Astrophys. J., 463, 8, Flat dark matter dominated models with hybrid adiabatic plus isocurvature initial conditions

Sugiyama, S., et al. 2023, arXiv:2304.00705, Phys. Rev. D, 108, 123521, Hyper Suprime-Cam Year 3 results: Cosmology from galaxy clustering and weak lensing with HSC and SDSS using the minimal bias model

Super-Kamiokande Collaboration. 1998, hep-ex/9807003, Phys. Rev. Lett., 81, 1562, Evidence for Oscillation of Atmospheric Neutrinos

Takahashi, R., Sato, M., Nishimichi, T., Taruya, A., & Oguri, M. 2012, arXiv:1208.2701, ApJ, 761, 152, Revising the Halofit Model for the Nonlinear Matter Power Spectrum

Tegmark, M. & Zaldarriaga, M. 2002, astro-ph/0207047, Phys. Rev. D, 66, 103508, Separating the early universe from the late universe: Cosmological parameter estimation beyond the black box

Tegmark, M., et al. 2004, astro-ph/0310725, ApJ, 606, 702, The Three-Dimensional Power Spectrum of Galaxies from the Sloan Digital Sky Survey

Thiele, L., Guan, Y., Hill, J. C., Kosowsky, A., & Spergel, D. N. 2021, arXiv:2105.03003, Phys. Rev. D, 104, 063535, Can small-scale baryon inhomogeneities resolve the Hubble tension? An investigation with ACT DR4

Torrado, J. & Lewis, A. 2021, arXiv:2005.05290, J. Cosmology Astropart. Phys., 2021, 057, Cobaya: code for Bayesian analysis of hierarchical physical models

Tristram, M., et al. 2024, A&A, 682, A37, Cosmological parameters derived from the final Planck data release (PR4), https://doi.org/10.1051/0004-6361/202348015

Troxel, M. A., et al. 2018, arXiv:1708.01538, Phys. Rev. D, 98, 043528, Dark Energy Survey Year 1 results: Cosmological constraints from cosmic shear

Tully, R. B., Courtois, H. M., & Sorce, J. G. 2016, arXiv:1605.01765, AJ, 152, 50, Cosmicflows-3

Turnbull, S. J., Hudson, M. J., Feldman, H. A., Hicken, M., Kirshner, R. P., & Watkins, R. 2012, arXiv:1111.0631, MNRAS, 420, 447, Cosmic flows in the nearby universe from Type Ia supernovae

Turner, M. S. & Wilczek, F. 1991, Phys. Rev. Lett., 66, 5, Inflationary axion cosmology

Turner, M. S., Wilczek, F., & Zee, A. 1983, Phys. Lett. B, 125, 35, [Erratum: Phys.Lett.B 125, 519 (1983)], Formation of Structure in an Axion Dominated Universe

Turner, R. J., Blake, C., & Ruggeri, R. 2022, arXiv:2207.03707, Mon. Not. Roy. Astron. Soc., 518, 2436, A local measurement of the growth rate from peculiar velocities and galaxy clustering correlations in the 6dF Galaxy Survey

Valerdi, M., Peimbert, A., & Peimbert, M. 2021, arXiv:2105.12260, MNRAS, 505, 3624, Chemical abundances in seven metal-poor H II regions and a determination of the primordial helium abundance

Valerdi, M., Peimbert, A., Peimbert, M., & Sixtos, A. 2019, arXiv:1904.01594, ApJ, 876, 98, Determination of the Primordial Helium Abundance Based on NGC 346, an H II Region of the Small Magellanic Cloud

van Engelen, A., et al. 2012, arXiv:1202.0546, ApJ, 756, 142, A Measurement of Gravitational Lensing of the Microwave Background Using South Pole Telescope Data

Verde, L., Schöneberg, N., & Gil-Marín, H. 2024, arXiv:2311.13305, ARA&A, 62, 287, A Tale of Many H_0

Vogt, S. M. L., Marsh, D. J. E., & Laguë, A. 2023, arXiv:2209.13445, Phys. Rev. D, 107, 063526, Improved mixed dark matter halo model for ultralight axions

Wang, L. & Steinhardt, P. J. 1998, The Astrophysical Journal, 508, 483–490, Cluster Abundance Constraints for Cosmological Models with a Time-varying, Spatially Inhomogeneous Energy Component with Negative Pressure

Wang, S., Hui, L., May, M., & Haiman, Z. 2007, arXiv:0705.0165, Phys. Rev. D, 76, 063503, Is Modified Gravity Required by Observations? An Empirical Consistency Test of Dark Energy Models

Weinberg, D. H., Mortonson, M. J., Eisenstein, D. J., Hirata, C., Riess, A. G., & Rozo, E. 2013, arXiv:1201.2434, Phys. Rep., 530, 87, Observational probes of cosmic acceleration

Weinberg, S. 1978, Phys. Rev. Lett., 40, 223, A New Light Boson?, https://link.aps.org/doi/10.1103/PhysRevLett.40.223

Weinberg, S. 2013, arXiv:1305.1971, Phys. Rev. Lett., 110, 241301, Goldstone Bosons as Fractional Cosmic Neutrinos

Wen, Y., Scott, D., Sullivan, R., & Zibin, J. P. 2021, arXiv:2011.09616, Phys. Rev. D, 104, 043516, Role of T_0 in CMB anisotropy measurements

White, M. et al. 2022, arXiv:2111.09898, JCAP, 02, 007, Cosmological constraints from the tomographic cross-correlation of DESI Luminous Red Galaxies and Planck CMB lensing

Xu, Y., Takahashi, K., Goriely, S., Arnould, M., Ohta, M., & Utsunomiya, H. 2013, arXiv:1310.7099, Nucl. Phys. A, 918, 61, NACRE II: an update of the NACRE compilation of charged-particle-induced thermonuclear reaction rates for nuclei with mass number A¡16

Zhou, Z. & Weiner, N. 2024, arXiv:2409.06771, arXiv e-prints, arXiv:2409.06771, Searching for Dark Matter Interactions with ACT, SPT and DES

APPENDIX

A. THEORY SPECIFICATIONS

For the results presented in this paper, we use multiple Einstein-Boltzmann codes to calculate theory predictions. We explore and define settings for both `camb` and `class` to ensure that the uncertainty in the theory calculations is well below the statistical error bars of the DR6 power spectra on all scales. In particular, some of the settings defined for the *Planck* baseline analyses require revision to give unbiased results with our new small-scale measurements, as pointed out in, e.g., Hill et al. 2022; McCarthy et al. 2022. For this work, we revise precision parameters for the calculation of the lensed CMB spectra, as well as baseline choices for non-linear modeling of the matter power spectrum, effects of baryonic feedback in the non-linear matter power spectrum model, recombination calculations, and the choice of BBN calculations (the latter is described in detail in §6.2). We obtain the baseline settings summarized in §3 and reported in Figs. 47 and 48 below.

To assess robustness of the theory specifications with respect to the data, we consider both cosmological parameter posteriors using different assumptions and single likelihood evaluations to study the impact on the χ^2 of a reference best-fit model. In general, we find that parameter posteriors are unbiased, but χ^2 values can vary across the parameter space, for both ΛCDM and extended models. We summarize the results of these investigations here:

- *Numerical accuracy settings*— Accuracy parameters for the calculations of the lensed CMB theory power spectra were studied in previous works and validated for sensitivity levels beyond that of ACT DR6 (see, e.g., Bolliet et al. 2024; Jense et al. 2025).

- *Recombination*— For recombination modeling, we compare the (previously-used-as-default) `RecFast` code with the alternative `HyRec` and `CosmoRec` codes, both of which can be manually installed within `camb`. When evaluating the DR6 CMB-only likelihood `ACT-lite` at the best-fit ΛCDM point from L25, we find $\Delta\chi^2_{\rm Recfast-HyRec} = 0.37$ and $\Delta\chi^2_{\rm Recfast-CosmoRec} = 0.49$, and with `HyRec` and `CosmoRec` agreeing within $\Delta\chi^2_{\rm HyRec-CosmoRec} = 0.12$. Moving away from the best-fit point, the differences increase and vary across parameter space, with `RecFast` calculations compared to either `HyRec` or `CosmoRec` reaching $\Delta\chi^2 \sim O(100)$. Looking at the contributions to this difference across multipoles, we find that it mostly comes from TT at $\ell \sim 2000$. No significant difference in parameter posteriors is found. Given that `Recfast` relies on fudge factors optimized for the *Planck* sensitivity but not beyond, and given that `CosmoRec` and `HyRec` have been proven to be consistent for precise calculations of hydrogen recombination — with `CosmoRec` implementing also more complex helium recombination (Chluba et al. 2012) — we choose to use `CosmoRec` as our baseline for use with `camb`. Since `CosmoRec` is not available with `class`, we use `HyRec` for models using this code.

- *Non-linear matter power spectrum*— Previous CMB analyses (e.g., Choi et al. 2020; Planck Collaboration 2020c) used `Halofit` or the 2016 version of `HMcode` to compute the non-linear matter power spectrum, which is necessary for modeling CMB lensing. Here, we switch to the updated 2020 version of `HMcode`. We adopt the dark-matter-only model with the default parameters. At the ΛCDM best-fit point, we find $\Delta\chi^2_{\rm Halofit-HMcode2020} = 0.09$.

- *Baryonic feedback in non-linear modeling*— To assess the impact of parameters describing baryonic feedback in `HMcode`, we run calculations with dark-matter-only versus dark-matter-plus-baryons, with the default settings for baryonic feedback. At the ΛCDM best-fit point, this gives $\Delta\chi^2_{\rm DM-DM+b} = 0.20$. We also test the impact of the strength of baryonic feedback, comparing our baseline with DM+baryons and with baryons having `HMcode_logT_AGN=8.0` (rather than 7.8), thus corresponding to a stronger feedback model with larger suppression of the small-scale matter power spectrum at late times. This gives $\Delta\chi^2_{\rm DM-DM+b+f} = 0.39$. For future analyses with Simons Observatory and CMB-S4 data, this effect will likely need to be accounted for in the modeling (as found in McCarthy et al. 2022).

Figures 47 and 48 give code snippets from our `Cobaya` yaml files summarizing the baseline analysis settings. These configurations give results within $\Delta\chi^2_{\rm camb-class} \sim O(10^{-2})$. Figure 49 shows validation across Einstein-Boltzmann codes for our baseline ΛCDM parameter constraints, including `camb`, `class`, and `CosmoPower`-based emulators; similar agreement is found also for extended models that are accessible in the three codes. In Table 4 we list all the models explored in this work and enumerate the theory and likelihood codes used for each analysis.

```
1  camb:
2    extra_args:
3      kmax: 10
4      k_per_logint: 130
5      nonlinear: true
6      lens_potential_accuracy: 8
7      lens_margin: 2050
8      lAccuracyBoost: 1.2
9      min_l_logl_sampling: 6000
10     DoLateRadTruncation: false
11     recombination_model: CosmoRec
```

Figure 47. Baseline settings used for `camb` theory calculations, updating the default assumptions of `camb v1.5`. Note that `halofit_version=mead2020` and BBN consistency from PRIMAT 2021 are already default settings in this `camb` version.

```
1  classy:
2    extra_args:
3      N_ncdm: 1
4      m_ncdm: 0.06
5      N_ur: 2.0308
6      T_cmb: 2.7255
7      YHe: BBN
8      non_linear: hmcode
9      hmcode_version: '2020'
10     recombination: HyRec
11     lensing: 'yes'
12     output: lCl,tCl,pCl,mPk
13     modes: s
14     l_max_scalars: 9500
15     delta_l_max: 1800
16     P_k_max_h/Mpc: 100.
17     l_logstep: 1.025
18     l_linstep: 20
19     perturbations_sampling_stepsize: 0.05
20     l_switch_limber: 30.
21     hyper_sampling_flat: 32.
22     l_max_g: 40
23     l_max_ur: 35
24     l_max_pol_g: 60
25     ur_fluid_approximation: 2
26     ur_fluid_trigger_tau_over_tau_k: 130.
27     radiation_streaming_approximation: 2
28     radiation_streaming_trigger_tau_over_tau_k: 240.
29     hyper_flat_approximation_nu: 7000.
30     transfer_neglect_delta_k_S_t0: 0.17
31     transfer_neglect_delta_k_S_t1: 0.05
32     transfer_neglect_delta_k_S_t2: 0.17
33     transfer_neglect_delta_k_S_e: 0.17
34     accurate_lensing: 1
35     start_small_k_at_tau_c_over_tau_h: 0.0004
36     start_large_k_at_tau_h_over_tau_k: 0.05
37     tight_coupling_trigger_tau_c_over_tau_h: 0.005
38     tight_coupling_trigger_tau_c_over_tau_k: 0.008
39     start_sources_at_tau_c_over_tau_h: 0.006
40     l_max_ncdm: 30
41     tol_ncdm_synchronous: 1.e-6
```

Figure 48. Baseline settings used for `class` theory calculations, updating the default assumptions of the public `class` version. In this work, we use a version of the code that has been updated to implement the latest `HMcode-2020` model for the non-linear power spectrum, provided by J. Lesgourgues (developed from `class v3.2.2`).
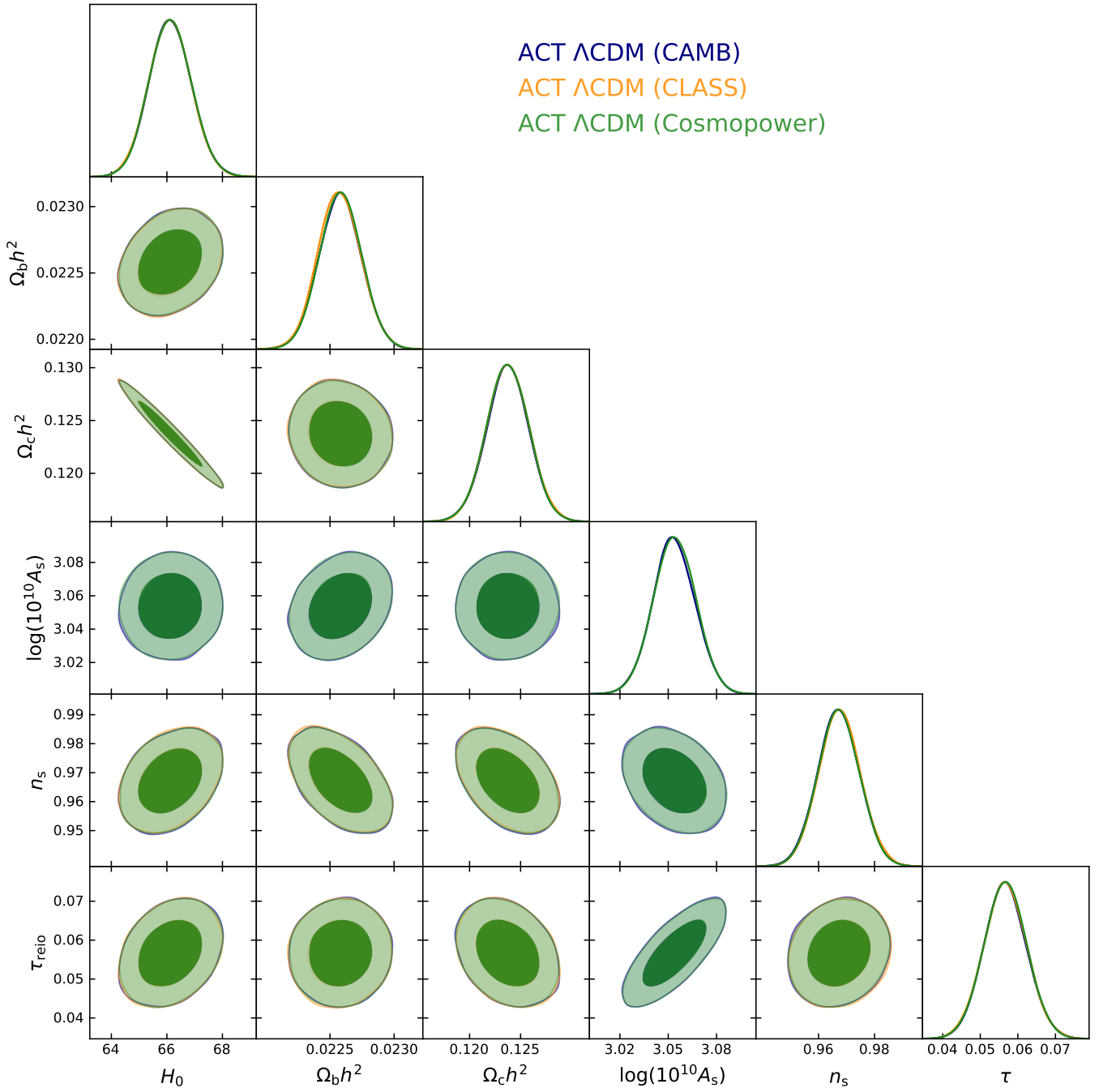
Figure 49. Comparison of baseline ΛCDM parameter posteriors, validating different approaches to compute the lensed CMB theory — using `camb` (blue), `CosmoPower` (green), or `class` (orange).

Model	Section	Theory Code	Likelihood
Running of scalar spectral index	§4.1	`camb`	`MFLike/ACT-lite`
$P_{\mathcal{R}}(k)$	§4.2	`camb`	`ACT-lite`
Isocurvature perturbations	§4.3	`class`	`MFLike`
Tensor modes	§4.4	`camb`	`ACT-lite`
Early dark energy	§5.1	`class`/`camb`/ `class` emulators (Qu et al. 2024a)	`MFLike`
Varying electron mass	§5.2.1	`class`	`MFLike`
Varying electron mass and curvature	§5.2.2	`class`	`MFLike`
Varying fine-structure constant	§5.2.3	`class`	`MFLike`
Varying fine-structure constant and curvature	§5.2.4	`class`	`MFLike`
Primordial magnetic fields	§5.3	modified `class`	`MFLike`
CMB temperature	§5.4	`class`	`MFLike`
Modified recombination history	§5.5	modified `class`	`MFLike`
Neutrino number, N_{eff}	§6.1.1	`camb`/ `camb` emulators (Jense et al. 2025)	`MFLike/ACT-lite`
Neutrino mass, $\sum m_\nu$	§6.1.1	`camb`/ `camb` emulators (Jense et al. 2025)	`MFLike/ACT-lite`
$N_{\mathrm{eff}} + \sum m_\nu$	§6.1.1	`camb`/ `camb` emulators (Jense et al. 2025)	`ACT-lite`
Neutrino self-interactions	§6.1.2	modified `camb`	`MFLike`
Helium and deuterium	§6.2	`camb`	`MFLike/ACT-lite`
Axion-like particles	§6.3	modified `camb`/ `camb` emulators	`ACT-lite`
DM-baryon interactions	§6.4.1	modified `class`	`MFLike`
DM annihilation	§6.4.2	`class`	`MFLike`
Self-interacting DR	§6.5.1	`class`	`MFLike`
Interacting DR-DM	§6.5.2	`class`	`MFLike`
Spatial curvature	§7.1	`camb`	`MFLike/ACT-lite`
Dark energy equation of state, w	§7.2	`camb`	`MFLike/ACT-lite`
Dark energy equation of state, w_0/w_{a}	§7.2	`camb`	`MFLike`
Interacting DE-DM	§7.3	modified `class`	`MFLike`
Modified gravity	§7.4	modified `camb`	`MFLike`

Table 4. Summary of models explored in this paper. For each case, we list the Einstein-Boltzmann code and likelihood that are used for each model, noting when chains have been run with more than one code (for robustness tests and reproducibility). The likelihood codes and the baseline ΛCDM results are presented in L25.

B. ACT DR6 VERSUS DR4 COSMOLOGY

Here we compare results for the baseline ΛCDM model derived in L25 from the DR6 maps with those from DR4 presented in Choi et al. (2020); Aiola et al. (2020). Figure 50 shows the subset of ΛCDM cosmological parameters measured by ACT for DR6 (L25) and DR4 (Choi et al. 2020), with the latter explored also in combination with *WMAP* and for different subsets of the data. Considering the 4-dimensional space of these parameters, we find that the DR6 and DR4 ACT-alone parameters differ at the 2.8σ level if we ignore correlations between the two datasets. This is therefore a lower limit on the difference if covariance were included. In particular, we find that the DR6 measurement of $\Omega_b h^2$ shifts upwards by 3σ compared to DR4. When ACT DR4 is combined with large-scale modes from *WMAP*, which was the nominal combination in Aiola et al. (2020), we find that DR6 agrees with the DR4 + *WMAP* ΛCDM best-fit model to within 1σ.[42]

In terms of understanding the difference between the cosmology preferred by ACT-alone for DR4 and the best-fit model for DR6 (or DR4 + *WMAP*), we note that Aiola et al. (2020) found that an artificial 5% re-calibration of TE compared to TT (dividing the DR4 TE bandpowers by 1.05) would bring the ACT-alone DR4 parameters into better agreement with DR4 + *WMAP* or *Planck*. This re-calibration had the effect of moving parameters along the degeneracy direction for $\Omega_b h^2 - n_s$ (see Fig. 14 of Aiola et al. 2020). In comparing CMB power spectra for DR4 and DR6, shown in Fig. 51, we find good agreement in TT and EE, and note that the TE residuals at $\ell < 2000$ with respect to the DR6 best-fit ΛCDM model are predominantly negative, indicating less power in the DR4 spectra compared to DR6. The DR6 TE spectra are more consistent with the model preferred by DR4 + *WMAP* and *Planck*. Although we have not re-analyzed the DR4 data at this stage, we speculate that our improved modeling of temperature-to-polarization leakage between DR4 and DR6 could impact the TE measurement. During the DR6 beam calibration analysis, we determined

Figure 50. Comparison of ΛCDM parameters (mean and 1σ error) estimated from different ACT datasets. The DR6 constraints (blue) are compared with various DR4 results from both ACT alone and ACT + *WMAP*, (Choi et al. 2020; Aiola et al. 2020). In all cases we are combining with a measurement of the optical depth to reionization from *Planck* Sroll2. The DR6 estimates are in good agreement with the DR4 + *WMAP* constraints, which comprised the baseline result presented in Aiola et al. (2020), but differ from the ACT-alone DR4 cosmology at $> 2.8\sigma$, with $\Omega_b h^2$ driving most of this difference. The two datasets can be reconciled by discarding the DR4 TE measurements at $\ell < 2000$, which could be impacted by beam modeling.

that the DR4 leakage estimation method was insensitive to low-ℓ ($\ell < 2000$) leakage. Given that in DR6 we find significant leakage at these large angular scales, we have reason to speculate that the $\ell < 2000$ leakage in DR4 could have been underestimated, both in central value and in uncertainty. A rough estimate suggests that the $\Delta D_\ell^{\rm TE}$ from underestimating the leakage has an RMS value between 2 and 4 $\mu{\rm K}^2$ for $350 < \ell < 1000$ and between 0.2 and 0.3 $\mu{\rm K}^2$ for $1000 < \ell < 2000$ — more details are given in Duivenvoorden et al. in prep. These numbers are estimated from the difference between the nominal DR6 leakage estimate and an estimate made using the DR4 leakage estimation
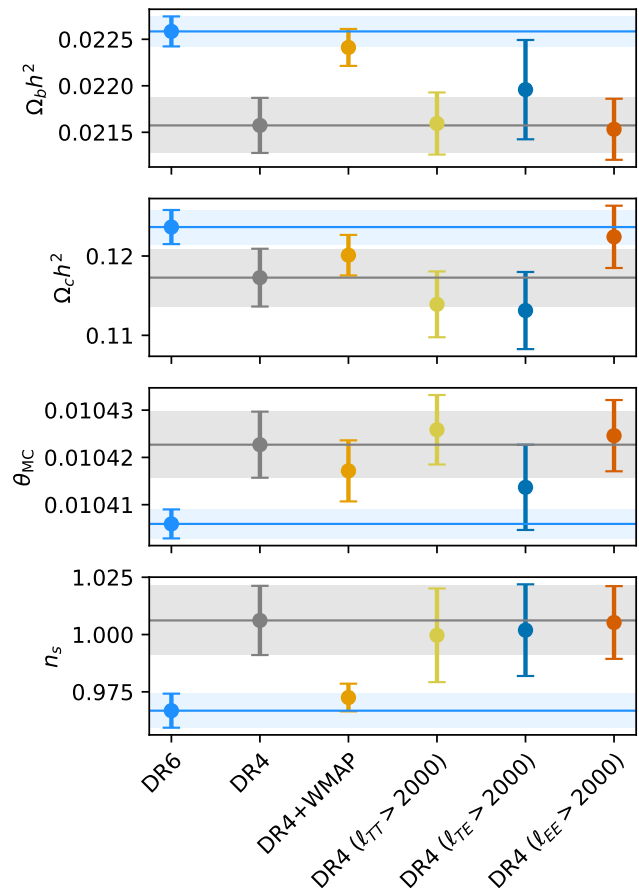
---

[42] Comparison of EDE constraints from DR4 and DR6 can be found in Appendix E.
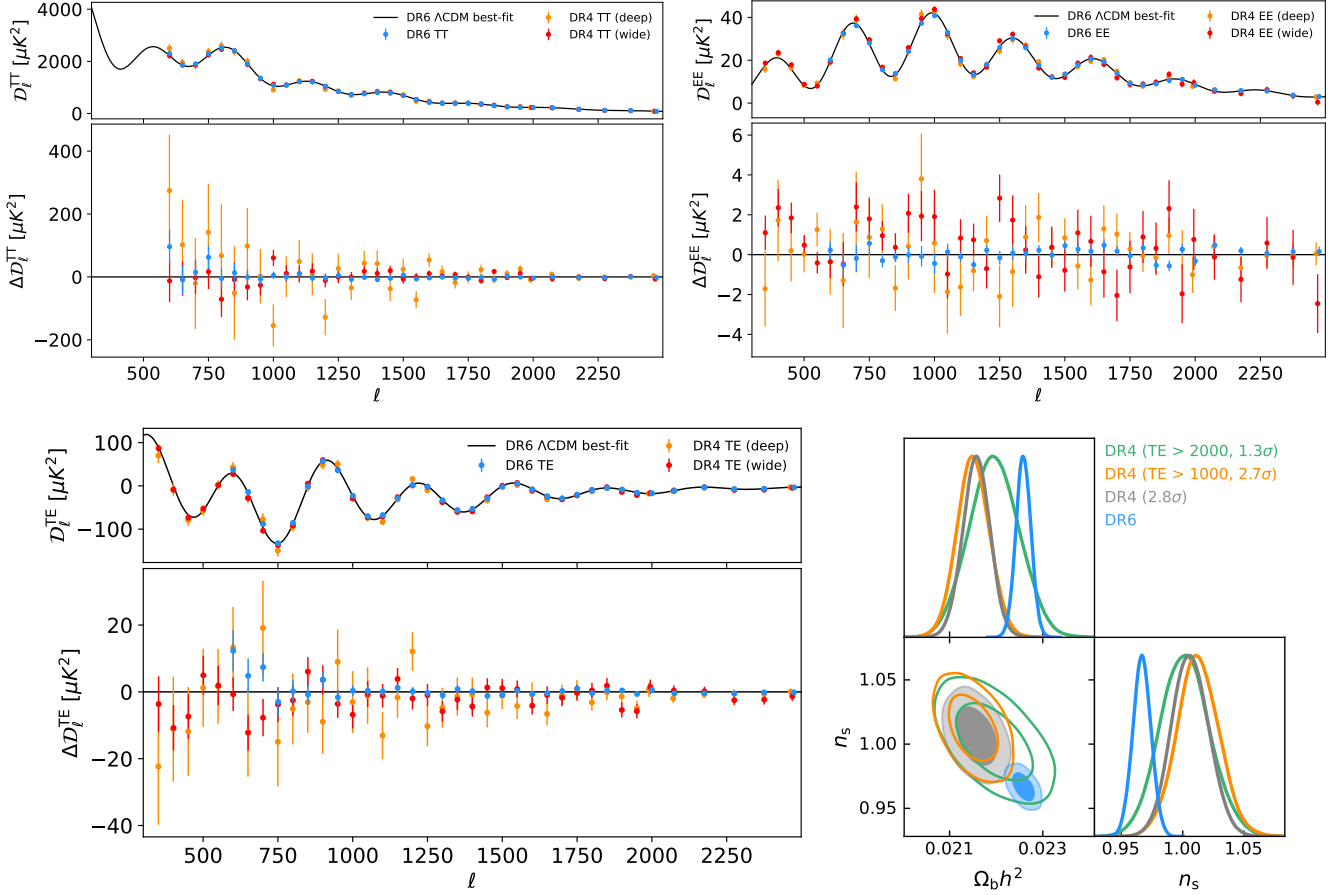
Figure 51. Comparison of the DR6 and DR4 CMB power spectra (TT in top left, EE in top right, and TE in bottom left) with respect to the DR6 ΛCDM best-fit model (L25). The DR4 residuals in TE are mostly negative at $\ell < 2000$, disfavoring the DR6 ΛCDM cosmology. The bottom right panel shows the $\Omega_b h^2 - n_s$ parameter space, which, as shown in Aiola et al. (2020), is very sensitive to the amplitude of the TE spectrum. Discarding the DR4 TE data at $\ell < 2000$ brings the DR6 and DR4 contours in closer agreement.

method. Other factors that might have contributed to a difference in TE between DR6 and DR4 are improvements in the map-making procedure (see N25): in DR6 we have not subtracted an estimate of the pickup (due to the ground and potential other sources) during map-making and we have upgraded to a pointing matrix that uses bilinear interpolation instead of nearest-neighbor interpolation. Although it is not understood how these two changes could influence the TE spectrum, it has not been verified that these upgrades would leave the DR4 TE spectrum unchanged. Figure 50 and the bottom right panel of Fig. 51 also show that simply removing data in TE at $\ell < 2000$ moves the DR4 limits into closer agreement with DR6. Cutting TT or EE at $\ell < 2000$ (Fig. 50) does not yield the same agreement, expanding parameter degeneracies in different directions. This exploration of TT and EE subsets also tests other aspects noted in the DR4 analyses, including the impact of the DR4 lack of power in TT and the $\ell < 1000$ region in EE where some deviations from ΛCDM (e.g., early dark energy and self-interacting neutrinos) were moderately preferred.

This assessment has been done assuming that the underlying model is ΛCDM; we do not rule out the possibility that the difference between DR4 and DR6 is due to the true model not being ΛCDM, as the two datasets do not fully overlap in angular scale, with DR4 having more statistical weight at smaller angular scales than DR6.

C. PRIMORDIAL MATTER POWER SPECTRUM COMPILATION

The primordial power spectrum constraints presented in §4.2 are derived sampling the primordial power over 30 bins centered on specific k wavenumbers, with individual flat uninformative priors as summarized in Table 5.

The measurement across bins presented in §4.2 can be mapped onto the linear matter power spectrum through the matter transfer function $\mathcal{T}(k) \equiv T(k)/k^2$ via

$$P_m(k, z = 0) = \frac{2\pi^2}{k^3} P_{\mathcal{R}}(k) \left(\frac{T(k)}{k^2} \right)^2 k^4$$
$$= 2\pi^2 k P_{\mathcal{R}}(k) \mathcal{T}^2(k), \qquad \text{(C1)}$$

where the dimensionless primordial power is converted to units of Mpc^3 through the $2\pi^2/k^3$ prefactor (note that $T(k)$ is dimensionless). As done in previous works, we use this relationship to show the CMB constraints on the primordial power spectrum alongside those from late-time probes such as galaxy surveys (e.g., Tegmark & Zaldarriaga 2002; Tegmark et al. 2004; Hlozek et al. 2012; Planck Collaboration 2020a; Chabanier et al. 2019). Our main results for the binned $P_{\mathcal{R}}(k)$ posterior distributions from P-ACT-LB (Fig. 6) are projected onto the linear matter power spectrum in Fig. 52. From Fig. 6 we note that P-ACT would give similar projections. We also show the P-ACT-LB best-fit ΛCDM model for both the linear and non-linear matter power spectrum.[43] Other constraints are shown from the Dark Energy Survey (DES) (Troxel et al. 2018), the Sloan Digital Sky Survey (SDSS) (Reid et al. 2010), the extended Baryon Oscillation Spectroscopic Survey (eBOSS) (Abolfathi et al. 2018), and the Hubble Space Telescope (HST) measurements of the UV galaxy luminosity function (UV LF) (Sabti et al. 2022). Note that P-ACT-LB detects non-zero power at $> 95\%$ CL up to $k = 0.43 \text{ Mpc}^{-1}$ whereas the *Planck*-alone constraints cut off at $k = 0.15 \text{ Mpc}^{-1}$. The bottom panel shows the residuals with respect to the P-ACT-LB best-fit ΛCDM linear power spectrum. At scales $k > 0.1 \text{ Mpc}^{-1}$, neighboring bins are more than 50% correlated. The fact that the highest k bins have mostly positive residuals is precisely why we find a slightly positive best-fit value for the running of the spectral index (in §4.1), although this is not statistically significant.

$k \times 10^2$ [Mpc^{-1}]	$e^{-2\tau} P_{\mathcal{R}}(k)$ Prior Range $\times 10^9$
0.01	$0.00 - 15.0$
0.03	$0.10 - 10.0$
0.10	$0.30 - 9.00$
0.32	$0.50 - 8.00$
1.06	$1.40 - 2.60$
1.23	$1.40 - 2.40$
1.43	$1.40 - 2.40$
1.66	$1.60 - 3.30$
1.92	$1.60 - 2.30$
2.23	$1.60 - 2.20$
2.59	$1.60 - 2.20$
3.00	$1.60 - 2.20$
3.48	$1.68 - 2.14$
4.03	$1.75 - 2.06$
4.68	$1.50 - 2.10$
5.42	$1.50 - 2.10$
6.29	$1.80 - 2.05$
7.29	$1.70 - 2.00$
8.45	$1.75 - 2.00$
9.81	$1.76 - 1.95$
11.4	$1.70 - 2.00$
13.2	$1.70 - 1.93$
15.3	$1.65 - 2.00$
17.7	$1.51 - 2.12$
20.6	$1.32 - 2.30$
23.8	$1.04 - 2.55$
27.7	$0 - 4.26$
32.1	$0 - 10.7$
37.2	$0 - 20.0$
43.1	$0 - 8.46$

Table 5. Central-bin wavenumber and prior ranges used for sampling $e^{-2\tau} P_{\mathcal{R}}(k)$ for each k bin.

[43] We use the `HMcode-2020` (Mead et al. 2021) dark-matter-only model of the non-linear power spectrum.
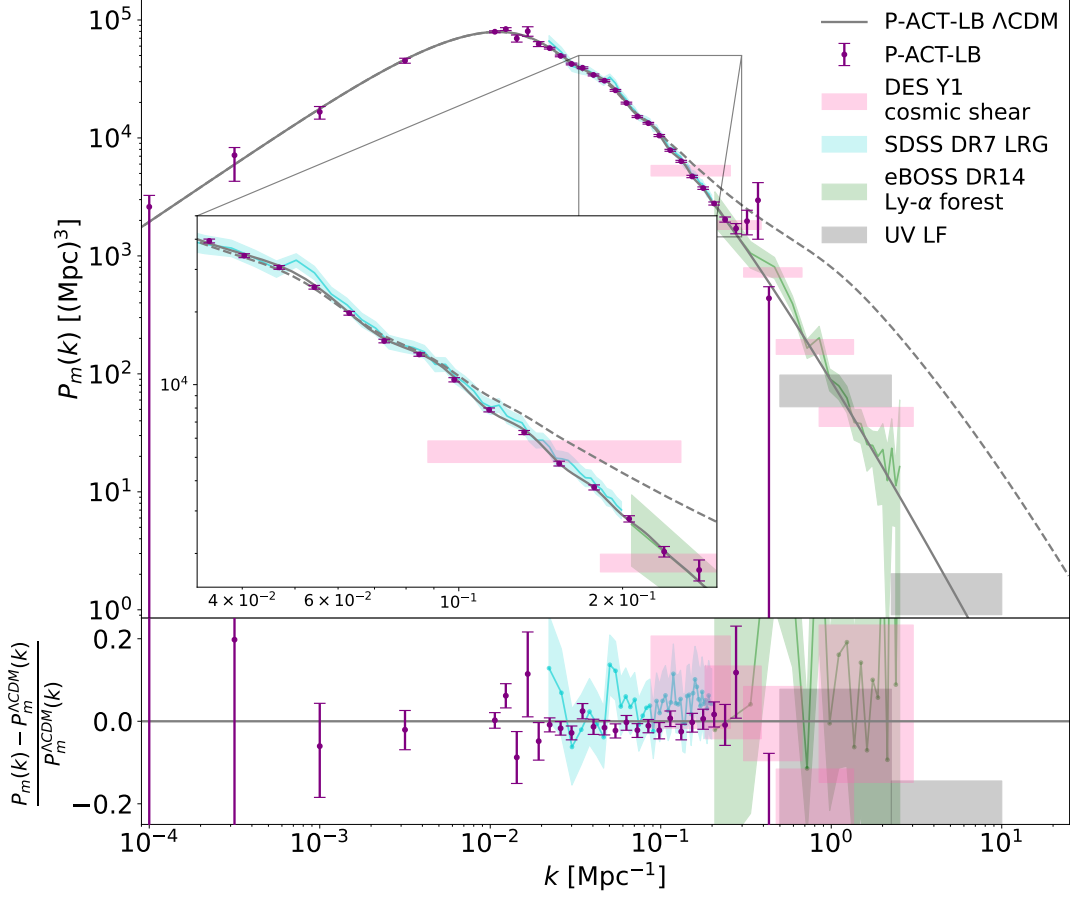
Figure 52. Constraints on the linear matter power spectrum. The P-ACT-LB best-fit ΛCDM linear matter power spectrum prediction is shown as a solid gray line; the dashed gray line shows the non-linear power spectrum computed from this best-fit ΛCDM model using `HMcode`. Our P-ACT-LB reconstruction of the binned linear $P_{\mathcal{R}}(k)$, presented in Fig. 6 in §4.2, is shown in purple. The P-ACT CMB dataset dominates this measurement. Other constraints are shown from DES-Y1 cosmic shear (Troxel et al. 2018), SDSS luminous red galaxies (Reid et al. 2010), eBOSS Lyman-α forest (Abolfathi et al. 2018), and HST measurements of the UV galaxy luminosity function (UV LF) (Sabti et al. 2022), as labeled. This plot was made based on code from Sabti et al. (2022) and Chabanier et al. (2019). The bottom panel shows the fractional residuals with respect to the P-ACT-LB best-fit ΛCDM linear power spectrum, with the y-axis optimized to highlight the scales more precisely measured.

D. ADDITIONAL CONSTRAINTS ON ISOCURVATURE

Table 6 presents the constraints on isocurvature models. In addition to the constraints on the amplitude of the primordial isocurvature power spectrum at two scales, we present constraints on the isocurvature power spectrum spectral index and the primordial isocurvature fraction,

$$\beta_{\mathrm{iso}}(k) \equiv \frac{\mathcal{P}_{\mathcal{II}}(k)}{\mathcal{P}_{\mathcal{RR}}(k) + \mathcal{P}_{\mathcal{II}}(k)}. \tag{D2}$$

Overall, we find no evidence of isocurvature perturbations and impose stringent constraints on a range of isocurvature scenarios.

Model and dataset	$10^{10} P_{\mathcal{II}}^{(1)}$	$10^{10} P_{\mathcal{II}}^{(2)}$	$100\,\beta_{\mathrm{iso}}^{(1)}$	$100\,\beta_{\mathrm{iso}}^{(2)}$	$n_{\mathcal{II}}$
Uncorrelated: ($n_{\mathcal{II}}=1$)					
CDI: Planck	< 0.9	< 0.9	< 3.7	< 4.2	1
CDI: P-ACT	< 1.1	< 1.1	< 4.4	< 4.9	1
CDI: P-ACT-LB	< 1.1	< 1.1	< 4.7	< 5.1	1
NDI: Planck	< 2.1	< 2.1	< 8.5	< 9.4	1
NDI: P-ACT	< 1.8	< 1.8	< 7.4	< 8.1	1
NDI: P-ACT-LB	< 1.8	< 1.8	< 7.4	< 8.1	1
Uncorrelated: (free $n_{\mathcal{II}}$)					
CDI: Planck	< 0.5	< 59	< 2.0	41^{+34}_{-41}	$2.4^{+1.1}_{-1.2}$
CDI: P-ACT	< 0.7	< 26	< 3.1	< 55	$2.0^{+1.1}_{-1.0}$
CDI: P-ACT-LB	< 0.7	< 26	< 3.1	< 55	$2.0^{+1.1}_{-0.9}$
NDI: Planck	< 1.5	$4.1^{+3.8}_{-4.1}$	< 6.3	16^{+13}_{-14}	$1.5^{+0.6}_{-0.7}$
NDI: P-ACT	< 1.6	< 6.1	< 6.7	< 23	$1.6^{+0.8}_{-1.0}$
NDI: P-ACT-LB	< 1.7	< 5.5	< 6.9	< 21	1.5 ± 0.9
Fully correlated: ($n_{\mathcal{II}} = n_{\mathcal{RR}}$)					
CDI: Planck	< 0.028	< 0.025	< 0.12	< 0.12	0.970 ± 0.010
CDI: P-ACT	< 0.025	< 0.023	< 0.11	< 0.11	$0.975^{+0.009}_{-0.010}$
CDI: P-ACT-LB	< 0.031	< 0.029	< 0.14	< 0.14	$0.977^{+0.007}_{-0.010}$
Fully anti-correlated: ($n_{\mathcal{II}} = n_{\mathcal{RR}}$)					
CDI: Planck	< 0.031	< 0.026	< 0.13	< 0.13	0.960 ± 0.010
CDI: P-ACT	< 0.027	< 0.023	< 0.11	< 0.11	$0.967^{+0.008}_{-0.010}$
CDI: P-ACT-LB	< 0.015	< 0.014	< 0.06	< 0.06	$0.972^{+0.007}_{-0.010}$

Table 6. Constraints on isocurvature perturbations for the models and dataset combinations considered in §4.3. We report the one-tailed 95% upper bound for parameters that are not detected; otherwise, we report the two-tailed 95% CL (chosen to facilitate comparison with results from Table 14 of Planck Collaboration 2020e).

E. ADDITIONAL CONSTRAINTS ON EARLY DARK ENERGY MODELS

Here we compare the constraints for EDE models with $n = 3$ (our baseline) and $n = 2$. Figure 53 shows the marginalized posterior comparisons for various dataset combinations, and Table 8 provides the numerical constraints. As for $n = 3$, we find no evidence of $n = 2$ EDE. The $n = 3$ model is analyzed using `CosmoPower`-based emulators of `class`, whereas the $n = 2$ model is run using `camb` due to instability of `class` for this model. These Boltzmann codes handle the EDE model in different ways: `class` solves the full perturbed Klein-Gordon equation, whereas `camb` uses an effective fluid approximation, described in Poulin et al. (2018). Some of the differences in these two approaches are described in Agrawal et al. (2023). We check that the two codes yield very similar constraints for the $n = 3$ model.

To facilitate comparisons with earlier work, we also compare constraints on the $n = 3$ EDE model from ACT DR4 (Hill et al. 2022) to those obtained here from ACT DR6, as shown in Fig. 54. We show results for ACT alone (DR6 versus DR4), P-ACT versus the combination of ACT DR4 with *Planck* 2018 TT data up to $\ell_{\max} = 650$, and P-ACT-LB$_{\text{BOSS}}$ versus the combination of ACT DR4 with *Planck* 2018 TT data ($\ell_{\max} = 650$), *Planck* 2018 CMB lensing data, and BAO data from BOSS (and pre-BOSS surveys). We consider results using BOSS BAO data here to ease the DR4-DR6 comparison. Significant portions of parameter space allowed by the DR4 data are excluded by the DR6 data, and the moderate hint of non-zero EDE in DR4 is no longer present in the more-sensitive DR6 dataset (see also Appendix B). However, we also see a narrow degeneracy direction in the parameter posteriors (e.g., in the f_{EDE}–$\Omega_c h^2$ panel) that is difficult to probe. Future experiments, such as the Simons Observatory and CMB-S4, will be needed to fully break this degeneracy and robustly detect or exclude pre-recombination EDE (see, e.g., Kou & Lewis 2025).

	$\Delta\chi^2$	Pref. (in σ)	$H_0^{(\text{EDE})}$	f_{EDE}	$\log_{10} z_c$
ACT	1.4	0.4	66.4	0.032	3.04
P-ACT	3.6	1.0	69.0	0.046	3.52
P-ACT-LB	5.5	1.5	70.3	0.064	3.50
W-ACT-LB	3.4	1.0	70.1	0.059	3.49

Table 7. The $\Delta\chi^2 = \chi^2_{\Lambda\text{CDM}} - \chi^2_{\text{EDE}}$ from the multifrequency likelihood MAP points for the $n = 2$ EDE model as compared to those found for ΛCDM for each dataset combination, and preference (in units of σ) for EDE using the likelihood-ratio test statistic. The MAP estimates for H_0, f_{EDE}, and $\log_{10} z_c$ in the EDE model are also shown. As with the $n = 3$ model, the data show no significant preference for non-zero EDE.

Dataset	$\Omega_c h^2$	$\Omega_b h^2$	$\ln 10^{10} A_s$	n_s	H_0	τ	f_{EDE}
ACT							
$n = 2$	$0.1272^{+0.0026}_{-0.0040}$	0.02259 ± 0.00020	3.061 ± 0.015	$0.962^{+0.020}_{-0.012}$	$67.5^{+0.9}_{-1.5}$	0.0574 ± 0.0056	< 0.091
$n = 3$	$0.1265^{+0.0024}_{-0.0036}$	0.02260 ± 0.00020	3.058 ± 0.015	$0.964^{+0.022}_{-0.014}$	$67.5^{+0.9}_{-1.7}$	0.0571 ± 0.0057	< 0.088
P-ACT							
$n = 2$	$0.1256^{+0.0033}_{-0.0055}$	$0.02264^{+0.00015}_{-0.00018}$	3.066 ± 0.015	0.9767 ± 0.0059	$69.3^{+1.0}_{-1.5}$	$0.0607^{+0.0056}_{-0.0067}$	< 0.11
$n = 3$	$0.1251^{+0.0031}_{-0.0055}$	$0.02267^{+0.00017}_{-0.00019}$	3.065 ± 0.015	$0.9785^{+0.0063}_{-0.0079}$	$69.3^{+0.9}_{-1.5}$	$0.0599^{+0.0055}_{-0.0066}$	< 0.12
P-ACT-LB							
$n = 2$	$0.1243^{+0.0030}_{-0.0053}$	$0.02269^{+0.00014}_{-0.00017}$	$3.070^{+0.012}_{-0.014}$	$0.9796^{+0.0048}_{-0.0055}$	$70.1^{+0.9}_{-1.5}$	$0.0634^{+0.0057}_{-0.0068}$	< 0.11
$n = 3$	$0.1233^{+0.0025}_{-0.0052}$	$0.02270^{+0.00015}_{-0.00018}$	$3.065^{+0.011}_{-0.013}$	$0.9809^{+0.0061}_{-0.0075}$	$69.9^{+0.8}_{-1.5}$	$0.0619^{+0.0056}_{-0.0066}$	< 0.12
W-ACT-LB							
$n = 2$	$0.1241^{+0.0024}_{-0.0056}$	0.02272 ± 0.00018	$3.067^{+0.012}_{-0.014}$	0.9755 ± 0.0061	$69.8^{+0.8}_{-1.6}$	$0.0630^{+0.0057}_{-0.0066}$	< 0.12
$n = 3$	$0.1233^{+0.0019}_{-0.0050}$	0.02273 ± 0.00019	$3.064^{+0.011}_{-0.013}$	$0.9766^{+0.0059}_{-0.0080}$	$69.8^{+0.7}_{-1.7}$	$0.0614^{+0.0056}_{-0.0066}$	< 0.12
P-ACT-LB$_{\text{BOSS}}$							
$n = 2$	$0.1246^{+0.0027}_{-0.0050}$	$0.02264^{+0.00015}_{-0.00017}$	$3.065^{+0.011}_{-0.013}$	$0.9769^{+0.0047}_{-0.0054}$	$69.4^{+0.8}_{-1.4}$	$0.0609^{+0.0054}_{-0.0064}$	< 0.11
$n = 3$	$0.1233^{+0.0021}_{-0.0045}$	$0.02265^{+0.00015}_{-0.00018}$	$3.061^{+0.011}_{-0.012}$	$0.9777^{+0.0053}_{-0.0071}$	$69.2^{+0.7}_{-1.3}$	$0.0600^{+0.0052}_{-0.0063}$	< 0.10

Table 8. Constraints on EDE for $n = 2$ and $n = 3$ models, for various dataset combinations. All numbers are reported as 68% confidence intervals, except f_{EDE}, which is given as a 95% upper bound.

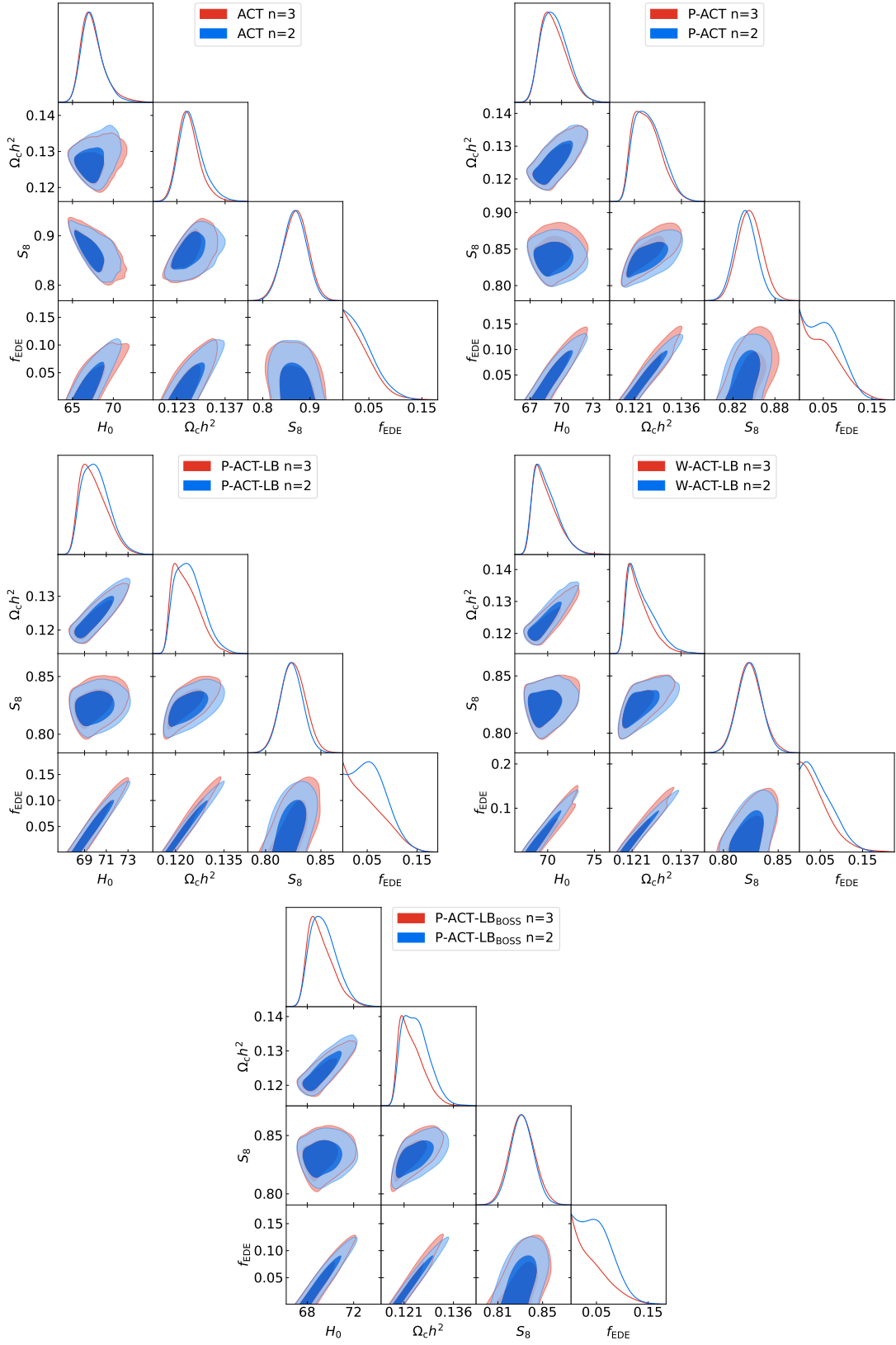**Figure 53.** Comparison of constraints from ACT (top left), P-ACT (top right), P-ACT-LB (middle left), W-ACT-LB (middle right), and P-ACT-LB$_{\text{BOSS}}$ (bottom) for EDE models with $n = 2$ (blue) and $n = 3$ (red).
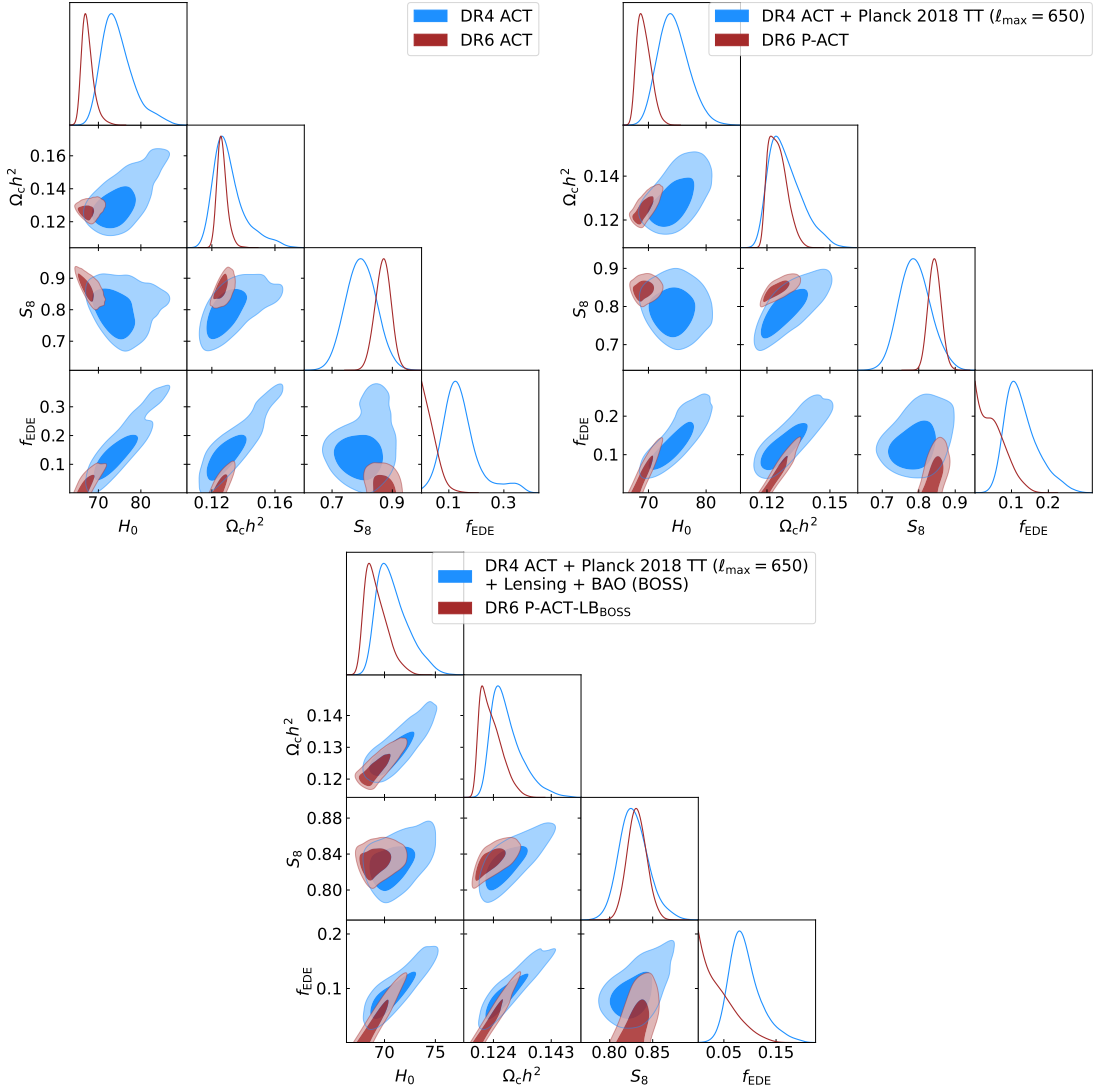
Figure 54. Comparison of constraints on the $n = 3$ EDE model from ACT (top left), P-ACT (top right), and P-ACT-LB$_{BOSS}$ (bottom) from the DR4 (blue) and DR6 (brown) data. The mild hint of non-zero EDE in DR4 (Hill et al. 2022) is not seen in the more-sensitive DR6 dataset. Beyond the significantly increased sensitivity, the DR6 dataset also benefits from improved map-making and systematic modeling compared to DR4, resulting in better-understood beams, transfer functions, and leakage corrections (see Appendix B for further discussion and details).

F. ADDITIONAL CONSTRAINTS ON MODIFIED RECOMBINATION

Figure 55. Marginalized parameter posteriors for the control points varied in the `ModRec` scenario analyzed in §5.5. The bottom (top) panels use DESI (BOSS) BAO. The dotted gray lines indicate the standard recombination scenario ($\tilde{q}_i = 0$).
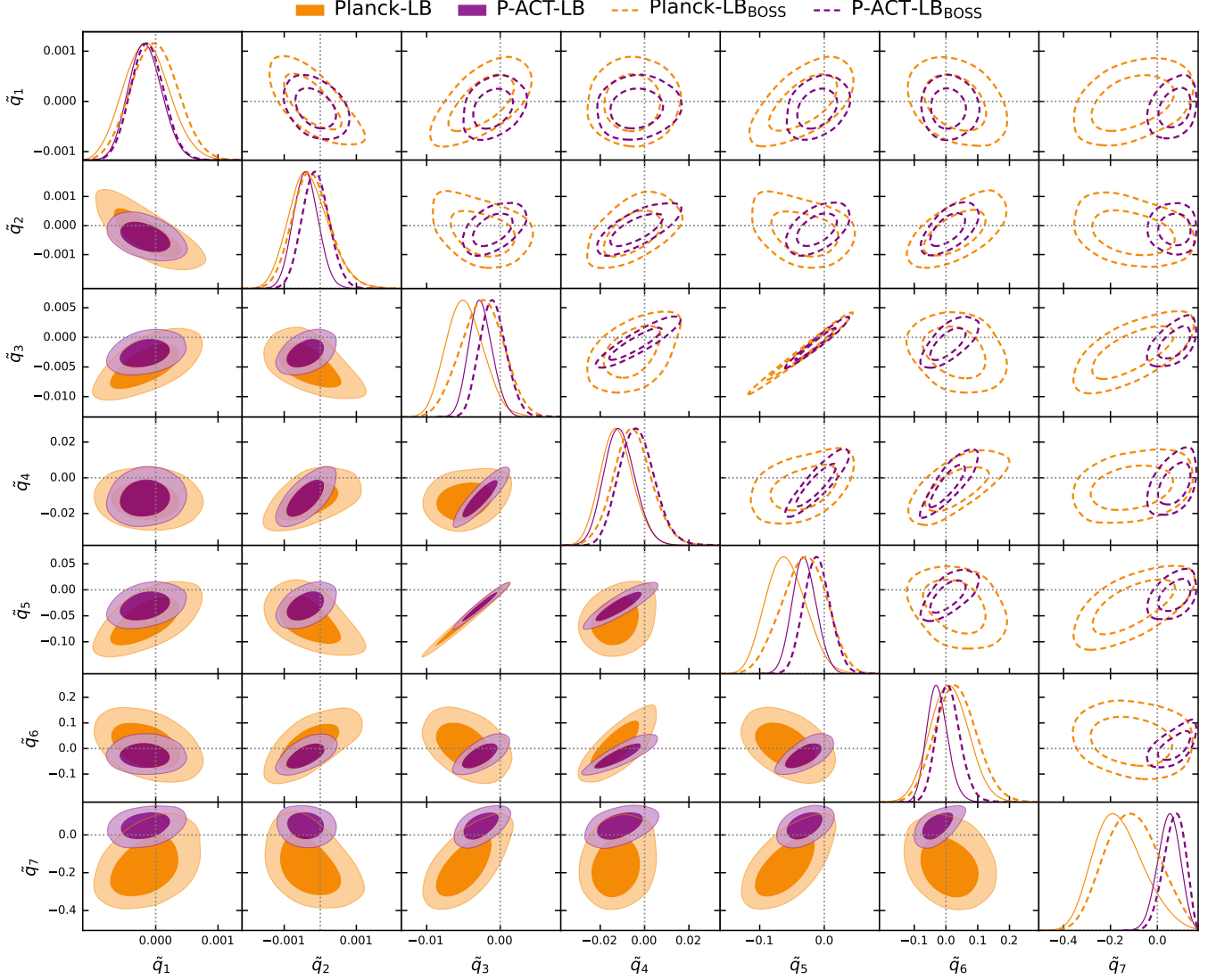
Figure 55 shows the marginalized parameter posteriors for the control points[44] varied in the `ModRec` scenario studied in §5.5. The lower triangle plot, shown with solid contours, compares the constraints from Planck-LB (orange) and P-ACT-LB (purple). The upper triangle plot, shown with dashed contours, compares the constraints from Planck-LB$_{\text{BOSS}}$ (orange) and P-ACT-LB$_{\text{BOSS}}$ (purple). Including ACT data significantly improves the constraints on the control points, yielding stringent bounds on the cosmological recombination history, which we find to be consistent with the standard recombination scenario ($\tilde{q}_i=0$; dotted gray lines) within 2σ across all control points analyzed in the `ModRec` model. Note that the control points in neighboring redshift bins can be highly correlated.

---

[44] See Lynch et al. (2024b) for the definition of $\tilde{q}_i$.

All Authors and Affiliations

Erminia Calabrese,[1, *] J. Colin Hill,[2, 3, †] Hidde T. Jense,[1] Adrien La Posta,[4] Irene Abril-Cabezas,[5, 6] Graeme E. Addison,[7] Peter A. R. Ade,[1] Simone Aiola,[3, 8] Tommy Alford,[9] David Alonso,[4] Mandana Amiri,[10] Rui An,[11] Zachary Atkins,[8] Jason E. Austermann,[12] Eleonora Barbavara,[13] Nicola Barbieri,[14, 15] Nicholas Battaglia,[16, 17] Elia Stefano Battistelli,[13] James A. Beall,[12] Rachel Bean,[16] Ali Beheshti,[18] Benjamin Beringue,[17] Tanay Bhandarkar,[19] Emily Biermann,[20] Boris Bolliet,[21, 6] J Richard Bond,[22] Valentina Capalbo,[13] Felipe Carrero,[23] Stephen Chen,[24] Grace Chesmore,[9] Hsiao-mei Cho,[25, 12] Steve K. Choi,[26] Susan E. Clark,[27, 28] Nicholas F. Cothard,[29] Kevin Coughlin,[9] William Coulton,[6, 5] Devin Crichton,[30] Kevin T. Crowley,[31] Omar Darwish,[32] Mark J. Devlin,[19] Simon Dicker,[19] Cody J. Duell,[33] Shannon M. Duff,[12] Adriaan J. Duivenvoorden,[34] Jo Dunkley,[8, 35] Rolando Dunner,[23] Carmen Embil Villagra,[5, 6] Max Fankhanel,[36] Gerrit S. Farren,[37, 38] Simone Ferraro,[37, 39, 38] Allen Foster,[8] Rodrigo Freundt,[16] Brittany Fuzia,[40] Patricio A. Gallardo,[9, 19] Xavier Garrido,[41] Martina Gerbino,[15] Serena Giardiello,[1] Ajay Gill,[42] Jahmour Givans,[35] Vera Gluscevic,[11] Samuel Goldstein,[2] Joseph E. Golec,[9] Yulin Gong,[16] Yilun Guan,[43] Mark Halpern,[10] Ian Harrison,[1] Matthew Hasselfield,[3] Adam He,[11] Erin Healy,[9, 8] Shawn Henderson,[25] Brandon Hensley,[44] Carlos Hervías-Caimapo,[23] Gene C. Hilton,[12] Matt Hilton,[45, 46] Adam D. Hincks,[47, 48] Renée Hložek,[43, 47] Shuay-Pwu Patty Ho,[8] John Hood,[49] Erika Hornecker,[47] Zachary B. Huber,[33] Johannes Hubmayr,[12] Kevin M. Huffenberger,[50] John P. Hughes,[51] Margaret Ikape,[47] Kent Irwin,[27] Giovanni Isopi,[13] Neha Joshi,[19] Ben Keller,[33] Joshua Kim,[19] Kenda Knowles,[52] Brian J. Koopman,[53] Arthur Kosowsky,[18] Darby Kramer,[54] Aleksandra Kusiak,[55, 6] Alex Laguë,[19] Victoria Lakey,[56] Massimiliano Lattanzi,[15] Eunseong Lee,[19] Yaqiong Li,[33] Zack Li,[39, 38] Michele Limon,[19] Martine Lokken,[57] Thibaut Louis,[41] Marius Lungu,[9] Niall MacCrann,[5, 6] Amanda MacInnis,[58] Mathew S. Madhavacheril,[19] Diego Maldonado,[36] Felipe Maldonado,[40] Maya Mallaby-Kay,[49] Gabriela A. Marques,[59, 60] Joshiwa van Marrewijk,[61] Fiona McCarthy,[5, 6] Jeff McMahon,[60, 49, 9, 62] Yogesh Mehta,[54] Felipe Menanteau,[63, 64] Kavilan Moodley,[46] Thomas W. Morris,[53, 65] Tony Mroczkowski,[66] Sigurd Naess,[67] Toshiya Namikawa,[5, 6, 68] Federico Nati,[69] Simran K. Nerval,[47, 43] Laura Newburgh,[53] Andrina Nicola,[70] Michael D. Niemack,[33, 16] Michael R. Nolta,[22] John Orlowski-Scherer,[19] Luca Pagano,[14, 15, 71] Lyman A. Page,[8] Shivam Pandey,[2] Bruce Partridge,[72] Karen Perez Sarmiento,[19] Heather Prince,[51] Roberto Puddu,[23] Frank J. Qu,[27, 28, 6] Damien C. Ragavan,[45] Bernardita Ried Guachalla,[27, 28] Keir K. Rogers,[73, 43] Felipe Rojas,[23] Tai Sakuma,[8] Emmanuel Schaan,[25, 28] Benjamin L. Schmitt,[19] Neelima Sehgal,[58] Shabbir Shaikh,[54] Blake D. Sherwin,[5, 6] Carlos Sierra,[9] Jon Sievers,[74] Cristóbal Sifón,[75] Sara Simon,[59] Rita Sonka,[8] David N. Spergel,[3] Suzanne T. Staggs,[8] Emilie Storer,[74, 8] Kristen Surrao,[2] Eric R. Switzer,[29] Niklas Tampier,[36] Leander Thiele,[76, 68] Robert Thornton,[77, 19] Hy Trac,[78] Carole Tucker,[1] Joel Ullom,[12] Leila R. Vale,[12] Alexander Van Engelen,[54] Jeff Van Lanen,[12] Cristian Vargas,[50] Eve M. Vavagiakis,[79, 33] Kasey Wagoner,[80, 8] Yuhan Wang,[33] Lukas Wenzl,[16] Edward J. Wollack[29] and Kaiwen Zheng[8]

[1] School of Physics and Astronomy, Cardiff University, The Parade, Cardiff, Wales, UK CF24 3AA

[2] Department of Physics, Columbia University, New York, NY 10027, USA

[3] Flatiron Institute, 162 5th Avenue, New York, NY 10010 USA

[4] Department of Physics, University of Oxford, Keble Road, Oxford, UK OX1 3RH

[5] DAMTP, Centre for Mathematical Sciences, University of Cambridge, Wilberforce Road, Cambridge CB3 OWA, UK

[6] Kavli Institute for Cosmology Cambridge, Madingley Road, Cambridge CB3 0HA, UK

[7] Dept. of Physics and Astronomy, The Johns Hopkins University, 3400 N. Charles St., Baltimore, MD, USA 21218-2686

[8] Joseph Henry Laboratories of Physics, Jadwin Hall, Princeton University, Princeton, NJ, USA 08544

[9] Department of Physics, University of Chicago, Chicago, IL 60637, USA

[10] Department of Physics and Astronomy, University of British Columbia, Vancouver, BC, Canada V6T 1Z4

[11] Department of Physics and Astronomy, University of Southern California, Los Angeles, CA 90089, USA

[12] NIST Quantum Sensors Group, 325 Broadway Mailcode 817.03, Boulder, CO, USA 80305

[13] Sapienza University of Rome, Physics Department, Piazzale Aldo Moro 5, 00185 Rome, Italy

[14] Dipartimento di Fisica e Scienze della Terra, Università degli Studi di Ferrara, via Saragat 1, I-44122 Ferrara, Italy

[15] Istituto Nazionale di Fisica Nucleare (INFN), Sezione di Ferrara, Via G. Saragat 1, I-44122 Ferrara, Italy

[16] Department of Astronomy, Cornell University, Ithaca, NY 14853, USA

[17] Universite Paris Cite, CNRS, Astroparticule et Cosmologie, F-75013 Paris, France

[18] Department of Physics and Astronomy, University of Pittsburgh, Pittsburgh, PA, USA 15260

[19] Department of Physics and Astronomy, University of Pennsylvania, 209 South 33rd Street, Philadelphia, PA, USA 19104

[20] Los Alamos National Laboratory, Bikini Atoll Rd, Los Alamos, NM, 87545, USA

[21] Department of Physics, Madingley Road, Cambridge CB3 0HA, UK

[22] Canadian Institute for Theoretical Astrophysics, University of Toronto, Toronto, ON, Canada M5S 3H8

[23] *Instituto de Astrofísica and Centro de Astro-Ingeniería, Facultad de Física, Pontificia Universidad Católica de Chile, Av. Vicuña Mackenna 4860, 7820436 Macul, Santiago, Chile*

[24] *Institute for Advanced Study, 1 Einstein Dr, Princeton, NJ 08540*

[25] *SLAC National Accelerator Laboratory 2575 Sand Hill Road Menlo Park, California 94025, USA*

[26] *Department of Physics and Astronomy, University of California, Riverside, CA 92521, USA*

[27] *Department of Physics, Stanford University, Stanford, CA*

[28] *Kavli Institute for Particle Astrophysics and Cosmology, 382 Via Pueblo Mall Stanford, CA 94305-4060, USA*

[29] *NASA/Goddard Space Flight Center, Greenbelt, MD, USA 20771*

[30] *Institute for Particle Physics and Astrophysics, ETH Zurich, 8092 Zurich, Switzerland*

[31] *Department of Astronomy and Astrophysics, University of California San Diego, La Jolla, CA 92093 USA*

[32] *Université de Genève, Département de Physique Théorique et CAP, 24 quai Ernest-Ansermet, CH-1211 Genève 4, Switzerland*

[33] *Department of Physics, Cornell University, Ithaca, NY, USA 14853*

[34] *Max-Planck-Institut fur Astrophysik, Karl-Schwarzschild-Str. 1, 85748 Garching, Germany*

[35] *Department of Astrophysical Sciences, Peyton Hall, Princeton University, Princeton, NJ USA 08544*

[36] *Camino a Toconao 145-A, Ayllu de Solor, San Pedro de Atacama, Chile*

[37] *Physics Division, Lawrence Berkeley National Laboratory, Berkeley, CA 94720, USA*

[38] *Berkeley Center for Cosmological Physics, University of California, Berkeley, CA 94720, USA*

[39] *Department of Physics, University of California, Berkeley, CA, USA 94720*

[40] *Department of Physics, Florida State University, Tallahassee FL, USA 32306*

[41] *Université Paris-Saclay, CNRS/IN2P3, IJCLab, 91405 Orsay, France*

[42] *Department of Aeronautics & Astronautics, Massachusetts Institute of Technology, 77 Mass. Avenue, Cambridge, MA 02139, USA*

[43] *Dunlap Institute for Astronomy and Astrophysics, University of Toronto, 50 St. George St., Toronto, ON M5S 3H4, Canada*

[44] *Jet Propulsion Laboratory, California Institute of Technology, 4800 Oak Grove Drive, Pasadena, CA 91109, USA*

[45] *Wits Centre for Astrophysics, School of Physics, University of the Witwatersrand, Private Bag 3, 2050, Johannesburg, South Africa*

[46] *Astrophysics Research Centre, School of Mathematics, Statistics and Computer Science, University of KwaZulu-Natal, Durban 4001, South Africa*

[47] *David A. Dunlap Dept of Astronomy and Astrophysics, University of Toronto, 50 St George Street, Toronto ON, M5S 3H4, Canada*

[48] *Specola Vaticana (Vatican Observatory), V-00120 Vatican City State*

[49] *Department of Astronomy and Astrophysics, University of Chicago, 5640 S. Ellis Ave., Chicago, IL 60637, USA*

[50] *Mitchell Institute for Fundamental Physics & Astronomy and Department of Physics & Astronomy, Texas A&M University, College Station, Texas 77843, USA*

[51] *Department of Physics and Astronomy, Rutgers, The State University of New Jersey, Piscataway, NJ USA 08854-8019*

[52] *Centre for Radio Astronomy Techniques and Technologies, Department of Physics and Electronics, Rhodes University, P.O. Box 94, Makhanda 6140, South Africa*

[53] *Department of Physics, Yale University, 217 Prospect St, New Haven, CT 06511*

[54] *School of Earth and Space Exploration, Arizona State University, Tempe, AZ, USA 85287*

[55] *Institute of Astronomy, Madingley Road, Cambridge CB3 0HA, UK*

[56] *Department of Chemistry and Physics, Lincoln University, PA 19352, USA*

[57] *Institut de Fisica d'Altes Energies (IFAE), The Barcelona Institute of Science and Technology, Campus UAB, 08193 Bellaterra, Spain*

[58] *Physics and Astronomy Department, Stony Brook University, Stony Brook, NY USA 11794*

[59] *Fermi National Accelerator Laboratory, MS209, P.O. Box 500, Batavia, IL 60510*

[60] *Kavli Institute for Cosmological Physics, University of Chicago, 5640 S. Ellis Ave., Chicago, IL 60637, USA*

[61] *Leiden Observatory, Leiden University, P.O. Box 9513, 2300 RA Leiden, The Netherlands*

[62] *Enrico Fermi Institute, University of Chicago, Chicago, IL 60637, USA*

[63] *NCSA, University of Illinois at Urbana-Champaign, 1205 W. Clark St., Urbana, IL, USA, 61801*

[64] *Department of Astronomy, University of Illinois at Urbana-Champaign, W. Green Street, Urbana, IL, USA, 61801*

[65] *Brookhaven National Laboratory, Upton, NY, USA 11973*

[66] *European Southern Observatory, Karl-Schwarzschild-Str. 2, D-85748, Garching, Germany*

[67] *Institute of Theoretical Astrophysics, University of Oslo, Norway*

[68] *Kavli IPMU (WPI), UTIAS, The University of Tokyo, Kashiwa, 277-8583, Japan*

[69] *Department of Physics, University of Milano - Bicocca, Piazza della Scienza, 3 - 20126, Milano (MI), Italy*

[70] *Argelander Institut fur Astronomie, Universität Bonn, Auf dem Hügel 71, 53121 Bonn, Germany*

[71] *Université Paris-Saclay, CNRS, Institut d'astrophysique spatiale, 91405, Orsay, France*

[72] *Department of Physics and Astronomy, Haverford College, Haverford, PA, USA 19041*

[73] *Department of Physics, Imperial College London, Blackett Laboratory, Prince Consort Road, London, SW7 2AZ, UK*

[74] *Physics Department, McGill University, Montreal, QC H3A 0G4, Canada*

[75] *Instituto de Física, Pontificia Universidad Católica de Valparaíso, Casilla 4059, Valparaíso, Chile*

88

^{76} Center for Data-Driven Discovery, Kavli IPMU (WPI), UTIAS, The University of Tokyo, Kashiwa, Chiba 277-8583, Japan

^{77} Department of Physics, West Chester University of Pennsylvania, West Chester, PA, USA 19383

^{78} McWilliams Center for Cosmology, Carnegie Mellon University, Department of Physics, 5000 Forbes Ave., Pittsburgh PA, USA, 15213

^{79} Department of Physics, Duke University, Durham, NC, 27708, USA

^{80} Department of Physics, NC State University, Raleigh, North Carolina, USA